Hunting for extrasolar planets around K giants

DISSERTATION

der Fakultät für Physik
der Ludwig-Maximilians-Universität München

zur Erlangung des Grades
Doktor der Naturwissenschaften
Dr. rer. nat.

vorgelegt von

MICHAELA P. DÖLLINGER
aus Regensburg

München, März 2008

1. Gutachter: Priv.-Doz. Dr. A. Weiss
2. Gutachter: Prof. Dr. A. Burkert
Tag der mündlichen Prüfung: 25. November 2008

"If we are alone in the universe,
then it is an awful waste of space."
(Carl Sagan)

Abstract

G–K giants are a class of stars that host extrasolar planets indicated by Radial Velocity (RV) variations in the stellar spectra. These stars show evidence of stellar oscillations (the so-called short-term RV variability) which can be used to determine additional properties of the stars. For a sample of 62 very bright K giants, spectra in the visual range with and without an iodine cell were obtained with the high resolution coudé echelle spectrograph mounted on the 2m telescope of the Thüringer Landessternwarte Tautenburg (TLS).

After the raw data reduction including bias-subtraction, flat-fielding and extraction using Image Reduction and Analysis Facility ($IRAF$) routines, precise RVs were calculated. For this purpose the resulting iodine absorption spectrum is superposed on top of the stellar spectrum to guarantee a stable wavelength reference against which the stellar RV is measured obtaining a RV accuracy of 3–5 $\mathrm{m\,s^{-1}}$. After around 3 years the statistics of the Tautenburg survey reflects the result of the discrimination between the different types of RV variability in the whole star sample. 13 K giants (21 %) belong to binary systems. Only 2 stars (3 %) show a "constant" RV behaviour. 17 stars (27 %) exhibit short-period RV variations possibly due to stellar oscillations. 6 stars (10 %) exhibit low-amplitude, long-term RV variations most likely due to planetary companions. For the remaining 24 K giants (39 %) the cause of RV variations is still undefined: possibly caused by stellar oscillations and/or rotational modulation as well as by planetary companions. Setiawan et al. (2004a) found comparable results in a study with the Fiber-fed Extended Range Optical Spectrograph ($FEROS$) in the southern hemisphere. Both studies seem to indicate, in contrast to what is observed among Main Sequence (MS) stars, that giant planets around giant stars are fairly common and do not favour metal-rich stars. From the published exoplanets only a small fraction (15) are giants, in contrast to the dominating MS stars. The reason for this is that the number of K giants so far surveyed is rather small in comparison to the monitored MS stars. Adding to my sample the 14 extrasolar planets from the literature, published by other authors, the first extended sample of hosting K giants is now available. To confirm the planetary companion candidates, the $HIPPARCOS$ photometry and the Hα activity was studied.

Furthermore for the whole Tautenburg sample spectra without the iodine cell and with a high Signal-to-Noise ratio (S/N $\geq$ 120) were taken to determine the Fe abundances [Fe/H] and other atmospheric stellar parameters such as the effective temperature $\mathrm{T_{eff}}$, the logarithmic surface gravity $\log g$ and the microturbulence velocity ξ from the spectra. The derived values are in very good agreement with the available literature values. The mass, radius and age of each star were determined by utilising theoretical isochrones and a modified version of Jørgensen & Lindegren's (2005) method. There exists an Age-Metallicity Relation (AMR) for my sample stars.

Zusammenfassung

Riesen der Spektraltypen G–K sind eine Sternklasse, die Exoplaneten besitzen. Die Exoplaneten werden durch Radialgeschwindigkeitsänderungen in den Sternspektren angezeigt. Diese Sterne zeigen aber auch Hinweise auf stellare Oszillationen (sog. kurzzeitige Radialgeschwindigkeitsveränderung), die genutzt werden, um zusätzliche Eigenschaften des Sterns zu bestimmen. Für eine Stichprobe von 62 sehr hellen K Riesen wurden Spektren im sichtbaren Wellenlängenbereich mit und ohne Jodzelle mit dem hochauflösenden Coudé Echellespektrographen aufgenommen, der am 2m Teleskop der Thüringer Landessternwarte Tautenburg (TLS) montiert ist.
Nach der Rohdatenaufbereitung (Biassubtraktion, Flatfielding und Extraktion), ausgeführt unter Verwendung von Image Reduction and Analysis Facility ($IRAF$) Routinen, wurden präzise Radialgeschwindigkeiten berechnet. Zu diesem Zweck ist das resultierende Jodabsorptionsspektrum dem Sternspektrum überlagert, um eine stabile Wellenlängenreferenz zu garantieren, gegen die dann die Radialgeschwindigkeit des Sterns gemessen wird. Bei dieser Messmethode wird eine Genauigkeit von 3–5 $\mathrm{m\,s^{-1}}$ erreicht. Nach etwa 3 Jahren spiegelt die Statistik des Tautenburgprogramms die unterschiedlichen Gründe für die Radialgeschwindigkeitsänderungen in der gesamten Sternstichprobe wider. 13 K Riesen (21 %) gehören zu Doppelsternsystemen. Nur 2 Sterne (3 %) zeigen ein "konstantes" Verhalten der Radialgeschwindigkeit. 17 K Riesen (27 %) zeigen möglicherweise kurzperiodische Radialgeschwindigkeitsänderungen verursacht durch stellare Oszillationen. 6 Sterne (10 %) zeigen langfristige Veränderungen der Radialgeschwindigkeit von niedriger Amplitude, die wahrscheinlich durch planetare Begleiter verursacht werden. Die verbleibenden 24 K Riesen (39 %) zeigen möglicherweise Radialgeschwindigkeitsänderungen verursacht durch stellare Oszillationen und/oder Rotationsmodulation sowie planetare Begleiter. Setiawan et al. (2004a) fand vergleichbare Ergebnisse in einer Studie mit dem Fiber-fed Extended Range Optical Spectrograph ($FEROS$) auf der Südhalbkugel. Bisher scheinen beide Untersuchungen im Gegensatz zu dem, was bei Hauptreihensternen beobachtet wurde, anzuzeigen, daß Riesenplaneten um Riesensterne ziemlich häufig sind und keine metallreichen Sterne bevorzugen. Von den publizierten Exoplaneten ist nur ein kleiner Anteil (15) im Orbit um Riesensterne erwähnt, im Gegensatz zu den dominierenden Hauptreihensternen. Ein Grund dafür ist, daß die Anzahl der bis jetzt beobachteten K Riesensterne ziemlich klein im Vergleich zu den überwachten Hauptreihensternen ist. Zusammen mit den Objekten meiner Stichprobe und den 14 in der Literatur von anderen Autoren erwähnten Exoplaneten steht jetzt die erste umfangreiche Stichprobe von K Riesen mit Exoplaneten zur Verfügung. Um die planetaren Begleiter zu bestätigen wurde die verfügbare $HIPPARCOS$ Photometrie und die H_α Aktivität untersucht.
Weiterhin wurden für die gesamte Tautenburgstudie Spektren ohne die Jodzelle mit einem sehr hohen Signal-zu-Rausch Verhältnis (S/N $\geq$ 120) aufgenommen, um damit

die Eisenhäufigkeit [Fe/H] und andere atmosphärische stellare Parameter wie die effektive Temperatur $T_{\rm eff}$, die logarithmische Oberflächengravitationsbeschleunigung $\log g$ und die Mikroturbulenzgeschwindigkeit ξ aus der Analyse der Spektren zu bestimmen. Die daraus abgeleiteten Werte sind in sehr guter Übereinstimmung mit den zur Verfügung stehenden Literaturwerten. Die Masse, der Radius und das Alter jedes Sterns wurden durch die Anwendung von theoretischen Isochronen und einer modifizierten Version der Methode von Jørgensen & Lindegren (2005) bestimmt. Ich finde eine Relation zwischen Alter und Metallizität (AMR) für die Sterne meiner Stichprobe.

Contents

List of Figures

List of Tables

Chapter 1

Introduction

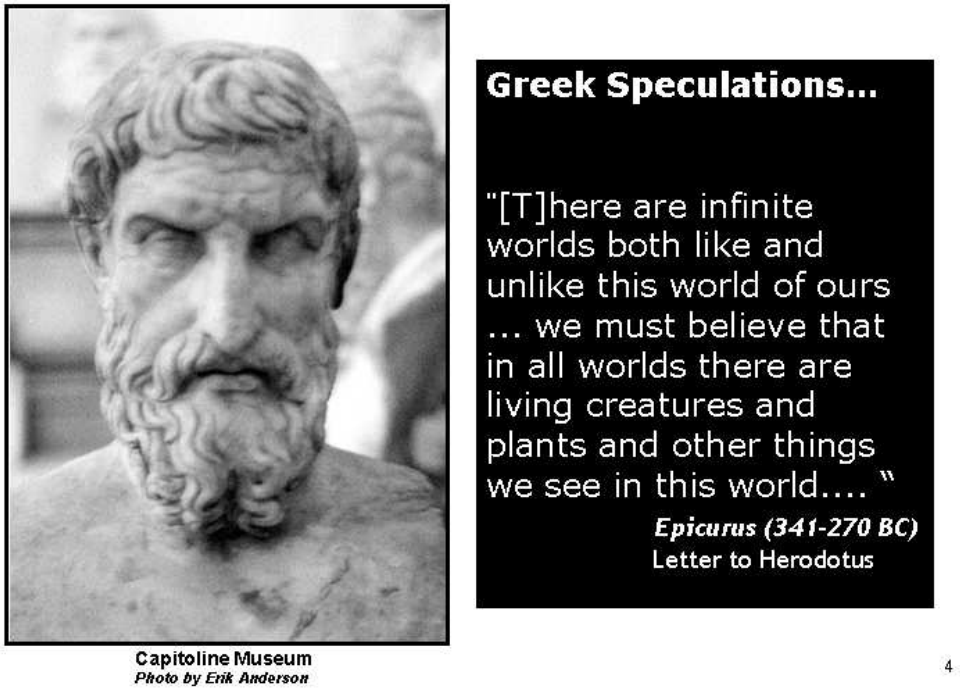

Figure 1.1: Epicurus (341–270 BC). Photo by Erik Anderson. Quotation by Epicurus.

Epicurus (341 BC, Samos – 270 BC, Athens; see Fig. 1.1) was an ancient Greek philosopher. Since his vision of the possibility of planets around stars other than our Sun, more than 2000 years of astronomical research and progress were necessary to confirm the hypothesis of the presence of planets around other stars (so-called exo-planets).
The first planet outside our solar system around a star similar to the Sun was discovered in 1995 around the star 51 Pegasi (G2.5 IV) located in the constellation Pegasus 15.4 pc from the Earth by Michel Mayor and Didier Queloz of the University of Geneva

using the Radial Velocity (RV) method at the Observatoire de Haute-Provence with the *ELODIE* spectrograph mounted on the 1.9m telescope (Mayor & Queloz 1995). The visual magnitude of the star is 5.49 mag and it has a metallicity of 0.20 ± 0.05 dex. With a stellar mass of 1.05 solar masses ($M_\odot$) and an age of 7.5–8.5 Gyrs – somewhat older than the Sun – it is slightly evolved off the Main Sequence (MS).

The planetary companion of 51 Pegasi – 51 Peg b is also the first representative of a special class of planetary companions known as the so-called "hot Jupiters". These are a kind of Jovian-mass gas giant planets orbiting their host stars in very short distances within 0.1 Astronomical Unit (AU) and on timescales of only a few days. In the case of 51 Pegasi the planetary companion with a "minimum mass" of 0.46 ± 0.2 Jupiter masses (M_{Jup}) orbits its parent star with a 0.052 ± 0.001 AU semi-major axis and within a 4.321 day period on an orbit with an eccentricity of 0.01 ± 0.003 (Mayor & Queloz 1995). Before the discovery of 51 Pegasi b it was assumed that giant planets only formed beyond 5 AU because, that distance onwards, the icy substances such as water, methane and ammonia could condense into solids, so planets had much more potential planet-forming material to incorporate. Consequently planetary companions with such close distances were not compatible with the accepted planet formation theories – the core accretion and the disk instability.

The core accretion theory includes the collisional accumulation of planetesimals by a growing solid core, followed by accretion of a gaseous envelope onto the core. The alternative mechanism for gas giant planet formation is the disk instability theory, where a gravitationally unstable region in a protoplanetary disk forms self-gravitating clumps of gas and dust, within which the dust grains coagulate and settle as sediment to form a central core (Boss 1997). According to the core accretion theory – planet formation from a protostellar accretion disk – the formation of planets so close to their host stars is not possible because there is simply insufficient mass in such small orbits. At the moment the most likely explanation for the formation of "hot Jupiters" is planetary migration. This scenario includes gravitational interactions between the planetary companion and the gas or planetesimals of a circumstellar disk resulting in orbital migration of the planet and a modification of the surface density of the disk. This is possible because the interaction is strong enough for masses in the regime of observed giant exoplanets to form a gap in the disk. This leads to a coupled evolution of planet and disk on a fuzzy timescale. Further material entering the gap moves the planet, and the gap inward on the accretion timescale of the disk (Type II migration) (Lin et al. 1996; Ward 1997) and changes the orbital parameters especially the semi-major axis of the planet. For terrestrial mass planets, surface density perturbations of the disk due to the planet are small and migration is driven by an asymmetry between interior and exterior torques. The inner spiral density waves exert a somewhat greater counterforce on the planet, causing it to migrate inwards on timescales that are short relative to the lifetime of the disk (Type I migration) (Lin et al. 1996; Ward 1997). The discussion of possible planet formation scenarios arising with the discovery of 51 Peg b is still ongoing due to the fact that 51 Peg b is not an exception.

Until now more than 200 extrasolar planets with different properties around MS stars have been detected via the RV technique which is the most successful planet detection method. The detection of so many planets beyond the solar system has also consequences for the accepted definition of a planet. The meaning of the word "planet" has changed in the course of time since its first coinage by the ancient Greeks who defined it as an astronomical object that appeared to wander against the field of fixed stars that were visible on the night sky (asteres planetai "wandering stars"). At this time only

5 planets – Mercury, Venus, Mars, Jupiter and Saturn – were known. In the end of the 16th century when, in astronomy, the heliocentric model became established over the geocentric view, the Earth was placed among the planets. Uranus, the seventh planet, was discovered by Sir William Herschel in 1781. The detection of Neptune in 1846 was based on mathematical predictions. Clyde Tombaugh detected Pluto in 1930 which was considered as the ninth planet in the solar system until August 24, 2006 when the International Astronomical Union (IAU) worked out a definition for a "planet".
According to this definition a "planet" is a celestial body, that, within the solar system,

- is in orbit around the Sun;
- has sufficient mass for its self-gravity to overcome rigid body forces so that it assumes a hydrostatic equilibrium (nearly round) shape; and
- has cleared the neighboourhood around its orbit;

or within another system,

- is in orbit around a star or stellar remnant;
- has a mass below the limiting mass for thermonuclear fusion of deuterium; and
- is above the minimum mass/size requirement for planetary status in the solar system.

Taking into account this definition, the solar system has only eight planets: Mercury, Venus, Earth, Mars, Jupiter, Saturn, Uranus and Neptune. Pluto didn't accomplish this definition and is now reclassified as a member of the dwarf planets together with Eris and Ceres and other Kuiper belt objects. Pluto was given the number 134340 and is also classified as the prototype of trans-Neptunian objects. It is a good example of the influence of new discoveries on our established knowledge.
In March 2008, 276 planets around other stars were discovered, but only a small fraction of the extrasolar planets are orbiting giant stars. Frink et al. (2002) discovered the first extrasolar planet around the K giant star HD 137759 (ι Dra). This was followed by the discovery of substellar companions to the stars HD 47536 (Setiawan et al. 2003a) and HD 122430 (Setiawan et al. 2003b). In the same year Sato et al. (2003) reported a planetary companion around HD 104985 (G9 III). Two planets around HD 59686 and HD 219449 were detected by Mitchell et al. (2003) and they mentioned two further planets around HD 54719 and HD 163917. Substellar companions have also been reported for HD 11977 (Setiawan et al. 2005) and HD 13189 (Hatzes et al. 2005). More recently Hatzes et al. (2006) confirmed that the initial RV variations found by Hatzes & Cochran (1993) in β Gem were in fact due to a planetary companion. This was confirmed by Reffert at al. (2006). Sato et al. (2007) published a planetary companion orbiting the Hyades giant ϵ Tau. Niedzielski et al. (2007) discovered an exoplanet to the KO giant HD 17092. Recently Johnson et al. (2007b) published an exoplanet around HD 167042. Thus until now only 14 planetary companions around G–K giants have been published by other authors. The reason for this is that the number of K giants so far surveyed is rather limited in comparison with the monitored MS stars. Any new discovery in this field represents important progress not only in the investigation of RV variability and its causes, but also in the planet formation theory because giants cover a little different stellar parameter regime (mass, radius, age) from MS stars and

allow in this way to investigate a slightly enlarged mass range to study the dependence of planet formation on the stellar mass. For this purpose an accurate determination of the stellar mass is essential. The mass of the star is also very important to verify the mass of planetary companions and the corresponding orbital parameters. Thus the accuracy of the stellar mass is crucial because giant stars with different masses and ages may occupy the same portion of the Hertzsprung-Russell-Diagram (HRD). There is considerable uncertainty unless a careful analysis is performed. The mass, radius and age of the star are determined by utilising theoretical isochrones and a modified version of Jørgensen & Lindegren's (2005) method. Accurate Fe abundances [Fe/H] and further atmospheric stellar parameters such as the effective temperature $T_{\rm eff}$, the logarithmic surface gravity $\log g$ and microturbulence velocity ξ for the host star derived from the spectra are the input for this method. The accurate [Fe/H] values for the G–K giants allow furthermore to search for correlations between the frequency of exoplanets and the metallicity of the host star. This point has been investigated for MS stars by Fischer & Valenti (2005) and Santos et al. (2000; 2003; 2004) but not for evolved stars. A sample of planet-hosting G–K giants is essential to make meaningful statistical statements about the frequency of planets around these type of stars.
Adding the 6 discovered planetary companions from the Tautenburg survey to the 14 exoplanets from the literature this first extended sample of 20 hosting G–K giants is now available for further studies to disentangle the secrets of planet formation.
With this extended sample of hosting G–K giants, it is also possible to compare the properties of these exoplanets and their evolved parent stars with the properties of the corresponding extrasolar planets around MS stars and their host stars. Through the consideration of different types of stars monitored in various planet search surveys there is the possibility to make predictions about the existence of several types of extrasolar planets depending on the host star and to compare these prognoses with the real results from the surveys. We would not expect the existence of "hot Jupiters", planets orbiting their parent stars within ≈ 0.05 AU, around cool evolved stars such as K giants because of their extendend envelopes of around 0.5 AU resulting in the absorption of the planetary companions. Since the first discoveries of substellar companions around K giants we can indeed confirm that in accordance with our considerations, "hot Jupiters" around this type of star do not exist. This behaviour is reasonable when we compare the size of the stellar radius of a giant and a MS star. When our Sun becomes a red giant in around 2.8 Gyrs its radius will be ≈ 0.5 AU, which is about 100 times its current size. Consequently Mercury, Venus and Earth will be engulfed. Mars and the planets further away will survive.
The Sun as a typical MS star has a radius of one solar radius ($R_\odot$). In general giants have radii of around 10 $R_\odot$. Giants of the Tautenburg sample show radii in the range of 5–37 $R_\odot$ (0.02–0.17 AU) corresponding to diameters of 0.04–0.34 AU (see Tab. 4.5). Consequently the size of the diameters of these stars already excludes the existence of "hot Jupiters" because they would be located within the target stars. In addition giants show stellar envelopes that any exoplanets would also be swallowed up by. Our understanding of the planet formation process and the properties of the different types of planetary companions increases with every new discovery enabled by various improvements in theory and in detection methods. This one day will culminate in the detection of a second Earth as predicted by Epicure long ago. At the moment the insufficient accuracy of our detection methods still inhibits us to reach this goal.

Chapter 2

Detection methods

Many different techniques are used to search for extrasolar planets. Each detection method has unique strengths and weaknesses and delivers information specific to the technique used on the properties of the host stars and of the detected planets. The most successful planet detection method is the Radial Velocity (RV) technique with (as of March 2008) 260 announced extrasolar planets within 224 planetary and 25 multiple planet systems. To compare 35 planets were detected by the transit method, 6 exoplanets were discovered by microlensing, and 5 planets were detected by imaging. Furthermore 3 planetary systems and 1 multiple planet system including 5 exoplanets around pulsars were discovered by timing. A short description will be given for the following planet detection methods: RV technique (see S2.1), astrometry (see §2.2), transits (see §2.3), gravitational microlensing (see §2.4) and direct imaging (see §2.5).

2.1 Radial velocity technique

The principle of the RV technique is graphically explained in Fig. 2.1.

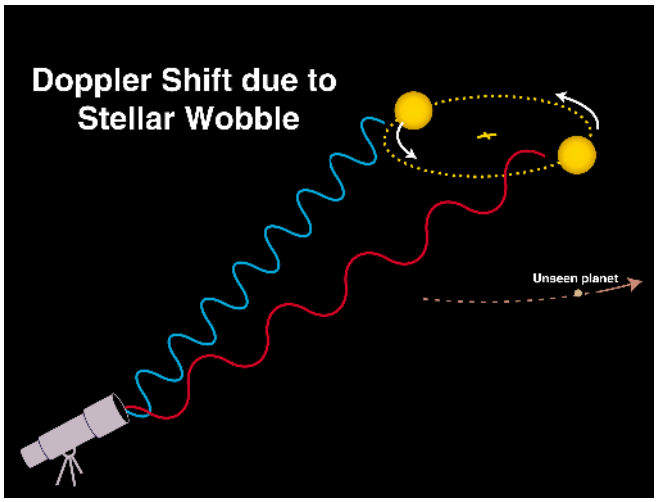

Figure 2.1: RV technique (http://obswww.unige.ch/ udry/planet/method.html).

A planetary companion orbiting a star produces a measurement ("wobble") of the star around the center of mass in a planetary system due to gravitational interactions between star and planetary companion. The resulting Doppler shift of the spectral lines can be detected in the spectra of the star taken over a long time span. As a consequence of the motion of the star, the light can be Doppler shifted to bluer (shorter) or redder (longer) wavelengths caused by approaching or receding the Earth. For the radial velocity method only stars with a sufficient number of narrow absorption lines are suitable. This requirement excludes Main Sequence (MS) stars of spectral type earlier than roughly F5 V because hotter stars have rotationally broadened lines. In addition the stellar photosphere must be sufficiently stable which eliminates active and pre-MS stars. K giant stars fit perfectly for the RV method because they are cool, they have lots of lines and the star rotates slowly. The RV technique is explained in more detail in §3.3.1.

2.2 Astrometry

Like the RV technique, astrometry indicates the existence of a planet from the motion of its host star around the common center of gravity. However the astrometric technique searches directly for tiny displacements of the star on the sky. If the mass difference between star and planet is very large, the planet motion along the orbit will produce a movement of the star over a long period. This can be observed with very precise instruments.
The astrometric signal is based on Kepler's Third Law and geometry and is given by:

$$\theta = \frac{ma}{MD} = \left(\frac{G}{4\pi^2}\right)^{1/3} \frac{m}{M^{2/3}} \frac{P^{2/3}}{D} \tag{2.1}$$

with
θ = semi-major axis
m = mass of planet
M = mass of star
a = orbital radius and
D = distance of star.

In the case of a circular orbit, the semi-major axis θ [radians] is independent of the orbital inclination which allows directly to determine the mass of the planetary companion by a given stellar mass. For non-circular orbits the inclination can be inferred by the observation of at least two orbital motion points in the plan of the sky. The additional information of the inclination angle delivered by astrometry can be used to determine the real mass of an exoplanet for which only the "minimum mass" $m \sin i$ is derived from radial velocity measurements. Astrometry is more sensitive to planets of nearby stars with larger orbital distances because the astrometric signal increases linearly with the semi-major axis a of the planetary orbit, in contrast to the radial velocity signal which scales with $1/\sqrt{a}$. The astrometric method is less suitable for massive stars and stars that are very far away. In contrast, RV measurements are independent of the distance, but are sensitive to companions with small orbital distances. Thus both detection methods complement each other perfectly.

2.3 Transits

The idea behind the transit method is the observation of a dip in the light curve of the star caused by the dimming of the stellar light caused by an orbiting planetary companion during its eclipse when the planet crosses the stellar disk as shown in Fig. 2.2.

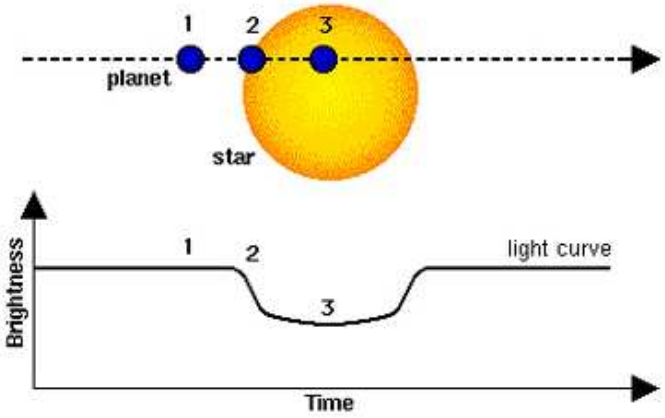

Figure 2.2: Principle of the transit detection method (http://www.cnes.fr/web/1403-constantly-stretching-the-limits-of-the-universe.php).

The characteristics of this change in the light curve such as amplitude and length are a function of the significant parameters of star and planet. The parameters include the ratio between exoplanet and stellar radii, brightness, stellar disk limb-darkening parameters and the inclination of the orbit. This last value is one of the limiting factors for the possibility of detecting transits because it depends on the probability of viewing a planetary system edge-on ($i \approx 90°$), a probability which depends on the distance between planetary companion and star (the semi-major axis of the planet orbit).
The second limitation is caused by the Earth's atmosphere during observations (air mass, absorption bands, seeing and scintillation) and observational conditions such as limited time coverage due to bad weather periods. A critical view at the dimmed stellar light curve is necessary to confirm the planet and to exclude further possible causes such as grazing eclipsing binary stars, background binaries, brown dwarfs, coronal effects or intrinsic stellar variations, flares and starspots. To do this, RV measurements and the determination of stellar parameters are essential.
The stellar parameters such as radius, orbital inclination i, density and surface gravity can be determined from the light curve if a mass from the radial velocity data is obtained.
Transits are rare, but potentially they bring a wealth of information.

2.4 Gravitational microlensing

Gravitational microlensing is another planet detection method. This technique is based on the gravitational lens effect which means that any massive object, acting as a lens, will bend the light of a bright background object which is called source.
The gravitational lens effect generates multiple distorted, magnified, and brightened

images of the background source. Gravitational lenses do not just distort light from the background object, they also magnify it. This is because gravitational lensing conserves surface brightness, so the distortion of the image of the source across a larger area of sky causes magnification. Even if the morphological change is too small to discern, an increase may be seen in an object's brightness as it is lensed. Microlensing is also achromatic which means that all wavelengths are affected equally. However the probability for a microlensing event is very small.

The lens effect can be distinguished between two types: microlensing and macrolensing. The criteria for the separation is the size of the mass of the lens. Single stars that have relatively low masses act as microlenses. The effect due to very massive objects such as galaxies or galaxy clusters is called macrolensing.

The timescale of the transient brightening depends on the mass of the foreground object as well as on the relative proper motion between the background source and the foreground lens. A low-mass lens such as a single star will pass in front of the source within a reasonable amount of time, seconds to years instead of years for a very massive macrolens such as a galaxy or cluster of galaxies. A microlens is thus a gravitational lens in which the lens can be practically observed to change in time.

In general as the lens moves in front of the source, the source will appear to brighten and then decline to normal as the lens moves away. This brightening as a function of time is known as a light curve. Since lens and source move relative to each other, the magnification, which depends on position, varies and a characteristic light curve is created.

The curve of such an event is very simple if the lens mass is concentrated in a single point. Than there are only two parameters contained in the light curve and that are the timescale and the amplification amplitude. These parameters depend on the lens mass, distance and velocity.

If the lensing object is a star with a planet orbiting it, then the planet can be detected as an additional microlensing event on top of that caused by the star. This can clearly be seen in Fig. 2.3, which shows the light curve of the star OGLE-05-390L including its planetary companion. In particular, OGLE-05-390L b is very interesting because this discovered exoplanet is, with 5.5 Earth masses ($M_\oplus$), the most Earth-like planet. The distance between the exoplanet and its host star, derived from the light curve besides the mass of the planet, is ≈ 2.6 the distance Earth–Sun. The Period is around 10 years. This value, not available from the gravitational microlensing method, was estimated from a Bayesian analysis. The host star is a red dwarf with 0.22 solar masses ($M_\odot$). In general the duration of the planet-induced deviation in the microlensing light curve can be very short ranging from hours to days. Light curves due to extrasolar planets can be very diverse and do not always deliver an unique mass separation fit. The derived property is not the planet mass, but only the mass ratio of the system consisting of host star and planet.

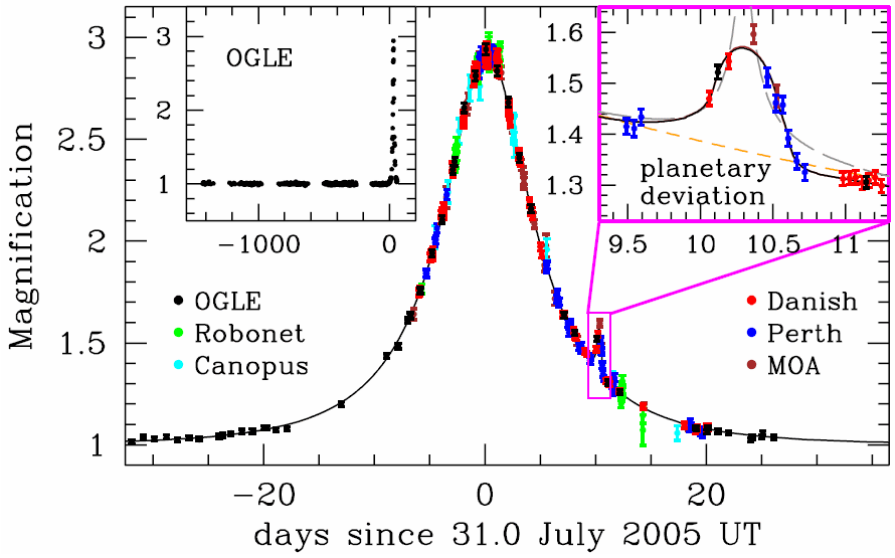

Figure 2.3: The observed light curve of the OGLE-05-390L microlensing event and best fit model plotted as a function of time. The data set consists of 650 data points from different observatories (Beaulieu et al. 2006).

2.5 Direct imaging

Indirect detection methods for extrasolar planets use the influence of the planetary companion on the host star. With the radial velocity technique, this is the movement of the host star caused by the gravitational influence of the exoplanet. With astrometry it is also the motion of the star and in transits the variation in the light curve (integrated stellar flux). Finally in the gravitational microlensing method, the temporal magnification of a background star due to a planetary system consisting of star and planet during its passage is observed. With the exception of a few planets all of the currently known exoplanets have been discovered by indirect methods, in particular the RV technique. Despite the success of these indirect methods they also have disadvantages, resulting in restrictions on the information on the properties of the detected planets. For example the RV technique can only provide the lower limit of the mass of the planetary companion as a consequence of the unknown inclination angle i of the orbit. Particularly all indirect detection methods cannot provide physical parameters such as the temperature, pressure, chemical composition and atmospheric structure of the exoplanets. These values can only be derived by direct detection and spectroscopy of the radiation from the exoplanets.
From this point of view the direct planet detection method complements the indirect methods. However direct imaging suffers from great difficulties due to the enormous brightness contrast between star and planet. The fact that the light coming from a planetary companion is much fainter than the signal from the host star requires the development of instruments that can provide a high contrast and spatial resolution which is a large disadvantage of this method. Fig. 2.4 shows the first directly imaged exoplanet. The substellar companion orbits the brown dwarf 2M1207.

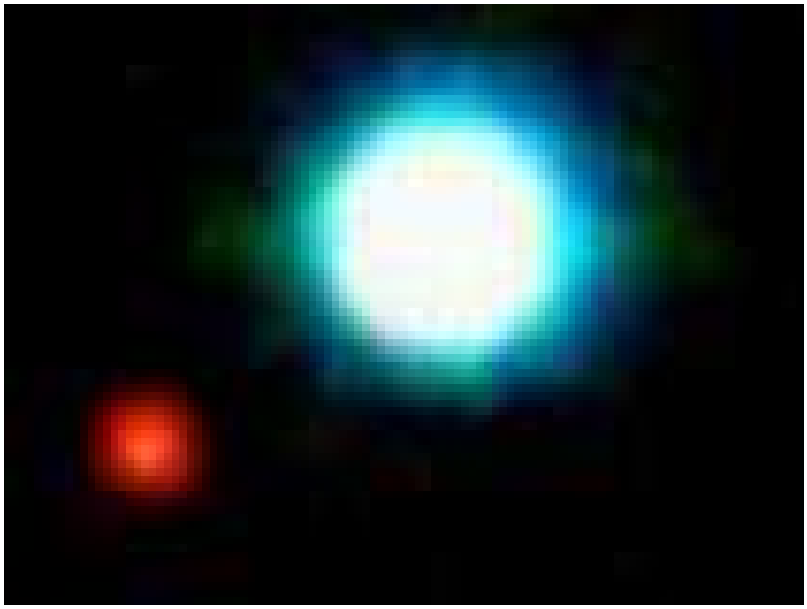

Figure 2.4: The brown dwarf 2M1207 and its planetary companion. The figure shows the first directly imaged exoplanet (http://www.newsimg.bbc.co.uk/media/images).

Chapter 3

Instrumentation and data reduction

Accuracy in the search for extrasolar planets has vastly been improved over the last two decades and continues to do so. For every planet detection method, there are demanding requirements on the telescopes and spectrographs. A good observation strategy is also very crucial for a successful search as well as time coverage unrestricted by geographical coordinates or bad weather conditions.

3.1 Instrument setup and targets

To apply the RV technique successfully in the search of exoplanets, it is necessary to have a suitable number of high Signal-to-Noise ratio (S/N) spectra.
The maximal exposure time for a spectrum is restricted by at least three factors:

- saturation (bright stars),
- cosmic rays (high energy sources) and
- rotation of Earth (very long exposure times can introduce additional broadening of the spectral lines in addition to shifts).

3.1.1 Spectrograph and iodine cell

All the spectra used in this thesis, with exception of a few follow-up observations, were taken by myself starting in February 2004 until July 2006 with the 2m Alfred-Jensch telescope at the Thuringa State Observatory (Thüringer Landessternwarte Tautenburg or TLS) using the high resolution coudé echelle spectrograph and an iodine absorption cell placed in the optical path. This is a grism crossed-dispersed echelle spectrometer that has a resolution of $R(\frac{\lambda}{\delta\lambda}) \sim 67{,}000$ and a wavelength coverage of 4630–7370 $\mathring{A}$ when using the so-called "visual" (VIS) grism. The high resolution and the large spectral range was required for the determination of Radial Velocities (RVs) and chemical abundances. A high resolving power was essential to guarantee a good wavelength separation, which means that wavelengths with a small wavelength separation of $\delta\lambda$ can be resolved. A large wavelength coverage was neccessary to achieve more accurate

Doppler shift measurements by using more spectral lines for radial velocity determinations and to provide enough Fe lines for abundance analysis.
Both criteria are best achieved by cross-dispersed echelle spectrographs which use two separate dispersing elements. The spectral resolution is reached with an echelle grating used in high orders. A second low-dispersion element such as a grism with an orthogonal dispersion axis guarantees that the overlapping orders of the main grating do not fall on the same pixels on the detector. This grating is a cross-disperser which produces a full echellogram on the detector.
Besides the required high resolution, the spectrograph must be as stable as possible to guarantee a constant and stable spectrograph Point Spread Function (PSF) – observed profile of an infinitely narrow line – which can change due to flexure or thermal expansion. Such a change can alter the measured position of line centroids, resulting in additional noise in the RV measurements.
To achieve stability of the PSF in Tautenburg, the echelle spectrograph is situated in a temperature-stabilised coudé room in the basement of the observatory. In addition the coudé echelle spectrograph is located in the coudé focus of the multipurpose Schmidt telescope and is fed by a so-called coudé train consisting of five flat mirrors. An echelle grating with 31.6 lines per mm and a f/46 collimator is used for the spectrograph. A beam of 150mm in diameter is produced by the collimator and the blaze-angle is 65°. The two-pixel resolution of 67,000 is reached during the observations by choosing a slit width of 0.52mm which corresponds to 1.2" in the sky. The spectrum is finally created by an f/3 camera of 450mm focal length onto a 2k x 2k CCD chip with 15μm pixels. The light is projected directly onto the entrance slit of the spectrograph so that the star can move along the slit during the night. As a consequence the centroid of the star in the slit can be slightly different in each observation, giving a translation into noise in the RV measurement.
At the beginning of the night the usual calibration images like Thorium Argons (ThAr), flat-fields and biases were taken. The science spectra – taken with and without the iodine absorption cell – were carried out with a total exposure time ranging between 5 and 10 minutes, depending on the stellar magnitude and weather conditions. The resulting Signal-to-Noise ratios were greater than 150 per wavelength pixel. The lowest S/N corresponded either to the faintest stars or to less optimal observing conditions such as clouds and bad seeing. For the faintest stars a minimum of counts is essential and for the brightest stars detection saturation must be avoided. In each observing night I took a spectra with the iodine cell for each star. The iodine absorption lines were produced by a temperature-regulated iodine absorption cell which was placed in the optical path of the telescope close to the entrance slit. The cell was heated to about 70°C and had to be kept at a stable temperature. The iodine cell produced iodine absorption lines that were superimposed on the observed stellar spectrum. They were used as a reference against which the radial velocity was measured. These lines cover a range of 1500 $\AA$ of the echelle spectrum and serve thus as a very precise wavelength scale which provides a specification of the spectrograph PSF in situ over the spectrum. The resulting composite spectrum enters the echelle spectrometer where it is convolved with the Instrumental Profile (IP) and dispersed nearly linearly in wavelength on the CCD.

3.1.2 The star sample

For the Tautenburg survey I prepared a target list. The star sample constituted of 62 K giants because they show a sufficient number of narrow absorption lines and a slow rotation which is essential for precise RV measurements. Giants are evolved stars that occupy a wide region of the cool portion of the Hertzsprung-Russell-Diagram (HRD). In the solar neighbourhood giants are low- and intermediate-mass (1–5 $M_{\odot}$) stars that have migrated off the Main Sequence (MS) and they will spend some hundred million years in this region, evolving along the Red Giant Branch (RGB). Fig. 3.1 shows the location of the sample stars in the HRD. G–K giants also occupy a region of the HRD where the evolutionary tracks of a wide range of spectral types (A–G) converge and so it is difficult to obtain accurate masses or to determine the spectral type of the progenitor star. As a consequence of this the mass determination is very important. The selection criteria are listed in the following. The target stars are well distributed over the sky in right ascension. Most of the sample stars have declinations greater than + 45° which are circumpolar at the Thüringer Landessternwarte Tautenburg and so visibility over most of the year is guaranteed. In addition the stars are very bright with absolute visual magnitudes M_V in the range 3 mag $\leq M_V \leq$ 6 mag which ensures short integration times and enables observing runs despite bad weather conditions. The absolute visual magnitudes for all targets are listed in Tab. 4.5. Moreover good *HIPPARCOS* parallaxes are available which are essential for further precise stellar parameter determinations such as mass, radius and age for each sample star. Known binaries were not excluded from the survey to guarantee an unbiased sample.

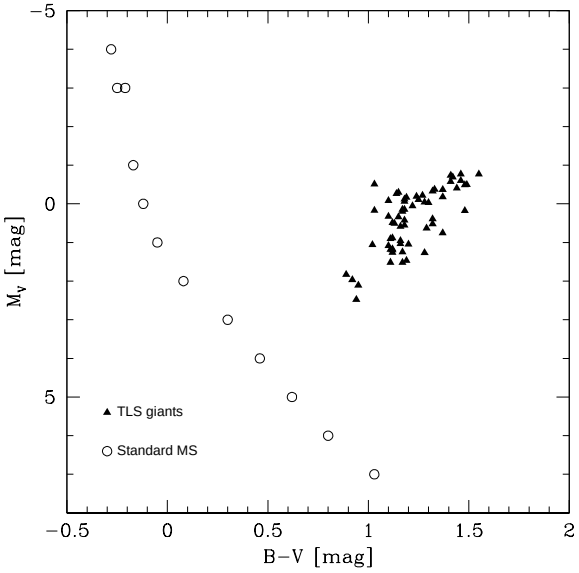

Figure 3.1: HRD of the Tautenburg star sample. The *TLS* giants are indicated with filled triangles. The empty circles represent the standard MS to give an impression of the location of the Tautenburg stars.

3.2 Raw data reduction with *IRAF* packages

IRAF is the Image Reduction and Analysis Facility software package (Barnes 1993) for the reduction and analysis of astronomical data. I used parts of this software to do the raw data reduction. During the observations at the beginning of the night in each observing run, bias and flat-field images were taken. After taking these so-called calibration images, spectra of the target stars were taken.
Bias frames are zero second exposures with the shutter closed. The counts are inserted by the electronics to ensure that no negative values exist. As the quality of the data can be increased by creating a mean bias through averaging several bias frames, the *IRAF* routine package *imcombine* was used. This averaged bias image was subtracted from all the science frames.
The flat-field images were obtained using the external flat-field screen mounted in the dome and with the same setup of the spectrograph. Flat-field images were used to correct the inhomogeneities of sensitivity of the detector. The lamps are continuous sources which mimic a pure black body emission, without spectral lines. A mean flat frame from the median of several individual flat-field images with the package *imcombine* was made removing pixels that detected a cosmic ray and are therefore saturated. They were replaced by compared consecutive images which were scaled to the same count rate, assuming the detector has a linear behaviour.
Spectra of a star are so-called object frames or science images. Flat-fielding of an object frame was made by dividing the object frame by the normalized flat frame with the package *imarith*. The normalization of the flat frame was made with the package *apflatten*. For each star and in each order of the spectrum, the spectrum was extracted from the science exposure using an individual aperture. The flat-field region was extracted with the same aperture. For each science image, a normalized flat-field was computed which was not corrected for the blaze angle of the grating respectively grism. This gave the opportunity to remove at least quantitatively the influence of the blaze angle on the science data under the assumption that the lamp is perfectly white. Every individual science image was then divided by its dedicated flat-field. The spectrum was extracted after the division by the flat-field image by considering the previously determined aperture. For each spectrum, a wavelength calibration was applied using the internal ThAr reference lamps.

3.3 Data analysis

After the raw data reduction which included bias subtraction, flat-fielding, extraction and wavelength calibration carried out with *IRAF*, the spectra were normalised. With the package *scombine* the 46 orders of the spectra were combined to one dimension. Further investigations were devoted to the RV and the abundances as well as the determination of the stellar parameters using and following well established standard procedures without modifications. The special programmes for both topics are explained in the next chapters.

3.3.1 Radial velocity technique

Before I will describe the determination of the radial velocities I will first give a short summary of the astronomical background. In planetary systems there are gravitational interactions among their members that appear as oscillating motions of the center of

mass and can be detected by the RV technique. The orbit of such a planetary system is defined by seven orbital elements (see Fig. 3.2). The meaning of each parameter is explained in the following:

- P, the orbital period;
- i, the inclination of the orbital plane with respect to the tangent plane of the sky (unknown and cannot be determined with the RV technique but with transits);
- Ω, the position angle (measured from North through East) of the line of nodes, which is the intersection of the orbital and tangent planes;
- ω, the angle between the direction of the ascending node (at which the star crosses the tangent plane while receding from the observer) and the periastron;
- a, the semi-major axis of the orbit;
- e, the eccentricity of the orbit;
- T, the time of passage through periastron.

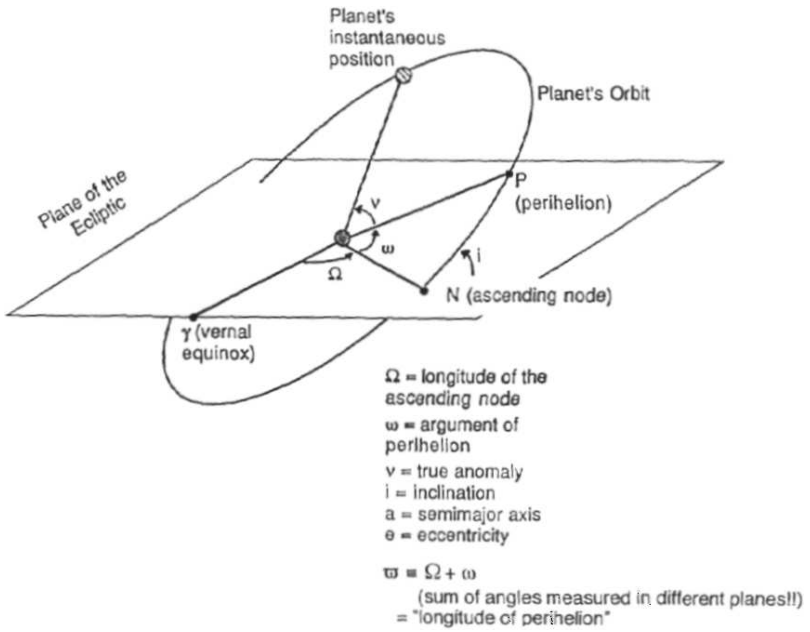

Figure 3.2: Orbital parameters (http://www.dtm.ciw.edu).

The detection of these slight perturbations in the line-of-sight velocity of the host star due to the effect of a planetary companion is the principle idea of the RV technique. The line-of-sight coordinate (z component) of the planet position can be expressed as

$$z = r \sin(\nu + \omega) \sin i \tag{3.1}$$

with
r, radial coordinate of the planet and
ν, true anomaly (position angle).
The radial velocity of the planet is obtained by differentiating Equation (Eq.) (3.1) with respect to time t:

$$\frac{dz}{dt} = [\cos(\nu + \omega) r\dot{\nu} + \sin(\nu + \omega)\dot{r}] \sin i. \tag{3.2}$$

The differentiation of the equation for the ellipsoid

$$r = \frac{p}{1 + e\cos\nu} = \frac{a(1 - e^2)}{1 + e\cos\nu} \tag{3.3}$$

with
p, half parameter and
e, eccentricity
delivers $\dot{r}$ with

$$\dot{r} = \frac{p^2}{(1 + e\cos\nu)^2} \frac{e}{p} \sin\nu\dot{\nu}. \tag{3.4}$$

Using Kepler's second law

$$r^2 \frac{dv}{dt} = c = \frac{2\pi}{P} ab \tag{3.5}$$

with
a, small semi-major axis and
b, large semi-minor axis
and inserting the expression (3.3) for r as well as (3.4) for $\dot{r}$ than the term dz/dt can be written as:

$$\frac{dz}{dt} = \frac{c \sin i}{p} [\cos(\nu + \omega)(1 + e\cos\nu) + \sin(\nu + \omega) e \sin\nu] \tag{3.6}$$

$$\frac{dz}{dt} = \frac{c \sin i}{p} [\cos(\nu + \omega) + \cos(\nu + \omega) e\cos\nu + \sin(\nu + \omega) e \sin\nu] \tag{3.7}$$

$$\frac{dz}{dt} = \frac{c \sin i}{p} [\cos(\nu + \omega) + e\cos\omega(\sin^2\nu + \cos^2\nu)]. \tag{3.8}$$

The radial velocity is also expressed as

$$v = \frac{dz}{dt} = K[\cos(\nu + \omega) + e\cos\omega] \tag{3.9}$$

with

$$K = \frac{2\pi}{P} \frac{a \sin i}{\sqrt{1 - e^2}}. \tag{3.10}$$

Taking into account the conservation of momentum

$$\sum_{i=1}^{n} \vec{p_i} = \sum_{i=1}^{n} m_i \vec{v_i} = constant \tag{3.11}$$

the radial velocity of the host star is:

$$v_{1z} = -\frac{m\frac{dz}{dt}}{M} = -\frac{1}{M} m \sin i \frac{2\pi}{P} \frac{a}{\sqrt{1-e^2}} [\cos(\nu+\omega) + e\cos\omega]. \tag{3.12}$$

And so the radial velocity curve V of the host star can be expressed as

$$V = \gamma + K_1[\cos(\nu+\omega) + e\cos\omega], \tag{3.13}$$

where γ is the radial velocity of the center of mass of the system, K_1 the velocity amplitude, and ν the true anomaly, the position angle measured from periastron (Heintz 1971; Murray & Dermott 1999). It is thus clear that the parameters P, T, e, and ω can be determined directly from the shape of the velocity time series but Ω and i cannot be determined from spectroscopic observations alone. The semi-major axis of the host star around the center of mass is related to K_1 by

$$a_1 \sin i = \frac{P}{2\pi} \sqrt{1-e^2} K_1. \tag{3.14}$$

According to Kepler's Third Law,

$$a^3 = (\frac{P}{2\pi})^2 G(m_1 + m_2), \tag{3.15}$$

where $a = a_1 + a_2$ is the semi-major axis of the relative orbit of the two components (host star and planet). Using $m_1 a_1 = m_2 a_2$, the following relation is derived

$$\frac{(m_2 \sin i)^3}{(m_1+m_2)^2} = \frac{P}{2\pi G} K_1^3 (1-e^2)^{3/2}. \tag{3.16}$$

The left-hand side of this equation is called the mass function *f(m)* of the system. If m_2 is mass of planet, $m_2 \ll m_1$ can be used to simplify. This gives

$$m_2 \sin i = (\frac{P}{2\pi G})^{1/3} K_1 m_1^{2/3} \sqrt{1-e^2}. \tag{3.17}$$

The value $m_2 \sin i$ can be derived from the radial velocity data provided that the mass of the central star m_1 is known. This quantity is often referred to as the "minimum mass" of the planetary companion and gives only a lower limit of the mass of the planet inferred by the RV method. The actual mass of the planetary companion can be considerably larger than the "minimum mass" $m_2 \sin i$ because the inclination angle i of the system is not known. For the large amount of published MS host stars a statistical analysis of a set of randomly oriented orbits was used to show that this uncertainty is statistically not so strong. In other words it is more likely to have mass errors < 50 % than > 50 %. Consequently the distribution of $m_2 \sin i$ is fairly representative of the true distribution of planetary mass. However the uncertainty is still unknown for individual objects. In the case of giant host stars the situation cannot be improved by statistical analysis due to the very small number of discovered planet-hosting giants. For both types of host stars only additional measurements using astrometry and direct

imaging can provide the inclination angle i of the planetary system and can solve the $\sin i$ ambiguity of the RV technique. Eq. (3.17) can be written in more convenient Jupiter masses (M_{Jup}) units as follows:

$$m_2 \sin i[M_{Jup}] = 3.5 \times 10^{-2} K_1[m\, s^{-1}] P^{1/3}[yr]. \tag{3.18}$$

In the case of our solar system Jupiter causes a 12.5 $\mathrm{m\,s^{-1}}$ "wobble" in the radial velocity of our Sun. In the literature the "minimum mass" $m_2 \sin i$ is as well written as $m_p \sin i$, $m \sin i$ or $M \sin i$.

To obtain the radial velocities of the Tautenburg sample a rigorous Doppler shift analysis was used consisting of a full model of the observed spectrum, including the shift of the stellar spectrum, the shift of the superimposed iodine lines, and the Point Spread Function (PSF) of the spectrograph (Valenti et al. 1996; Butler et al. 1996).

The observed composite spectrum was modeled by using two functions of wavelength: the bare, intrinsic stellar spectrum, I_s, and the transmission function T_{I_2}, of the I_2 absorption cell. The product of these two had to be convolved with the PSF and integrated over CCD-pixel bins to reproduce the observed spectrum. Trial shifts of the stellar and I_2 spectrum in Eq. (3.20) yielded a best fit to the observed composite spectrum. The spectrum taken with the iodine cell, $I_{obs}(\lambda)$, was modeled as

$$I_{obs}(\lambda) = k[I_s(\lambda + \Delta\lambda_s T_{I_2}\lambda + \Delta\lambda_{I_2})] \otimes PSF. \tag{3.19}$$

In this case $\Delta\lambda_s$ and $\Delta\lambda_{I2}$ are the shifts of the star spectrum and iodine transmission function, respectively, and the symbol $\otimes$ represents convolution. The constant k is proportional to the exposure level of the observation. In operation, $\Delta\lambda_s$, $\Delta\lambda_{I2}$, and k were determined by least-squares fitting to the observed, composite spectrum, I_{obs}. The final, corrected Doppler shift, $\Delta\lambda$, is simply given by

$$\Delta\lambda = \Delta\lambda_s - \Delta\lambda_{I_2}, \tag{3.20}$$

which was converted to a velocity by the Doppler formula.

I_s was obtained by observing each programme star without the I_2 cell in place. This gave $I_s \otimes$ PSF, not I_s as desired. The PSF was deconvolved from the spectrum using a Fourier division. The cell lines had to be independently accurately measured with a high resolution spectrograph to create a Fourier-Transform Spectrometer (FTS) I_2 spectrum. For this purpose the I_2-cell transmission function, T_{I_2}, was obtained by transporting the absorption cell to Kitt Peak National Observatory and using the FTS which gave a resolution of 300,000. The resulting I_2 transmission function was conveniently both oversampled and fully resolved, with no appreciable PSF of its own, thus ideally representing T_{I_2}.

The iodine transmission function, T_{I_2}, provided two other important elements in the modeling process. First, the FTS spectrum carries a highly absolute, vacuum wavelength scale, accurate to 1:10^8. Thus, each Lick Observatory spectrum taken through the I_2 cell automatically carries a superimposed wavelength scale having precision comparable to the best fundamental laboratory wavelengths. Second, the FTS iodine spectrum provides a reference spectrum with which the PSF of the TLS echelle spectra can be determined. The determination of the spectrograph PSF represented the final ingredient in Eq. (3.19) to solve for $\Delta\lambda_s$ and $\Delta\lambda_{I2}$. The PSF was determined as a function of position over the entire CCD format with a completely innovative strategy. Each stellar spectrum, taken through the I_2 cell, was divided by a bare template spectrum of that star, taken without the I_2 cell. This left the I_2 transmission function

convolved with the PSF, $T_{I_2} \otimes$ PSF, to an excellent approximation. With $T_{I_2} \otimes$ PSF, recovered from each observation, the PSF was extracted by using the known transmission function, T_{I_2}, obtained with the FTS at Kitt Peak. The extraction can be accomplished by a straightforward nonlinear least-squares approach in which different PSFs are tried until convolution with T_{I_2} yields a best fit with the recovered $T_{I_2} \otimes$ PSF. Since the PSF may be a function of wavelength, the analysis was carried out by using small pieces of spectrum at all locations over the echelle. This approach yielded the instantanous PSF for each observation at each wavelength, measured in situ. A complete description of this PSF-recovery technique is described in Valenti et al. (1992). The final Doppler shift was obtained from the average of the shifts of all stellar absorption lines (Marcy & Butler 1992).

Recapitulatory the idea of such a Doppler shift analysis is that the observed shift of a stellar spectrum consists of two parts, the actual Doppler shift and a small spurious shift caused by instrumental effects. A full modeling of the Instrumental profile (IP) is needed to analyze the composite spectrum: in fact spurious shifts between the narrow iodine lines and the much broader spectral lines can be introduced when the instrumental profile is not adequately considered. To avoid this in Tautenburg the iodine absorption cell method was used to measure long-term drifts of the spectrograph and thus to remove the instrumental shifts. It was possible because when starlight passes through the iodine absorption cell, which is at rest relative to the observatory, reference iodine absorption lines were superimposed that experience the same instrumental shifts as the stellar spectrum. Thus the spurious shifts are represented completely by the shifts of the iodine lines and were then applied as a correction to the observed shift of the stellar spectrum. The result is the Doppler shift of the star. The obtained Doppler shifts are relative to the stellar template, not absolute velocities. To achieve a radial velocity precision below 10 $\mathrm{m\,s^{-1}}$ simultaneous model of the instrumental profile by using iodine lines is essential.

The Doppler shifts have been measured and the radial velocities have been obtained using the programme *radialpsf*. *Radialpsf* was written mostly by Cochran and modified by Hatzes (Hatzes & Cochran 1993) to treat Tautenburg data. *Radialpsf* models the instrumental profile of the spectrograph (taking into account instrumental changes), iodine cell and star spectra to measure Doppler shifts. Since the IP changes along a spectral order, the spectrum was divided in segments (so-called chunks). About 130 chunks were used in the final analysis. Thus the spatial (and temporal) variations of the IP, which can introduce significant RV errors, can be modeled independently for each chunk. The RV shift in each chunk was calculated along with the IP using the IP reconstruction procedure outlined in Valenti, Butler & Marcy (1995) and a version of the Fahlman & Glaspey (1973) shift-detection algorithm. The RV measurements from all chunks were then combined weighted by the inverse square of the RV standard deviation for each chunk. The internal velocity error of a spectrum is calculated as the error of the mean velocity of all segments used for the analysis. The parameters for the instrument profile modeling were determined by using fast rotating featureless B stars. A detailed description of the technique is given in Desidera et al. (2003).

3.3.2 Determination of atmospheric stellar parameters

To determine the iron abundances [Fe/H], the effective temperature T_{eff}, the logarithmic surface gravity $\log g$ and microturbulence velocity ξ through detailed spectroscopic analysis, I used model atmospheres with the following assumptions: Local Thermodynamic Equilibrium (LTE), hydrostatic equilibrium, plane parallel geometry and flux constant. In detail for the Sun I used models from Edvardson et al. (1993) and for evolved stars I used a grid of Gustafsson's models et al. (1975).
To derive Fe abundances one needs to know the atomic parameters of the star and to have a reliable line list available. After assembling the line list and corresponding atomic data such as oscillator strengths $\log gf$ adopted by Pasquini et al. (2004), I visually inspected each line in all of the observed spectra, taken without the iodine cell (so-called templates), to check their profile and to discard blended lines. My final list included 144 Fe I and 8 Fe II lines spanning a spectral range from 5806.72 $\AA$ to 6516.08 $\AA$. For all the selected lines I adopted the physical properties such as excitation potentials listed in Pasquini et al. (2004).
Using a semi-interactive routine, I measured the Equivalent Widths (EWs) of all the lines assembled as described above. For all iron lines of the Tautenburg star sample, abundances were deduced from equivalent width measurements using an automatic line fitting procedure called *fitline*. This programme belongs to a *FORTRAN* software package developed by Francois (2005, private communication) and based on the algorithms of Charbonneau (1995), which perform both line detection and Gaussian fits of unblended lines. I made a selection of 100–120 unblended Fe I lines, depending on the quality of the spectra, spanning a spectral range from 5806.720 $\AA$ to 6858.150 $\AA$. I kept up to 8 of the detected unblended Fe II lines spanning a spectral range from 6084.110 $\AA$ to 6456.390 $\AA$.
The equivalent width W_λ, which is used to determine the iron content, range approximately from 5 to 150 m$\AA$. The equivalent width should be lower than 150 m$\AA$ because the code assumes that the profiles of the stellar lines can be represented by a Gaussian curve and this approximation is excellent as long as the equivalent width of the line is lower than $W_\lambda = 150$ m$\AA$ (Francois 2005, private communication).
With *inspector* each line was checked and those lines with a bad profile and/or a bad fit of the continuum fitting were eliminated from my line list. This step allows also to set interactively the position of the continuum. *Fitline* is then used a second time to recompute the equivalent widths of the lines for which the continuum has been adjusted. Afterwards the remaining spectral lines were identified with the programme *identify*. For about 5 % of the lines, the Gaussian profile adopted by *fitline* could not satisfactorily reproduce the observed profile. With these EWs, the microturbulence velocity ξ, the logarithmic surface gravity $\log g$, the effective temperature T_{eff} and then the iron abundance [Fe/H] of the studied star were derived, as I will describe below.

I used as a first guess the values typical of K giants as inferred from previous studies. Then I obtained the final constraints from the abundance analysis. The microturbulence velocity ξ is determined by assuming that the Fe I abundance does not depend on the EWs of the lines which corresponds in Fig. 3.3 (below left) to the minimization of the [Fe/H] versus EW slope. For this purpose a 1D fitting is computed to the iron abundances as a function of equivalent width. If the gradient of 1D fitting to the abundance equivalent width relation is zero, or $\leq 10^{-3}$, then it is assumed for all stars that the correct microturbulence has been obtained. If a significant positive or negative slope is measured, the microturbulence ξ is increased or decreased, respectively, and the iron abundances rederived. A ξ value is adopted by repeating this

steps until a zero slope results.

For the determination of the effective temperature T_{eff} I imposed an excitation equilibrium of Fe I and Fe II lines of different excitation potentials – the Fe I abundance is independent of the excitation potentials of the lines (top left). The logarithmic spectroscopic surface gravity $\log g$ was determined by using the ionisation equilibrium balance of Fe I and Fe II lines (see Fig. 3.3).

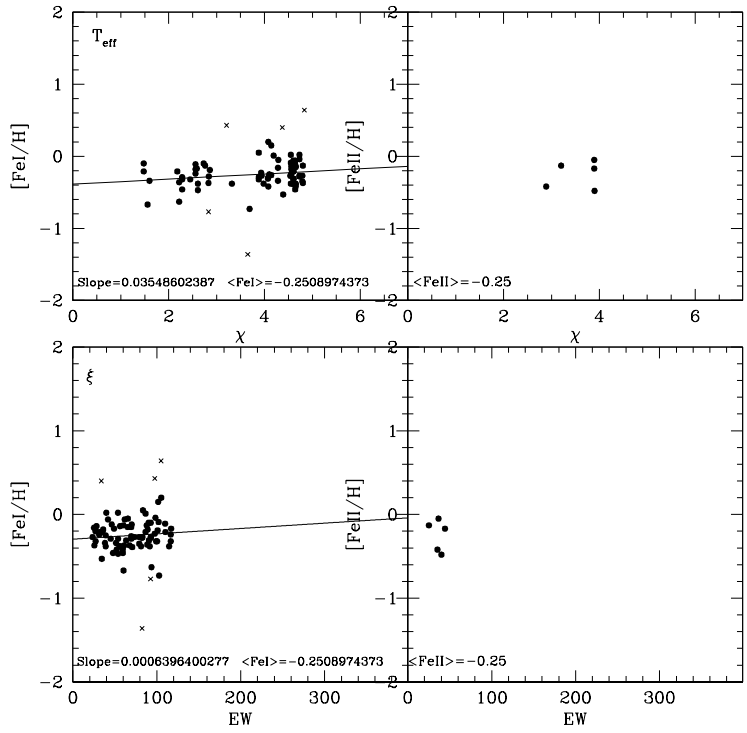

Figure 3.3: Determination of the stellar microturbulence velocity ξ (below left) and effective temperature T_{eff} (top left) for HD 73108 as an example. The dots represent the [Fe I/H] values (left) as well as the [Fe II/H] val ues (right). [Fe I/H] values with more than 2 σ variances are tagged with crosses. The FeI and FeII abundances are plotted against the equivalent width EW (below) and the excitation potential χ (top). The microturbulence velocit y of 1.2 $\mathrm{km\,s^{-1}}$ was determined by achieving an [Fe I/H] versus EW slope of $\leq 10^{-3}$. The exact value of the slope is plotted in the diagram (below left). The effective temperature of 4415 K was determined by approaching an [Fe I/H] versus χ slope of 0.036 (top left). The spectroscopic surface gravity $\log g$, with a value of 1.8 dex, was determined by the adaption of the derived <FeI> and <FeII> values of -0.25 dex (left and right).

To determine the spectroscopic surface gravity I computed a small grid of models from Edvardson et al. (1993) at the appropriate effective temperature T_{eff} for each star of the Tautenburg sample starting at the physical gravity and stepping 0.2 dex in $\log g$ from it in both directions. After approaching a promising value I refined the steps to 0.1 dex or less in $\log g$ until the final result was reached. For the spectro-

scopic gravities, a difference of 0.01 dex or less in the total iron abundance [Fe/H] as determined from <FeI> and <FeII> (see Fig. 3.3) was judged to meet the ionization-balance requirement. Hence for the ionization balance the uncertainty in the derived gravity was obtained by examining the sensitivity of Fe I and Fe II to gravity changes. The uncertainty depends very much on how much variation one allows between the total iron abundances as determined from Fe I and Fe II before determining that the ionization-balance criteria are not met. But at the end of the procedure a model from the small grid was usually capable of giving such an agreement. It should be noted that non-Local Thermodynamic Equilibrium (non-LTE) effects act mainly on Fe I, whereas Fe II shows a very small sensitivity to them. A good estimate of the true metallicity of the stars can thus be achieved using Fe II lines. The iron abundances in this work are derived for each star from the values of the Fe I and Fe II lines by minimizing the difference between both values (see Fig. 3.3). The entire process of defining the atmospheric parameters is iterated until a consistent set of model atmosphere parameters is finally obtained. The atomic parameters of the spectral lines of Fe I and Fe II are shown in Tab. 3.1. In this table the wavelengths of the Fe I and Fe II lines are given in $\mathring{A}$. The excitation energy of the lower energy level in the transition for all lines is given in electron Volt (eV). The oscillator strengths are also listed. The results for the atmospheric parameters of the whole star sample are listed in Tab. 4.1 in §4. The errors linked to the uncertainties in the stellar atmosphere parameters were estimated using "standard" procedures and assuming the following "standard" variations taken from the literature (Lambert & Ries 1981; Pasquini et al. 2004 and Luck 1991):

- Δ $T_{\rm eff}$ = $\pm$ 50 K,
- Δ $\log g$ = $\pm$ 0.2 dex, and
- Δ ξ = $\pm$ 0.2 km s^{-1}.

In detail Pasquini et al. (2004) analyzed the dependence of Fe I and Fe II on $\log g$, $T_{\rm eff}$ and ξ for one Population I (Pop I) giant. They found out that a systematic shift of 100 K in $T_{\rm eff}$, would for instance, produce a 0.2 dex shift in $\log g$ without changing substantially the derived Fe abundance. In addition the internal uncertainty in the microturbulence velocity ξ was estimated in this work based on the sensitivity of the slope of the assumed microturbulence velocity. A value of a change of $\pm$ 0.2 km s^{-1} was taken because it has a noticeable effect upon the slope of the relation and on the derived mean abundances.

Table 3.1: Atomic parameters of the spectral lines used for iron.

Species	λ [$\AA$]	χ [eV]	$\log gf$ [dex]	Species	λ [$\AA$]	χ [eV]	$\log gf$ [dex]
FE1	5806.720	4.61	-1.05	FE1	6330.840	4.73	-1.74
FE1	5809.220	3.88	-1.84	FE1	6335.340	2.20	-2.18
FE1	5814.810	4.28	-1.97	FE1	6336.830	3.69	-1.05
FE1	5833.940	2.61	-3.66	FE1	6353.850	0.91	-6.36
FE1	5855.090	4.60	-1.76	FE1	6355.040	2.84	-2.29
FE1	5856.080	4.29	-1.64	FE1	6358.690	0.86	-4.47
FE1	5859.600	4.55	-0.60	FE1	6380.750	4.19	-1.38
FE1	5861.110	4.28	-2.45	FE1	6392.540	2.28	-4.03
FE1	5862.370	4.55	-0.39	FE1	6393.610	2.43	-1.58
FE1	5881.280	4.60	-1.84	FE1	6408.030	3.69	-1.00
FE1	5905.690	4.65	-0.73	FE1	6411.660	3.65	-0.72
FE1	5909.970	3.21	-2.78	FE1	6419.940	4.73	-0.25
FE1	5916.260	2.45	-2.99	FE1	6421.350	2.28	-2.03
FE1	5927.800	4.65	-1.09	FE1	6430.860	2.18	-2.01
FE1	5930.190	4.65	-0.23	FE1	6469.210	4.83	-0.77
FE1	5934.670	3.93	-1.17	FE1	6475.630	2.56	-2.94
FE1	5956.710	0.86	-4.61	FE1	6481.880	2.28	-2.98
FE1	5969.580	4.28	-2.73	FE1	6498.950	0.96	-4.70
FE1	5983.690	4.55	-0.78	FE1	6518.370	2.83	-2.30
FE1	5987.070	4.79	-0.15	FE1	6533.930	4.56	-1.45
FE1	6003.020	3.88	-1.12	FE1	6546.250	2.75	-1.54
FE1	6016.600	3.55	-1.82	FE1	6556.810	4.79	-1.72
FE1	6024.050	4.55	-0.11	FE1	6569.220	4.73	-0.38
FE1	6027.060	4.07	-1.09	FE1	6571.180	4.29	-2.95
FE1	6054.080	4.37	-2.33	FE1	6574.250	0.99	-5.02
FE1	6056.010	4.73	-0.46	FE1	6575.040	2.59	-2.71
FE1	6065.490	2.61	-1.53	FE1	6581.210	1.48	-4.85
FE1	6078.500	4.79	-0.40	FE1	6591.310	4.59	-2.00
FE1	6079.000	4.65	-1.13	FE1	6593.870	2.43	-2.42
FE1	6082.720	2.22	-3.57	FE1	6597.560	4.80	-1.06
FE1	6093.670	4.60	-1.51	FE1	6608.040	2.28	-4.03
FE1	6094.360	4.65	-1.94	FE1	6609.120	2.56	-2.69
FE1	6096.660	3.98	-1.93	FE1	6627.540	4.55	-1.68
FE1	6098.280	4.56	-1.88	FE1	6678.000	2.69	-1.42
FE1	6105.150	4.54	-2.07	FE1	6699.140	4.59	-2.19
FE1	6120.240	0.91	-5.95	FE1	6703.580	2.76	-3.16
FE1	6151.620	2.18	-3.30	FE1	6705.110	4.61	-1.06
FE1	6157.730	4.08	-1.25	FE1	6710.320	1.48	-4.88
FE1	6159.380	4.61	-1.85	FE1	6713.770	4.80	-1.60
FE1	6165.360	4.14	-1.55	FE1	6715.390	4.59	-1.54

Continued overleaf ...

Table 3.1: Atomic parameters of the spectral lines used for iron.

... continuing from previous page.

Species	λ [$\AA$]	χ [eV]	$\log gf$ [dex]	Species	λ [$\AA$]	χ [eV]	$\log gf$ [dex]
FE1	6173.340	2.22	-2.88	FE1	6716.250	4.56	-1.85
FE1	6187.990	3.94	-1.72	FE1	6725.350	4.10	-2.30
FE1	6200.320	2.61	-2.44	FE1	6726.670	4.59	-1.09
FE1	6212.070	4.37	-2.69	FE1	6733.150	4.64	-1.58
FE1	6213.440	2.22	-2.49	FE1	6739.520	1.56	-4.80
FE1	6219.290	2.20	-2.43	FE1	6750.160	2.42	-2.59
FE1	6226.730	3.88	-2.20	FE1	6806.850	2.73	-3.20
FE1	6229.230	2.84	-2.97	FE1	6810.260	4.60	-1.11
FE1	6240.650	2.22	-3.21	FE1	6820.370	4.64	-1.31
FE1	6246.330	3.60	-0.88	FE1	6837.020	4.59	-1.80
FE1	6252.570	2.40	-1.69	FE1	6839.840	2.56	-3.38
FE1	6254.250	2.28	-2.44	FE1	6842.690	4.64	-1.22
FE1	6265.140	2.18	-2.53	FE1	6843.660	3.65	-0.86
FE1	6270.230	2.86	-2.61	FE1	6851.660	1.60	-5.25
FE1	6271.280	3.32	-2.81	FE1	6855.720	4.39	-1.75
FE1	6297.800	2.22	-2.74	FE1	6857.240	4.08	-2.16
FE1	6301.510	3.65	-0.60	FE1	6858.150	4.61	-1.06
FE1	6302.500	3.69	-0.91	FE2	6084.110	3.20	-3.97
FE1	6307.850	3.64	-3.27	FE2	6247.560	3.89	-2.52
FE1	6311.500	2.83	-3.22	FE2	6416.930	3.89	-2.85
FE1	6315.310	4.14	-1.23	FE2	6432.680	2.89	-3.73
FE1	6315.810	4.08	-1.71	FE2	6456.390	3.90	-2.31
FE1	6322.690	2.59	-2.43				

3.3.3 Estimation of other parameters such as age and mass

Star properties were derived from the comparison of stellar parameters with theoretical isochrones (Girardi et al. 2000) using a modified version of the Bayesian estimation algorithm of Jørgensen & Lindegren's (2005). The mathematical formulation is essential the same, but some relatively minor details are different in the modified version. In contrast to Jørgensen & Lindegren (2005) $\log T_{eff}$ was used instead of T_{eff}. Moreover Jørgensen & Lindegren (2005) just estimate the age. In addition to the age in my work other parameters such as $\log g$, mass and B–V were determined. The modified version avoids statistical biases and takes into account error estimates of all observed quantities. The method of Jørgensen & Lindegren (2005) in general has strengths and weaknesses. It is better than other methods often used, for instance the "isochrone fitting" one, because the different population probability along the isochrones is taken into account. This point is discussed in more detail in Jørgensen & Lindegren (2005). However it relies on the evolutionary tracks, which can be systematically too hot or too cool. This kind of systematic error has not been taken into consideration. Consequently I took not into account error estimates of the theoretical tracks and I used only the isochrones of Girardi et al. (2000). To check the accuracy of the method it would be necessary to use for my sample stars further sets of isochrones to compare the results. However such a test was beyond the scope of this work. To try to give at least a first estimate of the accuracy of the method and the applied isochrone set I used

already determined literature values of a few stars as input values for a comparison (see §4.4). The result of the modified Jørgensen & Lindegren's (2005) method is the total Probability Distribution Function (PDF) for each stellar property such as the age, mass, surface gravity and radius. This method, referred to here as the "PDF method", is described in detail in da Silva et al. (2006)[1], and essentially consists of the following:

- 1. Given a star of absolute magnitude $M_V \pm \sigma_{M_V}$, effective temperature $T_{\rm eff} \pm \sigma_{T_{\rm eff}}$ and metallicity [Fe/H] $\pm\, \sigma_{\rm [Fe/H]}$, we compute the probability P^{12} that it belongs to each small section $[\ell^1, \ell^2]$ of an isochrone of age t and metallicity [Fe/H]. This probability is proportional to

$$\exp\left[-\frac{(M_V - M'_V)}{2\sigma_{M_V}} - \frac{(T_{\rm eff} - T'_{\rm eff})}{2\sigma_{T_{\rm eff}}}\right],$$

  where M'_V and $T'_{\rm eff}$ characterise the mean point of $[\ell^1, \ell^2]$, and is also proportional to the expected number of stars in that section. This latter quantity is computed by integrating the Initial Mass Function (IMF) by number over the interval of initial masses $[m_{\rm i}^1, m_{\rm i}^2]$.

- 2. We loop over all isochrone sections, and over all isochrones in a wide range of ages and metallicities. The probabilities P^{12}, weighted by the age and metallicity distribution functions, are used to construct the PDFs of all stellar quantities of interest among those tabulated in the isochrones, for instance the age, mass, surface gravity, etc. For the metallicity distribution function we adopt a Gaussian of mean [Fe/H] and dispersion $\sigma_{\rm [Fe/H]}$, whereas the age distribution is assumed to be constant for all ages between 0.1 and 12 Gyr. The mean [Fe/H] for each star is listed in Tab. 4.1 and was determined with the method described in §3.3.2. The Fe dispersion has a value of $\pm$ 0.05 dex for all stars and is not separately listed in Fig. 3.4 to Fig. 3.14.

In this procedure, both the IMF and age distribution function might be considered as the Bayesian priors. Fig. 3.4 presents a few examples of PDFs, that illustrate both the behaviour of the PDFs and the quality of the parameter estimation we have. As in da Silva et al. (2006), most of the stars in the sample present typical PDFs, either single-peaked or with a dominant peak in the mass and age PDF. In these cases, the PDFs are Gaussian-like and in general are well represented by the mean value and sigma dispersion as measured from the PDF. The same happens for the PDFs of other quantities, such as $\log g$ and radius which are in general very narrow. For a few cases, and especially for stars in the red clump region of the CMD, mass and age PDFs become much broader and sometimes present double peaks, caused by stars in different evolutionary phases (e.g. red clump and first-ascent RGB) becoming equally likely. These entries will also be those with the largest quoted error in the mass and age determination. Fig. 3.5 through Fig. 3.14 present the PDFs of the remaining stars of the sample.

[1] The present implementation of the PDF method is publicly available via the web interface `http://stev.oapd.inaf.it/~lgirardi/cgi-bin/param`.

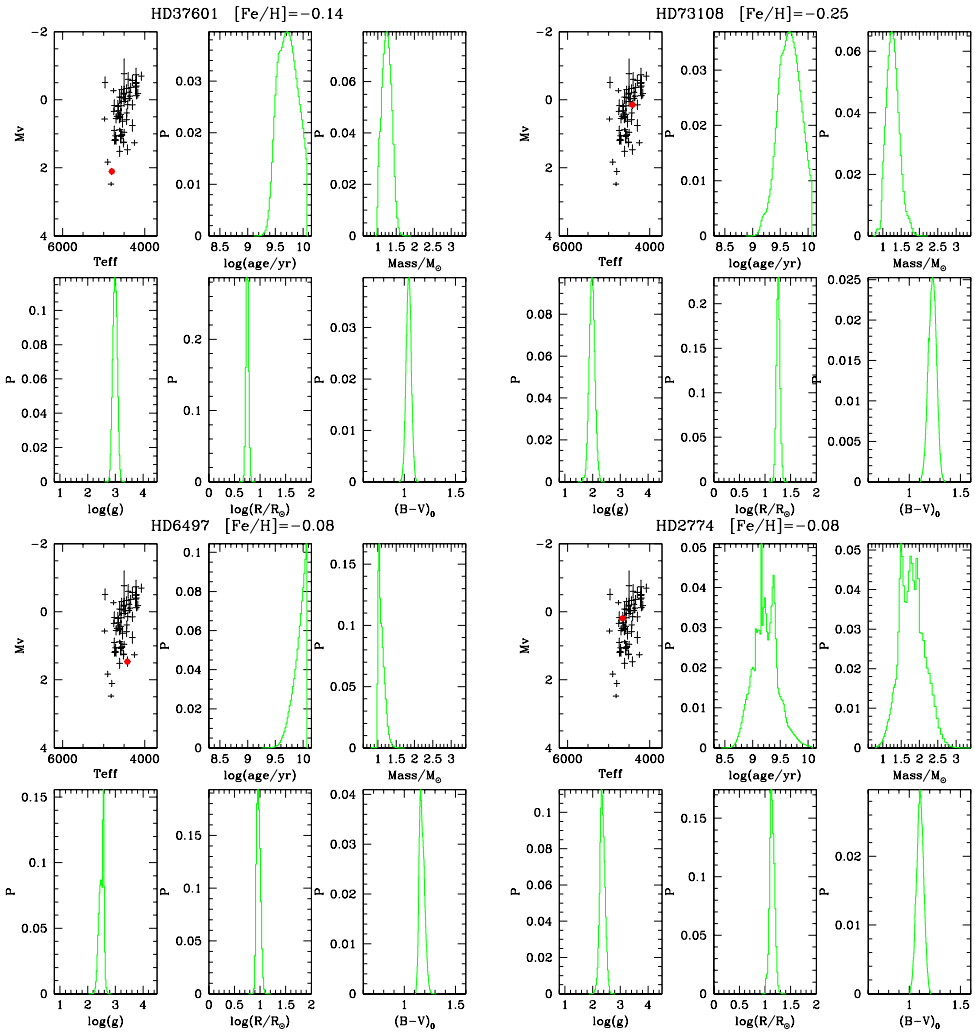

Figure 3.4: Examples of Probability Distribution Functions (PDFs) for my sample stars. For each star, one panel presents the position in the HRD (red dot). The five remaining panels show the PDF for $\log t$, M, $\log g$, $\log R$, and $(B–V)$. The solid lines (green) show the PDF assuming an internal error of 0.05 dex in the [Fe/H] determination ($\sigma_{\rm [Fe/H]}$). This value is the same for all stars in all PDF plots. The individual object name and the mean Fe abundance are given in the plot. The first 3 cases (HD 37601, HD 73108 and HD 6497) illustrate well-behaved cases that constitute the majority of my sample: the PDFs are either single-peaked or present a dominant peak that well defines the estimated parameters. The last case (HD 2774) instead is an example of more uncertain age and mass determination, for a star in the red clump region of the CMD. In general the results for the different parameters, expressed in the shape of the corresponding plots, are not derived independently from each other. Consequently there is a clear trend that the different parameters fit each other very well.

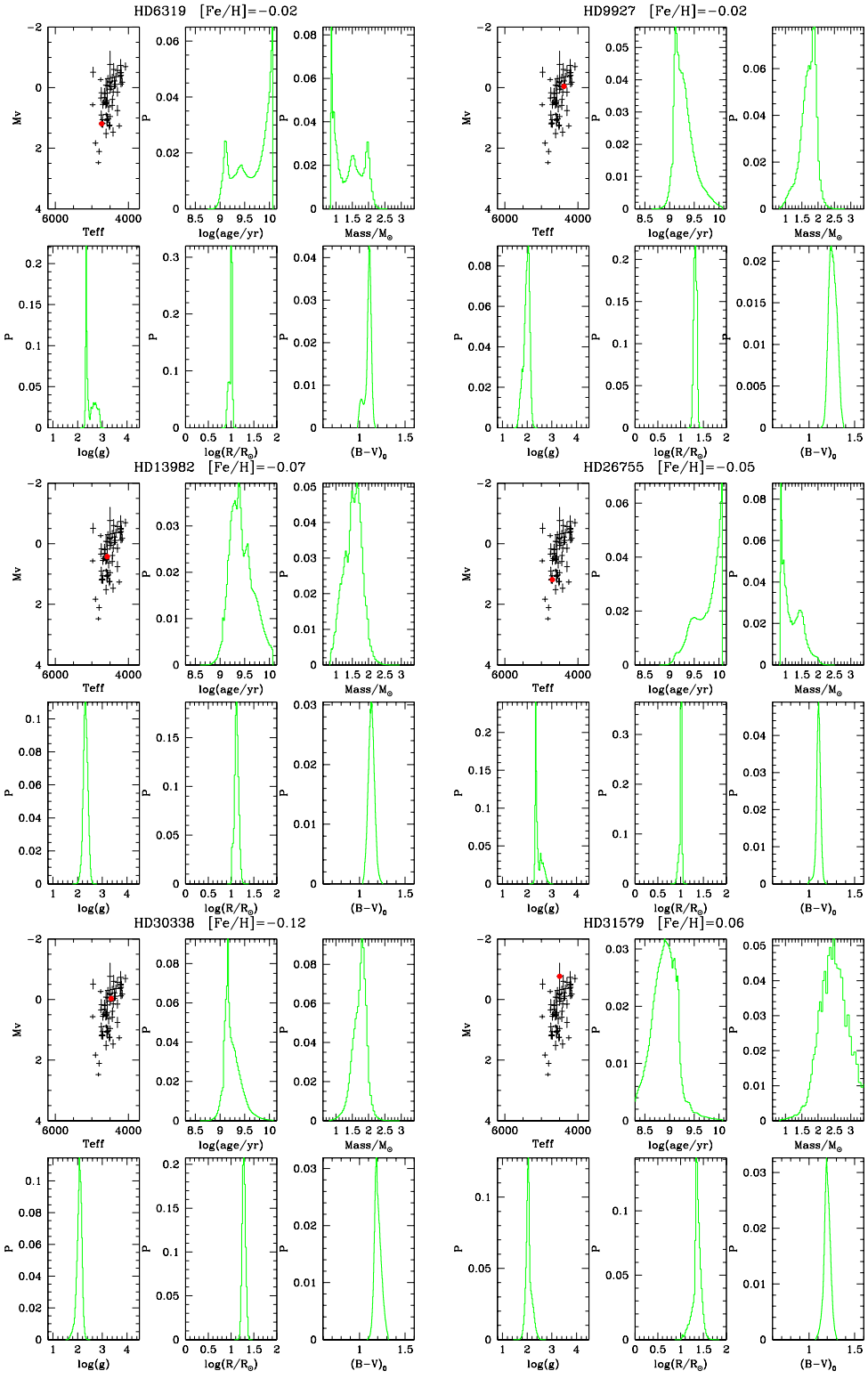

Figure 3.5: PDFs for my sample stars.

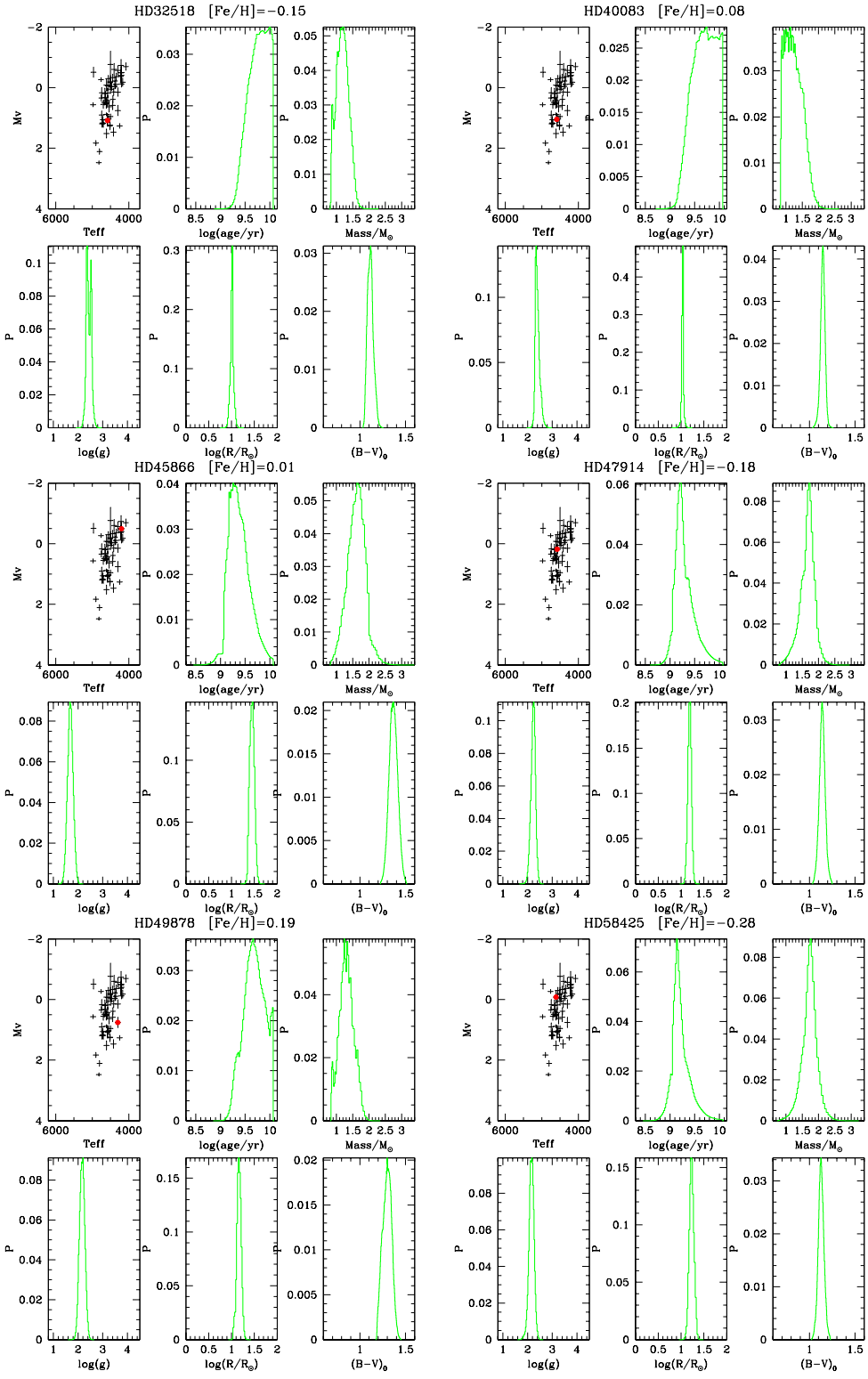

Figure 3.6: PDFs for my sample stars.

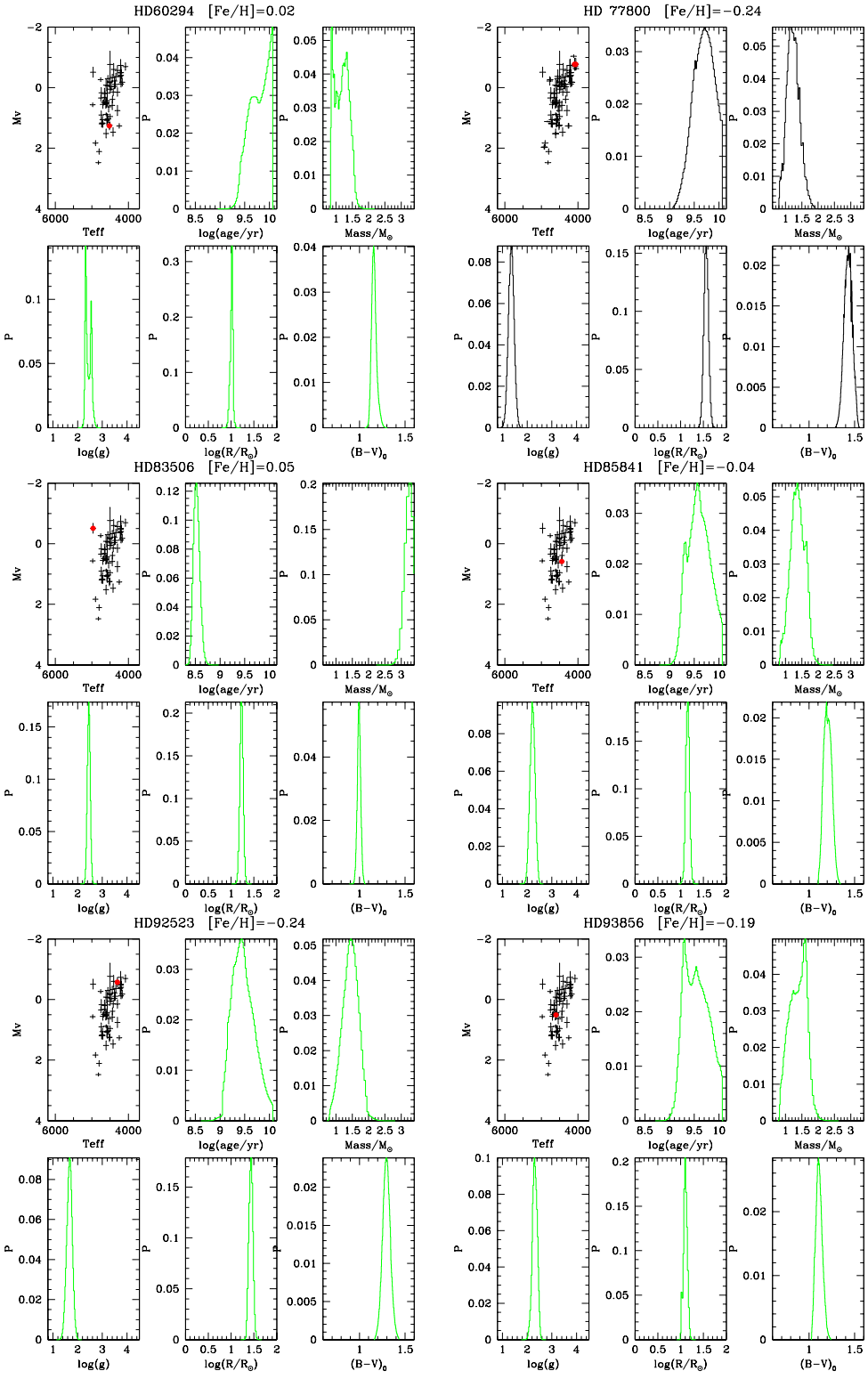

Figure 3.7: PDFs for my sample stars.

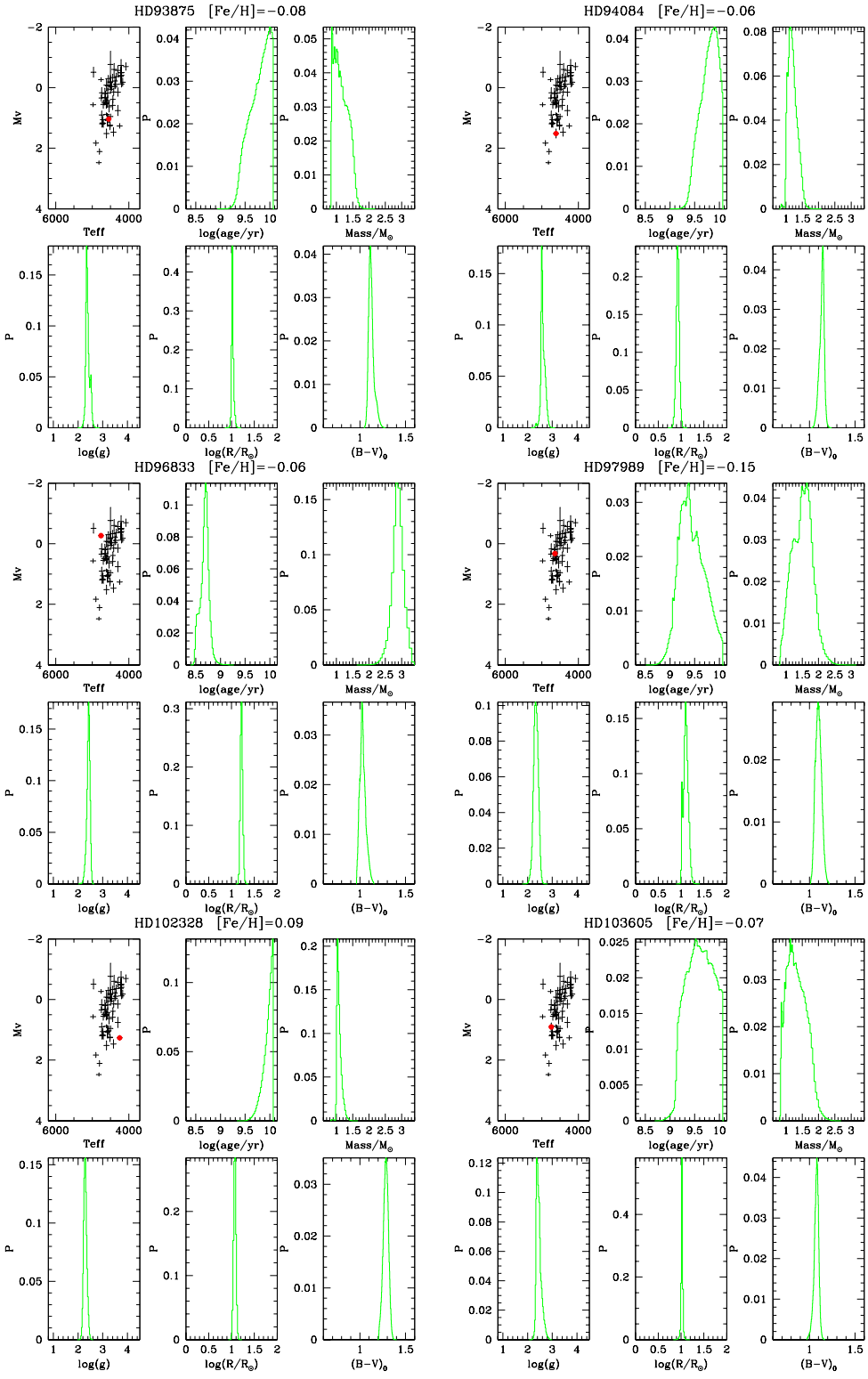

Figure 3.8: PDFs for my sample stars.

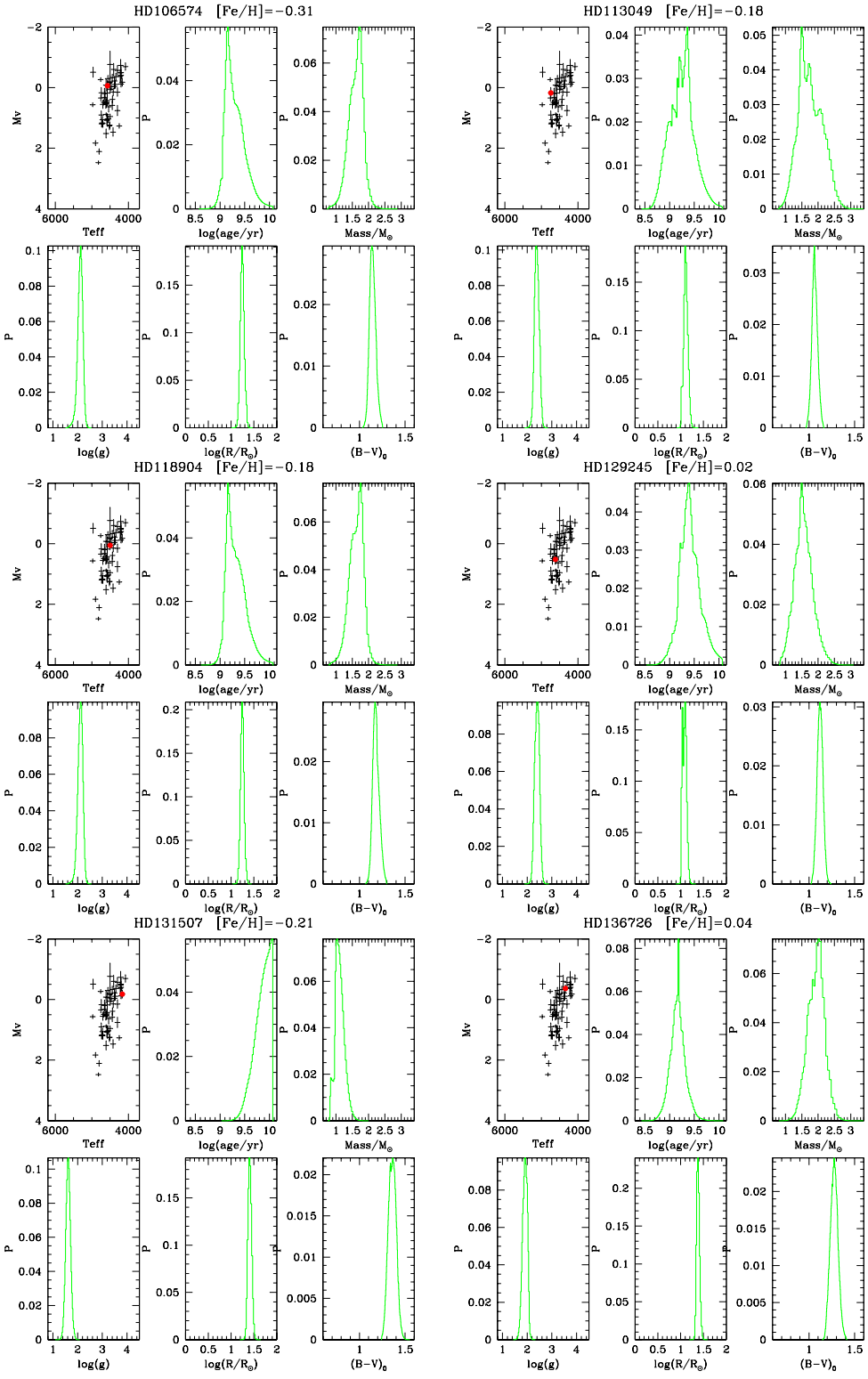

Figure 3.9: PDFs for my sample stars.

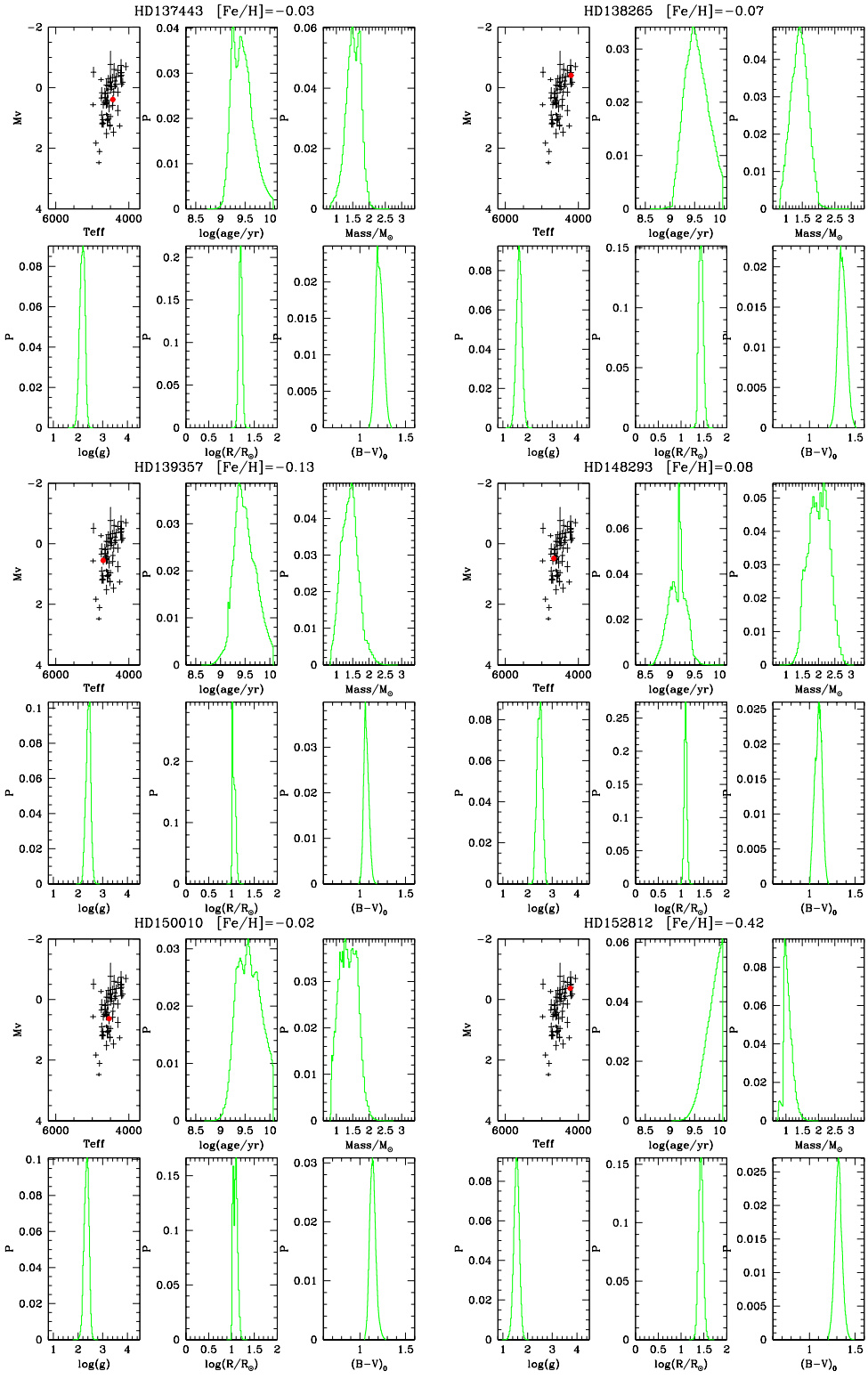

Figure 3.10: PDFs for my sample stars.

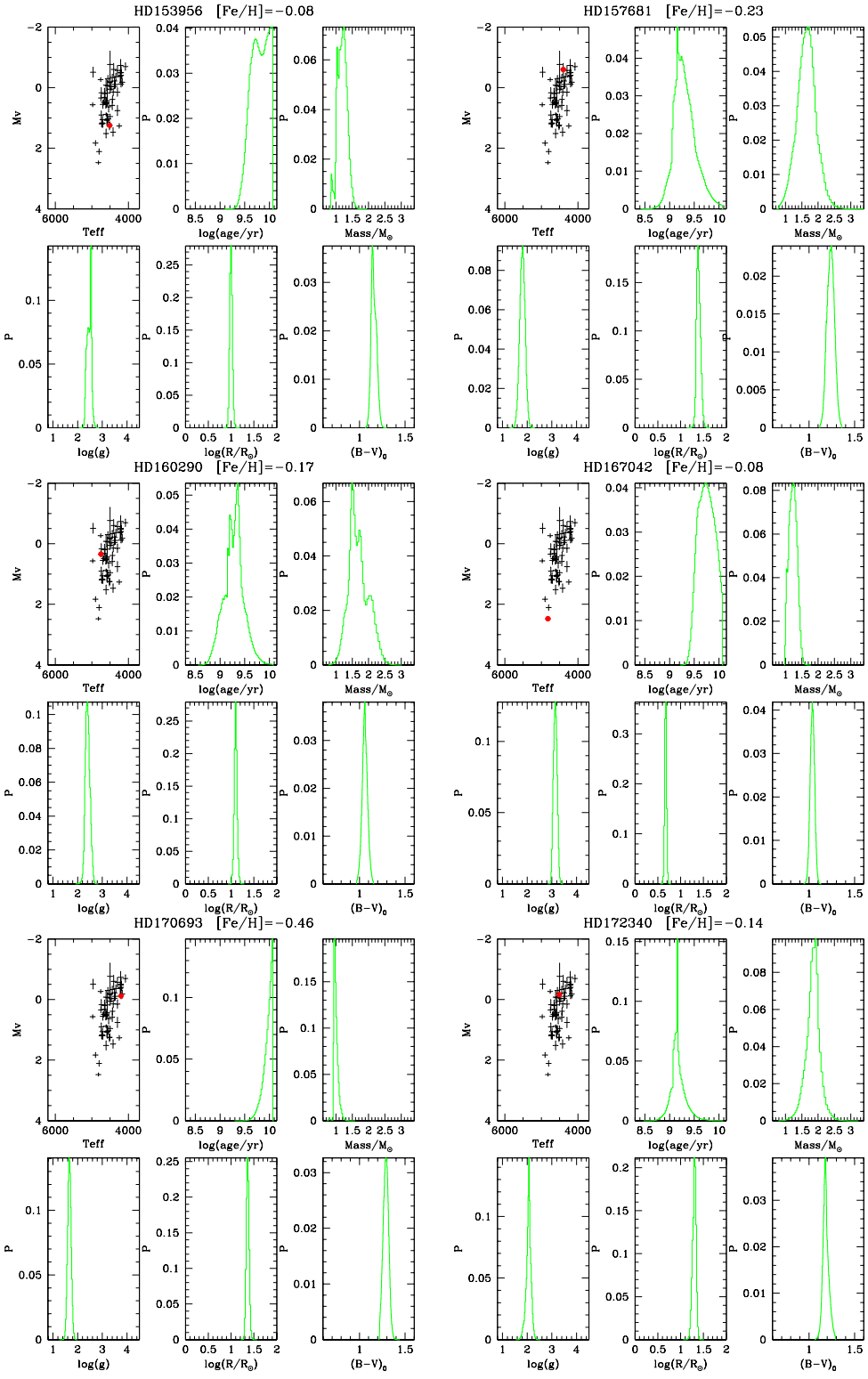

Figure 3.11: PDFs for my sample stars.

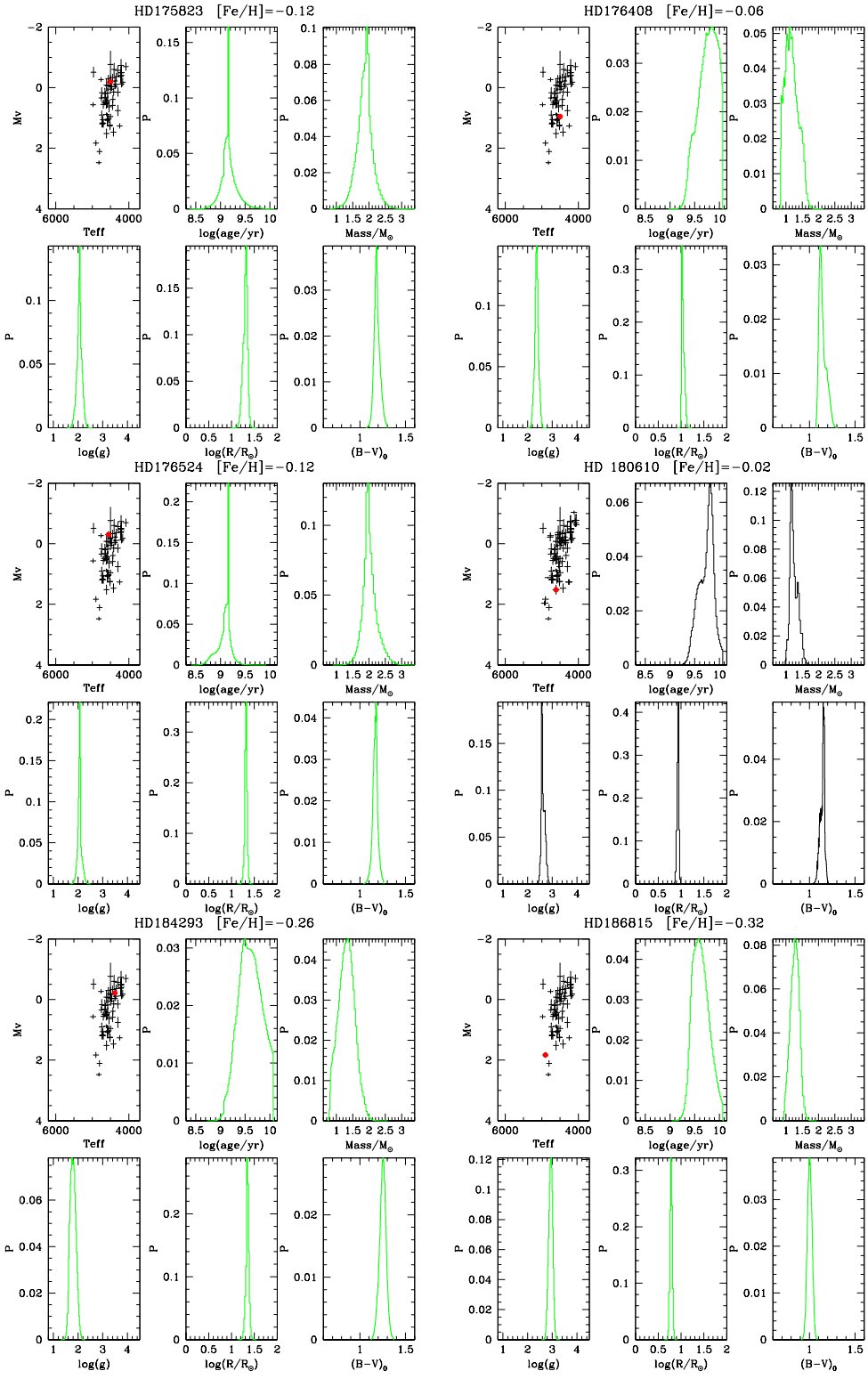

Figure 3.12: PDFs for my sample stars.

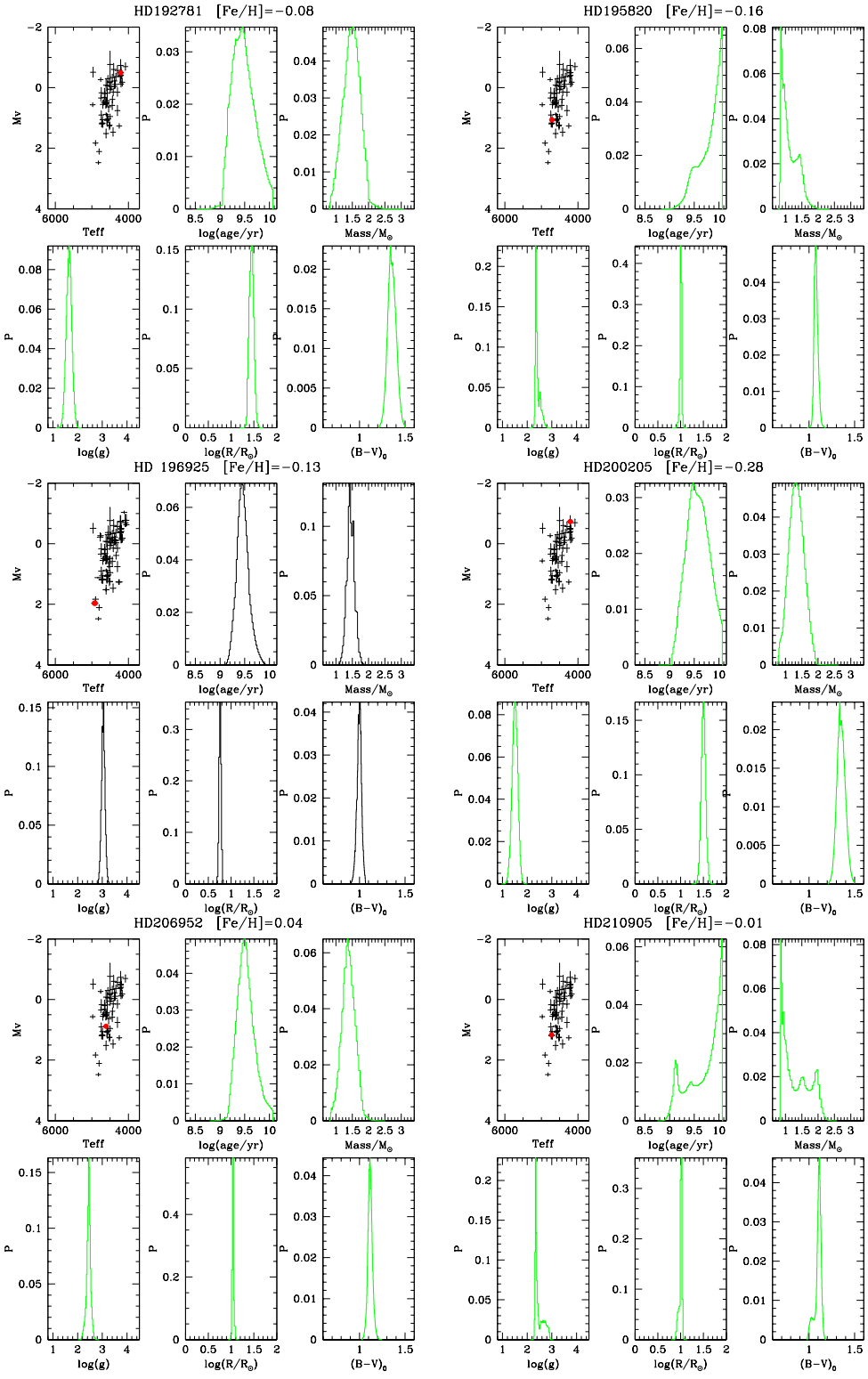

Figure 3.13: PDFs for my sample stars.

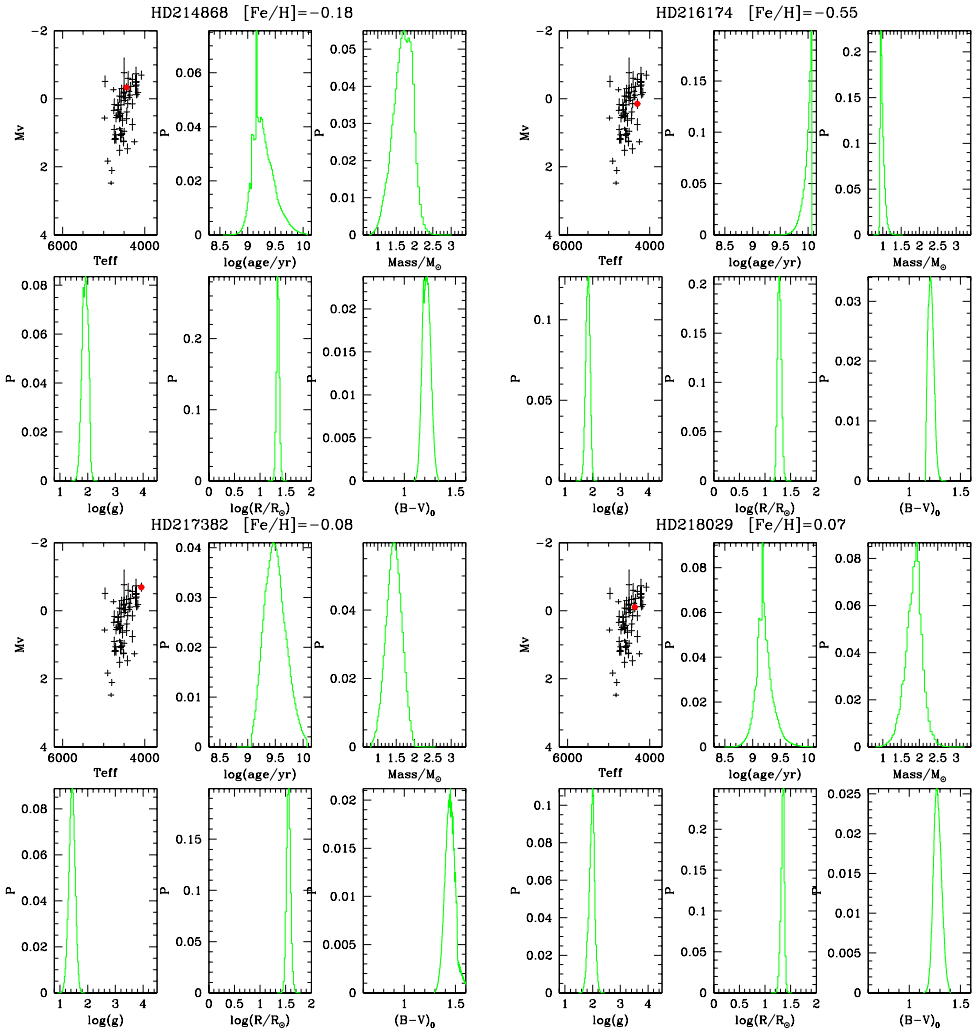

Figure 3.14: PDFs for my sample stars.

Chapter 4

Abundances and parameters

After determining the Fe abundances, it was essential to verify whether a zero point correction of the metallicity scale was necessary. I chose for this purpose two particularly well studied stars – HD 113226 (ϵ Vir) and HD 27371 (γ Tau) – analysed and published by da Silva et al. (2006).
These two stars belong to the Hyades. This cluster consists of an extremely well controlled sample of stars of the same age and metallicity as well as a common birth environment. Thus for the two very similar stars a large amount of stellar parameter values was already determined. The Hyades stars are not at the boundaries of my Fe abundances and effective temperatures. However well studied stars more similar to my Thüringer Landessternwarte Tautenburg (TLS) sample stars are not available. With this choice I had the possibility to compare the results from the northern hemisphere with a previous study in the South because da Silva et al. (2006) used also these two stars from Setiawan et al. (2004a) as reference stars in their southern giant survey carried out with the Fiber-fed Extended Range Optical Spectrograph ($FEROS$).
Averaging all entries of the Cayrel de Strobel et al. (2001) catalogue for HD 113226, da Silva et al. (2006) obtained [Fe/H] = 0.11 dex and $T_{\rm eff}$ = 5048 K, while for HD 27371 [Fe/H] = 0.11 dex and $T_{\rm eff}$ = 4967 K were derived. To find out possible offsets I analysed the $FEROS$ spectra of HD 113226 and HD 27371 with the method of §3.3.2. For star HD 27371 I derived [Fe/H] = 0.12 dex and for star HD 113226 I obtained the value [Fe/H] = 0.11 dex. Both values are in very good agreement with the averaged values from the literature.
So a zero point correction for the abundances was not necessary. My results would appear to be on the same scale as those of the da Silva et al. (2006) sample and are therefore suitable for further comparisons.
For the effective temperatures I derived $T_{\rm eff} = 5080$ K for HD 113226 and $T_{\rm eff} = 5180$ K for HD 27371. In comparison with da Silva et al. (2006) my values are higher of 6 K and 150 K for HD 113226 and HD 27371, respectively. The larger difference for HD 27371 is possibly caused by the interplay of the differences in the other stellar parameters as listed in the following.
The logarithmic surface gravity $\log g$ is 2.84 dex for HD 113226 and 2.68 dex for HD 27371. Both values are similar to da Silva et al. (2006) with 2.9 dex and 3.0 dex for HD 113226 and HD 27371, respectively. The two values for the microturbulence velocity ξ are 1.35 $\mathrm{km\,s^{-1}}$ and 1.75 $\mathrm{km\,s^{-1}}$ in comparison with the two 1.7 $\mathrm{km\,s^{-1}}$ values from da Silva et al. (2006).
I determined values for the Sun as an additional reference point. Using the model at-

mosphere from Edvardson et al. (1993) I derived 0.02 dex for [Fe/H], 5830 K for T_{eff}, 4.3 dex for $\log g$ and 0.9 km s^{-1} for ξ. The adopted solar parameters in literature are $T_{eff} = 5750$ K, $\log g = 4.4$ dex and $\xi = 0.9$ km s^{-1} using the same model atmosphere.

4.1 Summary of the results

The values for Fe abundance [Fe/H], effective temperature T_{eff}, logarithmic surface gravity $\log g$ and microturbulence velocity ξ of the spectral analysis for the two reference stars and the whole Tautenburg sample are listed in Tab. 4.1.

Table 4.1: Results of the Fe abundances and stellar parameters

HD	T_{eff} [K]	$\log g$ [dex]	[Fe/H] [dex]	ξ [km s^{-1}]
113226	5080	2.7	+0.11	1.35
27371	5180	2.5	+0.12	1.75
2774	4655	2.7	-0.079	1.3
6497	4420	2.4	-0.084	1.3
6319	4730	2.7	-0.018	1.4
9927	4380	1.9	-0.023	1.3
13982	4580	2.3	-0.069	1.4
26755	4700	2.9	-0.050	1.3
31579	4500	2.8	+0.058	1.4
30338	4470	2.2	-0.117	1.3
32518	4580	2.1	-0.154	1.2
37601	4800	2.6	-0.136	1.0
40083	4590	2.5	+0.084	1.3
45866	4200	2.2	+0.007	1.3
47914	4580	1.9	-0.182	1.4
49878	4300	2.7	+0.187	1.1
58425	4610	2.1	-0.277	1.0
60294	4520	2.4	+0.024	1.0
73108	4415	1.8	-0.251	1.2
77800	4090	1.6	-0.245	1.4
83506	4965	2.7	+0.053	1.7
85841	4440	1.9	-0.044	1.4
92523	4300	1.9	-0.242	1.3
93859	4600	2.1	-0.185	1.2
93875	4550	1.9	-0.084	1.3
94084	4610	2.2	-0.064	1.3
96833	4760	2.4	-0.055	1.5
97989	4640	1.8	-0.151	1.2
102328	4250	1.9	+0.092	1.3
103605	4740	2.8	-0.066	1.4
106574	4570	2.2	-0.314	1.2
113049	4740	2.2	-0.181	1.2
118904	4500	2.2	-0.178	1.3

Continued overleaf ...

Table 4.1: Results of the Fe abundances and stellar parameters

... continuing from previous page.				
Star	$T_{\rm eff}$ [K]	$\log g$ [dex]	[Fe/H] [dex]	ξ [km s^{-1}]
129245	4615	3.3	+0.022	1.4
131507	4165	1.5	-0.214	1.3
136726	4340	1.6	+0.037	1.6
137443	4435	2.6	-0.028	1.5
138265	4200	2.4	-0.074	1.1
139357	4700	2.9	-0.128	1.6
148293	4670	2.5	+0.080	1.3
150010	4540	2.8	-0.016	1.3
152812	4220	1.4	-0.418	1.3
153956	4510	2.3	-0.076	1.5
157681	4400	1.6	-0.230	1.5
160290	4750	2.7	-0.165	1.3
167042	4820	2.9	-0.080	1.0
170693	4200	1.0	-0.464	1.0
172340	4510	2.1	-0.135	1.4
175823	4500	2.1	-0.124	1.4
176524	4560	1.7	-0.115	1.3
176408	4500	2.3	-0.064	1.3
180610	4610	2.85	-0.016	1.45
184293	4380	1.9	-0.257	1.3
186815	4900	2.5	-0.319	0.9
192781	4210	2.3	-0.081	1.4
195820	4710	2.4	-0.164	1.1
196925	4910	2.8	-0.134	1.1
200205	4210	1.6	-0.280	1.4
206952	4610	2.4	+0.044	1.3
210905	4720	2.7	-0.006	1.4
214868	4440	2.1	-0.177	1.5
216174	4300	1.2	-0.549	1.2
217382	4080	1.8	-0.075	1.5
218029	4360	2.0	+0.070	1.3

4.2 Comparison with the literature

A comparison of the Fe abundances with previous high-resolution spectroscopic analyses is possible for 22 (36 %) of the 62 Tautenburg programme stars. The extent of the previous work is presented in a summary in Tab. 4.2. The values in Tab. 4.2 without reference are taken from my work. The main characteristics of the available stars for a comparison are taken either from the "Catalogue of [Fe/H] determinations" (Cayrel de Strobel et al. 1985) or directly from the "original papers" which are mentioned in the catalogue. There is one primary source of comparison for the current results – the McWilliam (1990) high-resolution spectroscopic survey of 671 G–K field giants with which I have 17 stars in common. The stellar spectra of this survey were taken from 1984 August to 1986 April with the coudé echelle spectrograph mounted

on the 2m telescope at the McDonald Observatory in Texas. A resolving power of 40,000 and a Signal-to-Noise ratio (S/N) of 100 was obtained. Two spectral regions were observed, centered at 6600 $\AA$ and 6750 $\AA$, each covering about 100 $\AA$. The stellar atmosphere parameters such as effective temperature $T_{\rm eff}$, logarithmic surface gravity $\log g$, Fe abundance [Fe/H] and microturbulence velocity ξ were determined using a similar spectrum synthesis programme for the high-resolution spectra. McWilliam (1990) assumed a Local Thermodynamic Equilibrium (LTE), plane-parallel geometry of the atmosphere and hydrostatic equilibrium. This means his spectra and stellar parameters, with the exception of the microturbulent velocity ξ, are derived in a manner comparable with my work. However after more than 15 years, there are also differences. For example in this work I used a greater resolving power of 67,000, a higher S/N of > 120 and an enlarged spectral coverage. Moreover the evolutionary tracks (Girardi et al. 2000), which I used in this work, were computed with updated opacities. The slightly different values in the stellar parameters between McWilliam (1990) and this work are perhaps caused by these upgrades.
In addition 5 different stars from my work are contained in the following analyses: Lambert & Ries (1981), Gratton et al. (1982), Luck (1991), Luck & Challener (1995) as well as more recently Johnson et al. (2007b).

Table 4.2: Summary of the atmospheric stellar parameters by other authors.

HD	$T_{\rm eff}$ [K]	$\log g$ [dex]	[Fe/H] [dex]	ξ [km s^{-1}]	reference
73108	4415	1.8	-0.251	1.2	
	4370	2.45	-0.26	2.0	McWilliam (1990)
	4400	1.61	-0.20	2.0	Luck (1991)
77800	4090	1.6	-0.245	1.4	
	3940	1.66	-0.23	2.2	McWilliam (1990)
83506	4965	2.7	+0.053	1.7	
	4710	2.77	+0.02	2.3	McWilliam (1990)
96833	4760	2.4	-0.055	1.5	
	4846	2.78	-0.07	2.0	Lambert & Ries (1981)
	4667	1.70	-0.18	2.2	Gratton et al. (1982)
	4550	2.53	-0.13	2.0	McWilliam (1990)
102328	4250	1.9	+0.092	1.3	
	4250	1.90	+0.09	2.5	Luck & Challener (1995)
131507	4165	1.5	-0.214	1.3	
	4140	1.99	-0.20	2.2	McWilliam (1990)
148293	4670	2.5	+0.080	1.3	
	4650	2.66	+0.07	2.1	McWilliam (1990)
160290	4750	2.7	-0.165	1.3	
	4440	2.59	-0.21	1.8	McWilliam (1990)
167042	4820	2.9	-0.08	1.0	
	5020	3.52	+0.05		Johnson et al. (2007b)
170693	4200	1.0	-0.464	1.0	
	4400	2.57	-0.44	2.0	McWilliam (1990)

Continued overleaf ...

Table 4.2: Summary of the atmospheric stellar parameters by other authors.

... continuing from previous page.					
HD	T_{eff} [K]	$\log g$ [dex]	[Fe/H] [dex]	ξ [km s^{-1}]	reference
176524	4560	1.7	-0.115	1.3	
	4520	2.55	-0.12	2.1	McWilliam (1990)
180610	4610	2.85	-0.016	1.45	
	4500	2.71	-0.01	1.8	McWilliam (1990)
184293	4380	1.9	-0.257	1.3	
	4290	2.34	-0.27	2.2	McWilliam (1990)
200205	4210	1.6	-0.280	1.4	
	4080	1.91	-0.30	2.4	McWilliam (1990)
206952	4610	2.4	+0.044	1.3	
	4570	2.66	+0.04	2.0	McWilliam (1990)
214868	4440	2.1	-0.177	1.5	
	4440	2.32	-0.25	2.4	McWilliam (1990)
216174	4300	1.2	-0.549	1.2	
	4440	2.53	-0.53	2.4	McWilliam (1990)
217382	4080	1.8	-0.075	1.5	
	4070	1.78	-0.11	2.1	McWilliam (1990)
218029	4360	2.0	+0.070	1.3	
	4290	2.28	+0.07	2.1	McWilliam (1990)

Scanning the data of the comparison between the stellar parameters of my work and the entries from other authors in Tab. 4.2, I find that there is general agreement for T_{eff}, $\log g$, [Fe/H] and microturbulence velocity ξ. A comparison of my results with the literature data (see Tab. 4.3) shows clear similarity. Fig. 4.1 clarifies the comparison of the Fe abundances, the effective temperatures and the logarithmic surface gravities visually. In accordance with the values contained in Tab. 4.2 and Tab. 4.3, the diagrams in Fig. 4.1 show the compared stellar parameters and confirm the agreement of the results of my work with the results from all previous high-resolution analyses.
In the following I will compare the stellar parameters of this work with previous studies. My Fe content shows an averaged difference of 0.008 dex which is within the assumed error of 0.05 dex for the iron abundances analysis of the spectra. This assumed error is in agreement with values published by Luck & Challener (1995). These authors assume also an error of 0.05 dex or slightly less ($\leq$ 0.02 dex) for Fe I, which has many lines. For species with a restricted number of lines, but more than five, they assume a larger error of 0.15 to 0.25 dex. The mean differences (this work - other references) in [Fe/H] are the following: -0.01 dex (McWilliam 1990), -0.015 dex (Lambert & Ries 1981), -0.125 dex (Gratton et al. 1982), +0.051 dex (Luck 1991), +0.002 dex (Luck & Challener 1995) and -0.13 dex (Johnson et al. 2007b). Scanning the data of the comparison Johnson et al. (2007b) and Gratton et al. (1982) show the largest discrepancies in Fe abundances. Gratton et al. (1982) shows also a large discrepancy of -0.11 dex in Fe abundance in comparison with Lambert & Ries (1981). However the values of Gratton et al. (1982) and McWilliam (1990), with a difference of -0.05 dex, are comparable. The large differences in the Fe abundance between Gratton et al. (1982) and the other two scales are probably a consequence of the differences of the other stellar parameters, namely effective temperature and surface gravity as well as

microturbulence velocity. These are all correlated in a three-dimensional plane in the atmospheric stellar parameter determination. Differences in the other stellar parameters are most likely also the cause for the large [Fe/H] discrepancies between Johnson et al. (2007b) and Gratton et al. (1982) in comparison with my work. HD 214868 shows the largest difference between my Fe abundance value (see Tab. 4.2) and those of my primary source McWilliam (1990). The discrepancy of this star is possibly caused by different microturbulence velocity values. In general the differences between my [Fe/H] values and the values of the other authors are negligible assuming an uncertainty of 0.05 dex. Thus my values of [Fe/H] agree with those of the literature. There is no trend visible in Fig. 4.1 (top left). The errrors seem to be random. However despite this good agreement one has to keep in mind that there are in principle two primary sources of possible error in the determined abundances: line-to-line scatter and errors in the stellar parameters due to non-Local Thermodynamic Equilibrium (non-LTE) effects. One assumption of the used abundance code in this work was LTE. But non-LTE effects in the atmospheres of red giants were reported by Ruland et al. in 1980. The non-LTE influences the ionization and excitation equilibrium populations of elemental species. According to McWilliam (1990) the iron is expected to be overionized relative to LTE due to the radiation field. As in G–K giants, iron is almost completely ionized, but small modifications in the ionization equilibrium caused by non-LTE can change the amount of neutral iron dramatically. They realized that lines of high excitation are more suitable for iron abundance determinations than lines of low excitation (Tomkin & Lambert (1983, observational investigations) and Steenbock (1985, theoretical non-LTE simulations)). This is due to the fact that these lines are formed deep in the atmosphere where both the continuous opacity and gas density are higher. A shorter mean-free photon path length and more frequent atomic collisions reduce the non-LTE effects significantly.

The second compared stellar parameter – the effective temperature $T_{\rm eff}$ – shows an averaged difference of 42.59 K. My temperature is 97 K higher than the McWilliam (1990) scale and 179 K higher than the Gratton et al. (1982) scale. My effective temperature values in comparison to Luck (1991) are 15 K too high. Luck & Challener (1995) derived exactly the same effective temperature as I found in my work. Contrary to these results, my temperature scale is 86 K cooler in comparison with Lambert & Ries (1981) and 200 K cooler in comparison with Johnson et al. (2007b). Taking into account all the entries from other authors there is consistent agreement with my work within the assumed error of 50 K. Thus there does not seem to be any temperature-dependent systematic effects between the various temperature scales by considering the averaged differences in effective temperature. This is due to the fact that the effective temperature was determined in the same way by choosing a $T_{\rm eff}$ such that the relation between iron abundances and lower excitation potential has zero slope. However considering the individual differences in the effective temperature for all stars, there is probably a visible tendency to have a difference of around 100 K in most of the compared stars. This trend is possibly visible in Fig. 4.1 (top right). There are also a few stars (HD 83506, HD 160290 and HD 167042) with very large differences (see Tab. 4.2) which are likely due to differences in the ξ values.

The third stellar parameter available for the comparison is the surface gravity $\log g$ which shows a difference of about 0.31 dex. The sample stars HD 167042, HD 176524, HD 184293 and HD 216174 show the largest discrepancies in $\log g$ probably caused by different ξ values. Comparisons of the stellar gravities between this work and previous studies in general show that the spectroscopic gravities derived here are, with

Table 4.3: Mean results of the comparison between my work and other authors.

Δ $T_{\rm eff}$	$\Delta \log g$	Δ [Fe/H]	Δ ξ
42.59 $\pm$ 50 K	0.31 $\pm$ 0.50 dex	0.008 $\pm$ 0.05 dex	0.82 8 $\pm$ 0.2 km s^{-1}

the exception of Luck (1991), somewhat lower than previous values. Thus there is a systematic offset visible in the compared $\log g$ values (see Fig. 4.1, lower left). With respect to McWilliam (1990) my gravities are on average 0.36 dex lower and with respect to Lambert & Ries (1981) 0.38 dex lower. On the other hand my values are around 0.19 dex higher in comparison to Luck (1991), and also 0.7 dex higher in comparison with Gratton et al. (1982). With respect to Johnson et al. (2007b) my gravities are 0.62 dex lower. Scanning together the varieties in the data I found in agreement with Luck (1991), a strong dependence of the gravity differences on the temperature difference is visible. In detail the stars with the largest temperature differences also show the largest differences in gravity. The sign and magnitude of the changes are as expected. Lowering the temperature lowers the degree of ionization, and to maintain the ionization ratio the gravity must also be lowered. The results of the comparison of my work with the study of Luck & Challener (1995) confirms this statement. As mentioned above there is no discrepancy in the effective temperature and as a consequence of this there is also no difference in gravity in both works.

I will now, as the last stellar parameter, compare the values of the microturbulence velocity ξ. My estimated internal uncertainty in ξ is $\pm$ 0.2 km s^{-1} based on the sensitivity of the slope to the assumed microturbulence velocity. A value of a change of 0.2 km s^{-1} has a noticeable effect upon the slope of the relation and on the derived mean abundances. Microturbulence velocities ξ for the programme stars are listed in Tab. 4.2. The mean differences (this work – other references) in ξ are in detail: -0.7 km s^{-1} (McWilliam 1990), -0.5 km s^{-1} (Lambert & Ries 1981), -0.7 km s^{-1} (Gratton et al. 1982), -0.8 km s^{-1} (Luck 1991) and -1.2 km s^{-1} (Luck & Challener 1995). Johnson et al. (2007b) published no values for ξ. The microturbulence velocity shows a large mean discrepancy of about -0.8 km s^{-1} which is not within the assumed error of 0.2 km s^{-1} (see Tab. 4.3). In detail the majority of my ξ values in the fifth column of Tab. 4.1 range between 1.0 and 1.7 km s^{-1} in contrast to the very high values of around 2.0 km s^{-1} listed in the fifth column of Tab. 4.2 from previous studies. Thus my microturbulence velocity ξ is systematically too low by about -0.8 km s^{-1} (see Fig. 4.1, below right) compared to the other entries. This discrepancy is caused by a different determination method between my work and my primary source as well as the other authors. This is due to the fact that McWilliam (1990) took the microturbulence velocity value of 2.0 $\pm$ 0.5 km s^{-1} of 72 Cyg for all his stars as the microturbulence standard. This procedure explains why in the following his determined microturbulence velocity ξ values are so high and very similar. Thus the large discrepancy of -0.8 km s^{-1} between his and my values for the microturbulence is due to the fact that I really determined the microturbulence velocity ξ for each star using high-excitation iron lines and the assumption that the derived iron abundance is independent of equivalent width. In contrast to McWilliam (1991) I took no values from a standard star. Luck (1991), Luck & Challener (1995), Lambert & Ries (1981) and Gratton et al. (1982) also show very high values for the microturbulence. As far as I have investigated, none of these authors determined the accurate values for each star.

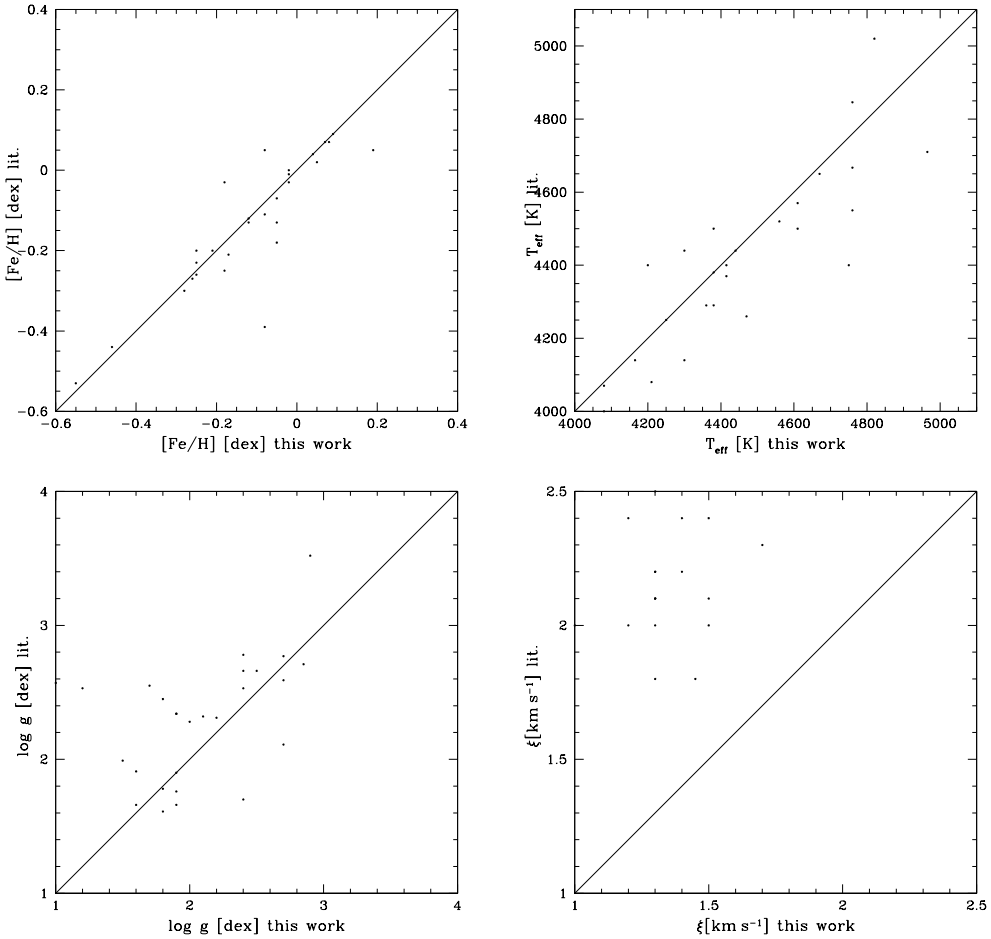

Figure 4.1: Comparison of my [Fe/H], $T_{\rm eff}$, $\log g$ and ξ values with the literature.

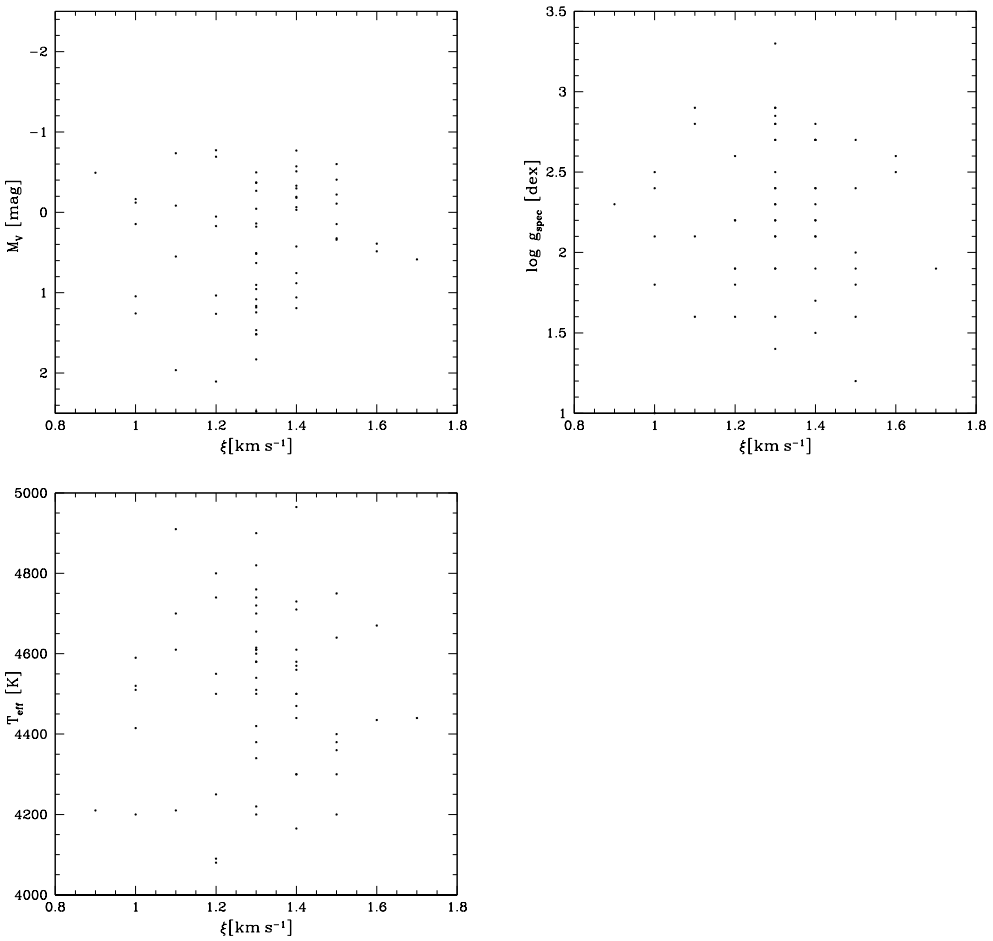

Figure 4.2: No correlations between microturbulent velocity ξ and M_V, $T_{\rm eff}$ as well as $\log g$.

In contrast to Gratton et al. (1982) the values of my microturbulence show no significant correlation with the absolute visual magnitude M_V as illustrated in Fig. 4.2 (top left). According to Gustafsson, Kjaergaard & Andersen (1974) and contrary to Gratton et al. (1982) I also found no correlation of ξ with $\log g$ (see Fig. 4.2, top right) as well as with $T_{\rm eff}$ as also shown in Fig. 4.2 (below left).

Finally general reasons for discrepancies in the compared parameters are possibly due to differences in the way the continua were set (equivalent widths), atomic data ($\log gf$ values) or atmospheric models. The estimation of the errors (see §3.3.2) for the iron abundances ($\pm$ 0.05 dex) and the stellar parameters such as effective temperature $T_{\rm eff}$ ($\pm$ 50 K) as well as logarithmic surface gravity $\log g$ ($\pm$ 0.50 dex) was very important, because these parameters will be used here for deriving stellar masses and radii from evolutionary tracks and any error in the first step would increase the error of the following derived stellar parameters. An exact stellar mass is particularly helpful for the mass determination of the planetary companion around host stars.

4.3 Additional Rigorous Tests

To check the reliability of the parameter estimation method the following rigorous tests were applied.

4.3.1 "Colour excess" $(B–V)–(B–V)_0$

To compare the results for my northern TLS sample with the results for our southern $FEROS$ stars I used parts of the text and figures of our previous article "Basic physical parameters of a selected sample of evolved stars" (da Silva et al. 2006) as cited in this chapter. The first test compared the estimated intrinsic colours $(B–V)_0$ with the observed colours $(B–V)$ for each star. The difference of both parameters is the so-called "colour excess" $(B–V)–(B–V)_0$.
Since $(B–V)_0$ values, derived from the total Probability Distribution Function (PDF) as explained in §3.3.3, result basically from spectroscopic $T_{\rm eff}$, error bars in the individual $(B–V)–(B–V)_0$ values contain mostly the 50 K error assumed for $T_{\rm eff}$. Fig. 4.3 presents $(B–V)–(B–V)_0$ as a function of distance (left) and $T_{\rm eff}$ (right) for the northern TLS (top) and the southern $FEROS$ stars (lower). The distances were determined from $HIPPARCOS$ parallaxes.
There are so-called "outliers" visible in the plots of both samples. These are stars which show a larger dispersion of the $(B–V)_0$ values in comparison with the bulk of other stars. Thus stars with $|(B–V)–(B–V)_0| \geq 0.1$ are defined as "outliers" and indicated with crosses in all plots.
The $FEROS$ "outliers" are clearly separated from the main distribution of the points. Consequently da Silva et al. (2006) excluded them from our statistical considerations in the paper. Thus not taking into account these defined "outliers" we found a mean of $(B–V)–(B–V)_0$ = -0.009 mag with a scatter of 0.031 mag. We considered this scatter as the typical error of our PDF method for determining the intrinsic colour of the southern sample.
In contrast to the $FEROS$ study, the TLS "outliers" are not so clearly separated from the main distribution of points and thus I keep the "outliers" in the sample and take them into account by the interpretation of the plots.
According to da Silva et al. (2006) the "outliers" with high $(B–V)–(B–V)_0$ values can be explained in general as stars with a significant reddening, stars for which the $HIPPARCOS$ catalogue has a wrong entry for $(B–V)$ or stars for which the parameter estimation (including $T_{\rm eff}$, [Fe/H] and $(B–V)_0$) substantially failed.
For the two $FEROS$ "outliers" in Fig. 4.3 (lower left) da Silva et al. (2006) considered the third alternative as the most likely one. Excluding these "outliers" the southern stars show no increase of $(B–V)–(B–V)_0$ with distance. This is, according to da Silva et al. (2006), reasonable because stars within distances less than $\sim$ 200 pc have only a small reddening.
Additionally to the "outliers", and contrary to the $FEROS$ sample, the TLS survey shows in Fig. 4.3 (top left) some hints, possibly supported by "outliers", for a correlation between $(B–V)–(B–V)_0$ and the distance from the Sun. To find out causes for this trend and for the TLS "outliers", as well as for the different $(B–V)–(B–V)_0$ behaviour of both samples, I checked the distance at which the TLS "outliers" are placed.
I found a range between 150–200 pc. Thus the bulk of TLS "outliers" is slightly further away than the bulk of $FEROS$ "outliers". However the bulk of "outliers" in the North is still within 200 pc which mostly excludes reddening as the cause for these "outliers", the increasing $(B–V)–(B–V)_0$ trend and the different behaviour of both samples.

Dust maps (Schlegel et al. 1998) cannot help to verify the reddening of the TLS stars because they are too nearby and not well covered by these maps. Consequently for the TLS "outliers" the two other explanations, wrong $HIPPARCOS$ entry for B–V or failed parameter estimation, are still available. However none of both is favoured at the moment. Thus the cause for the trend of increasing $(B–V)$–$(B–V)_0$ with distance in the North is still not clear.
The second test showed for the northern stars that obviously $(B–V)$–$(B–V)_0$ does not depend on the effective temperature T_{eff}, as shown in Fig. 4.3 (top right), which is probably caused by the limited range of T_{eff} represented in the TLS sample.
In contrast to the North, a correlation with a minimum difference at $\sim$ 4700 K and a maximum difference at $\sim$ 4000 K exists, according to da Silva et al. (2006), between colour excess and T_{eff} in the southern sample as shown in Fig. 4.3 (lower right).
The correlation is caused by errors in the theoretical T_{eff}-colour relation adopted in the Girardi et al. (2000) isochrones. This is due to the fact that theoretical isochrones are built using luminosity L and T_{eff}, then one uses T_{eff}-colour and T_{eff}-Bolometric Correction (BC) relations to convert them to the photometric system. These errors in the theoretical T_{eff}-colour relation amount to less than 0.05 mag, or equivalently to about 100 K for a given $(B–V)_0$. The possible systematic errors of 0.05 mag in the adopted T_{eff}-colour relation would imply errors smaller than 0.03 dex for the V-band BCs adopted for the same isochrones, which would then be the maximum mismatch between theoretical and observational M_V values. According to da Silva et al. (2006) these errors were small enough to be neglected.

4.3.2 Surface gravities

A further check was the comparison (see Fig. 4.4) between the logarithmic physical ("estimated") surface gravity $\log g_{phys}$ and the logarithmic spectroscopic surface gravity $\log g_{spec}$ values.
The physical surface gravity was estimated by adopting a stellar mass and radius. The mass was determined by using the effective temperature and luminosity with the evolutionary tracks of Girardi et al. (2000). Interpolation among the tracks provided the required mass. The uncertainty in the physical gravity is dominated by the uncertainty in M_V and stellar mass. One aspect of this uncertainty in the mass is the mass loss on the evolution of the stars. This aspect is taken into account in the used evolutionary tracks of Girardi et al. (2000).
In the case of a host star, mass loss also has consequences for the mass of the planet $m \sin i$. Lowering the mass of the host star in Eq. (3.17) also lowers the mass of the planet. Contrarily, increasing the mass of the host star increases the mass of the planet. Mass loss of the host star also lowers the gravitational potential and consequently enables the planet to migrate outwards. This is an additional effect on the planet caused by mass loss of the host star.

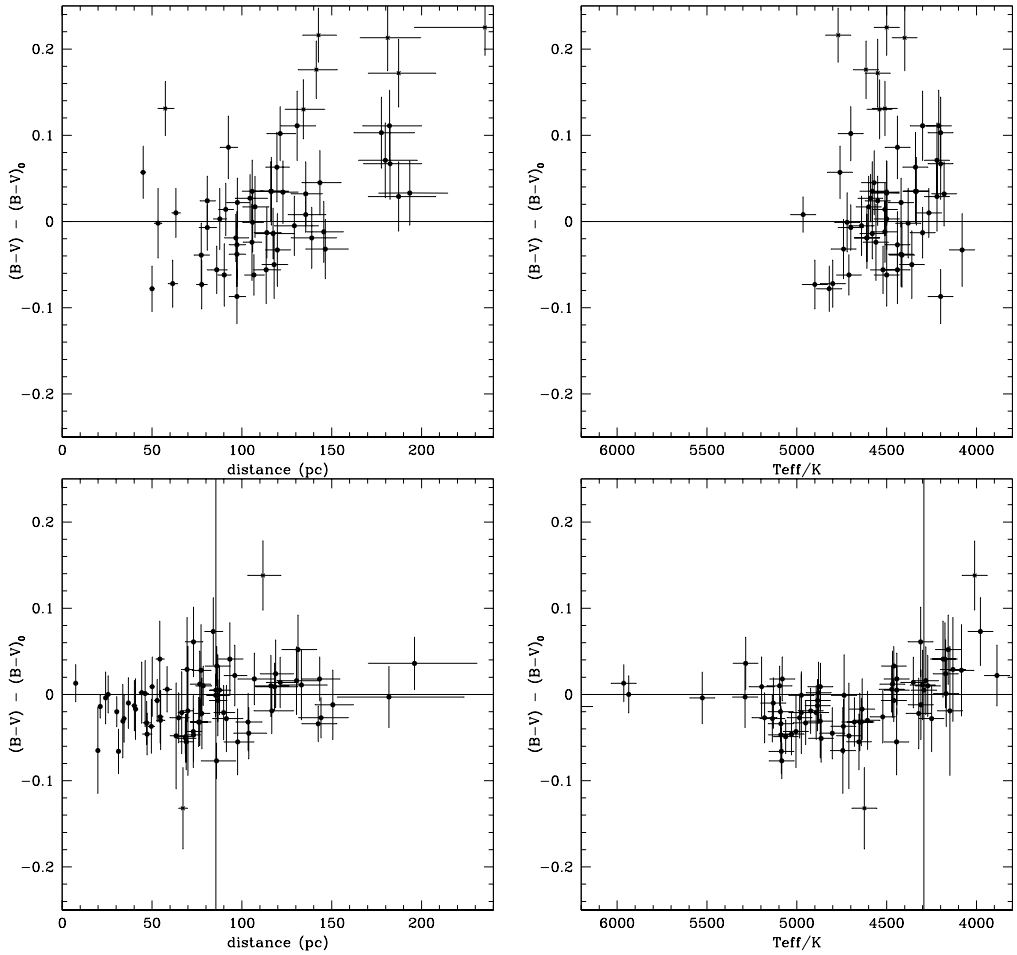

Figure 4.3: $(B–V)$–$(B–V)_0$ [mag] as a function of distance [pc] from the Sun (left) and T_{eff} [K] (right) for the Tautenburg (top) and *FEROS* (lower) sample. Stars with $|(B–V)–(B–V)_0| \geq 0.1$ are defined as "outliers" and marked as crosses in all plots. These are stars which show a larger dispersion of the $(B–V)_0$ values in comparison with the bulk of the other stars. The Tautenburg sample exhibits some correlation between $(B–V)$–$(B–V)_0$ versus distance (top left). However there is no trend between colour excess and T_{eff} visible in the northern sample (lower right). The *FEROS* sample shows the opposite behaviour in the two corresponding plots published in da Silva et al. (2006). Notice the absence of a clear trend of $(B–V)$–$(B–V)_0$ with distance (lower left). However the small differences for most of the stars (less than 0.05 mag) appears to be a function of T_{eff} (lower right).

The spectroscopic surface gravity was derived from the spectrum itself. It is based on the ionization balance of Fe I and Fe II and hence, upon the Fe I and Fe II oscillator strengths (see §3.3.2). The spectroscopic gravities are given in Tab. 4.1 and Tab. 4.4. The physical gravities are given in Tab. 4.4 to enable a comparison.

Table 4.4: Comparison of the spectroscopic and physical gravities.

HD	$\log g_{spec}$ [dex]	$\log g_{phys}$ [dex]
2774	2.7	2.36 ± 0.09
6497	2.4	2.50 ± 0.08
6319	2.7	2.47 ± 0.17
9927	1.9	1.96 ± 0.12
13982	2.3	2.32 ± 0.09
26755	2.9	2.44 ± 0.13
31579	2.8	2.05 ± 0.11
30338	2.2	2.07 ± 0.10
32518	2.1	2.44 ± 0.10
37601	2.6	2.99 ± 0.08
40083	2.5	2.40 ± 0.09
45866	2.2	1.68 ± 0.11
47914	1.9	2.22 ± 0.09
49878	2.7	2.17 ± 0.11
58425	2.1	2.15 ± 0.10
60294	2.4	2.44 ± 0.11
73108	1.8	1.98 ± 0.10
77800	1.6	1.36 ± 0.11
83506	2.7	2.46 ± 0.06
85841	1.9	2.22 ± 0.10
92523	1.9	1.67 ± 0.11
93859	2.1	2.31 ± 0.10
93875	1.9	2.39 ± 0.08
94084	2.2	2.62 ± 0.09
96833	2.4	2.25 ± 0.10
97989	1.8	2.33 ± 0.09
102328	1.9	2.29 ± 0.06
103605	2.8	2.45 ± 0.10
106574	2.2	2.10 ± 0.11
113049	2.2	2.37 ± 0.09
118904	2.2	2.10 ± 0.10
129245	3.3	2.40 ± 0.09
131507	1.5	1.62 ± 0.10
136726	1.6	1.90 ± 0.10
137443	2.6	2.04 ± 0.10
138265	2.4	1.66 ± 0.11
139357	2.9	2.41 ± 0.09
148293	2.5	2.49 ± 0.10
150010	2.8	2.34 ± 0.10

Continued overleaf ...

Table 4.4: Comparison of the spectroscopic and physical gravities.

... continuing from previous page.		
HD	$\log g_{spec}$ [dex]	$\log g_{phys}$ [dex]
152812	1.4	1.55 ± 0.11
153956	2.3	2.47 ± 0.09
157681	1.6	1.79 ± 0.10
160290	2.7	2.41 ± 0.09
167042	2.9	3.14 ± 0.07
170693	1.0	1.67 ± 0.07
172340	2.1	2.04 ± 0.10
175823	2.1	2.04 ± 0.11
176524	1.7	2.05 ± 0.08
176408	2.3	2.36 ± 0.08
180610	2.85	2.63 ± 0.07
184293	1.9	1.80 ± 0.12
186815	2.5	2.93 ± 0.08
192781	2.3	1.65 ± 0.11
195820	2.4	2.42 ± 0.09
196925	2.8	3.04 ± 0.07
200205	1.6	1.50 ± 0.11
206952	2.4	2.45 ± 0.08
210905	2.7	1.50 ± 0.11
214868	2.1	1.89 ± 0.10
216174	1.2	1.83 ± 0.08
217382	1.8	1.44 ± 0.11
218029	2.0	1.95 ± 0.11

The first comparison in §4.2 was between spectroscopic gravities derived in a comparable way. I shall now also compare the values of the physical with the spectroscopic surface gravity. Fig. 4.4 (top left) clearly shows that the Probability Distribution Function (PDF)-estimated physical values tend to be systematically lower than the spectroscopically derived ones. Including the five outliers, the mean averaged difference is -0.07 dex. There are some suggested explanations for this phenomenon in the literature. According to Luck & Lambert (1985) the most likely explanation for this effect – also visible for the Sun – is that the theoretical models are not able to predict the right opacity and thus perhaps influence primarily the pressure structure of the models. This could also account for the gravity dependence, which would be a temperature dependence as the gravities correlate with the temperature, as the missing opacity could easily increase in strength with decreasing gravity or temperature. Da Silva et al. (2006) offers the further possibility that our method – also used in my work – underestimates possibly stellar masses. To exclude this possibility at the moment only our two Hyades standard giants are available. A comparison of the results of both stars (da Silva et al. 2006) and of one Hyades reference giant (my work) with values from the literature show no significant differences in stellar mass. However two stars are not very representative and in addition both stars are very similar. Thus this can be at best only a first hint to exclude the possibility of an underestimation of stellar masses. To derive solid conclusions, a larger number of stars is essential. An alternative possibility given by da Silva et al. (2006), for the systematic and still not understood

deficient in the logarithmic physical surface gravity values, is that the spectroscopic $\log g$ values are simply too high. The latter interpretation is supported by the consideration that gravity is determined by imposing ionization balance. This means that the Fe abundance found – in my case – for the 8 Fe II lines is the same as the one retrieved for the more than 144 Fe I lines. This determination method implies that spectroscopic gravities depend on the interplay between the stellar parameters, in addition to the adopted line oscillator strengths, in the derivation of Fe abundances. In the case of Pop I giants this can be rather complicated because in this type of giants the Fe I vs. Fe II abundance depends on the gravity and to a great extent also on the temperature. In this work I used the iron oscillator strengths adopted by Pasquini et al. (2004). Luck & Challener (1995) used the iron oscillator strengths given in Fuhr et al. (1988). Pasquini et al. (2004) analyzed in this context the dependence of Fe I and Fe II on $\log g$, $T_{\rm eff}$ and ξ for one Pop I giant and the same set of lines. They found out that a systematic shift of 100 K in $T_{\rm eff}$ would, for instance, produce a 0.2 dex shift in $\log g$ without changing substantially the derived Fe abundance. The discrepancy between the values of the physical (derived from parallaxes) and the spectroscopic gravities are well-known (da Silva 1986) and the problem remains despite improving models and parallax measurements. To study this problem, Nilsen et al. (1997) compared the *HIPPARCOS*-based gravities with the values obtained from spectroscopy by several authors and they conclude that differences between the two methods could become larger than 0.3 dex in $\log g$. According to them, causes such as non-LTE effects on FE I abundances or thermal inhomogeneities cannot be excluded. Fuhrmann et al. (1997) used the logarithmic physical surface gravity $\log g_{phys}$ to get rid of one parameter in spectroscopic analyses and claim that this is the more accurate approach. For Red Giant Branch (RGB) stars an effect that is apparent if I plot the gravities either spectroscopic or physical against effective temperature is that the lower temperature stars tend to have lower gravities as shown in Fig. 4.4 (lower left and right) which corresponds to a classical Colour-Magnitude-Diagram (CMD). This phenomenon is most likely due to the cooler stars having higher luminosity, an effect also noticeable even when comparing B–V with M_V in Tab. 4.5.

According to Luck (1991) the effect that the lower temperature stars tend to have lower gravities cannot be due to the lower mass in the cooler stars, because the [Fe/H] ratios exhibit no plausible dependence on the effective temperature $T_{\rm eff}$ (see Fig. 4.5, top left) and logarithmic surface gravity $\log g$ (spectroscopic and physical) as shown in Fig. 4.5 (lower left and right). The existence of such a relation would be an indication of lower masses.

Contrarily Luck & Challener (1995) found that the [Fe/H] ratios derived from the spectroscopic gravity exhibit a moderately strong dependence of [Fe/H] on gravity in the sense that lower gravities show lower [Fe/H] ratios. On the other hand they found that the Fe abundance ratios derived using the physical gravities do not show such a dependence. The reason for this according to them is that lower gravity models have somewhat cooler temperature structures than higher gravity models and thus to achieve a fixed Fe I strength a lower iron abundance is mandated. This effect is dependent upon effective temperature. Lower effective temperatures show a larger sensitivity to gravity than do higher temperatures. Contrarily to my work they note a dependence on spectroscopic gravity derived [Fe/H] ratios with the effective temperature. In detail their [Fe/H] ratios with low values are associated with low effective temperatures.

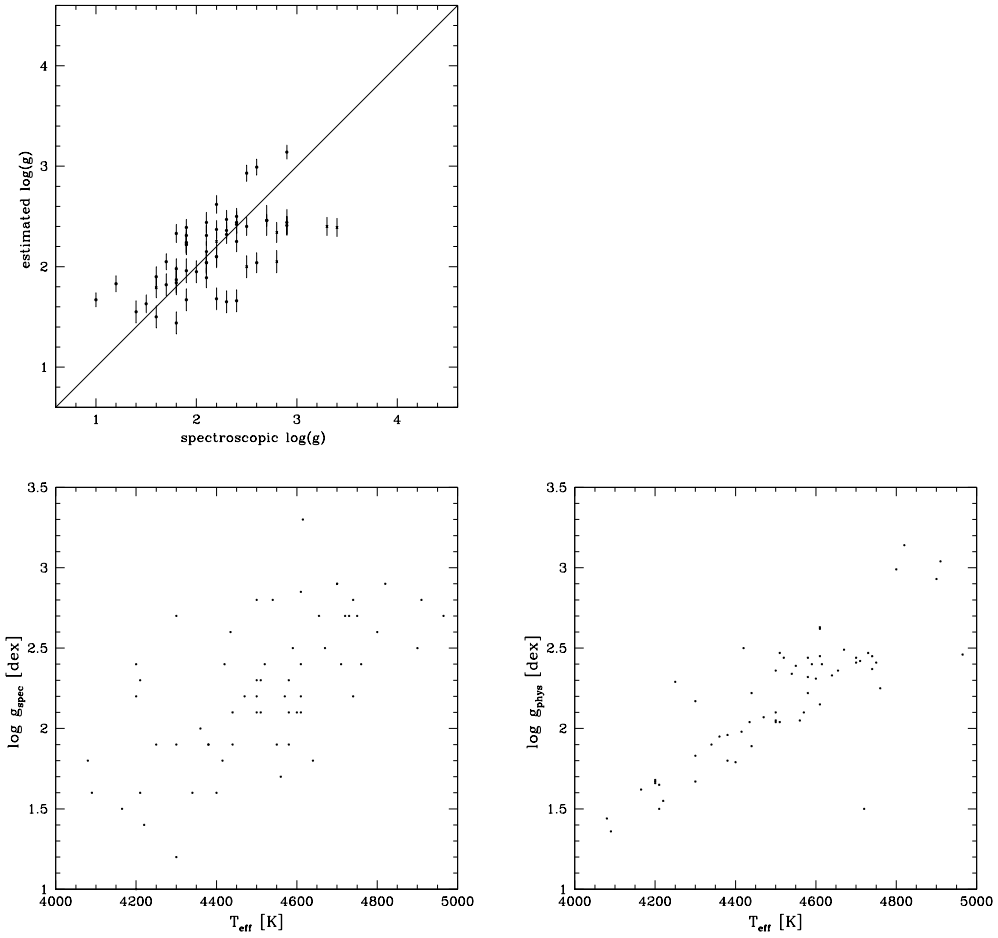

Figure 4.4: Comparison between the spectroscopic $\log g$ [dex] values derived from the spectra and the physical ("estimated") $\log g$ [dex] values from the photometry by means of our PDF method (top left). This systematic effect appears to be smaller than those in Fig. 4.1. Correlations between logarithmic spectroscopic (lower left) and physical (lower right) surface gravity and effective temperature $T_{\rm eff}$. The logarithmic spectroscopic surface gravity is less convincing due to the scatter.

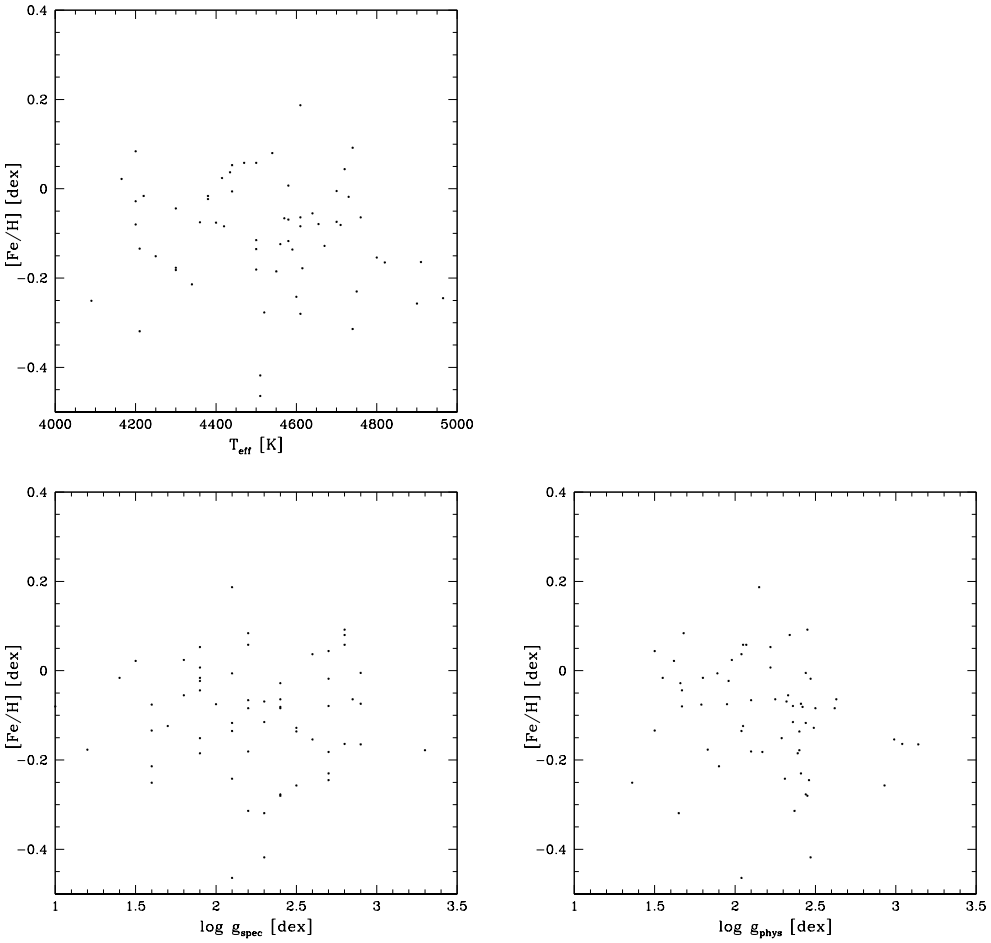

Figure 4.5: [Fe/H] abundances show neither dependence on the effective temperature $T_{\rm eff}$ (top) nor logarithmic surface gravity (spectroscopic $\log g_{spec}$ (lower left) and physical $\log g_{phys}$ (lower right)).

4.4 Ages and masses

As mentioned before, the mass, radius and age of each star from the Tautenburg sample are determined by utilising theoretical isochrones and a modified version of Jørgensen & Lindegren's (2005) method. The stellar mass is particularly important to verify the mass of planetary companions and the corresponding orbital parameters. This point is very essential because among giants, stars with different masses may occupy the same portion of the Hertzsprung-Russell-Diagram (HRD), and therefore a large uncertainty is present unless a careful analysis is performed. This uncertainty of the stellar mass is a function of the position of the sample stars in the HRD. Stars like giants are located in regions where the evolutionary tracks are closer together with corresponding larger errors than stars located between tracks further apart and well separated. Giants also suffer the so-called age-metallicity degeneracy which means that old metal-poor stars occupy the same portion of the CMD as young metal-rich objects. Having measured the metallicity of my TLS sample stars, it should be possible to resolve this degeneracy and to estimate stellar ages from the position in the CMD. Some degeneracy will still remain. For instance we cannot distinguish between first-ascent RGB and post Helium-flash (He-flash) stars, or between RGB and early-Asymptotic Giant Branch (early-AGB) stars according to da Silva et al. (2006).
The input parameters for each sample star were V, B–V, parallax with the corresponding error, logarithmic surface gravity $\log g$ and effective temperature $T_{\rm eff}$ as well as Fe abundance [Fe/H]. The first three values are taken from the $SIMBAD$ data base. For the whole programme stars trigonometric parallaxes with an accuracy better than 10 % from $HIPPARCOS$ were available because good distances are crucial to compute accurate absolute magnitudes. I derived the last three stellar parameters from the analysis of the stellar spectra. Then for every point in a dense grid of interpolated isochrones (Girardi et al. 2000) the probability P that the star could in reality be located there – which corresponds to a value for the age – was computed, given its nominal position in the three dimensional HR cube defined by log $T_{\rm eff}$, M_V and [Fe/H]. A Gaussian distribution for the observational errors was assumed. The integration over all points gave the likelihood distribution – G-function – for the possible ages of the star. The most probable age for the target star was then determined as the value for which the G-function has its maximum. The maximum of the G-function yields a well-defined age if the procedure is applied to a star located in a region of the HRD where the isochrones are well separated. In the case of giants this is not always true as mentioned above. To solve the problem of heavily crowded isochrones and age-metallicity degeneracy to estimate stellar ages from the position in the CMD the determination of the stellar metallicity is very helpful. Moreover the isochrones for the metal-poor isochrones are packed more closely. This is important for the TLS sample because a lot of target stars are metal-poor ([Fe/H] ≤ 0 per definition). Thus this determination method is as a consequence of all included and derived parameters not absolutely precise, because the effective temperature $T_{\rm eff}$ of a red giant is principally controlled by convection (Stothers & Chin 1995; Asida & Tuchman 1997; Wood 2006), which is very important for the modelling, and by its convective envelope opacity, which is largely a function of the abundance of heavy elements in the star (Hoyle & Schwarzschild 1955) according to Cole et al. (2005) and of the mass. But despite all these uncertainties the agreement of my results of my reference star – Hyades giant HD 27371 – with good-quality age and mass values from the literature is very good. For the Hyades turn-off age, as derived from models with overshooting, a value of 0.625 ± 0.05 Gyr is published by Perryman et al. (1998). Using the determination methods of this thesis we derived in da Silva

et al. (2006) the values 0.53 ± 0.09 Gyr and 2.70 ± 0.13 solar masses ($M_\odot$) for age t and mass M of HD 27371, respectively. Our age is consistent to within an accuracy of 1 σ. In this thesis I obtained the values 0.41 ± 0.04 Gyr and 2.83 ± 0.09 $M_\odot$. Both values are in agreement with the literature values. Tab. 4.5 shows all derived stellar parameters for the whole Tautenburg star sample. For a further comparison to estimate the accuracy of the Jørgensen & Lindegren's (2005) method and the applied isochrone set (Girardi et al. 2000) I used already determined values by other authors for a few stars as input values. In detail the Jørgensen & Lindegren's (2005) method was carried out for published stellar parameters (effective temperature $T_{\rm eff}$, Fe abundance [Fe/H], visual magnitude V and parallax π), which were derived in a comparable manner to my work, and their corresponding errors to compare my results (stellar age and mass) with the literature values. For the comparison I used the following three publications: "Retired A stars and their companions II: Jovian planets orbiting κ Borealis and HD 167042" (Johnson et al. 2007b), "A planetary companion to the Hyades giant ϵ Tau" (Sato et al. 2007) and "Structure and evolution of nearby stars with planets. II. Physical properties of $\sim$ 1000 cool stars from the SPOCS catalog" (Takeda et al. 2007). Johnson et al. (2007b) used the iochrones of Girardi et al. (2002). Sato et al. (2007) used the same evolutionary tracks (Girardi et al. 2000) which I used in my thesis. Takeda et al. (2007) constructed large and fine grids of theoretical stellar evolutionary tracks, computed with the Yale Stellar Evolution Code ($YSEC$), to model stellar parameters for the $SPOCS$ (Spectroscopic Properties of Cool Stars) stars (Valenti & Fischer 2005). The following stars were used for the comparison: HD 28305 (Sato et al. 2007), HD 167042 (Johnson et al. 2007b) and five stars (HD 9826, HD 75732, HD 120136, HD 143761 and HD 217014) published by Takeda et al. (2007). Tab. 4.6 shows in the first line for each star the input values and published parameters for age and mass. The second line for each star gives my derived values for the published stars. Despite the small number of stars which are available for the comparison, there seems to be a clear tendency that my derived values are consistent within the assumed errors with the values published by other authors. This trend is a first hint that the Jørgensen & Lindegren's (2005) method carried out with the isochrones of Girardi et al. (2000) works also well for at least one different isochrone set.

Table 4.5: Summary of the *TLS* stellar parameters.

HD	M_V [mag]	t [Gyr]	M [$M_\odot$]	R [$R_\odot$]	E_{B-V} [mag]	θ [mas]
2774	0.139 ± 0.178	1.690 ± 0.844	1.703 ± 0.318	13.73 ± 1.48	1.120 ± 0.034	1.059 ± 0.201
6319	1.192 ± 0.117	5.043 ± 3.759	1.144 ± 0.321	9.88 ± 0.78	1.117 ± 0.038	0.920 ± 0.122
6497	1.466 ± 0.142	8.482 ± 2.215	1.080 ± 0.077	9.30 ± 0.82	1.168 ± 0.028	0.888 ± 0.137
9927	-0.044 ± 0.086	2.148 ± 1.001	1.576 ± 0.267	20.95 ± 1.60	1.282 ± 0.040	3.656 ± 0.423
13982	0.425 ± 0.171	2.870 ± 1.495	1.401 ± 0.269	13.09 ± 1.37	1.145 ± 0.034	1.048 ± 0.193
26755	1.184 ± 0.130	5.760 ± 3.372	1.096 ± 0.243	10.02 ± 0.65	1.117 ± 0.026	1.154 ± 0.143
31579	-0.768 ± 0.434	0.822 ± 0.449	2.329 ± 0.466	23.01 ± 4.47	1.235 ± 0.032	0.910 ± 0.359
30338	-0.031 ± 0.122	1.786 ± 0.710	1.663 ± 0.231	18.99 ± 1.62	1.213 ± 0.037	1.672 ± 0.236
32518	1.082 ± 0.199	5.833 ± 2.582	1.133 ± 0.179	10.22 ± 0.87	1.114 ± 0.029	0.810 ± 0.143
37601	2.106 ± 0.093	5.355 ± 2.109	1.210 ± 0.124	5.62 ± 0.34	1.022 ± 0.027	0.850 ± 0.088
40083	1.045 ± 0.188	4.926 ± 2.604	1.156 ± 0.230	10.80 ± 0.54	1.173 ± 0.027	0.962 ± 0.131
45866	-0.497 ± 0.204	2.502 ± 1.185	1.500 ± 0.265	28.08 ± 3.25	1.387 ± 0.041	1.471 ± 0.309
47914	0.179 ± 0.145	2.089 ± 0.899	1.551 ± 0.233	15.40 ± 1.40	1.143 ± 0.033	1.528 ± 0.241
49878	0.756 ± 0.171	4.817 ± 2.347	1.239 ± 0.217	14.60 ± 1.60	1.322 ± 0.041	2.369 ± 0.445
58425	-0.083 ± 0.196	1.747 ± 0.702	1.620 ± 0.225	16.98 ± 1.92	1.119 ± 0.035	1.138 ± 0.232
60294	1.258 ± 0.140	6.054 ± 2.714	1.115 ± 0.200	10.19 ± 0.71	1.176 ± 0.027	1.103 ± 0.148
73108	0.146 ± 0.119	4.643 ± 2.113	1.229 ± 0.167	18.09 ± 1.46	1.219 ± 0.037	2.174 ± 0.295
77800	-0.772 ± 0.199	4.878 ± 2.328	1.181 ± 0.187	36.29 ± 4.19	1.428 ± 0.044	2.208 ± 0.458
83506	-0.510 ± 0.168	0.344 ± 0.058	3.184 ± 0.185	16.80 ± 1.41	1.022 ± 0.020	1.153 ± 0.186
85841	0.585 ± 0.143	3.969 ± 1.996	1.301 ± 0.223	14.15 ± 1.33	1.216 ± 0.039	1.160 ± 0.185
92523	-0.572 ± 0.159	3.039 ± 1.523	1.351 ± 0.243	27.12 ± 2.69	1.299 ± 0.040	1.931 ± 0.333
93856	0.507 ± 0.147	3.561 ± 1.966	1.288 ± 0.257	12.64 ± 1.22	1.113 ± 0.035	1.096 ± 0.180
93875	1.035 ± 0.116	6.091 ± 2.754	1.088 ± 0.191	10.56 ± 0.56	1.136 ± 0.028	1.217 ± 0.129
94084	1.515 ± 0.151	6.175 ± 2.460	1.174 ± 0.128	8.44 ± 0.68	1.129 ± 0.027	0.813 ± 0.122
96833	-0.267 ± 0.066	0.938 ± 0.403	2.063 ± 0.349	17.08 ± 0.98	1.083 ± 0.030	3.530 ± 0.310
97989	0.324 ± 0.205	2.993 ± 1.667	1.361 ± 0.274	12.64 ± 1.50	1.105 ± 0.034	0.910 ± 0.194
102328	1.263 ± 0.081	9.003 ± 2.003	1.070 ± 0.066	11.77 ± 0.71	1.291 ± 0.028	1.731 ± 0.169
103605	0.903 ± 0.132	3.975 ± 2.299	1.236 ± 0.257	10.48 ± 0.41	1.092 ± 0.028	1.008 ± 0.101
106574	-0.064 ± 0.165	2.083 ± 0.924	1.524 ± 0.229	17.54 ± 1.73	1.135 ± 0.037	1.137 ± 0.199
113049	0.172 ± 0.175	1.990 ± 0.970	1.554 ± 0.270	12.95 ± 1.41	1.062 ± 0.034	0.823 ± 0.156
118904	0.053 ± 0.141	2.199 ± 0.949	1.537 ± 0.219	17.57 ± 1.57	1.186 ± 0.036	1.331 ± 0.206
129245	0.517 ± 0.166	2.675 ± 1.256	1.446 ± 0.260	12.12 ± 1.17	1.144 ± 0.033	0.797 ± 0.138
131507	-0.180 ± 0.141	7.105 ± 2.590	1.081 ± 0.135	25.67 ± 2.36	1.357 ± 0.038	1.763 ± 0.276
136726	-0.366 ± 0.119	1.557 ± 0.538	1.804 ± 0.245	24.08 ± 1.84	1.307 ± 0.040	1.875 ± 0.246
137443	0.390 ± 0.124	4.445 ± 2.047	1.282 ± 0.178	17.2 ± 1.45	1.285 ± 0.039	1.37 ± 0.195
138265	-0.406 ± 0.190	3.527 ± 1.835	1.325 ± 0.247	27.22 ± 2.98	1.373 ± 0.041	1.388 ± 0.274
139357	0.550 ± 0.142	3.284 ± 1.614	1.313 ± 0.235	11.34 ± 0.91	1.078 ± 0.031	0.869 ± 0.127
148293	0.485 ± 0.092	1.396 ± 0.555	1.912 ± 0.307	12.55 ± 0.84	1.128 ± 0.038	1.295 ± 0.142
150010	0.631 ± 0.178	3.843 ± 2.069	1.268 ± 0.257	12.11 ± 1.27	1.160 ± 0.034	0.839 ± 0.156
152812	-0.372 ± 0.215	7.187 ± 2.651	1.035 ± 0.124	27.09 ± 3.16	1.301 ± 0.040	1.346 ± 0.291
153956	1.245 ± 0.099	6.282 ± 2.447	1.158 ± 0.140	9.96 ± 0.65	1.156 ± 0.030	1.018 ± 0.113
157681	-0.600 ± 0.200	2.240 ± 1.045	1.492 ± 0.255	24.66 ± 2.47	1.247 ± 0.038	1.267 ± 0.244
160290	0.340 ± 0.107	1.865 ± 0.795	1.615 ± 0.263	12.60 ± 0.89	1.063 ± 0.032	1.162 ± 0.139
167042	2.475 ± 0.055	5.651 ± 2.112	1.198 ± 0.116	4.70 ± 0.22	1.018 ± 0.026	0.874 ± 0.063

Continued overleaf ...

Table 4.5: Summary of the TLS stellar parameters.

... continuing from previous page.						
HD	M_V [mag]	t [Gyr]	M [$M_\odot$]	R [$R_\odot$]	E_{B-V} [mag]	θ [mas]
170693	-0.120 ± 0.101	9.209 ± 1.928	0.982 ± 0.059	23.10 ± 1.63	1.267 ± 0.031	2.209 ± 0.259
172340	-0.165 ± 0.152	1.684 ± 0.515	1.684 ± 0.183	19.74 ± 1.85	1.202 ± 0.035	1.262 ± 0.206
175823	-0.193 ± 0.214	1.726 ± 0.575	1.676 ± 0.195	19.59 ± 2.32	1.207 ± 0.037	0.942 ± 0.205
176524	-0.298 ± 0.105	1.383 ± 0.319	1.800 ± 0.130	20.24 ± 1.46	1.174 ± 0.044	1.784 ± 0.215
176408	0.955 ± 0.089	5.785 ± 2.530	1.117 ± 0.185	11.07 ± 0.77	1.157 ± 0.035	1.174 ± 0.130
180610	1.520 ± 0.050	5.422 ± 1.896	1.217 ± 0.115	8.52 ± 0.40	1.141 ± 0.025	1.596 ± 0.111
184293	-0.221 ± 0.142	4.020 ± 2.157	1.226 ± 0.242	22.28 ± 1.69	1.250 ± 0.036	1.453 ± 0.206
186815	1.830 ± 0.084	4.276 ± 1.655	1.235 ± 0.134	6.03 ± 0.34	0.963 ± 0.028	0.723 ± 0.069
192781	-0.492 ± 0.194	3.102 ± 1.585	1.380 ± 0.252	28.00 ± 3.16	1.369 ± 0.041	1.430 ± 0.289
195820	1.059 ± 0.113	6.359 ± 3.237	1.051 ± 0.201	10.09 ± 0.45	1.082 ± 0.023	0.880 ± 0.085
196925	1.964 ± 0.071	2.922 ± 0.845	1.423 ± 0.114	5.74 ± 0.30	0.996 ± 0.025	0.848 ± 0.072
200205	-0.735 ± 0.195	4.096 ± 2.109	1.217 ± 0.219	31.38 ± 3.47	1.339 ± 0.043	1.624 ± 0.326
206952	0.882 ± 0.054	3.338 ± 1.299	1.325 ± 0.193	11.00 ± 0.40	1.141 ± 0.025	1.898 ± 0.116
210905	1.165 ± 0.117	4.096 ± 2.109	1.217 ± 0.219	31.38 ± 3.47	1.339 ± 0.043	1.624 ± 0.326
214868	-0.331 ± 0.112	2.157 ± 0.896	1.527 ± 0.239	22.41 ± 1.47	1.234 ± 0.036	2.254 ± 0.265
216174	0.147 ± 0.143	9.640 ± 1.776	0.973 ± 0.051	19.14 ± 1.62	1.183 ± 0.029	1.564 ± 0.236
217382	-0.692 ± 0.125	3.080 ± 1.350	1.391 ± 0.215	35.86 ± 3.29	1.453 ± 0.042	2.786 ± 0.416
218029	-0.108 ± 0.133	1.895 ± 0.743	1.663 ± 0.246	21.87 ± 1.78	1.300 ± 0.039	1.726 ± 0.246

Table 4.6: Summary of the compared stellar parameters.

HD	V [mag]	π [mas]	T_{eff} [K]	[Fe/H] [dex]	t [Gyr]	M [$M_\odot$]
28305	3.53 ± 0.05	21.04 ± 0.82	4901 ± 20	0.17 ± 0.04	0.625 ± 0.050	2.7 ± 0.1
					0.480 ± 0.078	2.812 ± 0.118
167042	5.97 ± 0.05	20.0 ± 0.51	5020 ± 75	0.05 ± 0.06	2.2 ± 1.0	1.64 ± 0.13
					2.191 ± 0.432	1.575 ± 0.13
9826	4.09 ± 0.05	74.25 ± 0.72	6213 ± 44	0.12 ± 0.03	3.12 ± 0.24	1.31 ± 0.02
					2.652 ± 0.363	1.277 ± 0.016
75732	5.95 ± 0.05	79.80 ± 0.84	5253 ± 44	0.31 ± 0.03	> 7.24	0.96 ± 0.05
					> 5.633 ± 4.309	0.908 ± 0.027
120136	4.50 ± 0.05	64.12 ± 0.70	6387 ± 44	0.25 ± 0.03	1.64 ± 0.52	1.34 ± 0.05
					1.034 ± 0.573	1.309 ± 0.018
143761	5.40 ± 0.05	57.38 ± 0.71	5823 ± 44	-0.14 ± 0.03	11.04 ± 0.88	0.96 ± 0.02
					9.855 ± 1.169	0.966 ± 0.020
217014	5.49 ± 0.05	65.10 ± 0.65	5787 ± 44	0.15 ± 0.03	6.76 ± 1.64	1.05 ± 0.04
					3.775 ± 2.638	1.043 ± 0.035

Chapter 5

Tautenburg survey

The data discussed in this work were obtained in the Tautenburg Observatory Planet Search ($TOPS$) programme at the Thüringer Landessternwarte Tautenburg (TLS). One part of my work was devoted to the search for planet-hosting K giants in the Northern hemisphere.

5.1 Status of the radial velocity monitoring

The Radial Velocities (RVs) for the monitored K giants were calculated from the stellar spectra, taken with the iodine cell, using the programme *radialpsf* (Hatzes & Cochran 1993) as explained in §3.3.1. Afterwards the derived RVs were plotted against the Julian Date (JD) in a so-called RV curve. The shape of this plot, including RV amplitude and period, gives first indications of the different types of RV variations. These are stars showing constant RVs, while some show short-period (Smith et al. 1987; Hatzes & Cochran 1994a) RV variations of several days possibly caused by stellar oscillations and then there are long-term (Hatzes & Cochran 1993) RV variations of hundreds of days probably due to stellar and planetary companions and/or rotational modulation (surface inhomogeneities such as starspots). A second way to verify RV behaviour is the extraction of significant frequences in the RV data obtained using the time series analysis method of Lomb-Scargle periodograms (Scargle 1982). This type of plot will be explained in detail in §6.1.1 as a confirmation tool for exoplanets where the corresponding significant periods were used as input values to derive orbital solutions with the orbital fitting programme *GaussFit* (see §6.2.1). To discriminate between the different types of RV variability I used as a third hint the value of the standard deviation σ_{RV} because this value was determined for all 62 K giants. The corresponding σ_{RV} values are listed in Tab. 5.1 and plotted in Fig. 5.1.

Table 5.1: RV variations of K giants of the Tautenburg star sample.

HD	σ_{RV} $[m\,s^{-1}]$	HD	σ_{RV} $[m\,s^{-1}]$	HD	σ_{RV} $[m\,s^{-1}]$
2774	30.41	93859	190.15	160290	32.9
6319	35.77	93875	32.67	167042	27.18
6497	32.71	94084	102.46	170693	86.12
9927	37.46	96833	23.87	172340	19.98
13982	44.28	97989	9.72	175823	24.32
26755	3505.77	102328	40.03	176408	702.06
31579	152.53	103605	16.42	176524	4958.33
30338	45.44	106574	110.98	180610	158.14
32518	74.66	113049	2572.86	184293	85.16
37601	16.41	118904	28.64	186815	29.4
40083	52.09	129245	40.5	192781	46.56
45866	55.72	131507	39.84	195820	34.23
47914	320.78	136726	130.28	196925	9.63
49878	18.44	137443	61.74	200205	128.98
58425	4398.7	138265	387.09	206952	121.94
60294	10.8	139357	119.01	210905	30.11
73108	144.55	148293	11.78	214868	32.06
77800	78.29	150010	38.17	216174	120.05
83506	208.92	152812	1507.02	217382	40.9
85841	232.66	153956	2096.5	218029	13.66
92523	134.82	157681	137.42		

The sample stars in the upper part of Fig. 5.1 (left) show variable σ_{RV} values which I used to characterise the RV behaviour. As clearly seen in the lower part of Fig. 5.1 (left) the different types of RV variability are spread over the whole Colour-Magnitude-Diagram (CMD) and are not clustered or restricted to special regions. The exoplanet candidates in particular are distributed over the entire Red Giant Branch (RGB). Therefore selection effects can be excluded to mimic the features of the diagrams. Apart from the radial velocities, I used $HIPPARCOS$ photometry (see §6.1.2) and Hα variations (see §6.1.3) as input data sets for times series anlaysis to confirm individual RV variability for each sample star, derived from these three RV criteria, in particular to confirm planetary companions. The criteria, which have to be fulfilled in my work for each type of RV variability, are listed in Tab. 5.2.

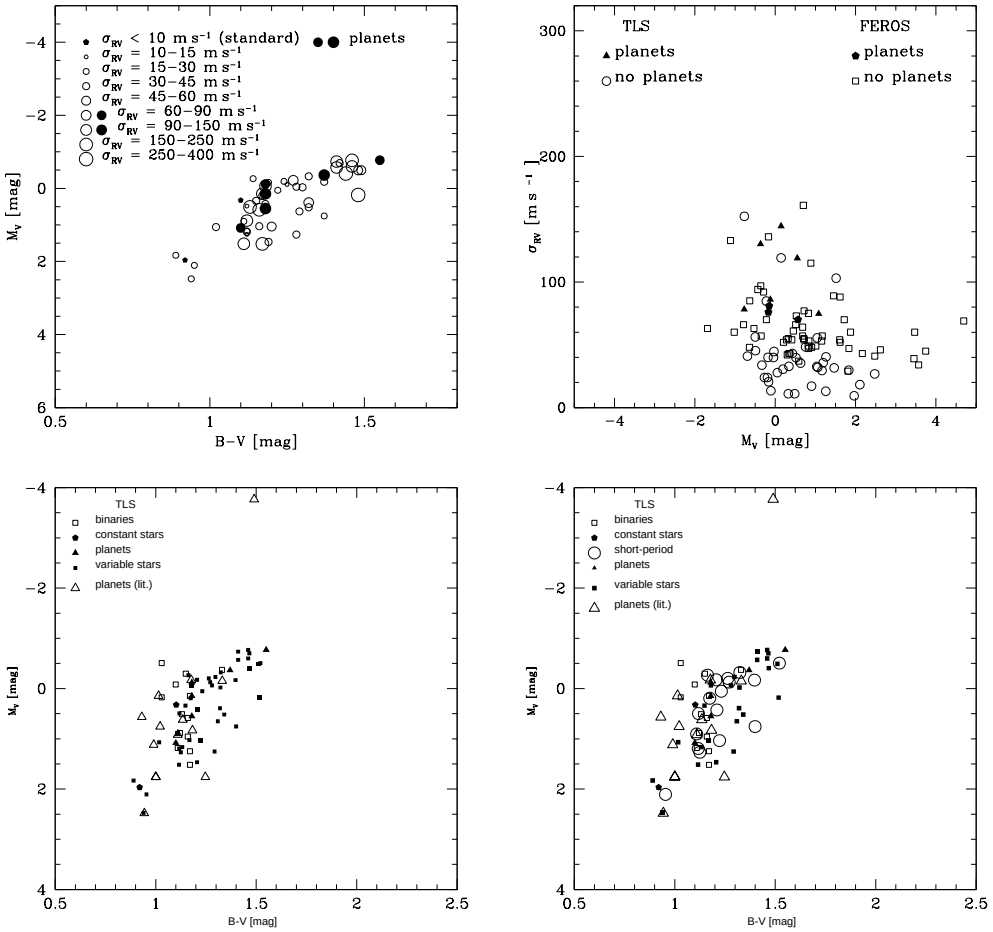

Figure 5.1: Trends of RV variability – given by σ_{RV}, listed in Tab. 5.1 – along the RGB. The scale of the dots gives the σ_{RV} value. The σ_{RV} in the upper part of the RGB is not significantly larger than those in the lower and middle part as well as in the clump region (top left). Setiawan et al. (2004a) published an increase of spread and of minimum variability with increasing luminosity for the southern study carried out with the Fiber-fed Extended Range Optical Spectrograph ($FEROS$). This trend is not visible in the northern TLS star sample. The different types of RV variability for the Tautenburg sample are shown in the lower part of the left side. A similar plot, however with the modification that the short-period RV variability is shown individually and not as a part of the variable stars in common, is shown in the lower part on the right side. Exoplanets from the literature are added in both plots. RV variability as a function of the stellar absolute visual magnitude M_V for the Tautenburg and the $FEROS$ sample (top right). The binaries are eliminated. TLS stars hosting giant planets are indicated with filled triangles in contrast to filled pentagons for the $FEROS$ survey. Tautenburg stars without planets are marked with empty circles and $FEROS$ stars without planets are tagged with squares.

Table 5.2: Criteria to discriminate between different types of RV variability.

RV variability	σ_{RV} $[m\,s^{-1}]$	P [days]	Δ *HIPPARCOS* [%]	Δ Hα [%]
"constant"	< 10		< 2	< 2
pulsations	10-60	< 80	> 10	> 10
stellar binary	150-5000	> 500	< 10	< 10
planetary companion	60-150	$> 100^{(a)}$	< 10	< 10
inhomogeneities (e.g. starspots)	< 100	< 80	> 10	> 10

$^{(a)}$ $P_{Planet} \neq P_{HIPPARCOS} \neq P_{H\alpha} \neq P_{Rotation}$

5.1.1 Standard stars and RV trends

An important result after approximately 3 years monitoring the giant *TLS* sample is the detection of only 2 stars (3 %) – HD 196925 (74 Dra) and HD 97989 – which show RV variations lower than 10 m s^{-1} at all timescales analysed. The RV data sets of these two stars are shown in Fig. 5.2.
It confirms that K giants are RV variables. This was first suggested by Walker et al. (1989), and from photometry by Edmonds & Gilliland (1996) using Hubble Space Telescope (HST) photometry.
For my work I define their RV behaviour as "constant" to use both giants as standard stars. However I know that the term "constant" is relative and very subjective. It depends on the measurement error and the behaviour of the sample. Looking with enough precision and sampling there are probably no "constant" K giant stars. To exclude other RV variations on short-period and/or long-term timescales due to radial and/or non-radial stellar oscillations, stellar (binaries) and substellar companions as well as rotational modulation (starspots) I applied time analysis tools such as the Lomb-Scargle diagram (see §6.1.1) to the RVs, *HIPPARCOS* and Hα data to search for significant frequences in all these data sets.
The *HIPPARCOS* photometry and the Hα activity confirmed the lack of significant frequences in the data RV data of HD 196925 (74 Dra) and HD 97989. Thus both K giants are suitable as RV standards because there are no indications of exoplanets, pulsations and/or rotational modulation. Plots of the RV monitoring (top), periodograms of the radial velocities (middle) and *HIPPARCOS* photometry (lower) are shown for both stars in Fig. 5.2.

The fact that the "constant" star 74 Dra is a low luminosity is consistent with the fact that a decreasing "oscillation" amplitude is expected with increasing gravity. Döllinger et al. (2005) found that stars show RV and photometric variability, which seems to increase with increasing luminosity. According to Frandsen et al. (2007) this could either be due to a combination of activity and granulation, or to pulsations, either self-excited (Mira-like) or driven by convective motions (solar-like). Edmonds & Gilliland (1996) has found similar evidence for increased variability for stars in the globular cluster 47 Tucanae.
A strict limit of < 10 m s^{-1} for the RV variability and in addition a good time coverage as essential criteria for a standard star exclude further low-amplitude sample stars such as HD 37601, HD 49878, HD 60294, HD 103605 and HD 148293 as RV standards.
By comparison Setiawan et al. (2004a) used τ Cet as a "constant" star which showed RV variability of less than 28 m s^{-1} from their measurements.

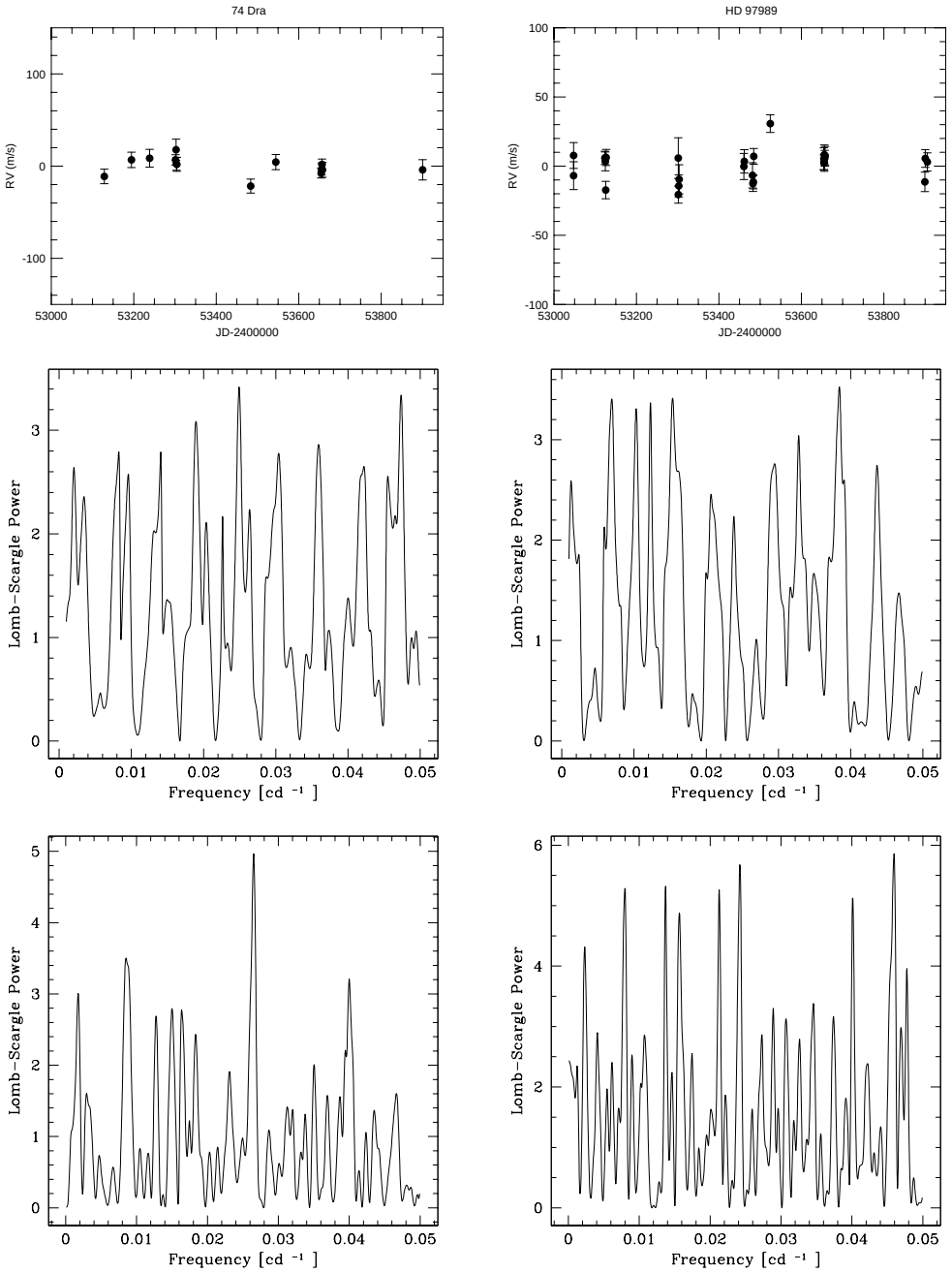

Figure 5.2: Plots of the RV monitoring (top), scargle periodograms of the RVs (middle) and the *HIPPARCOS* photometry (lower) of the *TLS* standard stars 74 Dra (left) and HD 97989 (right). RV plotted against JD and scargle power plotted against frequency. The unit of the frequency is cycles/day [cd^{-1}].

The lower RV variability (see Fig. 5.2) of my standard stars is caused by the approximately 5 times higher RV precision (3–5 $\mathrm{m\,s^{-1}}$) of the Tautenburg spectrograph in contrast to *FEROS* (25 $\mathrm{m\,s^{-1}}$). Thus for the detection of "constant" stars, the accuracy of the instrument plays an important role and it is reasonable to expect that a higher RV precision results in a lower percentage of "constant" stars. This is probably the cause for the higher percentage of RV variables detected in the *TLS* survey which is quite obvious in Fig. 5.1 (right). This figure shows the RV variability as a function of M_V for the Tautenburg and the *FEROS* sample. I found no strong evidence of increasing σ_{RV} with position along the RGB in the upper and lower part of Fig. 5.1 (left). The size of the symbols for each star is proportional to its RV variability in the upper part of Fig. 5.1 (left).

5.1.2 Short-period RV variations

Moreover the statistics of the programme contain 17 stars (27 %) which show short-period RV variations possibly due to radial and/or non-radial stellar oscillations. Evidences for radial and/or non-radial stellar pulsations in G–K giant stars were already published in Arcturus (Smith et al. 1987; Hatzes & Cochran 1994a), β Oph (Hatzes & Cochran 1994b), α UMa (Buzasi et al. 2000) and ξ Hya (Frandsen et al. 2002). The timescale of short-period RV variability, indicated by RV variations in the Lomb-Scargle periodograms, range in the literature from a few hours to $\approx$ 2–10 days (Hatzes & Cochran 1994b). Recently Hatzes & Cochran (1998) detected a period of $\approx$ 50 days in the spectral line bisector variations in Aldebaran which they attributed to oscillations due to the fact that starspots of this period would imply a very high rotation rate which is not published for Aldebaran. Spectral line bisectors, the locus of midpoints of the spectral line from the core to the continuum, have proved to be a useful technique for measuring the asymmetries in the shapes of spectral line profiles according to Hatzes (1996). Spectral line bisectors have been used to discern the convection pattern of the stellar surface (Dravins 1987; Gray 1982) and stellar surface inhomogeneities such as cool starspots (Toner & Gray 1988; Dempsey et al. 1992).
Checking the RV variability of my sample from night-to-night or within short observed time spans, I found peak-to-peak RV amplitude variations of up to $\approx$ 100 $\mathrm{m\,s^{-1}}$ on timescales of hours till around 80 days. Thus my period values, derived from Lomb-Scargle periodograms and estimated from RV plots, are in good agreement with the literature. However both time limit values are only first estimates because my sampling was unable to find exact periods. Thus I cannot prove that these RV variations are really pulsations. But planetary companions and rotational modulation caused by starspots can be excluded as causes for the observed RV variability. It is impossible for a giant to have a planet in such a short-period orbit because an exoplanet with an orbital period of less than 100 days would have an orbit which is smaller than the stellar radius of a giant star and would be swallowed up by the parent star. Rotational modulation of the period of this time span would imply that the star rotates very fast ($v \sin i \geq 100$ $\mathrm{km\,s^{-1}}$). However, such high values are not published for any of the target stars.

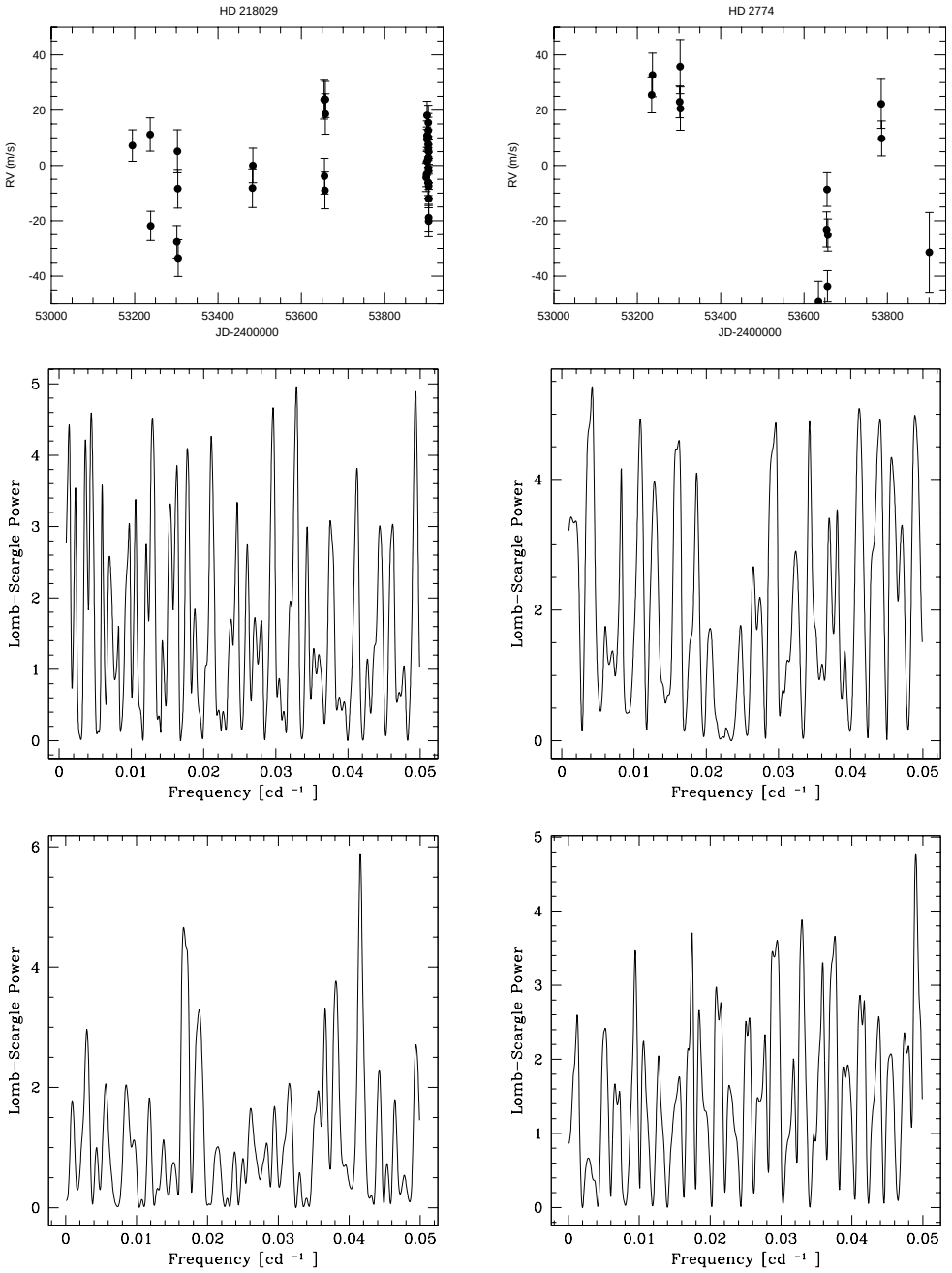

Figure 5.3: Plots of the RV monitoring, scargle periodograms of the RVs and the *HIPPARCOS* photometry of the possible pulsating *TLS* stars HD 218029 (left) and H D 2774 (right). RV plotted against JD and scargle power plotted against frequenc y.

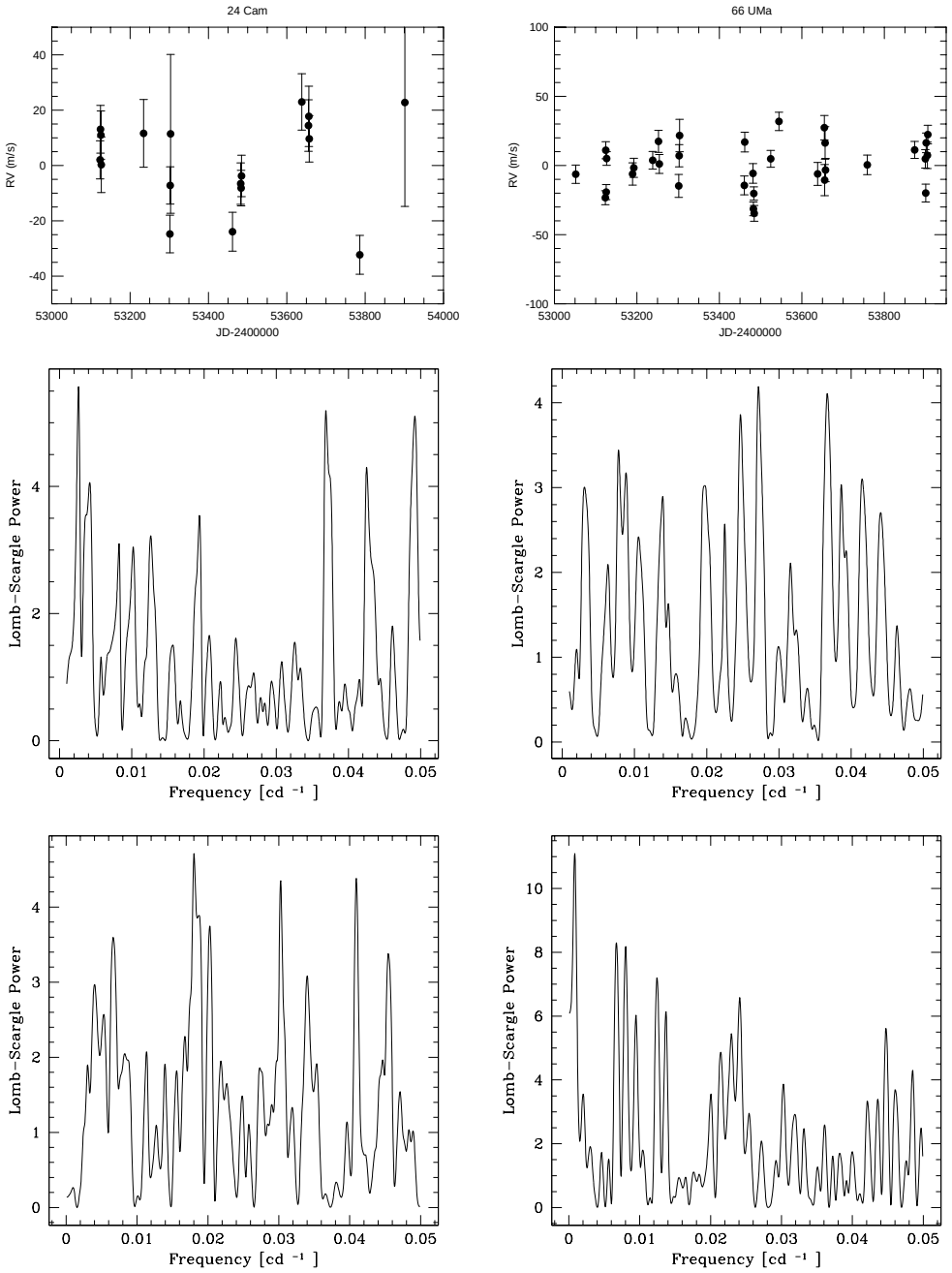

Figure 5.4: Plots of the RV monitoring, scargle periodograms of the RVs and the *HIPPARCOS* photometry of the possible pulsating *TLS* stars 24 Cam (left) and 66 UMa (right). RV plotted against JD and scargle power plotted against frequency.

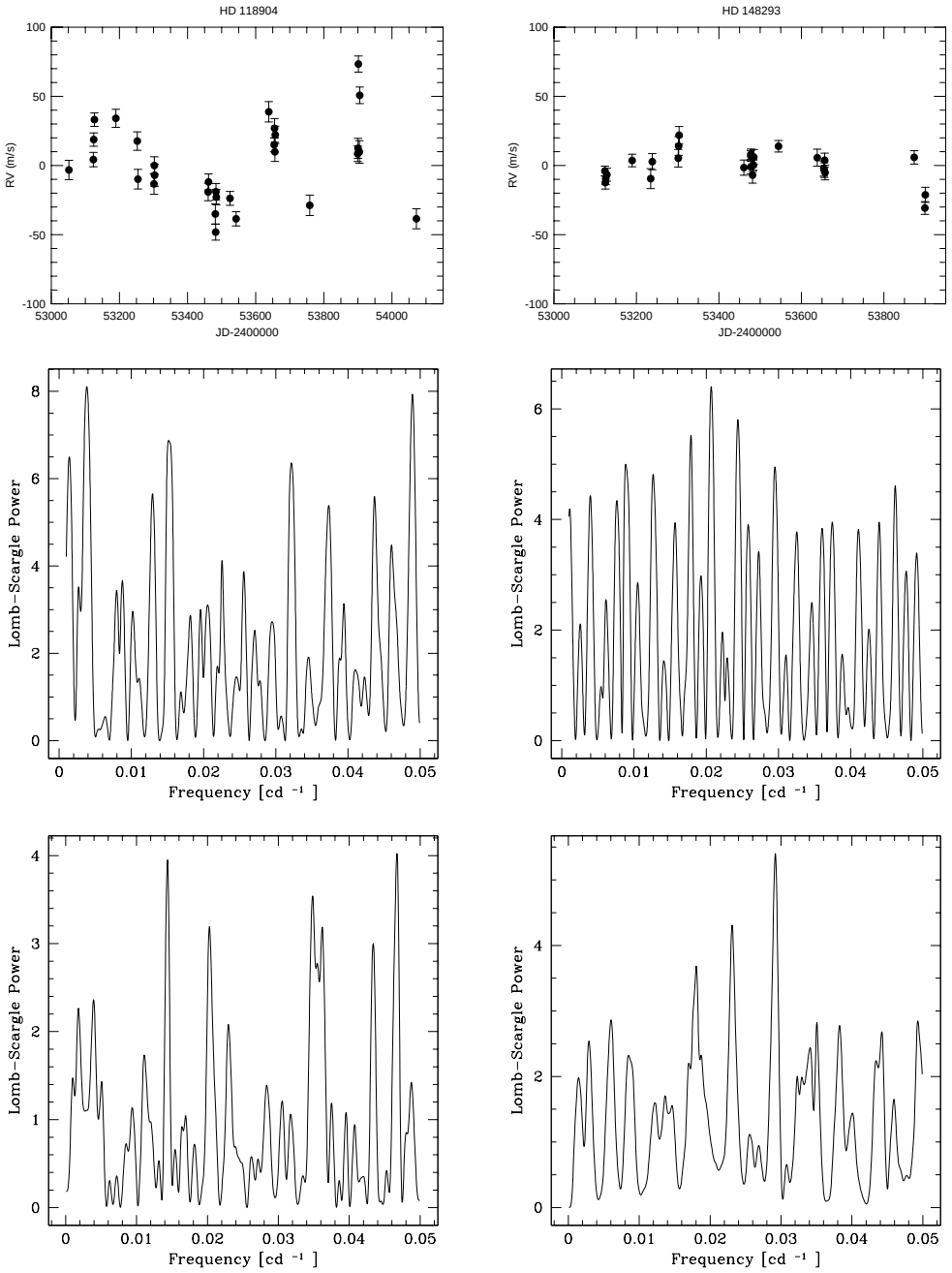

Figure 5.5: Plots of the RV monitoring, scargle periodograms of the RVs and the *HIPPARCOS* photometry of the possible pulsating *TLS* stars HD 118904 (left) and HD 148293 (right). RV plotted against JD and scargle power plotted against frequency.

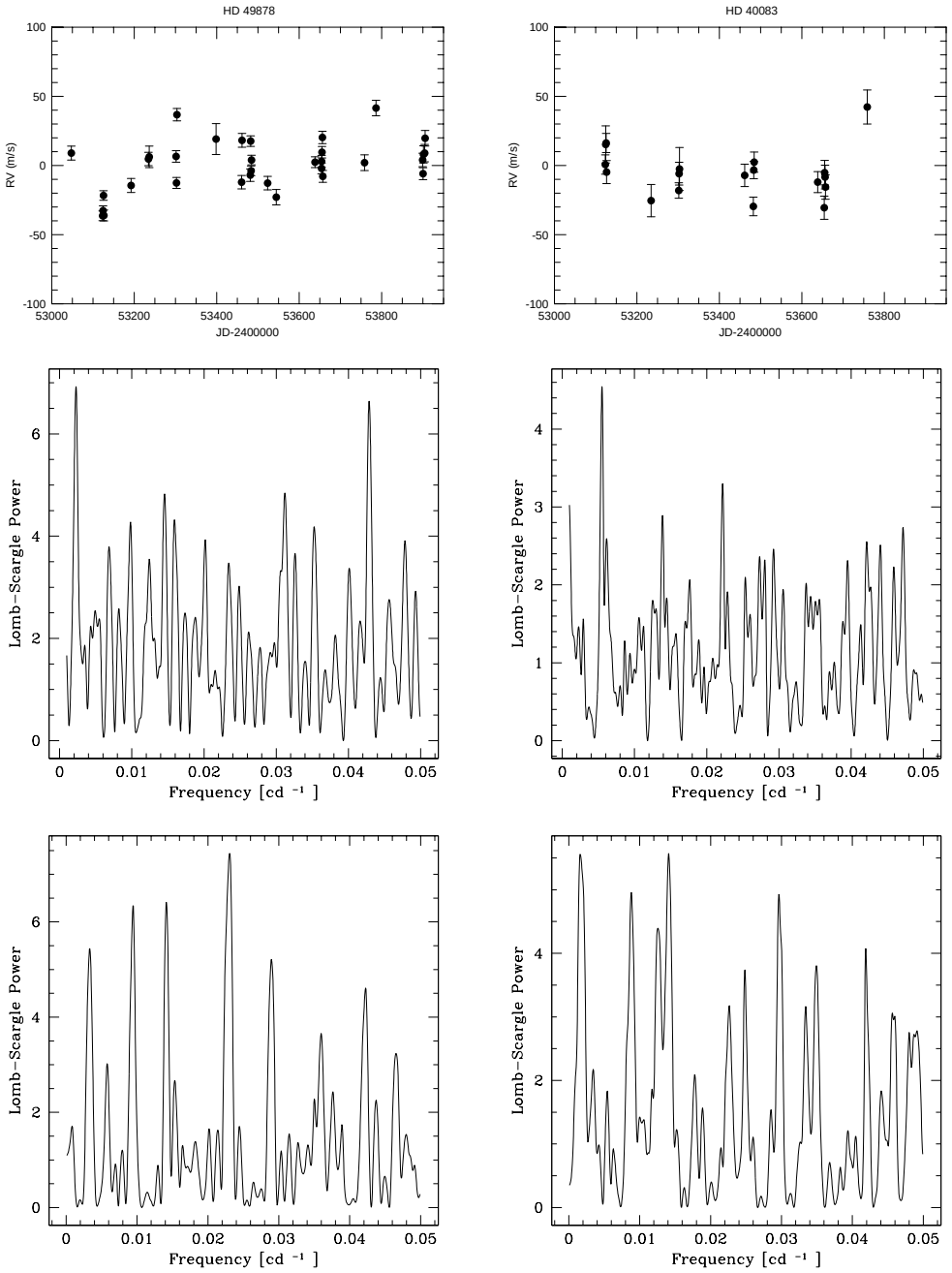

Figure 5.6: Plots of the RV monitoring, scargle periodograms of the RVs and the *HIPPARCOS* photometry of the possible pulsating *TLS* stars HD 49878 (left) and HD 40083 (right). RV plotted against JD and scargle power plotted against frequency.

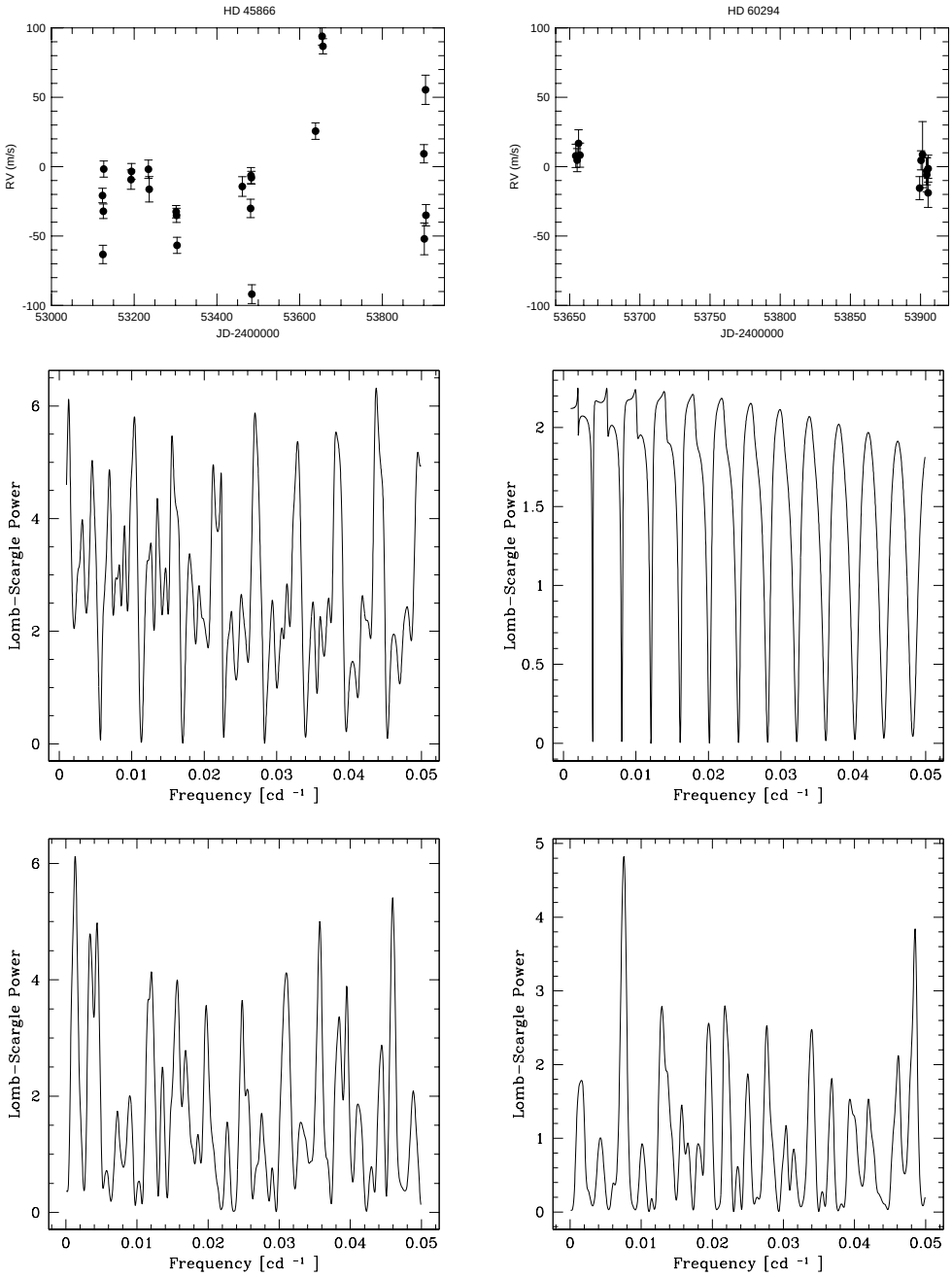

Figure 5.7: Plots of the RV monitoring, scargle periodograms of the RVs and the *HIPPARCOS* photometry of the possible pulsating *TLS* stars HD 45866 (left) and HD 60294 (right). RV plotted against JD and scargle power plotted against frequency. For both stars it is possible that only the first peak is significant and the other peaks are caused by aliasing. The reason for the "shape" of the scargle periodograms of the RVs for these stars is still not clear.

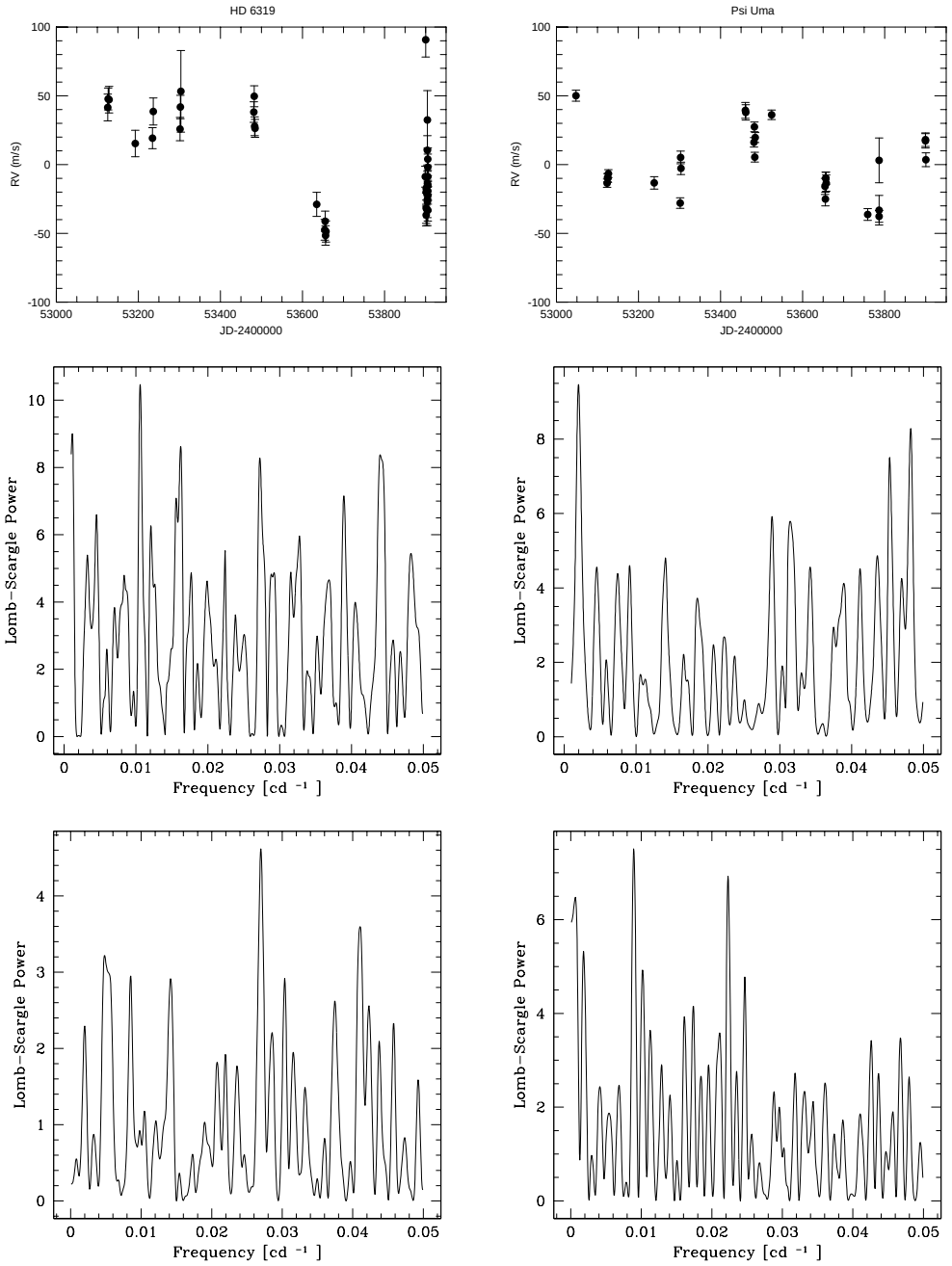

Figure 5.8: Plots of the RV monitoring, scargle periodograms of the RVs and the *HIPPARCOS* photometry of the possible pulsating *TLS* stars HD 6319 (left) and Psi Uma (right). RV plotted against JD and scargle power plotted against frequency.

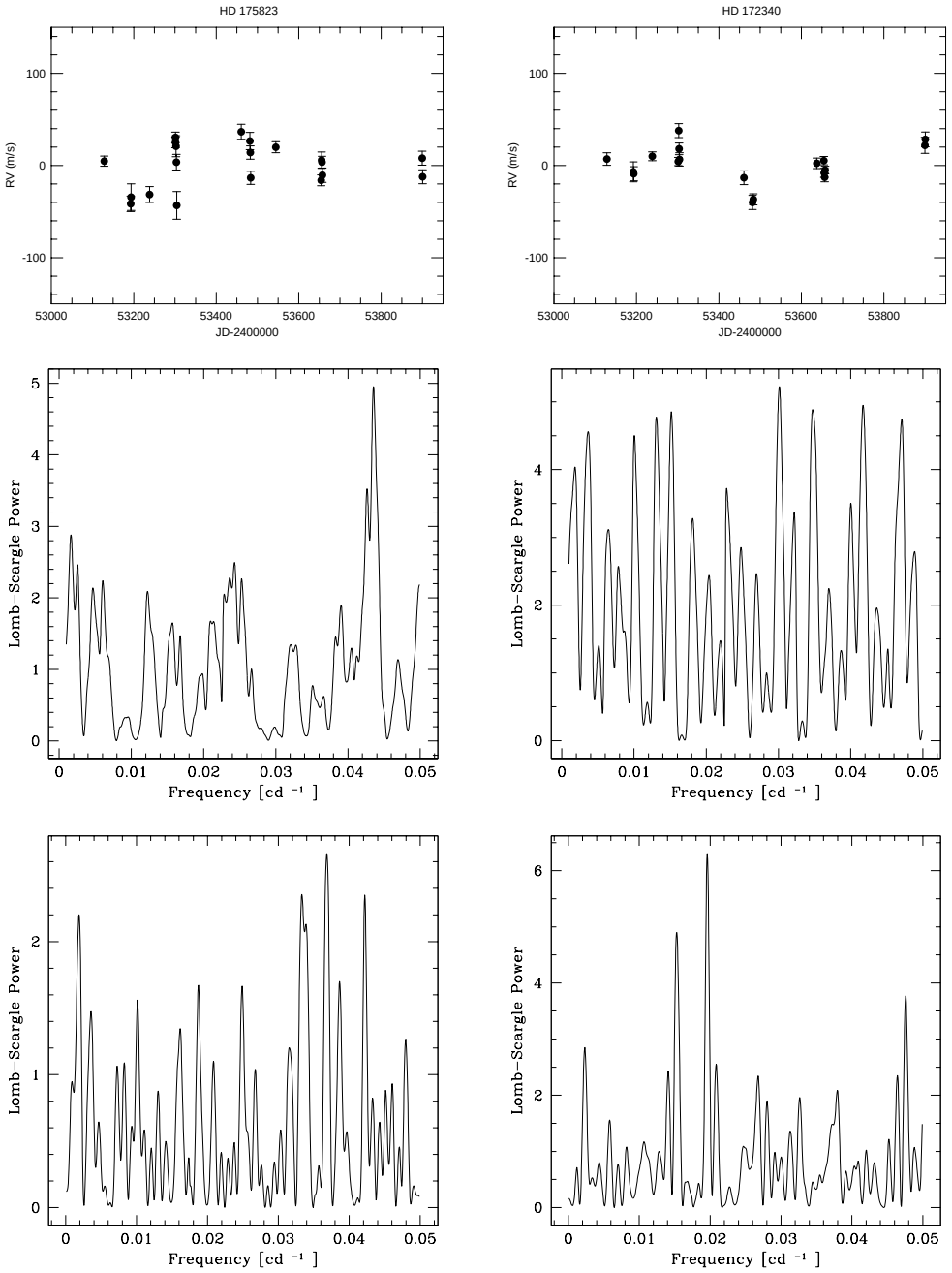

Figure 5.9: Plots of the RV monitoring, scargle periodograms of the RVs and the *HIPPARCOS* photometry of the possible pulsating *TLS* stars HD 175823 (left) and HD 172340 (right). RV plotted against JD and scargle power plotted against frequency.

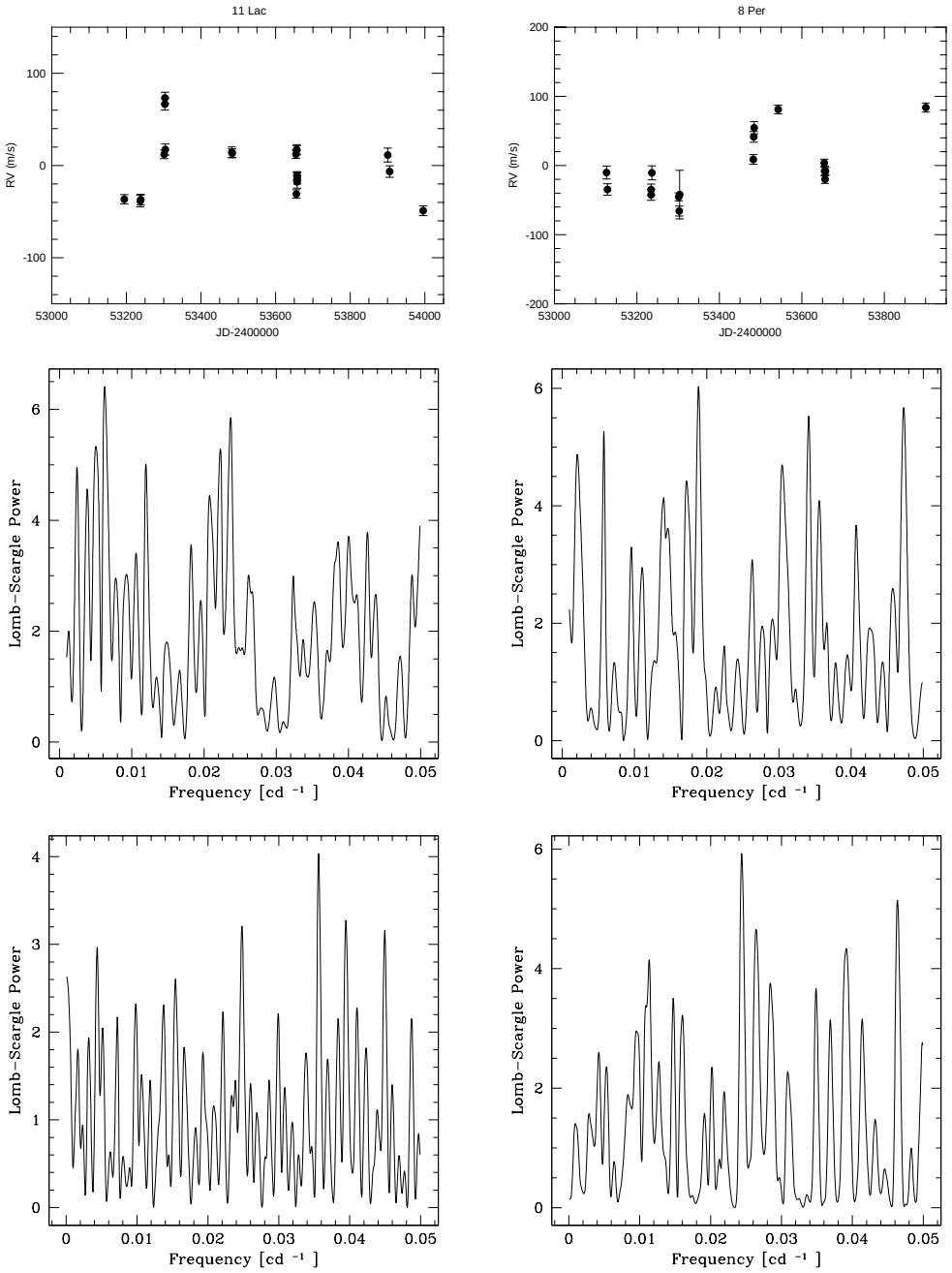

Figure 5.10: Plots of the RV monitoring, scargle periodograms of the RVs and the *HIPPARCOS* photometry of the possible pulsating *TLS* stars 11 Lac (left) and 8 Per (right). RV plotted against JD and scargle power plotted against frequency.

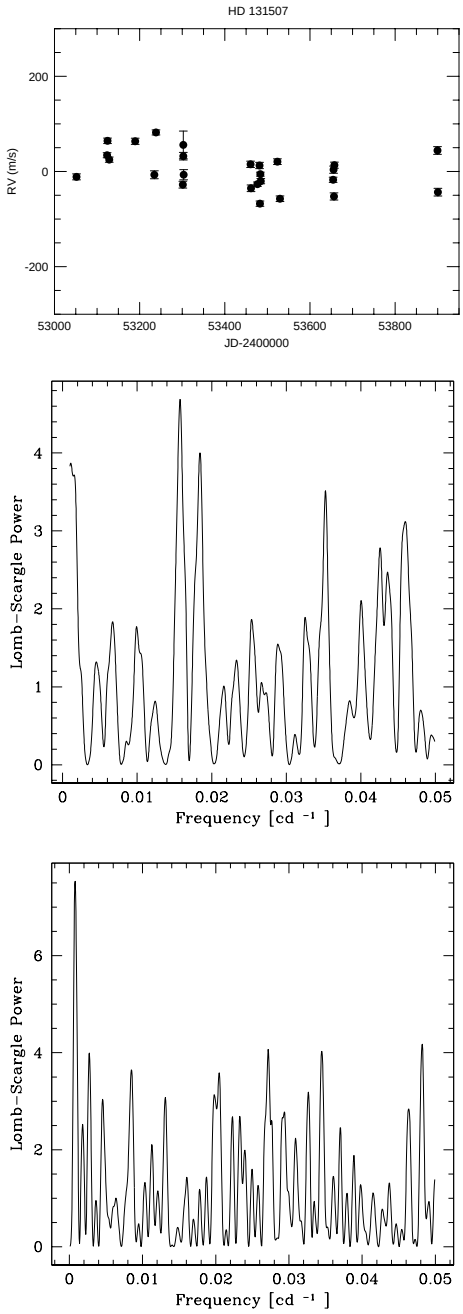

Figure 5.11: Plots of the RV monitoring, scargle periodograms of the RVs and the *HIPPARCOS* photometry of the possible pulsating *TLS* star HD 131507 (left). RV plotted against JD and scargle power plotted against frequency.

The short-period variations in the radial velocities are accompanied by variations in the *HIPPARCOS* photometry showing similar timescales but at lower scargle power. This is probably due to the poor number of available spectra for each star. To determine accurate and significant oscillation frequences in the RV data, indicated by high scargle powers, it is essential to observe each star at least once per night and several times per month. However, this was not the goal of this work. Thus at the moment my survey shows evidence of short-term variability of unknown origin that is most likely due to pulsations.
The following *TLS* sample stars possibly belong to the pulsating K giants: HD 218029, HD 2774, HD 37601 (24 Cam), HD 103605 (66 UMa), HD 118904, HD 148293, HD 49878, HD 40083, HD 45866, HD 60294, HD 6319, HD 96833 (Ψ UMa), HD 175823, HD 172340, HD 214868 (11 Lac), HD 13982 (8 Per) and HD 131507.
The RV variations, periodograms of the RVs and of the *HIPPARCOS* photometry of these target stars are presented in Fig. 5.3 through Fig. 5.11.

5.2 Stellar and planetary companions

This section deals with long-term RV variations caused by stellar and planetary companions. The discrimination between both possibilities and the exclusion of rotational modulation as the reason for the long-period RV variations will be explained in the next subsections.

5.2.1 Binaries

In the case of stellar companions the most important discrimination criteria for long-term RV variations are the comparatively very large RV amplitudes in the range of $\mathrm{km\,s^{-1}}$ and the long periods of more than several hundreds of days. This is due to the fact that only the high masses of stellar companions, and not from planets, can cause these high amplitudes. Rotational modulation caused by starspots is also not able to produce such high RV amplitudes. The large period as the second criterion excludes furthermore short-period RV variations due to stellar oscillations. The third criterion, the turnaround points of the orbit (see HD 176524 (υ Dra) in Fig. 5.18), is not visible in all RV curves. This is because as a consequence of the large periods it was only possible to obtain a small part of the corresponding long orbits during my time-restricted observations. Thus the RV curves of a part of the binary candidates show only a snapshot of the whole orbit, expressed by the linear RV changes. Only a few stars show at least one turnaround point (HD 153956 (see Fig. 5.17, left), HD 26755 (see Fig. 5.16, right) and HD 152812 (see Fig. 5.15, right). For the other stars the observing time in comparison to the orbital period is too small and thus only parts of the orbit are plotted.
However, all these points are only indications. The final proof for a binary system is the calculation of an orbit. However, to calculate such an orbit successfully, at least one turnaround point should be visible in the RV curve and enough data points should be available. So far only HD 176524 has fulfilled all these conditions and will be explained in more detail in §5.2.2. For the other 12 candidates more data are needed. But at the moment for all 13 stars (21 %) of my sample the most probable reason for the RV variations is that the stars belong to binary systems. This is because they show very high peak-to-peak RV amplitudes ranging from around 300 $\mathrm{m\,s^{-1}}$ to 6000 $\mathrm{km\,s^{-1}}$ and very large changes in the RV amplitudes over time. 43 UMa (see Fig. 5.12, left) shows

for instance a change in RV amplitudes of around -600 $\mathrm{m\,s^{-1}}$ within 1000 days. The expected periods of these binaries are more than several hundreds of days because the plots of the available RV monitoring show at best only one turnaround point.
Typical RV amplitudes for binaries with masses in solar masses ($\mathrm{M_\odot}$) of $M_1 = 1.5\ \mathrm{M_\odot}$ and $M_2 < 1.5\ \mathrm{M_\odot}$ as well as a period of around 1000 days are published (see Tab. 1) in Setiawan et al. (2004b). One of these binaries, HD 179799, shows an RV amplitude of $5.99 \pm 0.40\ \mathrm{km\,s^{-1}}$ and a period of 856.1 ± 39.1 days. The system consists of two components with 1.5 and 0.3 $\mathrm{M_\odot}$.
Stars with possibly stellar companions in the *TLS* sample are HD 93859 (43 UMa), HD 85841, HD 180610 (54 Dra), HD 216174, HD 83506 (27 UMa), HD 206952 (11 Cep), HD 176408 (48 Dra), HD 152812, HD 113049, HD 26755, HD 153956, HD 58425 and HD 176524 (υ Dra).
Fig. 5.12 through Fig. 5.18 show the RV variations, periodograms of the RVs and of the *HIPPARCOS* photometry of the possible binary candidates. With the exception of HD 176524 there are no previous publications available for the other 12 stars. Moreover there are no clear spectroscopic indications for binarity in the spectra of the *TLS* binary candidates possibly with the exception of HD 176524 (υ Dra) because HD 176524 is listed in the literature as a spectroscopic binary (see §5.2.2). Strong hints for spectroscopic binaries would be when a spectral line periodically doubles and then merges into a single line, indicating the presence of two stars giving opposite Doppler shifts.
The percentage of binaries, which is a first result of the Tautenburg survey, is in very good agreement with results derived from previous studies. Setiawan et al. (2004a) confirmed 11–13 binaries (14–17 %) in their *FEROS* sample which consists of 77 giant. In a past study, Mermilliod et al. (2001) found in spectroscopic surveys with the *CORAVEL* spectrograph studying giants in open clusters a percentage of 26 % binaries. This value is also consistent with my results. In comparison, the frequency of binary systems consisting of red giants is lower than the frequency of binary systems consisting of solar-type stars (Duquennoy & Mayor 1991) which is due to their extended envelopes.

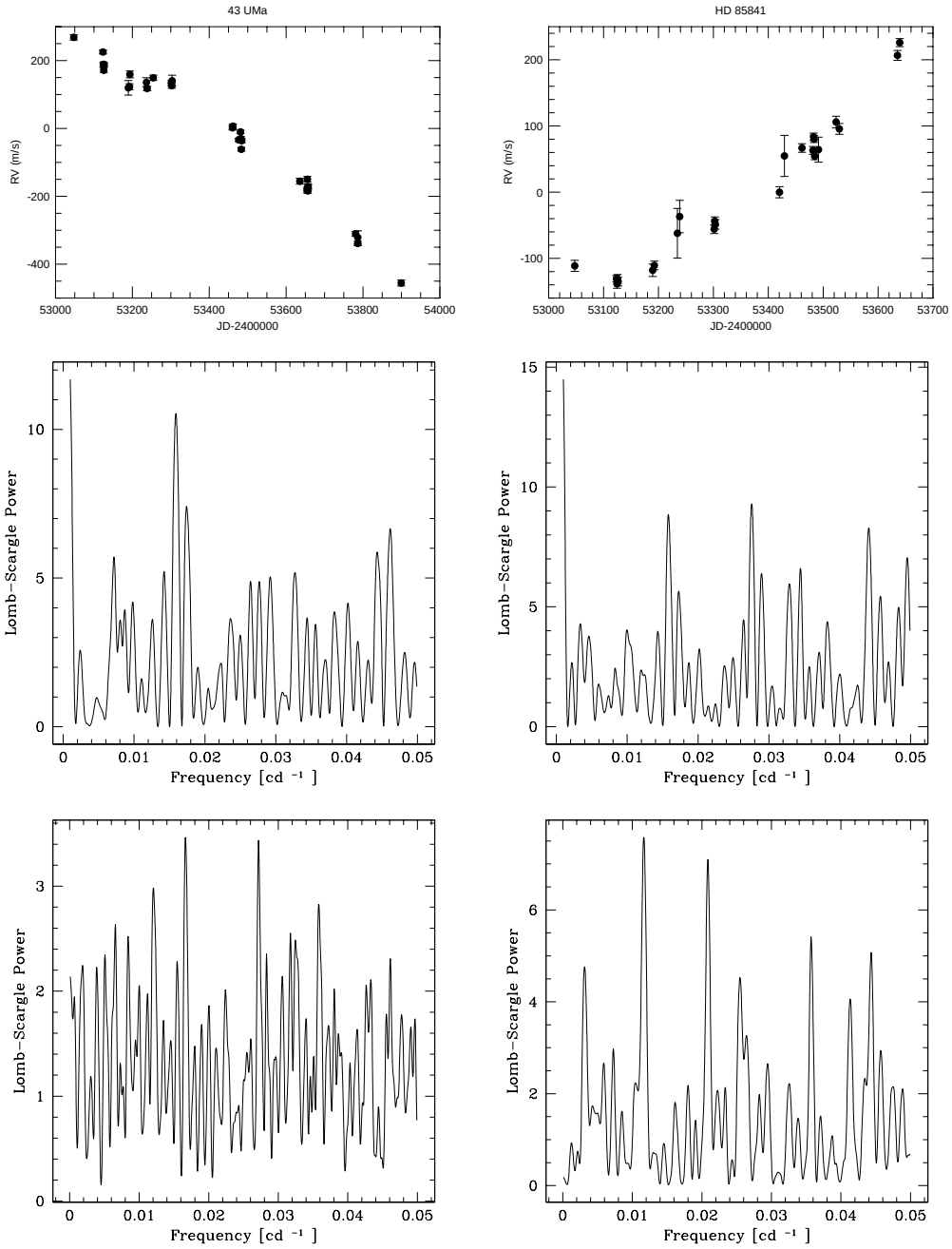

Figure 5.12: Plots of the RV monitoring, scargle periodograms of the RVs and the *HIPPARCOS* photometry of the possible *TLS* binaries 43 UMa (left) and HD 85841 (right). RV plotted against JD and scargle power plotted against frequency.

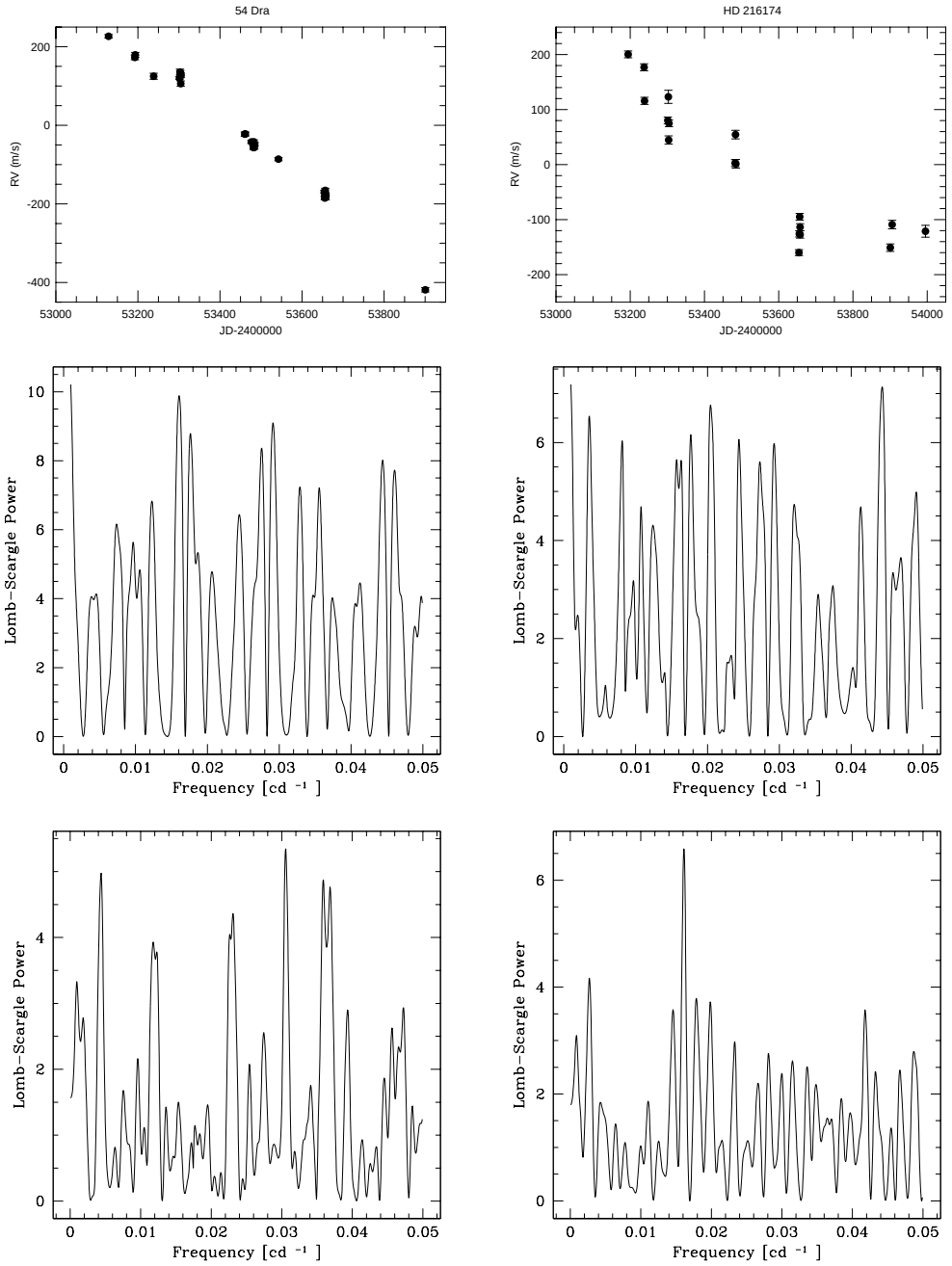

Figure 5.13: Plots of the RV monitoring, scargle periodograms of the RVs and the *HIPPARCOS* photometry of the possible *TLS* binaries 54 Dra (left) and HD 216174 (right). RV plotted against JD and scargle power plotted against frequency.

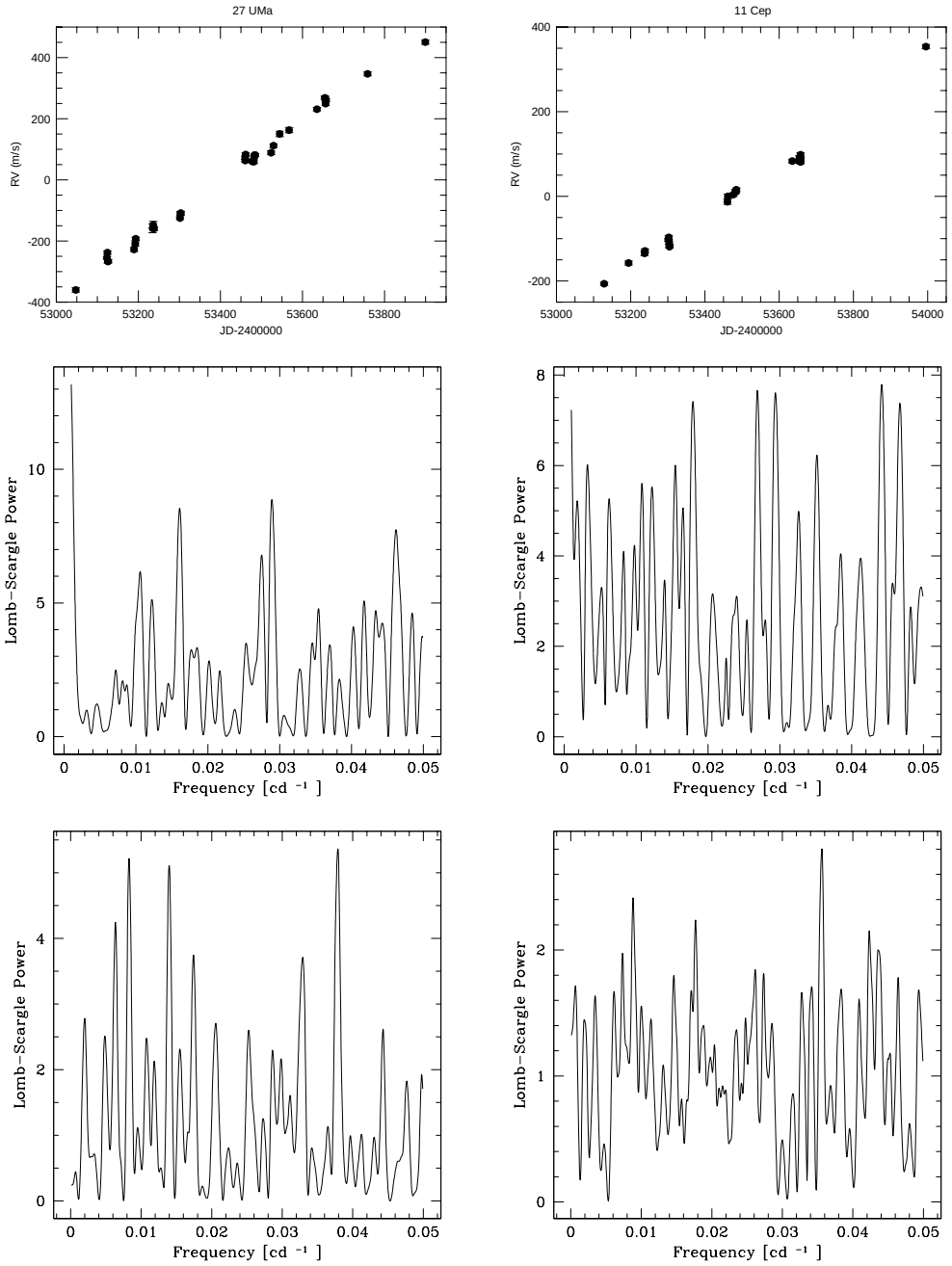

Figure 5.14: Plots of the RV monitoring, scargle periodograms of the RVs and the *HIPPARCOS* photometry of the possible *TLS* binaries 27 UMa (left) and 11 Cep (right). RV plotted against JD and scargle power plotted against frequency.

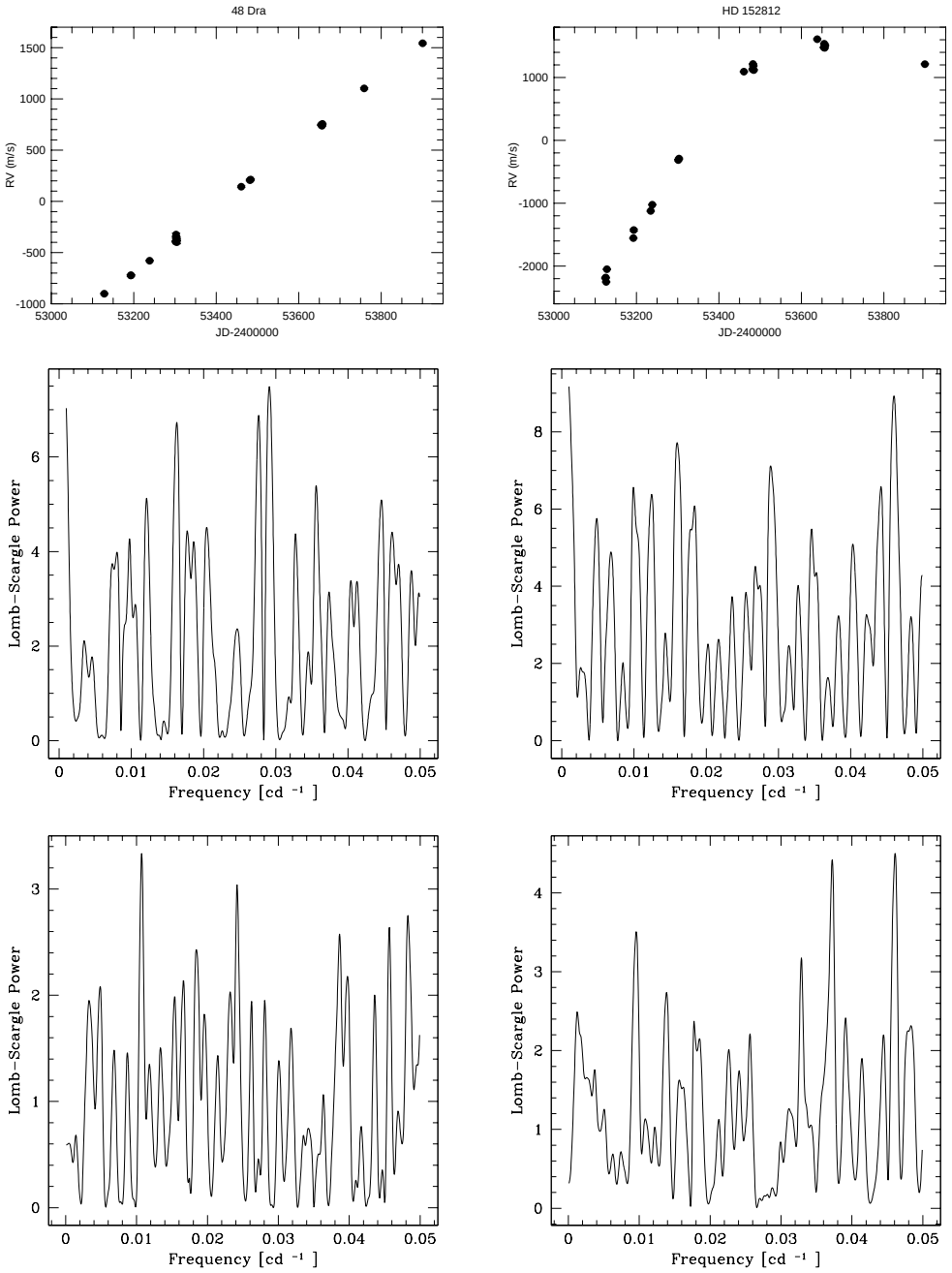

Figure 5.15: Plots of the RV monitoring, scargle periodograms of the RVs and the *HIPPARCOS* photometry of the possible *TLS* binaries 48 Dra (left) and HD 152812 (right). RV plotted against JD and scargle power plotted against frequency.

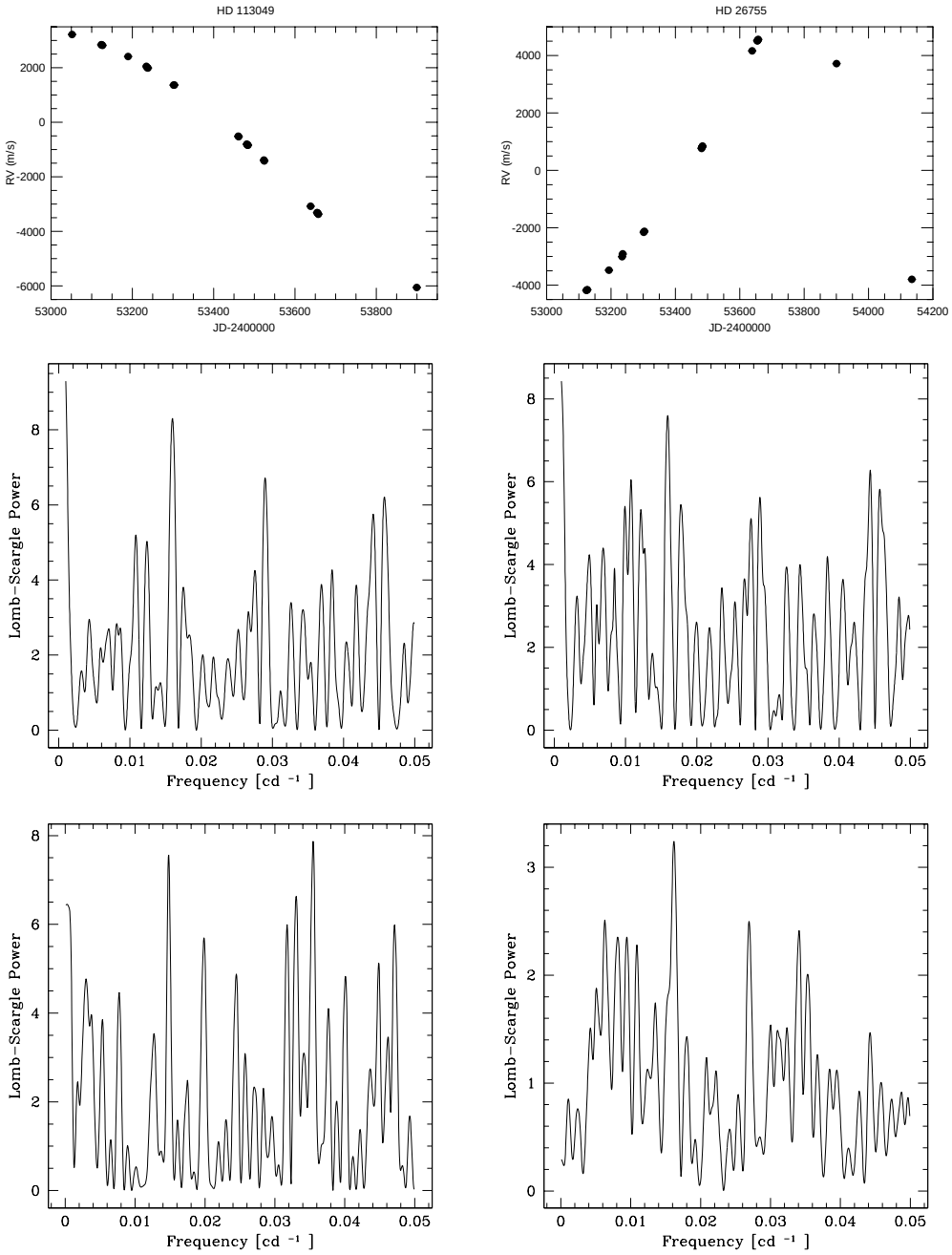

Figure 5.16: Plots of the RV monitoring, scargle periodograms of the RVs and the *HIPPARCOS* photometry of the possible *TLS* binaries HD 113049 (left) and HD 26755 (right). RV plotted against JD and scargle power plotted against frequency.

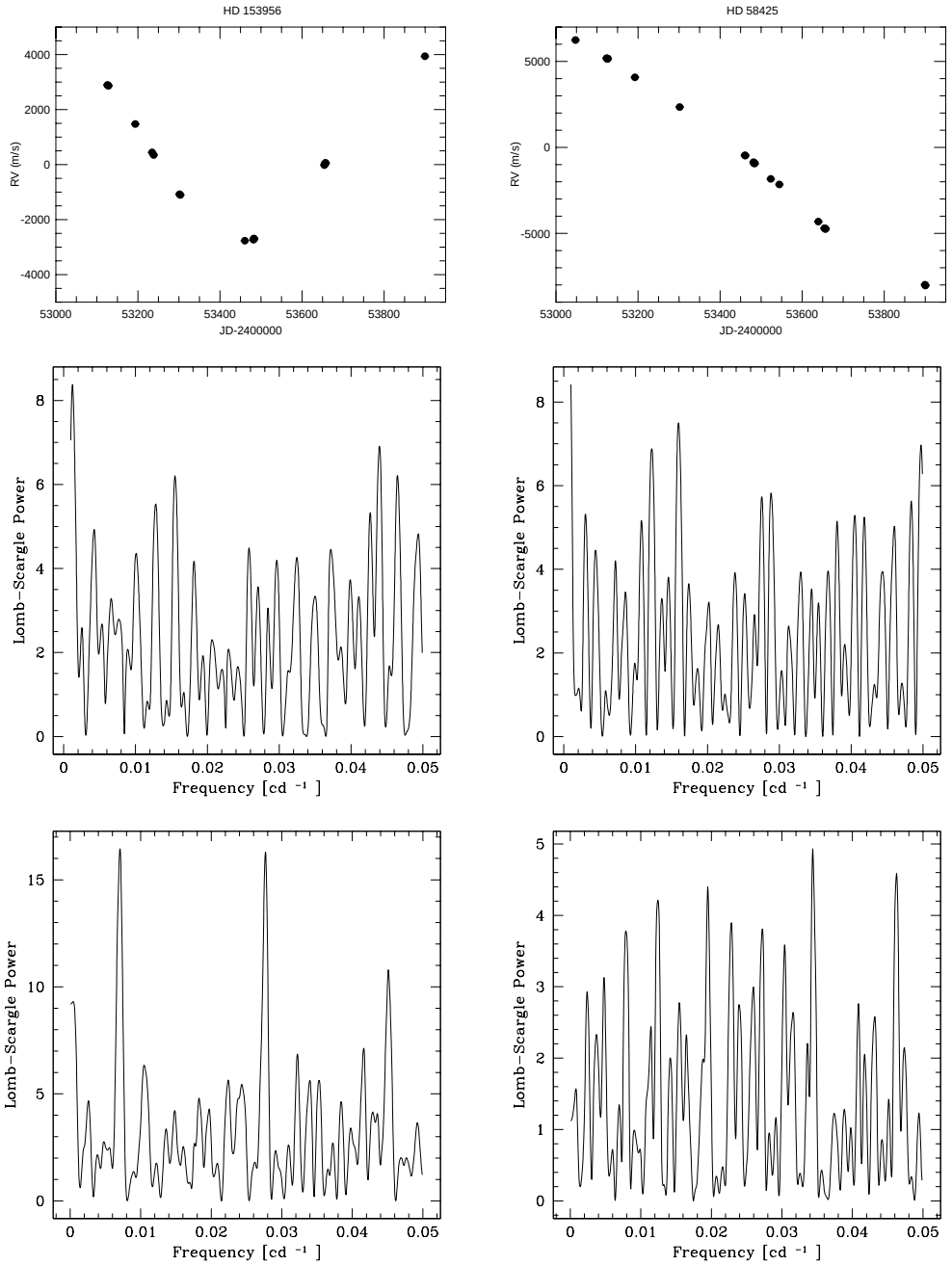

Figure 5.17: Plots of the RV monitoring, scargle periodograms of the RVs and the *HIPPARCOS* photometry of the possible *TLS* binaries HD 152812 (left) and HD 58425 (right). RV plotted against JD and scargle power plotted against frequency.

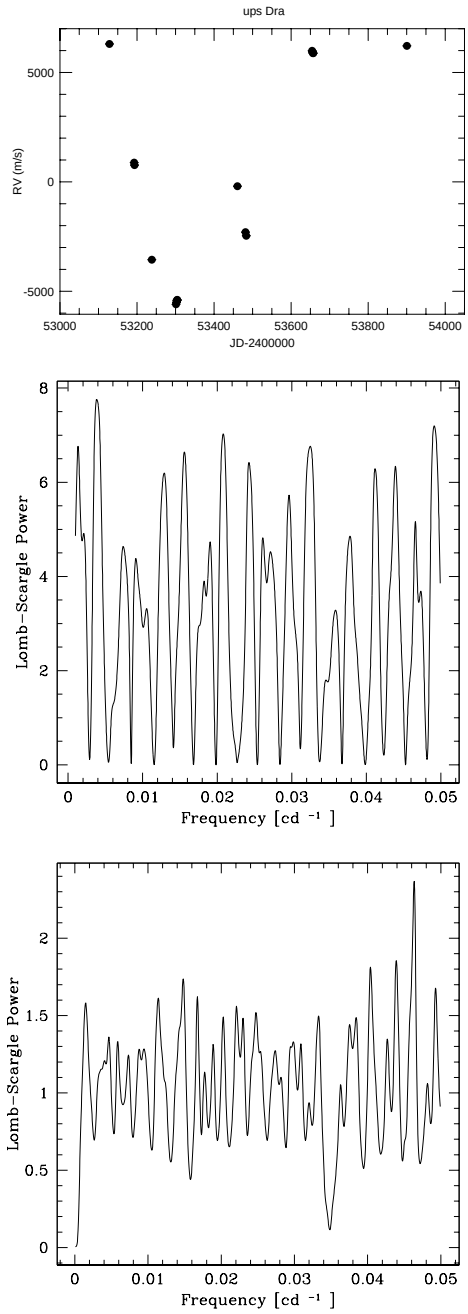

Figure 5.18: Plots of the RV monitoring, scargle periodograms of the RVs and the *HIPPARCOS* photometry of the possible *TLS* binary ups Dra. RV plotted against JD and scargle power plotted against frequency.

Table 5.3: Stellar parameters of υ Dra

Spectral type	K4 III	
m_V	4.827 ± 0.005	[mag]
M_V	-0.298 ± 0.105	[mag]
B–V	1.158 ± 0.005	[mag]
Parallax	9.47 ± 0.46	[mas]
Distance	45.73 ± 2.22	[pc]
$M_*{}^{(a)}$	1.800 ± 0.130	[$M_\odot$]
$R_*{}^{(a)}$	20.24 ± 1.46	[$R_\odot$]
$t^{(a)}$	1.383 ± 0.319	[Gyr]
$T_{\rm eff}{}^{(a)}$	4560 ± 70	[K]
$[Fe/H]^{(a)}$	-0.115 ± 0.04	[dex]
$\log g^{(a)}$	1.7 ± 0.15	[dex]
micro turbulence$^{(a)}$	1.3 ± 0.8	[km s^{-1}]

$^{(a)}$ from my analysis

5.2.2 HD 176524 (υ Dra)

As a representative for stars hosting a stellar companion – binaries – I discuss in detail the K0 III giant υ Dra (= HD 176524 = HR 7180 = HIP 92782) whose radial velocity measurements are shown in Fig. 5.18 at the top. This star is very important because it is the only binary of the *TLS* for which previous data is available. Consequently I included it in my sample to see how well I could recover the orbit of a known binary. Moreover the binary is well known and thus this can be a test of my precision. Furthermore I am looking for planets and so I do not want to bias my sample against binaries. After all, finding a planet in a binary would be an interesting result. Griffin et al. (1983) published "A SPECTROSCOPIC ORBIT FOR υ DRACONIS". In this publication photoelectric RV observations were used to determine the orbital parameters of υ Dra. Thus I have the opportunity to compare my orbital solution derived from the RV monitoring of the Tautenburg survey with an independent solution in the literature. The visual magnitude of this binary is $V = 4.827$ mag. The *HIPPARCOS* parallax is 9.47 ± 0.46 mas and this implies M_V = -0.298 ± 0.105 mag. The stellar parameters of υ Dra are summarized in Tab. 5.3.

The late-type star υ Dra is part of the Tautenburg programme because with a declination of 71° it is placed near the North Pole and thus visible over the whole year. Nicolet (1978) arranged the means of several sets of UBV photometry available in the literature. The first RV determination was carried out at the Lick Observatory in the year 1907. First hints of RV variability were found very soon by K. Burns and were published by Campbell & Albrecht (1910) – six RV measurements – as well as by Campbell (1910). After this time υ Dra were observed frequently with the photoelectric RV spectrometers at Cambridge (Griffin 1967) and Victoria (Fletcher et al. 1982) according to Griffin (1982). In 1980 the observations at Cambridge started to determine an orbit for the well-known spectroscopic binary. In the case of Victoria, υ Dra was a member of a control sample of 40 K giants and the measurements took place from 1979 to 1982. The topic of the survey was to investigate the binary frequency of a sample of barium stars (McClure 1983) in comparison to the control sample. The spectral classification of HD 176524 is K0+ III–IIa Ba 0.2 (Keenan & Pitts 1980) which means that υ Dra is itself a mild barium star and a known spectroscopic binary.

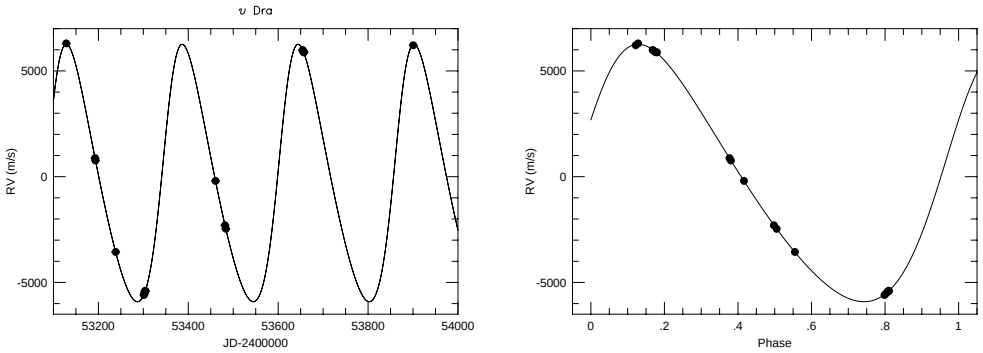

Figure 5.19: Computed RV curve from the RVs observed at *TLS* for υ Dra (left). Radial velocity measurements for υ Dra phased to the orbital period (right). The line represents the orbital solution.

According to Griffin (1982), bright stars with a mild barium content show a higher binary frequency than normal K giants. For further comparisons the previous RVs – 35 in total – are listed in Tab. 1 in Griffin (1982). For their own observations Griffin (1982) determined an orbital solution with a period of 258.48 days. Their period is in very good agreement with my determined period of 257.90 days. The right part of Fig. 5.19 shows the so-called phase diagram for υ Dra. In this plot the RV measurements are phase-folded to the orbital period.

The mean residuals for the Lick, Victoria and Cambridge observations are respectively $+0.38 \pm 0.47$, -0.20 ± 0.13 and $+0.20 \pm 0.16$ km s^{-1}. The *TLS* residuals with a value of 20.22 m s^{-1} corresponding 0.02 km s^{-1} have a much better accuracy in contrast to the previous studies. The second improvement is that I have determined the stellar mass ($M_\star = 1.80\ M_\odot$ which enabled me to compute the mass of the stellar companion with the resulting mass of 305.62 Jupiter masses (M_{Jup}). However, binarity could influence the accuracy of mass determination by resulting in not unique estimates of stellar parameters, which is expressed through double-peaked Probability Distribution Functions (PDFs). Tab. 5.4 shows left the results of the orbital solution from Griffin (1982) and right from my work.

Table 5.4: Orbital parameters for the companion to HD 176524.

	Griffin (1982)	my work
P [days]	258.48 ± 0.04	257.90 ± 0.18
$T_{periastron}$[JD]	41977 ± 5	53611.1357 ± 1.25
K [kms^{-1}]	5.99 ± 0.18	6.09 ± 0.02
σ(O–C)[ms^{-1}]	200 ± 160	20.22
e	0.21 ± 0.03	0.196 ± 0.003
ω[deg]	298 ± 8	294 ± 1.47
$f(m)$ [solar masses ($M_\odot$)]	0.0054 ± 0.0005	0.0057 ± 0.0007
a[AU]	1.431	1.014

5.2.3 Exoplanets

The most important result of my work is the detection of 6 stars (10 %) which show low-amplitude (60–400 m s^{-1}), long-term radial velocity variations on timescales of a few hundreds of days possibly due to planetary companions. The exoplanet candidates are HD 73108 (4 UMa), HD 77800 (11 UMa), HD 139357, HD 136726 (11 UMi), HD 170693 (42 Dra) and HD 32518. These stars are plotted in Fig. 5.20. A detailed analysis for all candidates hosting planetary companions will be carried out in §6.2.

5.2.4 Rotational modulation

For the following 24 (39 %) K giants (see Fig. 5.21 through Fig. 5.32) the type of RV variability is still not clear: HD 93875 (42 UMa), HD 137443, HD 160290 (Y Her), HD 210905, HD 195820, HD 9927 (ups Per), HD 192781, HD 217382, HD 102328, HD 106574, HD 31579 (8 Cam), HD 6497, HD 129245, HD 30338, HD 150010, HD 167042, HD 184293, HD 186815, HD 157681, HD 47914 (55 Aur), HD 92523, HD 200205, HD 94084 and HD 138265.
I will try to give an approach by using a excludability. The RV curves of these candidates show definitive variations. Therefore a constant RV behaviour can be excluded. If each system is not caught at turning point, the relative low RV amplitudes most likely exclude that the stars belong to binary systems. In addition the shape of the RV curve for each star is unlikely for binaries. For short-period RV variations the RV amplitudes are too large and the available frequences, derived from the time series analysis of the data sets (RV, $HIPPARCOS$ and Hα), show, despite their relatively low scargle power, a clear tendency to larger periods. Consequently the most likely causes for the long-term RV variability are rotational modulation and/or planetary companions.
However, a clear discrimination at this time between both possibilities is not possible. Further investigations are needed to decide between both causes. If rotational modulation is the real reason then this would be caused by surface inhomogeneities such as starspots. This is because surface features which migrate due to stellar rotation result in rotational modulation and also create asymmetries in the spectral line profiles. This would be detected as variations in the radial velocity with the period of the star. This hypothesis can be tested by obtaining an upper limit on this rotation period determined from the star's projected rotational velocity and radius. If the periods of the radial velocity are much larger than this maximum rotational period ($P_{Rotation}$), then rotational modulation by surface inhomogeneities can be excluded as an explanation

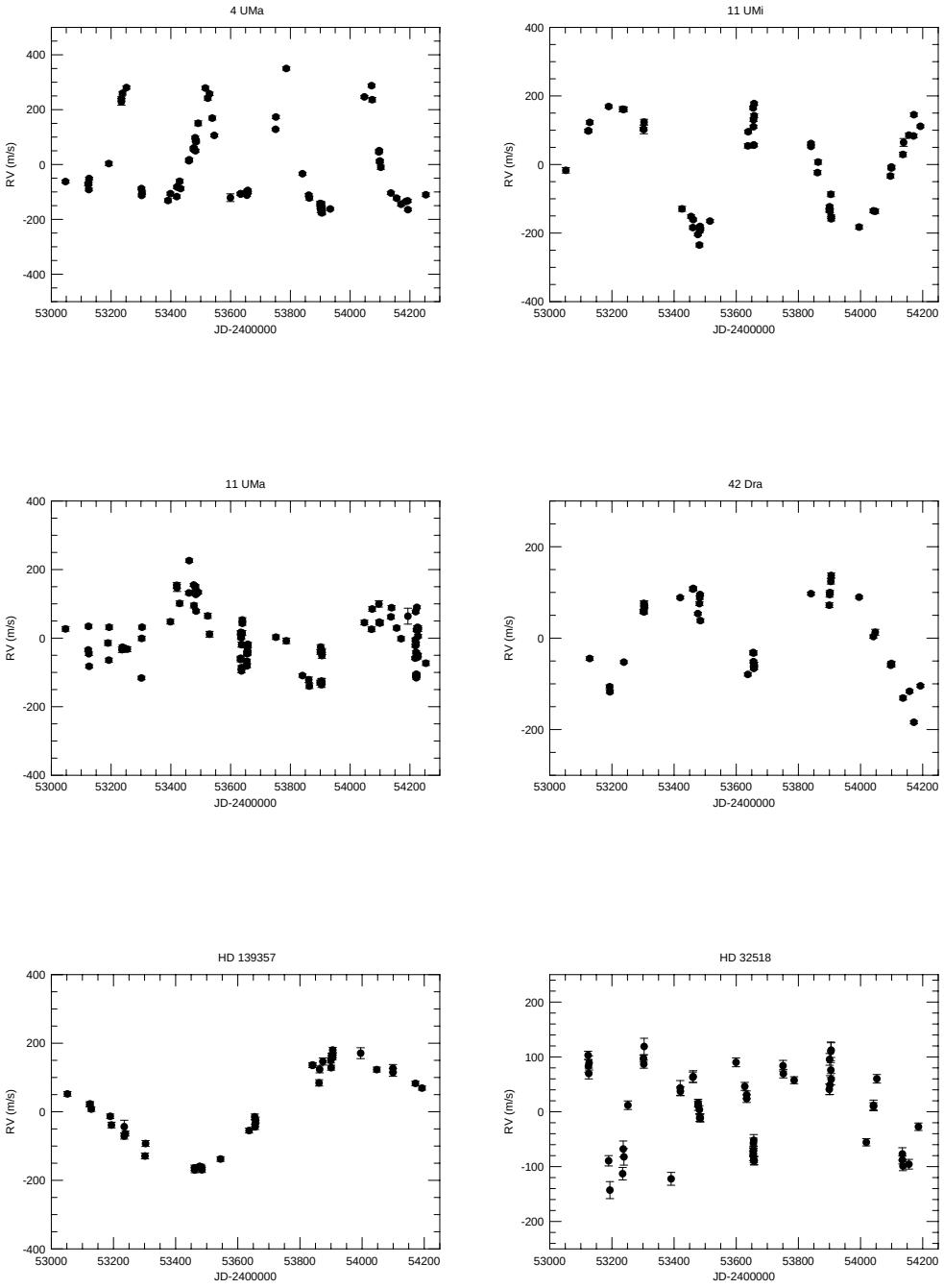

Figure 5.20: Plots of the RV monitoring of TLS stars hosting planetary companions. RV plotted against JD .

for the RV variations (Hatzes & Cochran 1993). This criterion (see Tab. 5.2) was used to confirm the planetary companions (see §6.2) of my work to exclude starspots which can cause a periodic RV variation similar to the one expected by the presence of a planet. A good example is HD 166435 (Queloz et al. 2001).

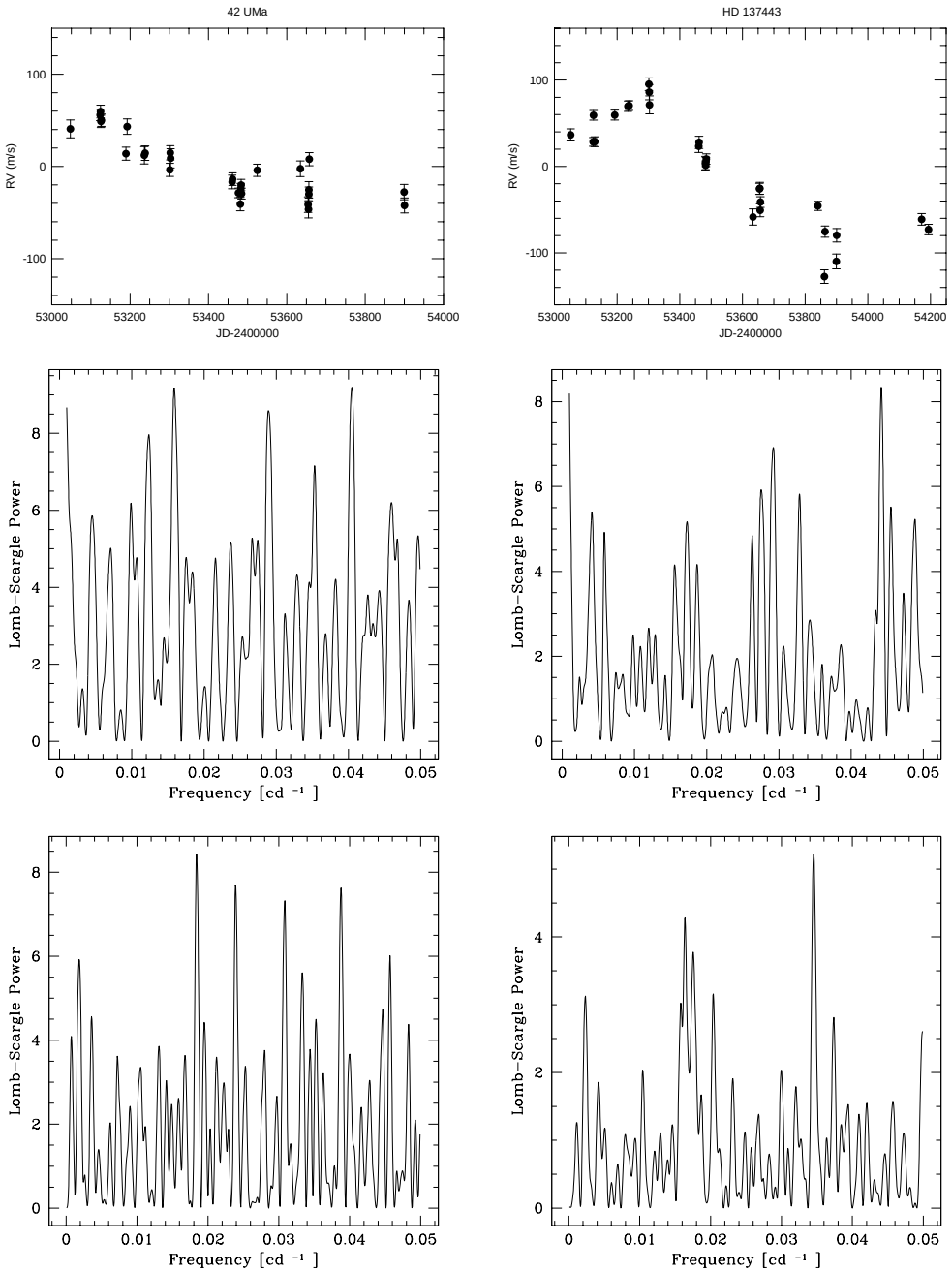

Figure 5.21: Plots of the RV monitoring, scargle periodograms of the RVs and the *HIPPARCOS* photometry of the *TLS* stars 42 UMa (left) and HD 137443 (right). RV p lotted against JD and scargle power plotted against frequency.

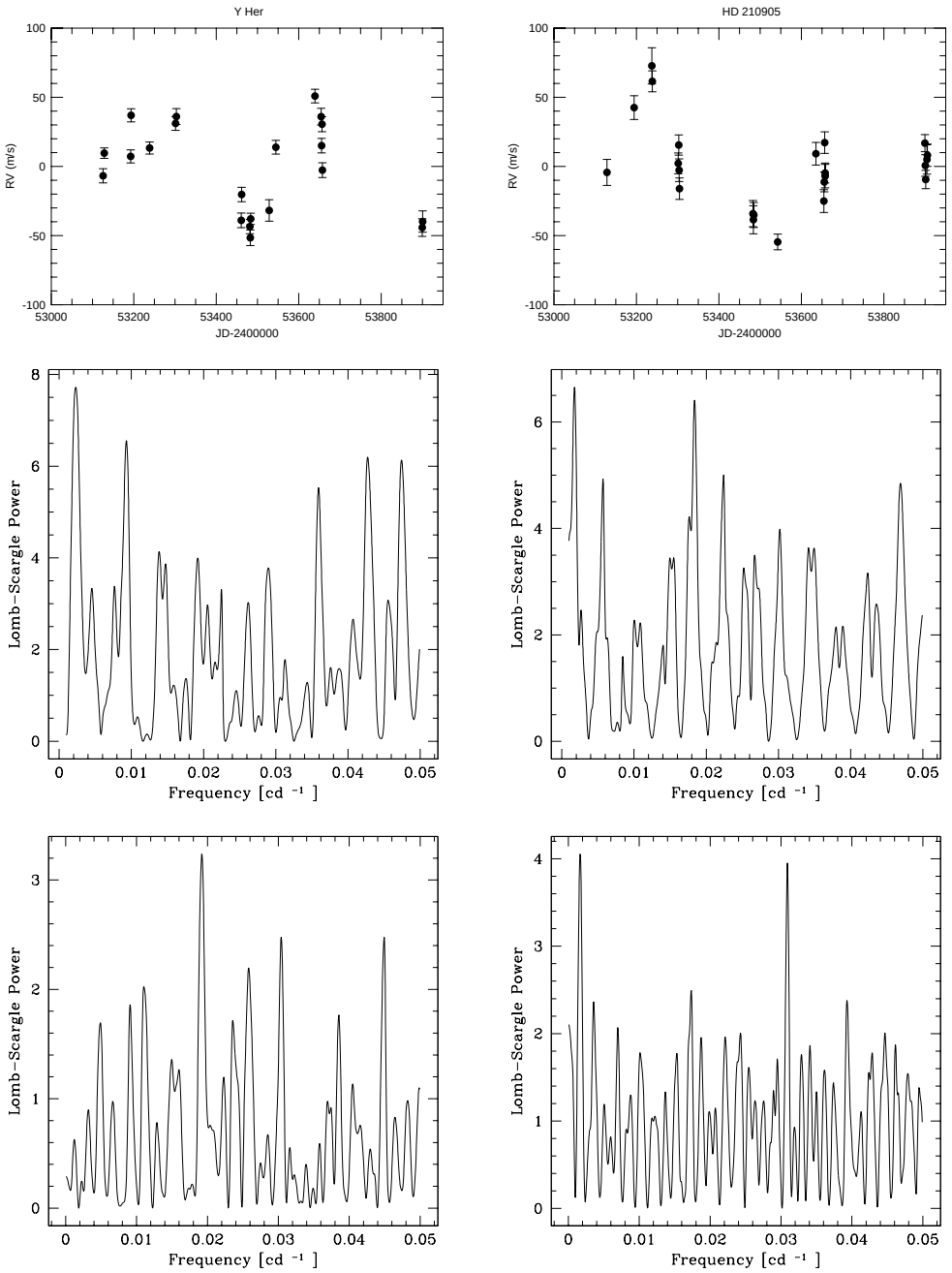

Figure 5.22: Plots of the RV monitoring, scargle periodograms of the RVs and the *HIPPARCOS* photometry of the *TLS* stars Y Her (left) and HD 210905 (right). RV plotted against JD and scargle power plotted against frequency.

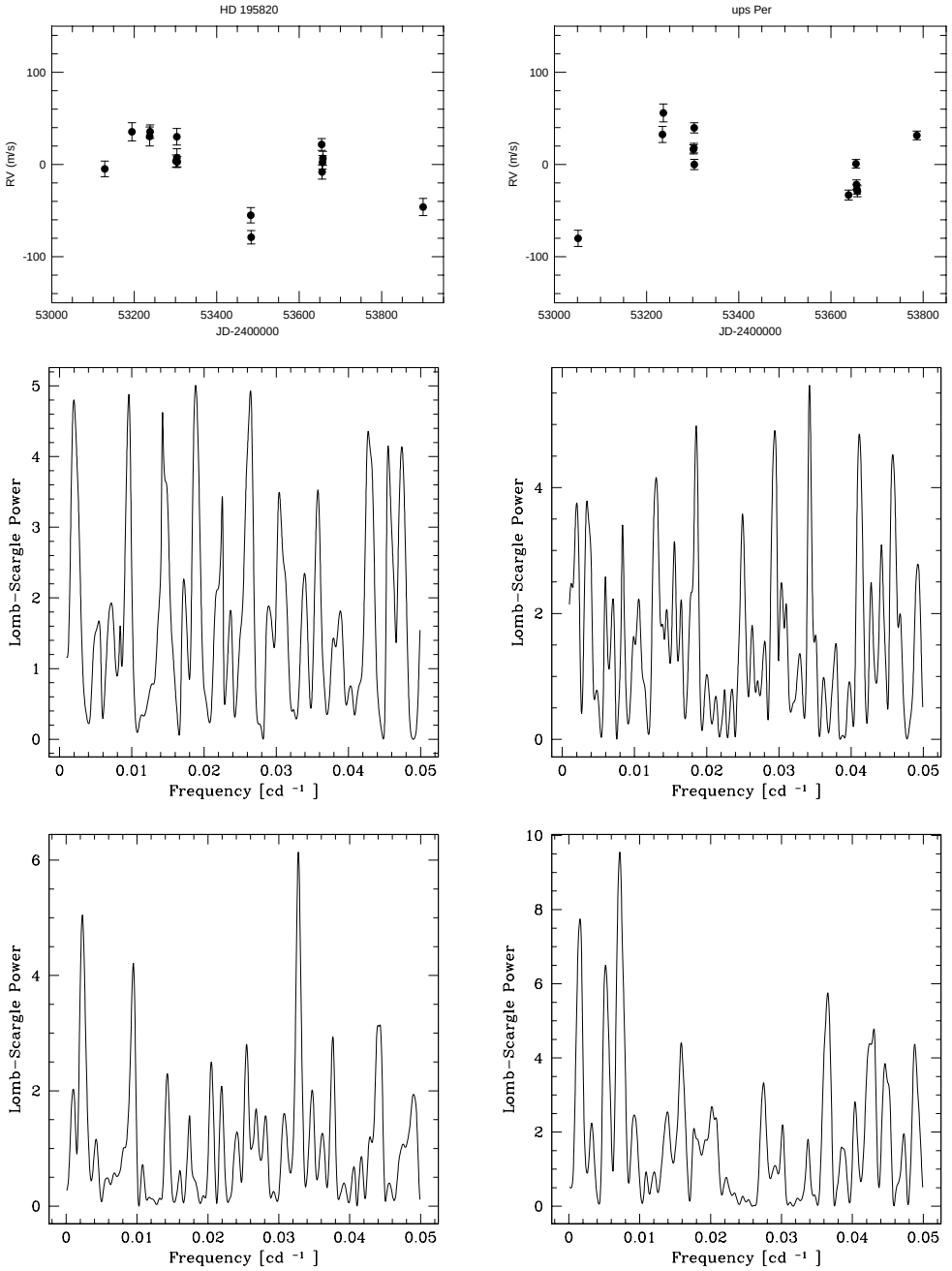

Figure 5.23: Plots of the RV monitoring, scargle periodograms of the RVs and the *HIPPARCOS* photometry of the *TLS* stars HD 195820 (left) and ups Per (right). RV plotted against JD and scargle power plotted against frequency.

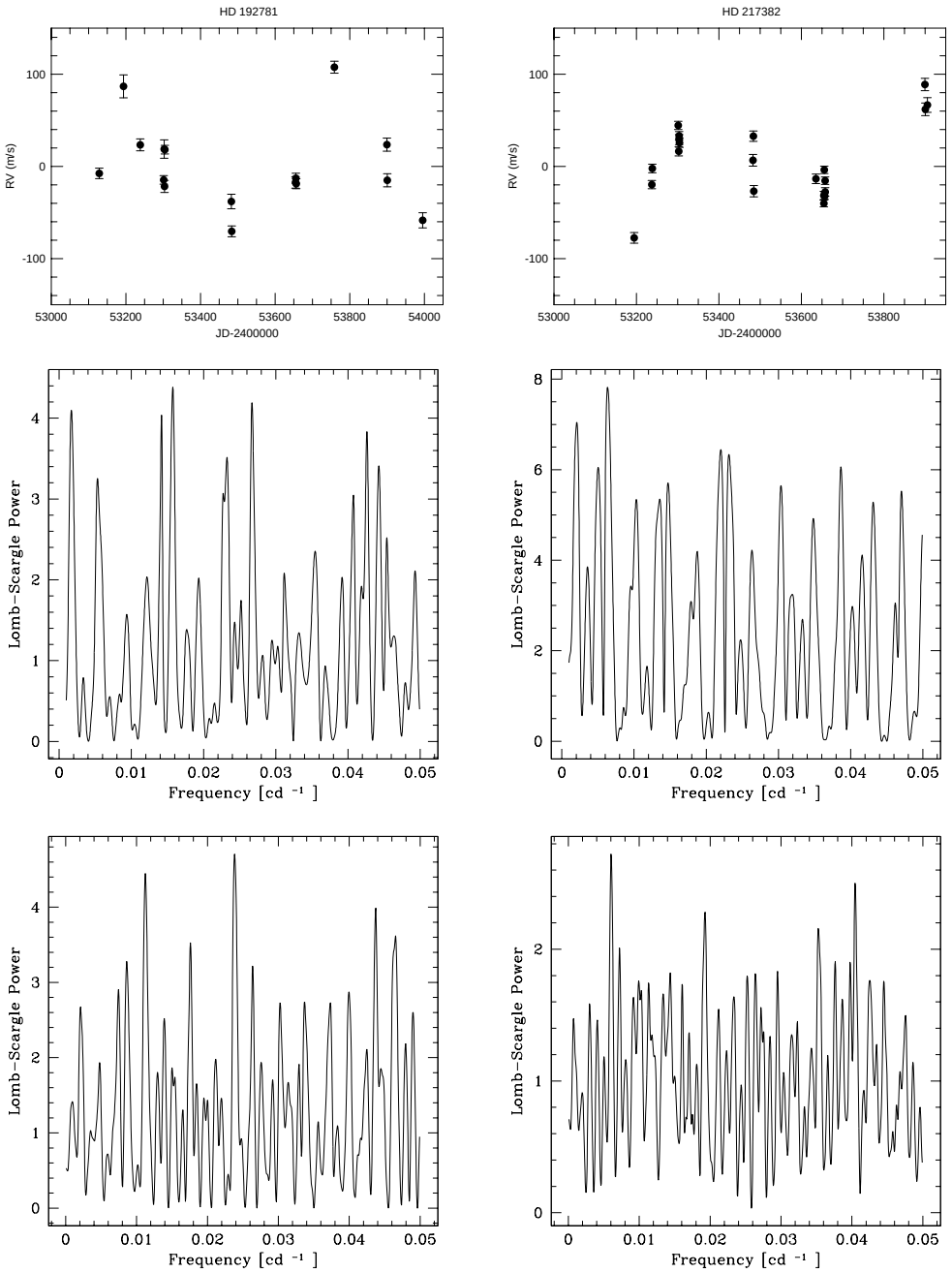

Figure 5.24: Plots of the RV monitoring, scargle periodograms of the RVs and the *HIPPARCOS* photometry of the *TLS* stars HD 192781 (left) and HD 217382 (right). RV plotted against JD and scargle power plotted against frequency.

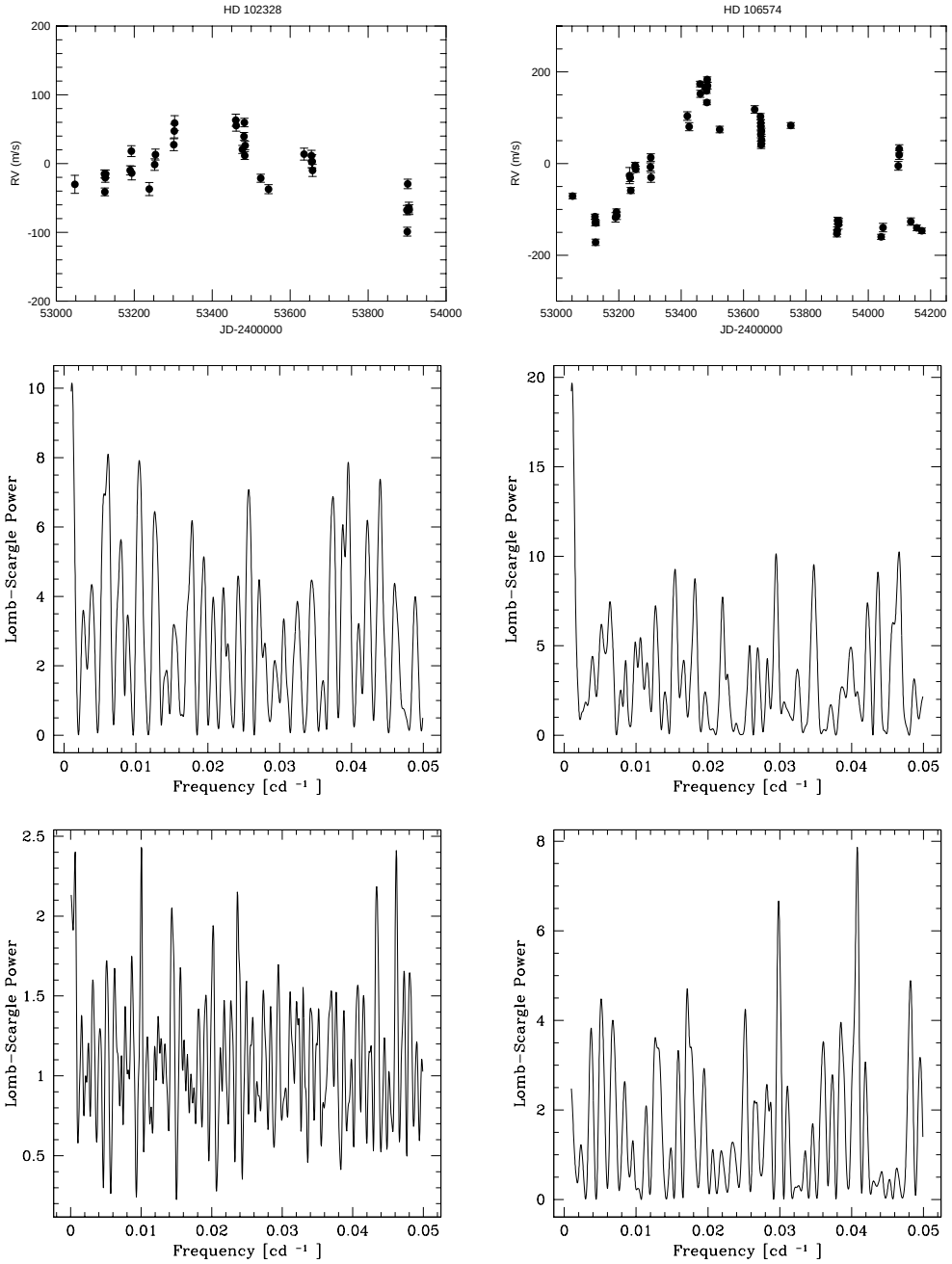

Figure 5.25: Plots of the RV monitoring, scargle periodograms of the RVs and the *HIPPARCOS* photometry of the *TLS* stars HD 102328 (left) and HD 106574 (right). RV plotted against JD and scargle power plotted against frequency.

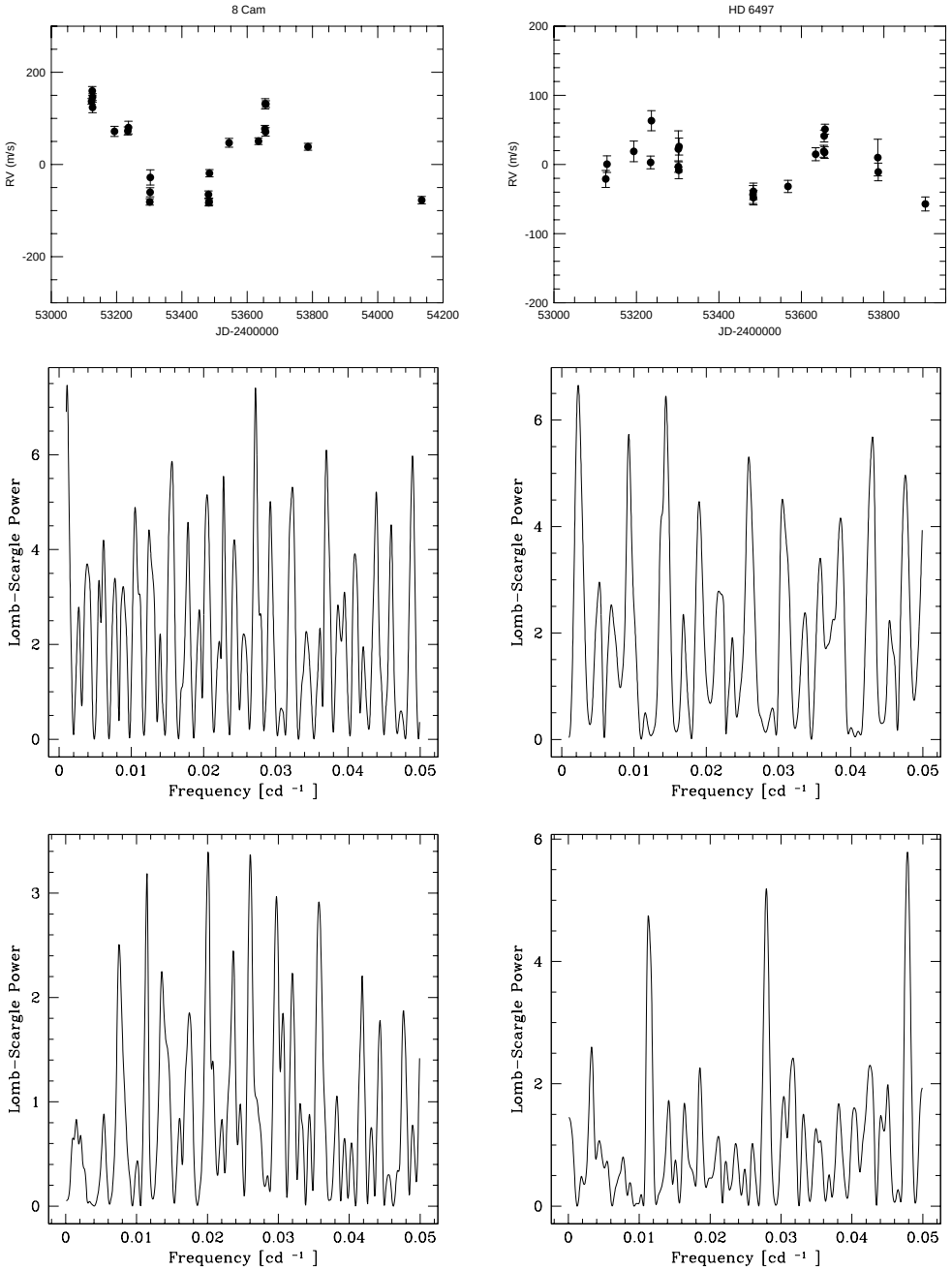

Figure 5.26: Plots of the RV monitoring, scargle periodograms of the RVs and the *HIPPARCOS* photometry of the *TLS* stars 8 Cam (left) and HD 6497 (right). RV plotted against JD and scargle power plotted against frequency.

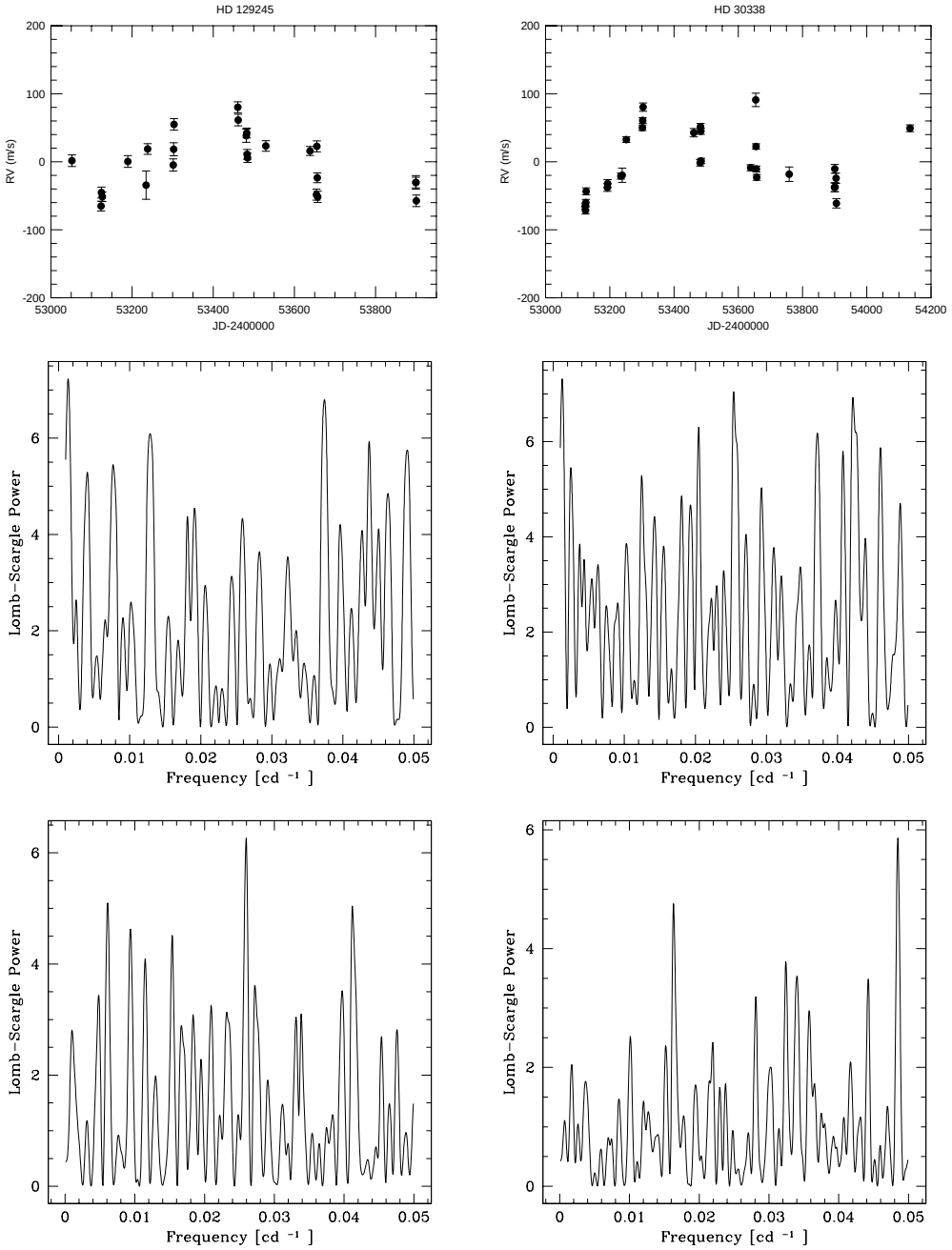

Figure 5.27: Plots of the RV monitoring, scargle periodograms of the RVs and the *HIPPARCOS* photometry of the *TLS* stars HD 129245 (left) and HD 30338 (right). RV plotted against JD and scargle power plotted against frequency.

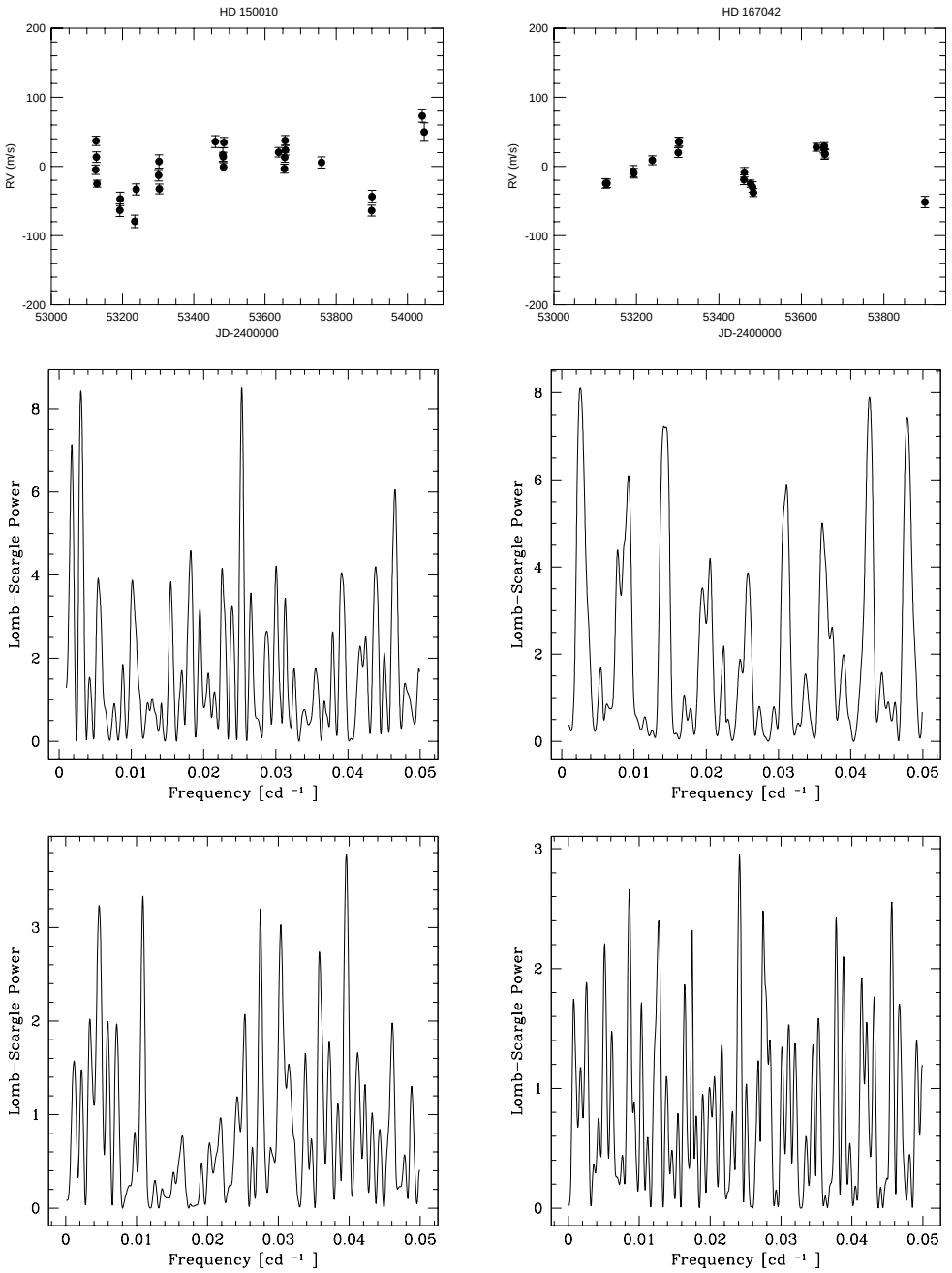

Figure 5.28: Plots of the RV monitoring, scargle periodograms of the RVs and the *HIPPARCOS* photometry of the *TLS* stars HD 150010 (left) and HD 167042 (right). RV plotted against JD and scargle power plotted against frequency.

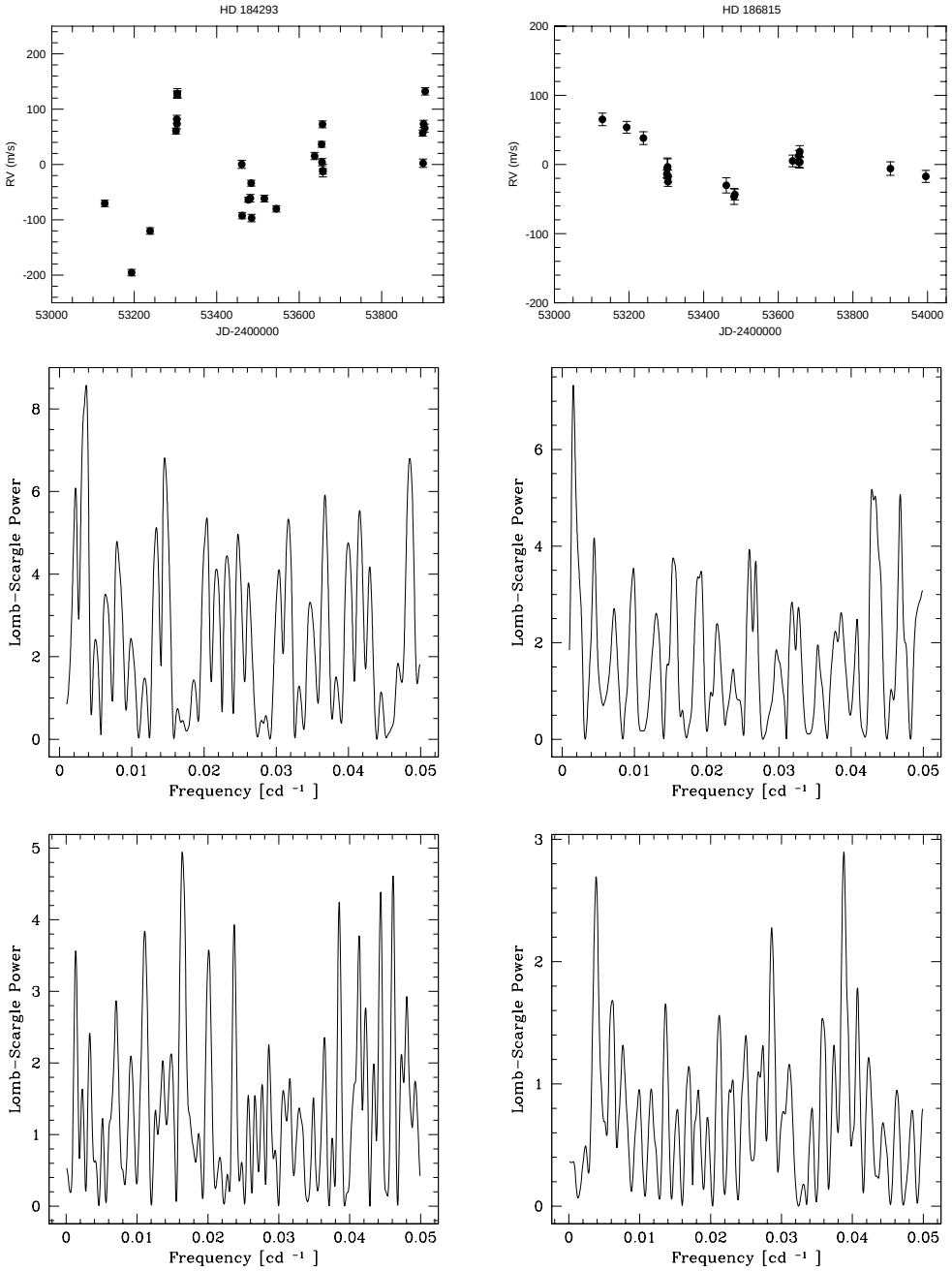

Figure 5.29: Plots of the RV monitoring, scargle periodograms of the RVs and the *HIPPARCOS* photometry of the *TLS* stars HD 184293 (left) and HD 186815 (right). RV plotted against JD and scargle power plotted against frequency.

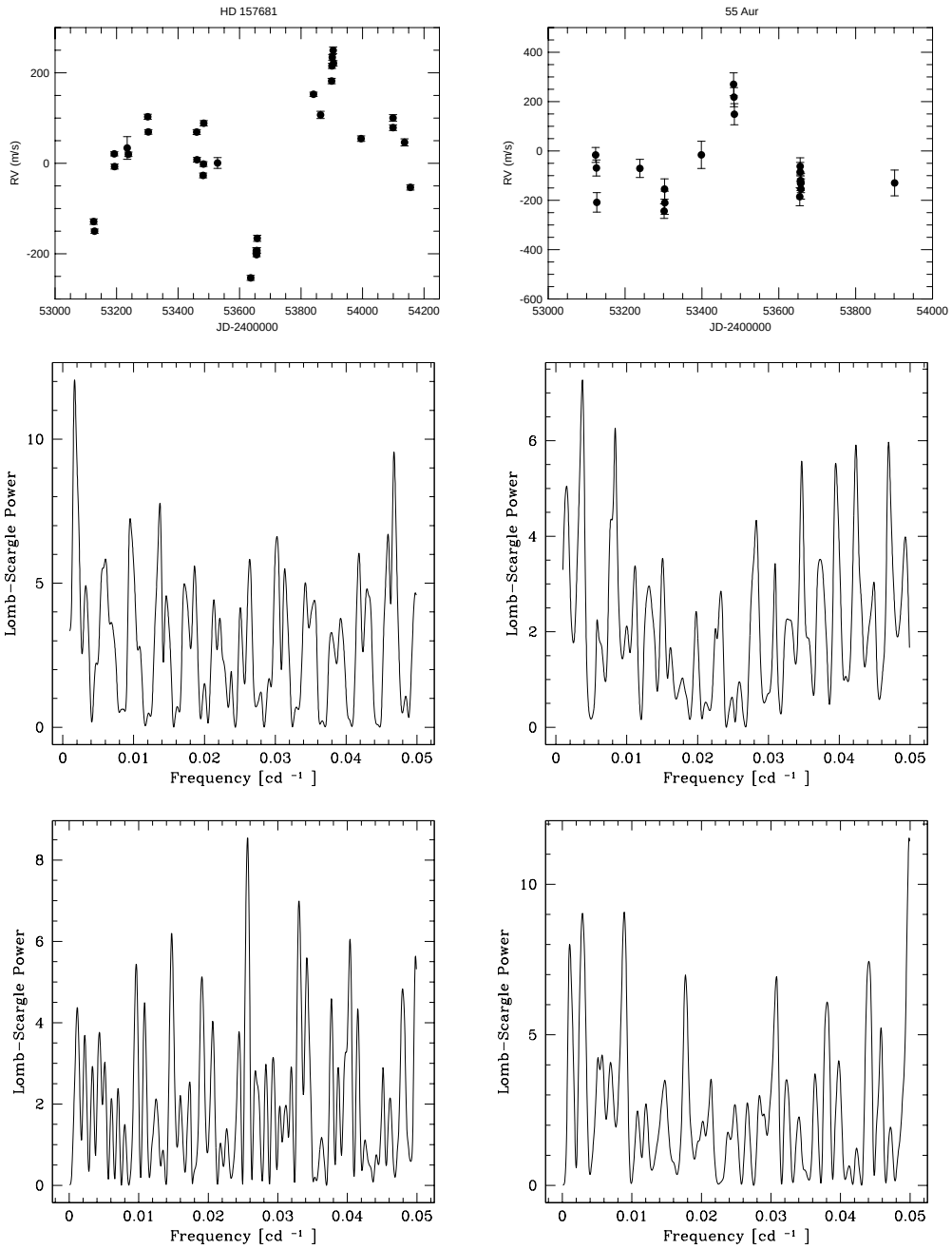

Figure 5.30: Plots of the RV monitoring, scargle periodograms of the RVs and the *HIPPARCOS* photometry of the *TLS* stars HD 157681 (left) and 55 Aur (right). RV plotted against JD and scargle power plotted against frequency.

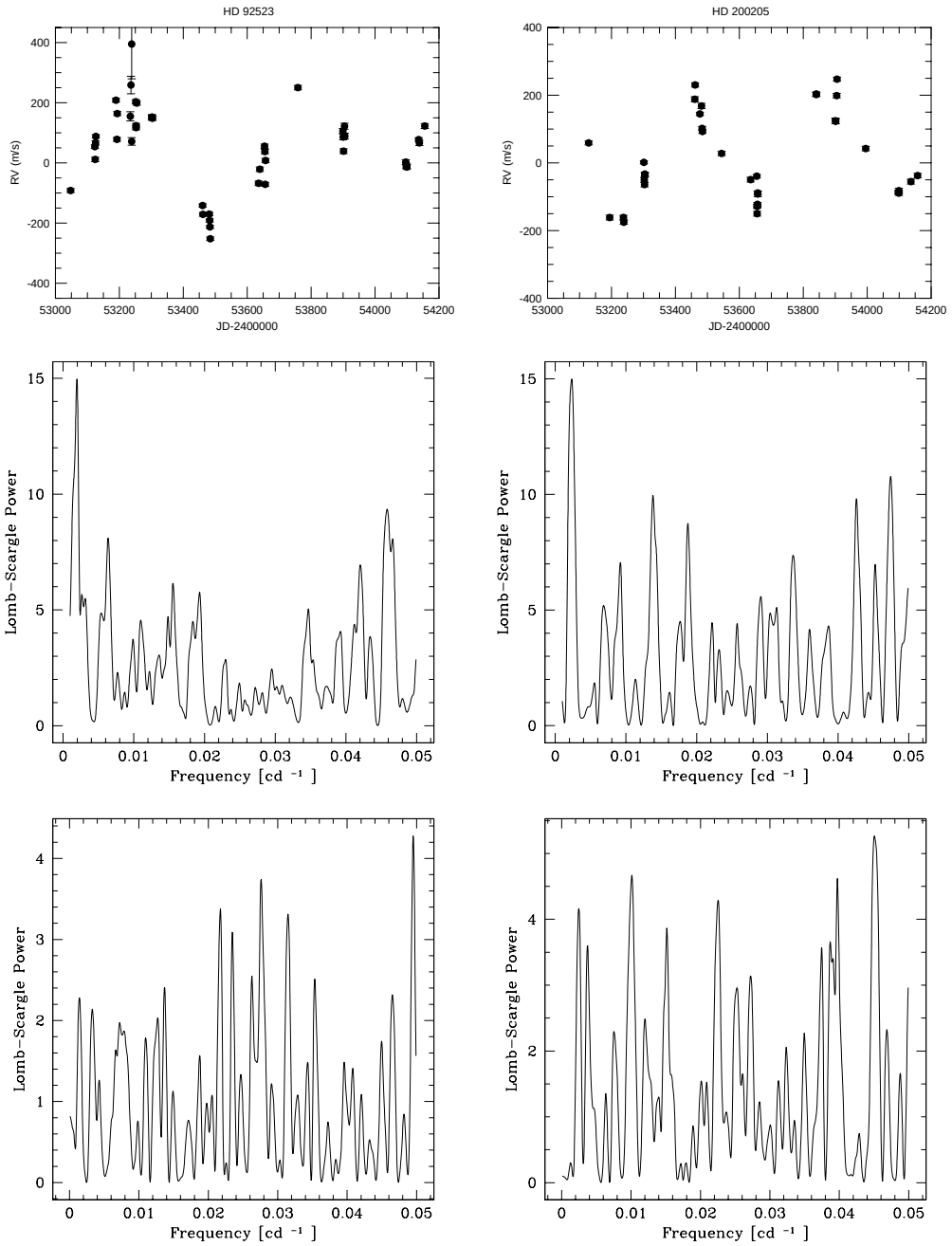

Figure 5.31: Plots of the RV monitoring, scargle periodograms of the RVs and the *HIPPARCOS* photometry of the *TLS* stars HD 92523 (left) and HD 200205 (right). RV plotted against JD and scargle power plotted against frequency.

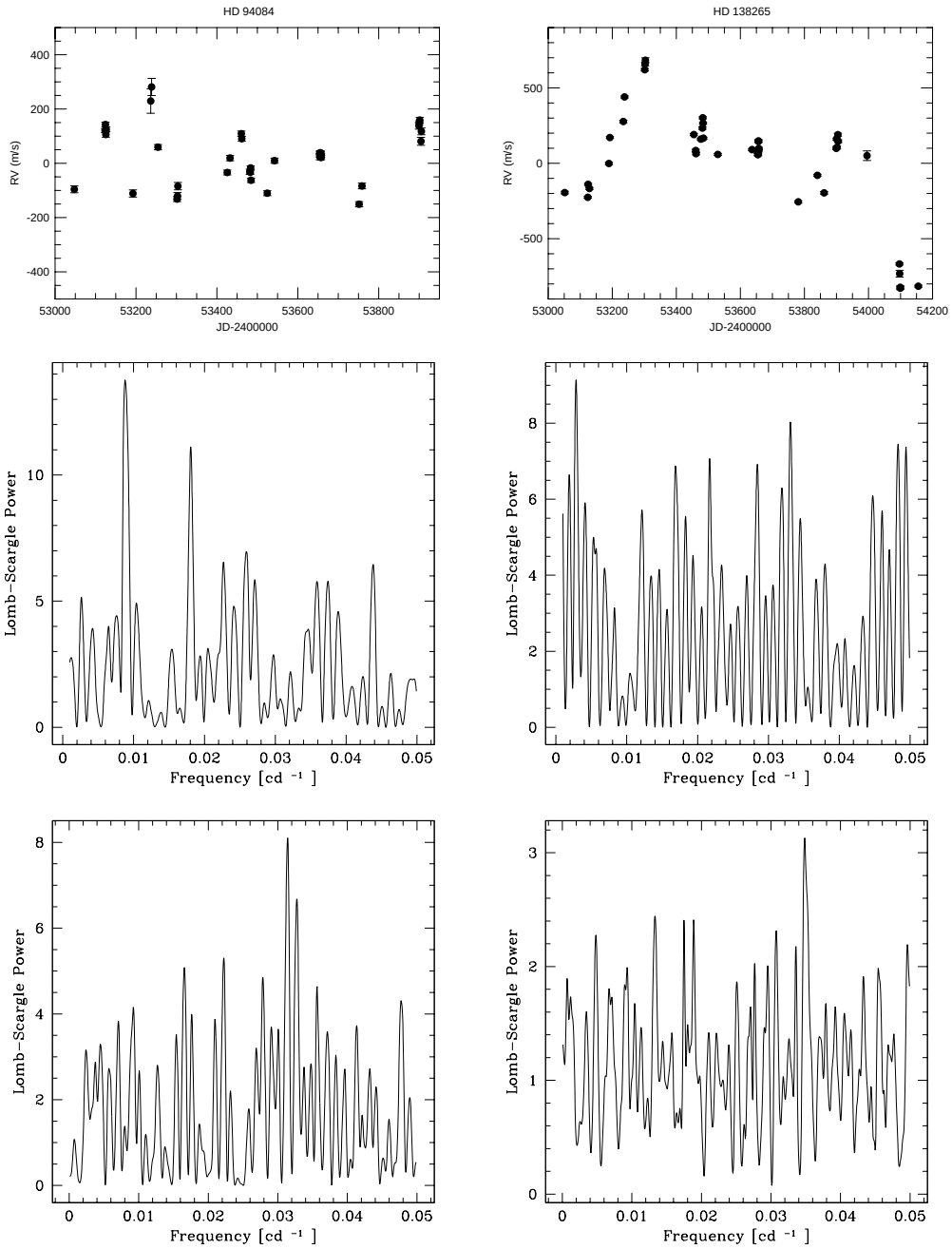

Figure 5.32: Plots of the RV monitoring, scargle periodograms of the RVs and the *HIPPARCOS* photometry of the *TLS* stars HD 94084 (left) and HD 138265 (right). RV plotted against JD and scargle power plotted against frequency.

Chapter 6

Planetary companions

Until now more than 250 planetary companions around solar-type Main Sequence (MS) stars have been detected via the Radial Velocity (RV) method. However, most of these exoplanets are in orbit around stars each with a mass of approximately one solar mass ($M_\odot$). As a consequence of this, the understanding of how the stellar mass influences planet formation, particularly for more massive stars, is very poor. An increasing number of RV searches tried to find planets around low-mass (0.2–1.0 $M_\odot$) stars (Delfosse et al. 1999; Endl et al. 2003). For instance GJ 876 (M4 V) with 0.3 $M_\odot$ possesses a planet with a "minimum mass" of $m \sin i \approx 2$ M_{Jup} in a 60-day orbit (Delfosse et al. 1998). Jovian planets were found around GJ 849 (Butler et al. 2006) and GJ 317 (Johnson et al. 2007a). Neptune-mass planets were discovered around GJ 436 (Butler et al. 2004), GJ 581 (Bonfils et al. 2005) and GJ 674 (Bonfils et al. 2007). Planets with "minimum masses" below 10 Earth masses ($M_\oplus$) were detected in the GJ 876 (Rivera et al. 2005) and GJ 581 (Udry et al. 2007) systems. Endl et al. (2008) published the detection of a new low-mass planet in a 10.24-day orbit around the M dwarf GJ 176. There are also on-going attempts to search for extrasolar planets around early-type A–F stars (Galland et al. 2005a).

During these surveys two substellar companions were discovered. The first detected exoplanet is a 9.1 Jupiter masses (M_{Jup}) companion in a 388-day orbit around the F-type star HD 33564 (1.25 $M_\odot$) published by Galland et al. (2005b). Moreover a brown dwarf (25 M_{Jup}) candidate in a 28-day orbit was found (Galland et al. 2006) orbiting HD 180777 (A9 V). By comparison these surveys have been less successful so far possibly due to the lower RV precision. The reason is that early-type MS stars are not particularly suitable for RV surveys because they are hotter and have fewer spectral lines which in addition are broadened significantly by the high rotation rates common among A–F type stars. In the search for extrasolar planetary companions around more massive stars, an alternative approach is to look at intermediate-mass (1.5–4.0 $M_\odot$) stars that have evolved off the MS and up the giant branch. These stars are cooler and thus have plenty of stellar lines. This, together with their slower rotation rates, make them amenable to high precision RV measurements. But two difficulties are encountered in this approach. First, unlike MS stars, K giants of different masses can have similar effective temperatures. Secondly, as with MS stars, giants show intrinsic variations due to stellar oscillations. These short-period ($\approx$ 2–10 days) variations (see §5.1.2) are probably caused by radial and/or non-radial p-mode oscillations (Hatzes & Cochran 1994a) and add intrinsic RV "noise" making the detection of extrasolar planets more difficult. However these oscillations offer the possibility to apply astero-

seismology to derive in a second way stellar parameters (Hatzes & Zechmeister 2007) such as the stellar mass.

Despite these obstacles, searching for planets around giants can deliver information about the process of planet formation around stars with intermediate mass. Hatzes & Cochran (1993) found first hints of substellar companions around giants. They discovered long-period RV variations in three K giant stars and they proposed two viable hypotheses for these variations in radial velocity: substellar companions or rotational modulation. The expected rotational periods of K giants are several hundreds of days which are comparable with the observed RV periods. If a large surface inhomogeneity (e.g. starspot) exists on the surface this would create distortions of the spectral line profiles which would be detected as a RV variation with the rotation period of the star. For these reasons the nature of the long-period RV variations was not clear. Subsequent studies have established that giant stars can indeed host extrasolar planets. The first exoplanet around a K giant star was discovered by Frink et al. (2002). This was followed by the discovery of substellar companions to the stars HD 47536 (Setiawan et al. 2003a) and HD 122430 (Setiawan 2003b). In the same year Sato et al. (2003) reported a planetary companion around HD 104985. Substellar companions have also been published for HD 11977 (Setiawan et al. 2005) and HD 13189 (Hatzes et al. 2005). More recently Hatzes et al. (2006) confirmed that the initial RV variations found by Hatzes & Cochran (1993) in β Gem were in fact due to a planetary companion. This was confirmed by Reffert at al. (2006). Sato et al. (2007) announced a planetary companion to the Hyades giant ϵ Tau. An exoplanet to the K0 giant HD 17092 was published by Niedzielski et al. (2007). Recently Johnson et al. (2007b) detected an extrasolar planet around HD 167042. But the number of exoplanets around evolved stars is so far very limited. The discovery of the companion to 4 UMa (Döllinger et al. 2007) adds to the growing list of giants hosting substellar companions (see Hatzes et al. 2006 and references therein). Moreover 5 further candidates were detected in the Thüringer Landessternwarte Tautenburg (TLS) survey (Döllinger et al. 2008a). Adding these additional planetary companion candidates to the published ones, the first extended sample of 20 giant stars hosting exoplanets is now available. The estimated masses for the giant stars hosting planets from the TLS and the southern Fiber-fed Extended Range Optical Spectrograph ($FEROS$) survey as well as from the literature range from 1 to 3 $M_{\odot}$. These planets have properties, similar to the characteristics of the exoplanet around 4 UMa, with masses in the range of 2–14 M_{Jup} and orbital periods of several hundred days (see discussion by Hatzes et al. 2006). The range of the planetary mass is probably a consequence of the detection limit of the radial velocity technique. The discoveries of exoplanets around giants are important because this type of host star probes a slightly different stellar mass regime in comparison with MS objects which are the targets of most planet searches. For most of these discoveries the planet hypothesis for the RV variations was established due to a lack of variations in other measured quantities with the RV period. Spots or stellar pulsations are expected to produce additional variations with the RV period in the lines of the stellar "activity indicators" Ca II H&K (not covered in the Tautenburg high resolution spectra) and Hα (see §6.3.1), the $HIPPARCOS$ photometry, and in the spectral line shape. These variations were not found in the giant stars believed to host extrasolar planets. In the case of HD 137759 (ι Dra) the high eccentricity of the orbit established its Keplerian nature (Frink et al. 2002). The same argument was adopted for the discovered exoplanet around the K giant star 4 UMa (Döllinger et al. 2007) to confirm the planetary companion.

6.1 Confirmation tools

6.1.1 Lomb-Scargle periodogram

There are a variety of techniques for studying data as a function of the period of a possible periodic component. One possibility is the least-squares fitting of sine waves to the data and studying the variance of the residuals as a function of the period (Barning 1963; Lomb 1976). The technique explained here is that of periodogram analysis where the statistical distribution of the periodogram is based on the Discrete Fourier Transformation (DFT). I used this Lomb-Scargle periodogram method (Lomb 1976; Scargle 1982 and Black & Scargle 1982) to compute the power spectra of all my RV, $HIPPARCOS$ and Hα data sets to search for possible velocity, photometric and chromospheric variations. The classical definition of the periodogram was replaced by Scargle (1982) for two reasons: the modified version has simple statistical behavior, and it is equivalent to the reduction of the sum of squares in least-squares fitting of sine waves to the data. In addition it has time-translation invariance. This modified periodogram has the following form:

$$P_X(\omega) = \frac{1}{2}\left\{ \frac{\left[\sum_j \cos\ \omega(t_j-\tau)\right]^2}{\sum_j \cos^2\ \omega(t_j-\tau)} + \frac{\left[\sum_j \sin\ \omega(t_j-\tau)\right]^2}{\sum_j \sin^2\ \omega(t_j-\tau)} \right\}, \tag{6.1}$$

where τ is defined by

$$\tan(2\omega\tau) = \frac{\sum_j \sin\ 2\omega t_j}{\sum_j \cos\ 2\omega t_j}. \tag{6.2}$$

The times of observation are expressed by t_j with j=1,2,3...N_0. N_0 is the number of data points and $\omega = 2\pi f$ is an arbitrary frequency. If the N_0 data points are evenly spaced in time, a natural set of frequencies exists at which to evaluate the periodogram,

$$\omega_n = \frac{2\pi n}{T}, \tag{6.3}$$

where T is the total time interval of the observations and n = 0,1,2,...,$N = N_0$ the integer. The number of frequencies sampled in the periodogram is $N \leq N_0/2$. The fundamental frequency $\omega_1 = 2\pi/T$ corresponds to the lowest frequency about which there is information in the data. The so-called Nyquist frequency, $\omega_N = \pi N_0/T$, corresponds to the highest frequency about which there is information in the data. Astronomical data are often not evenly spaced in time, in which case the fundamental frequency remains well-defined, but the concept of the Nyquist frequency is undefined. The starting point of the statistical analysis is the simple but very useful result that the power at a given frequency is exponentially distributed. Replacing the random variable $P_X(\omega)$ by Z, the probability distribution is

$$p_z(z)dz = Pr(z < Z < z + dz) = exp(-z)dz, \tag{6.4}$$

where z is the height of a peak in the periodogram. Hence the cumulative distribution function is

$$F_Z(z) = Pr(Z < z) = \int_0^z p_Z(z')dz' = 1 - exp(-z). \tag{6.5}$$

The related quantity $\Pr(Z > z) = \exp(-z)$, gives the statistical significance of a large observed power at a preselected frequency. That is, as the observed power becomes larger, it becomes exponentially unlikely that such a power level can be due to a chance noise fluctuation. Now consider the maximum value (peak) in the spectrum. Let $Z = max_n \mathrm{P}(\omega_n)$, where the maximum is over some set of N frequencies such that the $\mathrm{P}(\omega_n)$ are independent random variables. Then the multiplicative property yields for this case

$$Pr(Z > z) = 1 - F_Z(z) = 1 - [1 - exp(-z)]^N. \tag{6.6}$$

Sometimes there is a different notation in the literature. The statistical significance of a peak in the power spectrum is estimated by computing the False Alarm Probability (FAP). It is given by the expression

$$F = 1 - [1 - exp(-Z_m)]^N, \tag{6.7}$$

where Z_m is the height of the peak in the normalized power spectrum and N is the number of independent frequencies (Horne & Baliunus 1986; Joshi & Joshi 2005). The significance of a peak can be expressed by a rule of thumb: Scargle power ≥ 15 is probably real. Scargle power $\leq$8 is probably not, power between 10–15 is interesting and should be investigated further. Power between 8–10 may or may not be real depending on the number of data points. A problem in analyzing the data can arise from the so-called aliasing. It is due to periodicity in the data format. A type of pseudoaliasing occurs if there is quasiperiodicity in the data format. This often happens in astronomical work where one finds diurnal, monthly, or annual effects evident in the observational programme. Such quasiperiodicity would lead to alias peaks displaced from the peak at $\omega = \omega_0$ by multiples of 2π radians per day, month, or year. To be sure that peaks in the different power spectra are not due to aliasing, I have removed sine curves of their periods from the original time series. I find that these peaks get removed in the power spectra of time series obtained after subtraction.

6.1.2 *HIPPARCOS* data

The data were collected during the *HIPPARCOS* (HIgh-Precision PARallax COllecting Satellite) mission. The main goal of the *HIPPARCOS* satellite was to make astrometric measurements. As a by-product precise photometric measurements were provided by two experiments.

The Tycho experiment was defined by the following:

- Number of stars: > 400 000
- Limiting magnitude: B = 10–11 mag
- Positional accuracy: 0.03 arcsec (B = 10 mag)
- Photometric accuracy: 0.05 mag in B and V (per observation)
- Observation per star: approximately 100.

In the Tycho experiment the information was contained in the peak height of the signal produced by a star passing over the star mapper slits. The Tycho photometry was obtained in two passbands, $\mathrm{B_T}$ and $\mathrm{V_T}$, resembling the B and V passbands of the Johnson system. The photometric data were derived from the photon counts by the

star mapper B_T and V_T photomultipliers. The epoch photometry records provide the B_T and V_T magnitudes and their standard errors with a reference epoch.
The *HIPPARCOS* epoch photometry (Perryman et al. 1997; van Leeuwen et al. 1997) covers 118,204 stars and contains an average of $n = 110$ observations per star.
I checked and downloaded from *SIMBAD* this available data – expressed as *HIP* names – for the *TLS* stars. The *HIPPARCOS* photometry contains data for the whole *TLS* sample over 3 years.

6.1.3 Hα activity

Several studies have shown that the central core of Hα forms in the stellar chromosphere. Consequently stars of different chromospheric activity show a different shape (depth and breadth) of the Hα core (Pasquini & Pallavicini 1991). By measuring the variations of the core of Hα with respect to the adjusted continuum it is therefore possible to investigate the presence and variability of chromospheric active regions. Thus it has been widely demonstrated that the Hα line can be used as a good "activity indicator" of chromospheric emission (Herbig 1985; Pasquini & Pallavicini 1991 and Freire Ferrero et al. 2004). To determine the chromospheric contribution to the Hα profile, possible contaminations with telluric lines have to be subtracted. With the spectra of the Tautenburg star sample this subtraction was not possible because it required the observation of "telluric standards" (early-type rapid rotating stars) at different lines every night, and these were not available. A "telluric standard" was not observed because I did not know at the time that the Hα would be useful and did not forsee it as part of my analysis. Afterwards I did, but I had no additional observing runs. As a consequence, I was unable to detect the chromospheric emission component filling in the Hα core with the "classical" spectral synthesis method which subtracts a "synthetic" profile from the active star profile (Barden 1985, Frasca & Catalano 1994). Despite this difficulty I wanted to use the "activity indicator" Hα to discriminate between the different types of RV variability. This should be possible because it is reasonable that a different chromospheric activity contributes in a different way to the RV variations. RV variability caused by rotational modulation (e.g. starspots) for instance should also be detectable in changes of the depth and breadth of the core of the chromospheric "activity indicator" Hα. Thus this additional information of stellar chromosphere can be used to confirm independently rotational modulation detected in the RV data. Furthermore planetary companions can be confirmed by the lack of changes in Hα. For this purpose I decided to consider two regions around the Hα line center, one very narrow of $\pm$ 0.6 $\AA$ and taken far from strong telluric lines (in particular the one at 6564 $\AA$) and the second one wider by $\pm$ 50 $\AA$. To extract the chromospheric contribution I used the IDL[1] programme abHalpha.pro written by Biazzo (2007, private communication). This programme shifts all the spectra to a common rest wavelength, and measures the ratio between the area around $\pm$ 0.6 $\AA$ of the Hα line center (blue area in Fig. 6.1) and the area around $\pm$ 50 $\AA$ of the Hα line center (area with very small dots in Fig. 6.1) to detect changes in the chromospheric activity over time in the spectra of selected programme stars.
I used 74 Dra, one of my "constant" RV standard stars, as an internal reference because this star shows radial velocity variations at a very low level which corresponds to the RV accuracy limit of about 3–5 $\mathrm{m\,s^{-1}}$. As a consequence of this the only changes would be due to telluric lines and observing conditions such as air mass. After running the

[1]IDL (Interactive Data Language) is a data visualization and analysis platform.

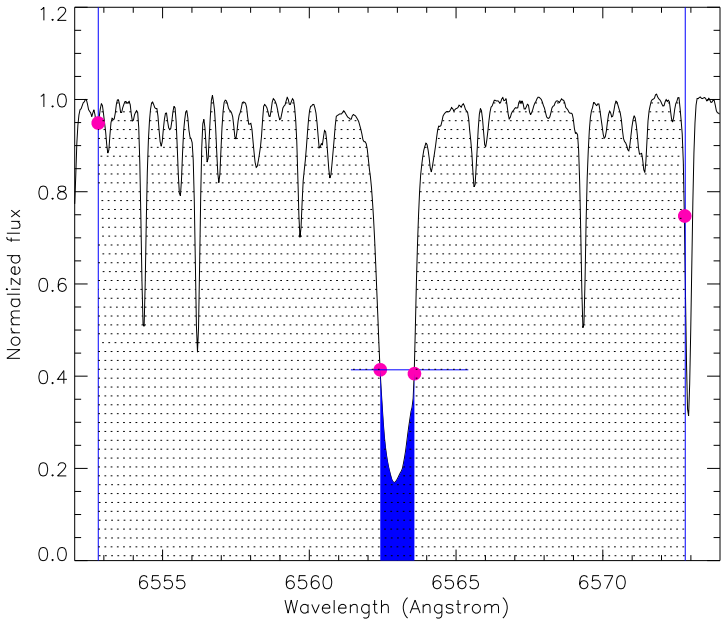

Figure 6.1: Example of a spectrum around the Hα, and selected for determining the chromospheric contribution. The blue area is around $\pm$ 0.6 $\AA$ of the Hα line center, while the dotted area is around $\pm$ 50 $\AA$ of the Hα line center. The pink dots represent the limits of these two selected regions.

programme, 74 Dra shows a change of around 1 % in Hα activity. Taking into account that this star was not observed every night in all observing runs this value can only give a hint as to the internal error of the programme. For the planetary companions the value for the Hα activity ranges between 3–8 % after subtraction around 1 % for the standard deviation. The time analysis of the thus derived Hα activity will be discussed in more detail for the TLS planet candidates in §6.2.

Table 6.1: Stellar parameters of 4 UMa

Spectral type	K1 III	
m_V	4.599 ± 0.005	[mag]
M_V	0.146 ± 0.119	[mag]
B–V	1.197 ± 0.005	[mag]
Parallax	12.92 ± 0.71	[mas]
Distance	62.39 ± 3.43	[pc]
$M_*{}^{(a)}$	1.234 ± 0.15	[$M_\odot$]
$R_*{}^{(a)}$	18.11 ± 1.47	[$R_\odot$]
$t^{(a)}$	4.604 ± 2.0	[Gyr]
$T_{\rm eff}{}^{(a)}$	4415 ± 70	[K]
$[Fe/H]^{(a)}$	-0.251 ± 0.04	[dex]
$\log g^{(a)}$	1.8 ± 0.15	[dex]
microturbulence$^{(a)}$	1.2 ± 0.8	[km s^{-1}]

$^{(a)}$ from my analysis

6.2 Candidates

6.2.1 4 UMa

Results derived from precise stellar radial velocity measurements of the K1 III giant star 4 UMa (= HD 73108 = HR 3403 = HIP 42527) and presented in this chapter were published in the article "Discovery of a planet around the K giant star 4 Ursae Majoris" (Döllinger et al. 2007). Parts of the text and figures of this chapter have been taken from this publication.
4 UMa has a visual magnitude of $V = 4.599$ mag. The *HIPPARCOS* parallax is 12.92 ± 0.71 mas and this causes an absolute magnitude of $M_V = 0.146 \pm 0.119$ mag. The stellar parameters of 4 UMa are summarized in Tab. 6.1.

For 4 UMa, the 5 other host stars and the remaining target stars the stellar parameters were either derived from my analysis of so-called templates (spectra without the iodine cell) or were taken from the literature. From high-quality spectra I determined accurate Fe abundances [Fe/H] as well as effective temperatures $T_{\rm eff}$, logarithmic surface gravities $\log g$ and microturbulence velocities ξ (see §4.1). These parameters, with the exception of the microturbulence velocity, were used together with the V-band magnitude, as derived from *HIPPARCOS* parallaxes, as input values to estimate mass, age, radius, $(B–V)_0$ and physical surface gravity (see §4.3.2) of each programme star by using theoretical isochrones and a modified version of Jørgensen & Lindegren's (2005) method (see §3.3.3).
A total of 46 spectra of 4 UMa were taken over a period of around 3 years using the iodine cell as a wavelength reference.
A Lomb-Scargle periodogram was then used to search for periodic signals in the radial velocity data to obtain a first guess for initial values for the orbital fitting programme *GaussFit* (Jefferys, Fitzpatrick & McArthur 1988; McArthur, Jefferys & McCartney 1994). However, periods obtained from the Lomb-Scargle periodogram (see §6.1.1) are only first indications of significant frequencies in the data and can be different from the more precise final periods derived from the orbital solution and calculated with *GaussFit*.
The time series of the RV measurements for 4 UMa is shown in Fig. 6.2 (left). The

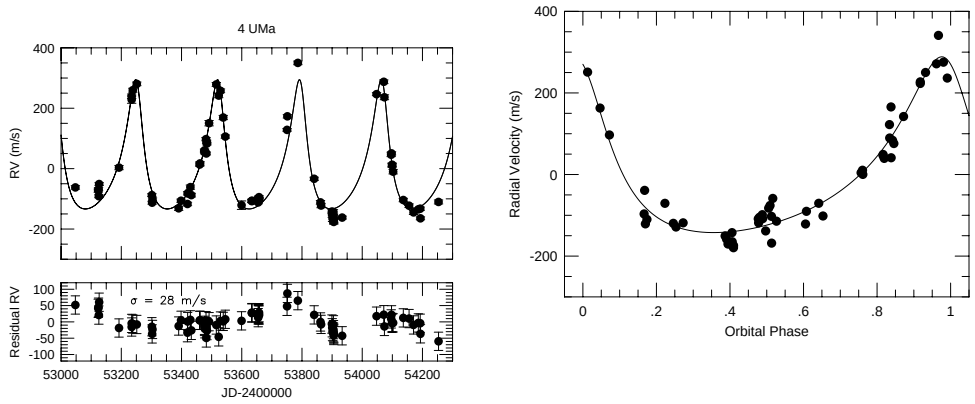

Figure 6.2: Radial velocity measurements for 4 UMa (top left). The solid line is the orbital solution. RV residuals (lower left) in $\mathrm{m\,s^{-1}}$ after subtracting the contribution of the planet orbit (top left). Radial velocity measurements for 4 UMa phased to the orbital period (right). The line represents the orbital solution. The right figure is taken from Döllinger et al. (2007).

radial velocity data reveal an obvious sinusoidal variation in the RV curve of 4 UMa with a period variation of 271.90 days and with a semiamplitude of $K = 214.92\ \mathrm{m\,s^{-1}}$. The shape of the RV curve is not a pure sine wave and is therefore the first hint of Keplerian motion. Thus a Keplerian orbit with an eccentricity of $e = 0.42 \pm 0.02$ is the most reasonable explanation for the radial velocity variations. Fig. 6.2 (right) shows the RV variations phase-folded to the orbital period.

A similar high value for the eccentricity was found for the companions to HD 11977 ($e = 0.4$, Setiawan et al. 2005) and HD 13189 ($e = 0.27$, Hatzes et al. 2006). It seems that the planetary companions to giant stars can have the wide range of orbital eccentricities (see Fig. 6.21) that is shown by planets orbiting solar-type MS stars. However, the number of exoplanets around giants is probably too limited to derive strict conclusions. In any case eccentric orbits are interesting since so far it was expected that planets form in circular orbits similar to our solar system.
The orbit yields a mass function (see Eq. (3.16)), *f(m)* = (2.078 ± 0.247) x 10^{-7} $\mathrm{M_\odot}$. Using the mass of $\mathrm{M_\star} = 1.23 \pm 0.15\ \mathrm{M_\odot}$ of the host star the mass function delivers a "minimum mass" of $m \sin i = 7.20 \pm 0.82\ \mathrm{M}_{Jup}$ for the substellar companion orbiting the K giant 4 UMa. The orbital fit to the data is very well. In fact, the observed minus computed root mean square (rms) scatter, σ(O–C), of $\approx 30\ \mathrm{m\,s^{-1}}$ about the orbital solution is a little large with a factor of ten higher than at the best achievable RV accuracy of about 3–5 $\mathrm{m\,s^{-1}}$. This is perhaps an indication of another periodic signal in the data. All the orbital elements are listed in Tab. 6.2.

The first periodic signal in the RV data was identified by using a Lomb-Scargle periodogram (Lomb 1976; Scargle 1982) which confirmed the presence of strong power

Table 6.2: Orbital parameters for the companion to 4 UMa.

P [days]	271.90 ± 1.96
$T_{periastron}$ [JD]	53525.8604 ± 4.31
K [ms^{-1}]	214.92 ± 7.10
σ(O–C) [ms^{-1}]	27.47
e	0.424 ± 0.02
ω [deg]	22.573 ± 4.42
$f(m)$ [solar masses ($M_\odot$)]	(2.078 ± 0.247) x 10^{-7}
a [AU]	0.88 ± 0.04

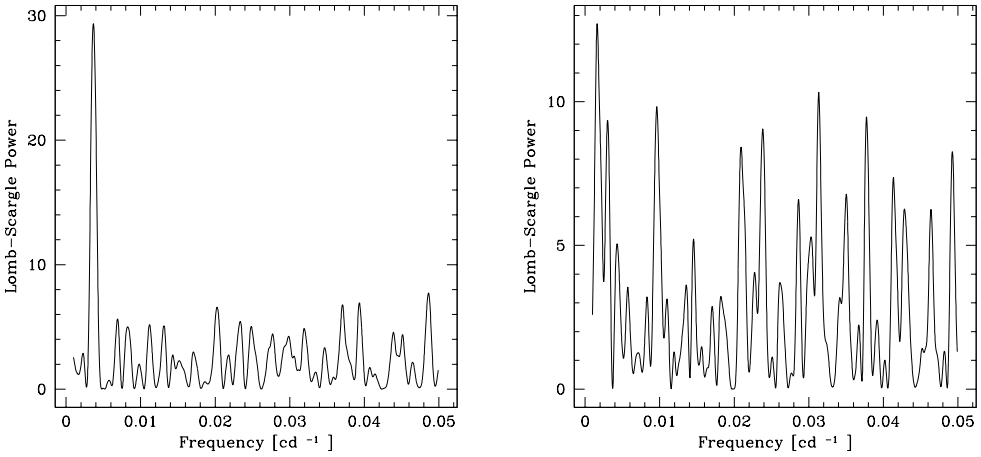

Figure 6.3: Lomb-Scargle periodogram of the RV data for 4 UMa (left). The peak with strong power at frequency $\nu = 0.00367\mathrm{c\,d^{-1}}$ corresponds to a period of 272.48 days. Lomb-Scargle periodogram of the RV residuals of 4 UMa (right). The strongest peak corresponds to a period of 675.68 days.

at a frequency of $\nu = 0.00367\mathrm{c\,d^{-1}}$ ($P = 272.48$ days). The False Alarm Probability (FAP) of this peak using the prescription in Scargle (1982) is estimated to be $\approx 10^{-8}$. The periodogram is plotted in Fig. 6.3 (left).

The left part of Fig. 6.2 shows in the lower panel the RV residuals after removal of the orbital contribution due to the planetary companion. There are clear variations with a period much larger than the orbital period. This is confirmed by the Lomb-Scargle periodogram of the RV residuals shown in Fig. 6.3 (right). The Lomb-Scargle periodogram shows a strong peak at a frequency of $\nu = 0.00148\,\mathrm{c\,d^{-1}}$ ($P = 675.68$ days). The statistical significance of this signal was estimated using a bootstrap randomization technique (Kürster et al. 1997). The measured RV values were randomly shuffled keeping the observed times fixed and a periodogram for the shuffled data computed. After 2×10^5 shuffles there was no instance where the random fake data periodogram data had higher power than the data periodogram in the frequency range. This indicates that the FAP $< 2 \times 10^{-6}$. This signal is thus statistically significant and does not arise by chance from noise.

To confirm the planetary companion I also analysed the *HIPPARCOS* photometry

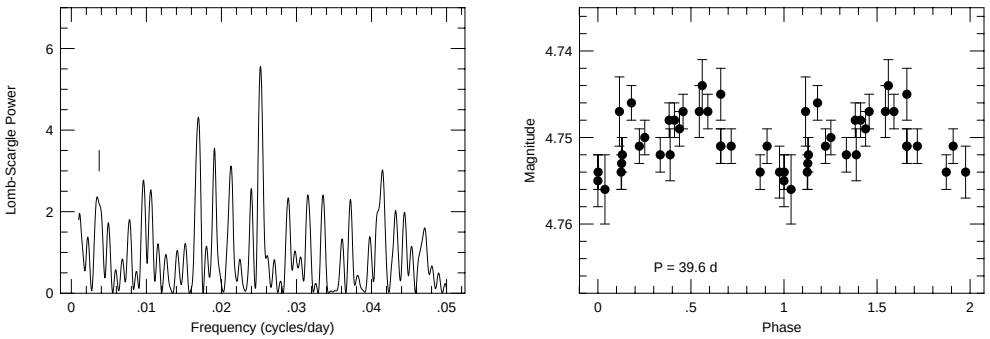

Figure 6.4: Lomb-Scargle periodogram of the *HIPPARCOS* photometry for 4 UMa (left). The vertical line marks the orbital frequency. *HIPPARCOS* photometry for 4 UMa phased to the 39.7-day photometric period (right). Both figures are taken from Döllinger et al. (2007).

of 4 UMa to see whether variations with the 272-day period – period of the planetary companion – are present. The *HIPPARCOS* data contain 27 observations (daily averages). Fig. 6.4 (left) shows the Lomb-Scargle periodogram of the *HIPPARCOS* photometry after averaging the multiple measurements taken within a few hours of each other. One obvious outlier that had a value more than 10 σ from the mean was eliminated from the data prior to calculating the periodogram. Although there is a weak peak near the orbital frequency this is not significant and there are several peaks with more power. The highest peak with a scargle power of ≈ 6 is at a frequency of 0.0252 $\mathrm{c\,d^{-1}}$ ($P = 39.70$ days). Fig. 6.4 (right) shows the photometry phased to this period. The FAP for this peak was estimated using the bootstrap randomization technique. After 100,000 such shuffles 19 % of the random data periodograms showed power greater than the real periodogram. This peak is most likely not significant because of the relatively low scargle power and in addition no significant peak exists at the corresponding frequency in the periodogram of the RV data.

Rotational modulation as the reason for the 676-day period in the RV data can be excluded because of the lack of a significant peak at this frequency in the Lomb-Scargle periodogram of the Hα variations over time, which were determined using the programme abHalpha.pro (see §6.1.3). Fig. 6.5 shows the Lomb-Scargle periodogram of the Hα variations with time. The highest peak with a scargle power of ≈ 8 is at a frequency of 0.0223 c d^{-1} ($P = 44.88$ days). No corresponding significant peaks exist in the RV data or in the *HIPPARCOS* photometry at this frequency. The reason for the variations in Hα are therefore probably due to telluric lines caused by clouds and influenced by high air mass observations because there is a trend of Hα variations with high values for the air mass.

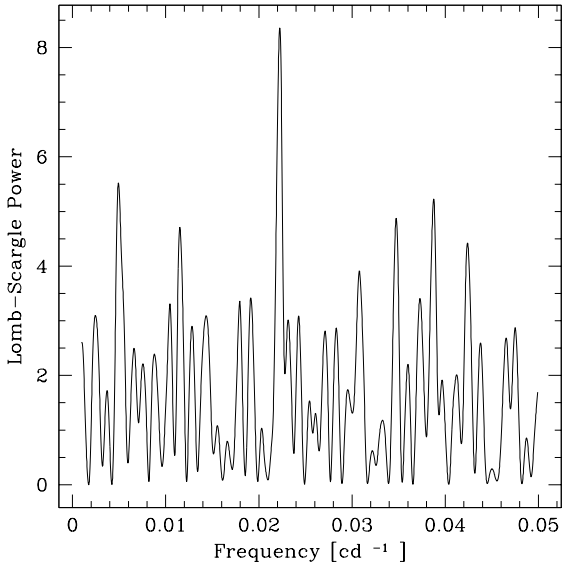

Figure 6.5: Lomb-Scargle periodogram of the Hα variations of 4 UMa. There is no significant frequency detectable which would be a hint for rotational modulation.

The radial velocity measurements indicate that the giant 4 UMa hosts a giant extrasolar planet. The corresponding RV variations are more confident due to a substellar companion and not to rotational modulation for the following reasons:

- The orbit is highly eccentric and such a saw-toothed RV pattern is difficult to reproduce with rotational modulation from spots or possibly even from stellar oscillations. Indeed, the high eccentricity of the companion to HD 137759 (ι Dra) was the convincing argument that this was a true companion (Frink et al. 2002).

- The *HIPPARCOS* photometry and the Hα data does not show any significant variations at the orbital period.

- The periodogram shows a second statistically significant period at 676 days in the RV residuals – subtraction of the 272-day RV period – for 4 UMa. Recapitulating two periods of several hundred days were detected and both are unlikely to be due to rotation. This is because in the first case the RV variations of the dominant long-lived and coherent 272-day RV period – as mentioned above – is

well-fit by an eccentric Keplerian orbit which is a clear hint that this signal is due to a planetary companion. In the second case the detected 676-day period is unlikely to be due to rotational modulation because a similar signal does not appear in the *HIPPARCOS* photometry which should be visible if rotational modulation is the the reason for the 676-day RV period. I caution the reader that the *HIPPARCOS* measurements were not taken at the same time. However, the investigation of the Hα activity also excludes rotational modulation as a reason of the 676-day period detected in the RV residuals and in the end the second planetary companion assumption is favoured.

4 UMa, with an Fe abundance of -0.25 $\pm$ 0.4 dex, is according to the general definition of "metal-poor" ([Fe/H] $<$ -1.0 dex), "slightly" metal-poorer than the MS and Post-Main sequence (PM) stars, and it is as metal-rich as the average solar neighbourhood. However, for my thesis I redefined this well-defined term. In my work an Fe abundance lower ([Fe/H] $<$ -0.1 dex) than solar means "metal-poor". According to this new definition 4 UMa is metal-poor. This redefinition will be valid for all stars and in all chapters. It is interesting that 4 UMa is metal-poor because MS stars hosting exoplanets tend to be metal-rich (see §7) compared to stars that do not posses exoplanets (Santos et al. 2004). Other authors (Schuler et al. 2005; da Silva et al. 2006) have also found evidence that planet-hosting giant stars are metal-poor. Recently Endl et al. (2008) wrote about one of the most metal-poor planet-hosting stars. They estimated an [Fe/H] = -0.1 $\pm$ 0.2 dex for GJ 176.

Table 6.3: Stellar parameters of 11 UMa

Spectral type	K5 III	
m_V	5.156 ± 0.005	[mag]
M_V	-0.772 ± 0.199	[mag]
B–V	1.152 ± 0.005	[mag]
Parallax	6.54 ± 0.60	[mas]
Distance	31.58 ± 2.90	[pc]
$M_*{}^{(a)}$	1.181 ± 0.195	[$M_\odot$]
$R_*{}^{(a)}$	36.29 ± 4.19	[$R_\odot$]
$t^{(a)}$	4.878 ± 2.328	[Gyr]
$T_{\rm eff}{}^{(a)}$	4090 ± 70	[K]
$[Fe/H]^{(a)}$	-0.245 ± 0.04	[dex]
$\log g^{(a)}$	1.6 ± 0.15	[dex]
micro turbulence$^{(a)}$	1.4 ± 0.8	[km s^{-1}]

$^{(a)}$ from my analysis

6.2.2 11 UMa

A second planetary companion was possibly dectected around the K5 III giant 11 UMa (= HD 77800 = HR 3609 = HIP 44857). This candidate is also very bright with a visual magnitude of $V = 5.156$ mag and thus observations were possible despite bad weather conditions. The parameters of the parent star are summarized in Tab. 6.3.

The resulting Lomb-Scargle periodogram of the RV data, consisting of 99 stellar spectra taken with the iodine absorption cell, is shown in the left part of Fig. 6.6. The plot contains 4 periods with a significant power. The strongest peak is present at a frequency of $\nu = 0.00174\,\mathrm{c\,d^{-1}}$ ($P = 574.71$ days) and it is clearly visible in Fig. 6.6 (left). The FAP of this peak using the prescription in Scargle (1982) is estimated to be 3.0×10^{-8}. The second peak is placed at a frequency $\nu = 0.00299\,\mathrm{c\,d^{-1}}$, which corresponds to a period of $P = 334.45$ days. A FAP of 9.85×10^{-6} is calculated for this peak. The scargle power of both peaks is 21.9 and 16.1, respectively. In addition there are two considerably weaker peaks with a similar scargle power of only ≈ 11.8 at the frequencies $\nu = 0.04588\,\mathrm{c\,d^{-1}}$ ($P = 22.75$ days) and $\nu = 0.02$ c d^{-1} ($P = 50$ days). The last peak is not visible in the periodograms of the *HIPPARCOS* and Hα data. Afterwards the 574.7-day value was used as an initial value for one of the orbital fitting parameters.

After running the programme *GaussFit*, an orbital solution was calculated and fitted to the time series of RV measurements. The radial velocity data reveal an obvious sinusoidal variation in the RV curve of 11 UMa with a period variation of 651.91 days and a RV semiamplitude of $K = 109.47$ m s^{-1}. There is a discrepancy visible between the derived period values. The orbital fitting programme delivered a value of 651.91 days contrary to a value of 574.71 days derived from the Lomb-Scargle periodogram of the RV data. The period of 334.45 days was excluded because it was not possible to calculate a reasonable orbit for this value. Thus the most likely explanation for the discrepancy is due to the two different determination methods based on different operation methods. Contrarily to the Lomb-Scargle periodogram, which is based on a Discrete Fourier Transformation (DTF) and searches for significant frequencies by splitting up the data in sine parts, the period search with the orbital fitting programme takes into account the whole data set. The orbital fit does not appear to be a pure

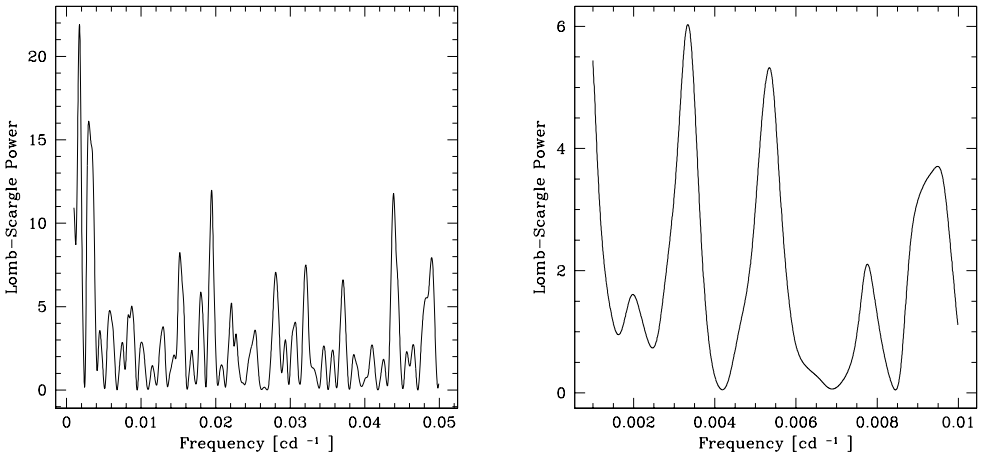

Figure 6.6: Lomb-Scargle periodogram for 11 UMa (left) including significant peaks at different frequencies. Lomb-Scargle periodogram of the RV residuals – subtraction of the 652-day period – of 11 UMa (right). There is no strong peak corresponding to a significant frequency available which would indicate a further period.

Table 6.4: Orbital parameters for the companion to 11 UMa.

P [days]	651.91 ± 7.11
$T_{periastron}$ [JD]	53469.3372 ± 5.01
K [ms^{-1}]	109.47 ± 17.12
σ(O–C) [ms^{-1}]	54.03
e	0.703 ± 0.07
ω [deg]	6.237 ± 8.96
$f(m)$ [solar masses (M$_\odot$)]	(3.190 ± 0.379) x 10^{-8}
a [AU]	1.56 ± 0.07

sine wave and a Keplerian orbit with an eccentricity of $e = 0.70 \pm 0.07$ is the most reasonable explanation for the radial velocity variations. Such a high eccentric orbit for a planet around a giant star is only known by ι Dra ($e = 0.7$). The right part of Fig. 6.7 shows the RV variations phase-folded to the orbital period.
All orbital elements are listed in Tab. 6.4.
A "minimum mass" of $m \sin i = 3.72 \pm 0.82$ M$_{Jup}$ for the substellar companion, orbiting the K giant star 11 UMa, is derived.

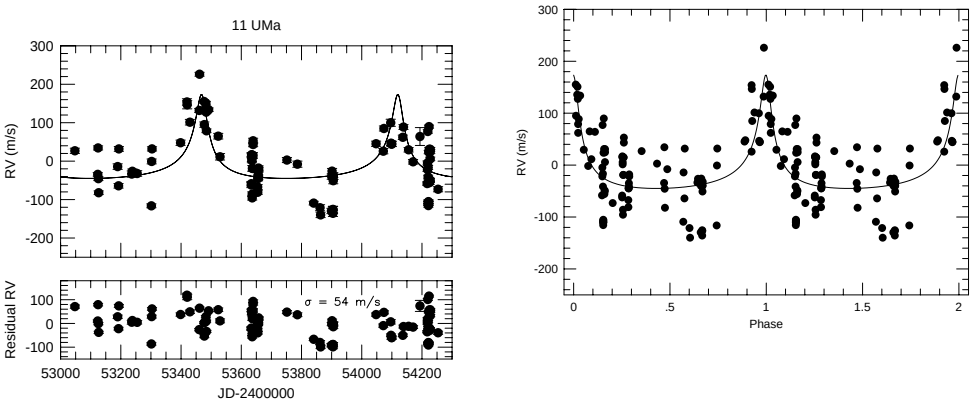

Figure 6.7: Radial velocity measurements for 11 UMa (top left). The solid line is the orbital solution. Variations in the RV residuals (lower left) in $\mathrm{m\,s^{-1}}$ are shown after subtracting the contribution of the planet (top left). Radial velocity measurements for 11 UMa phased to the orbital period (right). The line represents the orbital solution. Data from the second phase are repeated data points from the first phase to make more clear the course of the curve.

The orbital fit for the K giant 11 UMa is not entirely satisfactory because although the RV curve fits the data reasonably, there are points that differ significantly from the orbital solution. Moreover the σ(O–C) scatter about the orbital solution with a value of $\approx 54\ \mathrm{m\,s^{-1}}$, a factor of twenty larger than the typically achieved RV accuracy, is very large. This is possibly an indication for another periodic signal in the data. However, at the moment the 651.91-day period is the best orbital fit for the available data. Rotational modulation caused by surface inhomogeneities can be excluded as the cause for the RV variability because the 651.91-day period is not present in the stellar activity parameters such as *HIPPARCOS* photometry and Hα data.

To clarify this point and to check again the presence of the 334.5-day period a search for further signals was carried out for the residuals after removal of the orbital contribution due to the planetary companion (651.91 days) from the RV data. The lower panel of Fig. 6.7 (left) shows the residuals. There are RV variations but with no special frequency. This is confirmed by the Lomb-Scargle periodogram of the residuals shown in the right part of Fig. 6.6. The Lomb-Scargle periodogram shows no strong peaks.

Apart from long-term RV variations, K giants show in addition RV variations on timescales of several days and amplitudes of up to $100\ \mathrm{m\,s^{-1}}$ due to stellar oscillations. This type of RV variability could be the reason for the scatter of the points in the RV residuals. If this is the case 11 UMa would clearly be a pulsating star hosting an exoplanet. This would offer the opportunity to determine the stellar mass of the parent star by using asteroseismology and comparing the result with the value of the mass of

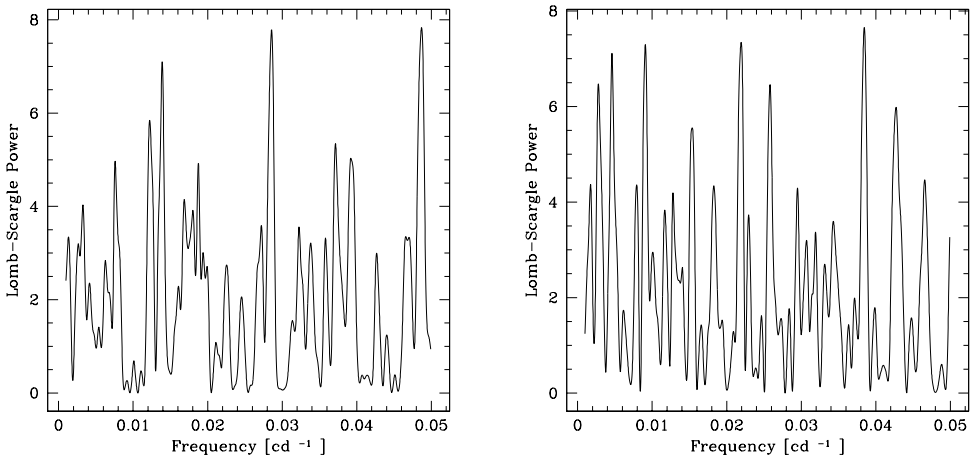

Figure 6.8: Lomb-Scargle periodogram of the *HIPPARCOS* photometry for 11 UMa (left). Lomb-Scargle periodogram of the 11 UMa Hα variations (right). There is no significant frequency detectable which would be a hint for rotational modulation.

the host star determined with the Jørgensen & Lindegren's (2005) method (see §4.4). To confirm the substellar companion and the possible additional stellar oscillation I also analysed the *HIPPARCOS* photometry of 11 UMa. The *HIPPARCOS* data contain 272 observational entries. The left part of Fig. 6.8 shows the Lomb-Scargle periodogram of the *HIPPARCOS* photometry. Variations with the 652-day period of the the planetary companion are not present and their absence excludes rotational modulation and confirms the planetary companion hypothesis. Interestingly the "highest" peak in the *HIPPARCOS* photometry, with a power of 7.8, is placed at a frequency of $0.0488\,\mathrm{c\,d^{-1}}$ corresponding to a period of $P = 20.49$ days. In general a peak with such a low scargle power is not significant. However in this case it is interesting because it could be an indication for stellar pulsations due to the fact that time analysis of the RV data revealed a comparable period of 22.75 days. In addition the periodogram of the investigated Hα activity also shows a peak with similar scargle power of 7.7 and a period of 25.95 days. Apart from this peak I found no significant frequency in the right part of Fig. 6.8. The three frequencies – RV data, *HIPPARCOS* photometry and Hα variability – are very similar and seem to indicate stellar oscillations as the reason for the RV scatter in the residuals after subtracting the orbital solution from the RV measurements. Taking into account the highly eccentric orbit and the absence of significant peaks in the stellar activity parameters at the orbital period, a substellar companion around the pulsating K giant 11 UMa is the most likely explanation for the detected RV variations. The host star 11 UMa is also metal-poor.

Table 6.5: Stellar parameters of 11 UMi

Spectral type	K4 III	
m_V	5.024 ± 0.005	[mag]
M_V	-0.366 ± 0.119	[mag]
B–V	1.395 ± 0.005	[mag]
Parallax	8.37 ± 0.46	[mas]
Distance	40.42 ± 2.22	[pc]
$M_*{}^{(a)}$	1.804 ± 0.245	[$M_\odot$]
$R_*{}^{(a)}$	24.08 ± 1.84	[$R_\odot$]
$t^{(a)}$	1.557 ± 0.538	[Gyr]
$T_{\rm eff}{}^{(a)}$	4340 ± 70	[K]
$[Fe/H]^{(a)}$	+0.037 ± 0.04	[dex]
$\log g^{(a)}$	1.6 ± 0.15	[dex]
micro turbulence$^{(a)}$	1.6 ± 0.8	[km s^{-1}]

$^{(a)}$ from my analysis

Table 6.6: Orbital parameters for the companion to 11 UMi.

P [days]	518.48 ± 4.11
$T_{periastron}$ [JD]	52854.9623 ± 29.88
K [ms^{-1}]	191.30 ± 7.15
σ(O–C) [ms^{-1}]	27.50
e	0.096 ± 0.01
ω [deg]	115.830 ± 22.66
$f(m)$ [solar masses ($M_\odot$)]	(3.708 ± 0.441) x 10^{-7}
a [AU]	1.54 ± 0.07

6.2.3 11 UMi

The parent star 11 UMi (= HD 136726 = HR 5714 = HIP 74793) is the third giant hosting a planetary companion in the Tautenburg sample. The stellar parameters of this K4 III giant star are summarized in Tab. 6.5.

A total of 52 spectra of 11 UMi were taken during my work with the iodine cell. The time series of the corresponding RV measurements is shown in the left part of Fig. 6.9.

The orbit fitted to the RV curve shows a period variation of 518.48 days with a semiamplitude of $K = 191.30$ m s^{-1}. The initial value for calculating the orbital solution was taken from the Lomb-Scargle periodogram – shown in Fig. 6.10 (left) – which reveals the existence of only one peak with an indeed significant scargle power of 23.6 at a frequency of $\nu = 0.00193$ c d^{-1} corresponding to a period of $P = 518.48$ days. The FAP of this highest peak is estimated to be $\approx 2.9 \times 10^{-9}$. Contrary to 11 UMa both derived period values fit each other very well.

The right part of Fig. 6.9 shows the RV variations phase-folded to the orbital period. An exoplanet with a "minimum mass" of $m \sin i = 11.20 \pm 2.47$ M_{Jup} orbits the K giant 11 UMi. All the orbital elements are listed in Tab. 6.6.

Fig. 6.10 (right) shows the periodogram of the residuals after the time analysis. There is no significant peak visible, which confirms the absence of further periodic

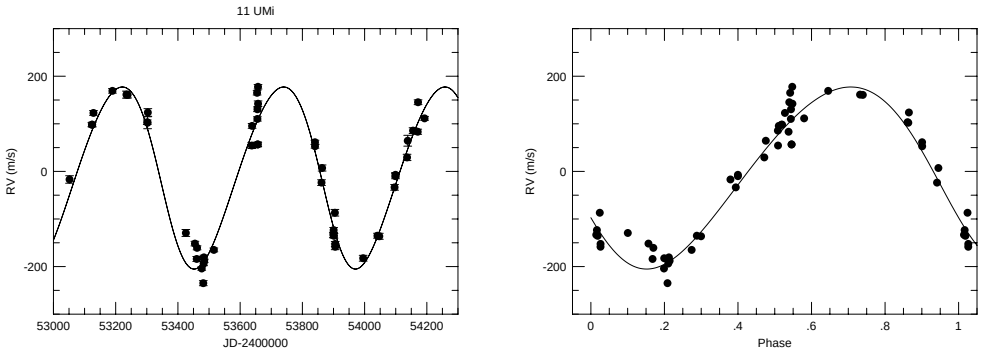

Figure 6.9: Radial velocity measurements for 11 UMi (left). The solid line is the orbital solution. Radial velocity measurements for 11 UMi phased to the orbital period (right). The line represents the orbital solution.

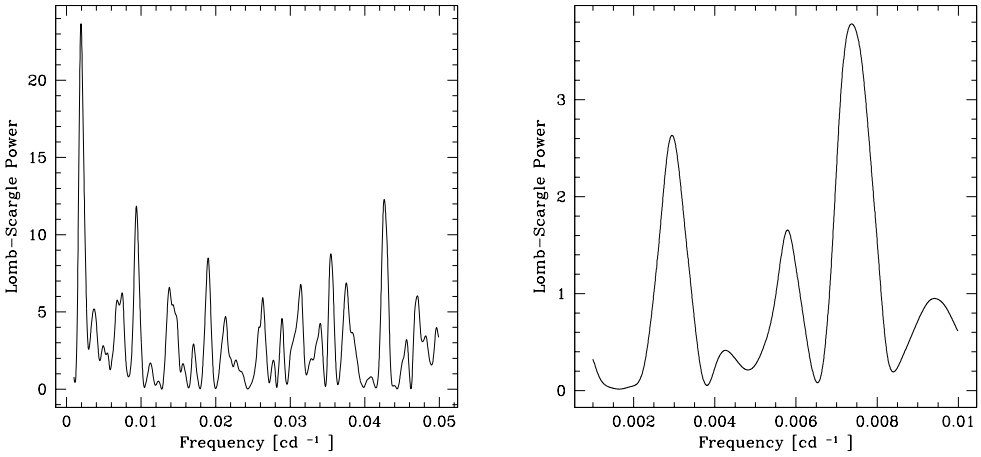

Figure 6.10: Lomb-Scargle periodogram for 11 UMi (left). It exists a very high peak with the scargle power 23.7 at a frequency $\nu = 0.00193\mathrm{c\,d}^{-1}$ corresponding to a period of 518.48 days. Lomb-Scargle periodogram of the RV residuals of 11 UMi. There is no further strong frequency in the data after substraction of the orbital period of 518.48 days.

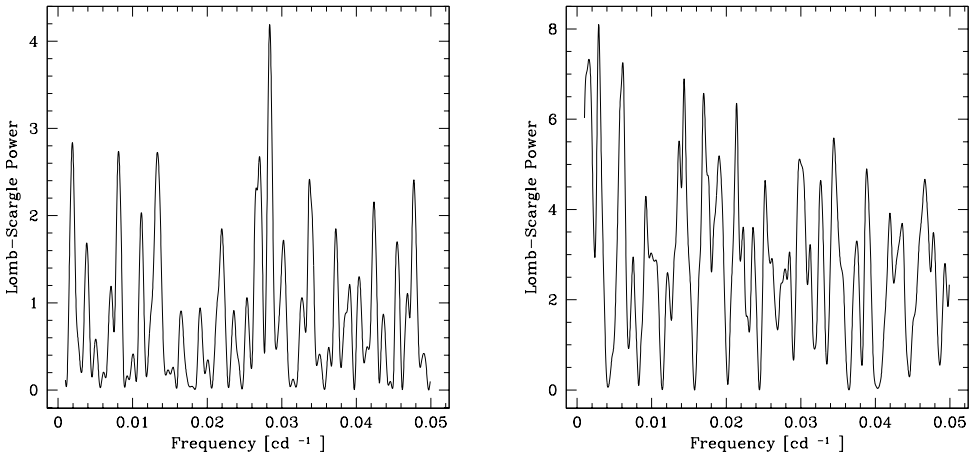

Figure 6.11: Lomb-Scargle periodogram of the *HIPPARCOS* photometry for 11 UMi (left). Lomb-Scargle periodogram of the 11 UMi Hα variations (right). There is no really significant frequency detectable which would be a hint for rotational modulation.

signals in the RV data apart from the orbital period of the planetary companion. As clearly seen in Tab. 6.6, the planetary companion of 11 UMi orbits its parent star in a nearly circular Keplerian orbit with an eccentricity of $e = 0.096 \pm 0.01$. Thus the RV curve is a pure sine wave. This behaviour is contrary to what is known from 4 UMa and 11 UMa and has consequences for the verification of the planet hypothesis. In the case of an eccentric saw-tooth shape of the RV curve, the most striking argument to confirm the exoplanet was that rotational modulation caused by stellar starspots cannot mimic this kind of curve (Frink et al. 2002). However, this argument is not valid for a circular orbit. Consequently, to confirm the planetary companion of 11 UMi, rotational modulation has to be excluded using stellar activity parameters such as *HIPPARCOS* photometry and Hα data. The Hipparcos data contain 112 observations. Both periodograms – photometry (see Fig. 6.11, left) and Hα (see Fig. 6.11, right) – show no significant peak at the orbital frequency which excludes, in combination with the good orbital fit, rotational modulation due to surface inhomogeneities such as starspots as the cause for the RV variability. A second planetary companion is also not reasonable due to the lack of frequencies in the residuals. Tab. 6.6 lists a rms scatter of 27.5 $\mathrm{m\,s^{-1}}$. Stellar oscillations are a possible explanation. In the Lomb-Scargle periodogram of the RV data a small peak appears with a scargle power of 12 at a frequency of $\nu = 0.0427\ \mathrm{c\,d^{-1}}$ corresponding to a period of 23.41 days. The period would fit pulsations and is probably confirmed by a very weak peak at a frequency of $0.0284\ \mathrm{c\,d^{-1}}$ ($P = 35.21$ days) in the *HIPPARCOS* photometry. The host star is slightly metal-rich in comparison with the other planet-hosting stars in the Tautenburg sample. But nevertheless it is also metal-poor compared to previous results of MS stars which tend to be metal-rich (Santos et al. 2004).

Table 6.7: Stellar parameters of 42 Dra

Spectral type	K1.5 III	
m_V	4.833 ± 0.005	[mag]
M_V	-0.120 ± 0.101	[mag]
B–V	1.19 ± 0.005	[mag]
Parallax	10.28 ± 0.48	[mas]
Distance	49.64 ± 2.32	[pc]
$M_*{}^{(a)}$	0.982 ± 0.059	[$M_\odot$]
$R_*{}^{(a)}$	23.10 ± 1.63	[$R_\odot$]
$t^{(a)}$	9.209 ± 1.928	[Gyr]
$T_{\rm eff}{}^{(a)}$	4200 ± 70	[K]
$[Fe/H]^{(a)}$	-0.464 ± 0.04	[dex]
$\log g^{(a)}$	1.0 ± 0.15	[dex]
micro turbulence$^{(a)}$	1.0 ± 0.8	[km s^{-1}]

$^{(a)}$ from my analysis

6.2.4 42 Dra

42 Dra (= HD 170693 = HR 6945 = HIP 90344) is another host star. It shows the classical eccentric, saw-toothed RV curve which is used as a clear argument for hosting a planetary companion. This is due to the fact that activity-related RV variations cannot mimic Keplerian motion with a high orbital eccentricity over a long timescale. The precise stellar radial velocity measurements of 42 Dra including the orbital fit are shown in the left part of Fig. 6.12. The stellar parameters of 42 Dra are summarized in Tab. 6.7.

The RV curve of the giant 42 Dra shows a period variation with a semiamplitude of $K = 112.51$ m s^{-1}.

A time series analysis using a Lomb-Scargle periodogram as shown in Fig. 6.13 (left) confirms the presence of a peak with a strong scargle power of 17.2 at a frequency of $\nu = 0.00196$ c d^{-1} ($P = 510.20$ days). This value is slightly different from the final period of 477.80 days which were calculated with the orbital fitting programme *GaussFit*. One reason for the discrepancy is already discussed in §6.2.2 for 11 UMa. However in the case of 42 Dra the period derived from the Lomb-Scargle periodogram is higher than the value derived from the orbital fitting programme. Another cause for the above mentioned discrepancy is possibly connected with the eccentricity of the planetary companion. It is possible that the orbital fitting programme delivers less accurate values for eccentric orbits in comparison to nearly circular orbits. This is probably also the case for the other exoplanets in non-circular orbits around their host stars (see §6.2.1 and §6.2.2). At the moment there is no clear explanation for the discrepancy in the case of 42 Dra. The FAP of the 510-day period is estimated to be $\approx 1.39 \times 10^{-6}$. A Keplerian orbit with an eccentricity, $e = 0.368 \pm 0.06$ is at the moment the most reasonable explanation for the RV variations.

A further peak with a scargle power of 11.6 appears at frequency $\nu = 0.05$ c d^{-1} ($P = 20$ days) in Fig. 6.13 (left). However this peak is less significant than the peak at 510.20 days. This second peak disappears after subtracting the orbital solution. Consequently it has to be an alias frequency and thus cannot possibly be real. Fig. 6.12 (right) shows the RV variations phase-folded to the orbital period. All the orbital elements are listed in Tab. 6.8.

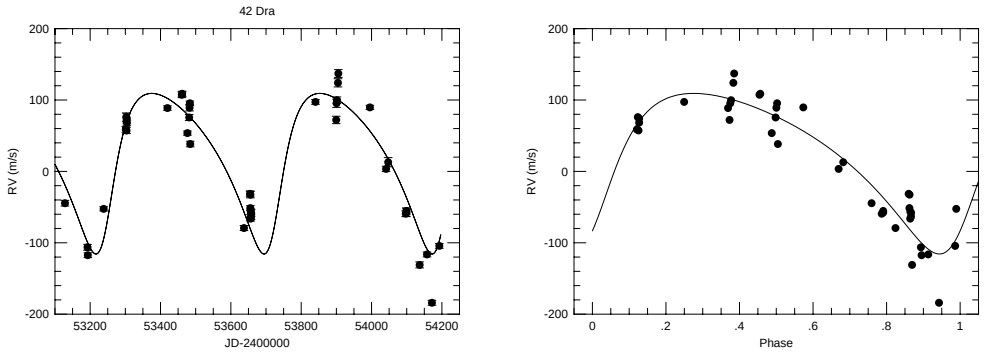

Figure 6.12: Radial velocity measurements for 42 Dra (left). The solid line is the orbital solution. Radial velocity measurements for 42 Dra phased to the orbital period (right). The line represents the orbital solution.

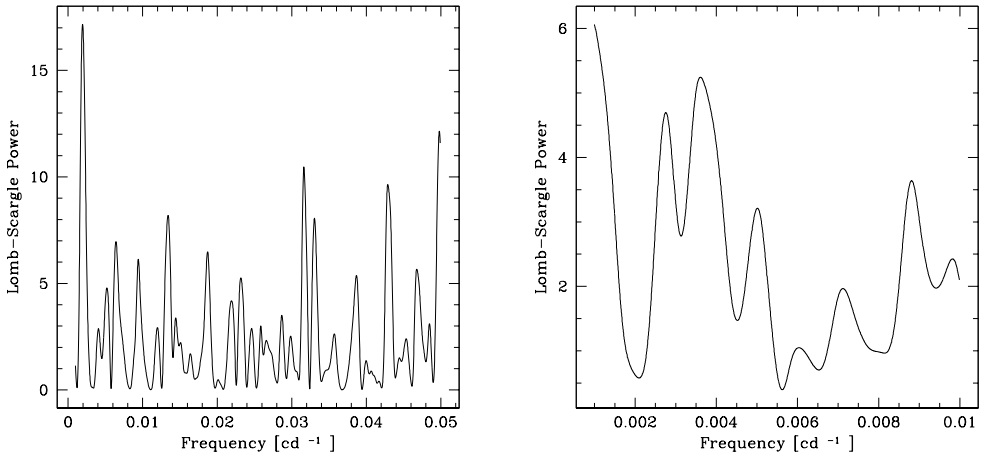

Figure 6.13: Lomb-Scargle periodogram for 42 Dra (left). There is a very high peak with the scargle power 17.2 at a frequency $\nu = 0.00196\,\mathrm{c\,d^{-1}}$ corresponding to a period of 510.20 days. Lomb-Scargle periodogram of the RV residuals of 42 Dra (right). There is no strong peak visible.

Table 6.8: Orbital parameters for the companion to 42 Dra.

P [days]	477.83 ± 6.67
$T_{periastron}$ [JD]	53721.3271 ± 15.25
K [ms^{-1}]	112.51 ± 7.60
σ(O–C) [ms^{-1}]	27.13
e	0.368 ± 0.06
ω [deg]	224.628 ± 13.12
$f(m)$ [solar masses (M$_\odot$)]	(5.668 ± 0.674) x 10^{-8}
a [AU]	1.19 ± 0.01

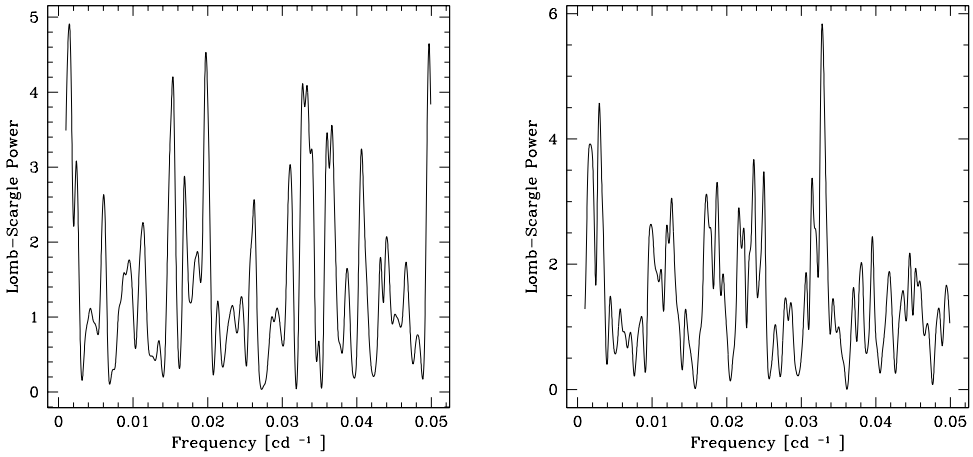

Figure 6.14: Lomb-Scargle periodogram of the *HIPPARCOS* photometry for 42 Dra (left). Lomb-Scargle periodogram of the 42 Dra Hα variations (right).

The orbital fit to the data is satisfactory. There are only very few points that differ from the orbital solution. The K giant 42 Dra hosts probably a planetary companion with a "minimum mass" of $m \sin i$ = 3.98 ± 0.87 M$_{Jup}$. Fig. 6.13 (right) shows the Lomb-Scargle periodogram of the RV residuals after removal the orbital contribution caused by the exoplanet. There are definitely no variations with a period similar to the orbital period of 477.80 days. To confirm the planetary companion I analysed the *HIPPARCOS* photometry consisting of 104 entries and the Hα activity of 42 Dra. Fig. 6.14 (left and right) show the periodogram of the photometry and the Hα activity, respectively. There is neither in the *HIPPARCOS* nor in the Hα data a significant peak at the orbital frequency visible which would be a hint for rotational modulation.

With the exception of a weak peak with the scargle power of 8 at a frequency of $\nu = 0.033\mathrm{c\,d}^{-1}$ (P = 30.30 days) there is no higher peak in the Hα data. There is a peak with a 20-day period visible in the RV periodogram. However the above mentioned peak is not visible in the *HIPPARCOS* photometry. Consequently there is no unique indication for pulsations. 42 Dra is the most metal-poor planet-hosting star of the Tautenburg survey and comparable with HD 47536 (da Silva et al. 2006) and HD 13189 (Schuler et al. 2005) as listed in Tab. 6.13.

Table 6.9: Stellar parameters of HD 32518

Spectral type	K1 III	
m_V	6.436 ± 0.005	[mag]
M_V	1.082 ± 0.199	[mag]
B–V	1.107 ± 0.005	[mag]
Parallax	8.52 ± 0.78	[mas]
Distance	41.14 ± 3.77	[pc]
$M_*{}^{(a)}$	1.133 ± 0.179	[$M_\odot$]
$R_*{}^{(a)}$	10.22 ± 0.87	[$R_\odot$]
$t^{(a)}$	5.833 ± 2.582	[Gyr]
$T_{\rm eff}{}^{(a)}$	4580 ± 70	[K]
$[Fe/H]^{(a)}$	-0.154 ± 0.04	[dex]
$\log g^{(a)}$	2.1 ± 0.15	[dex]
micro turbulence	1.2 ± 0.8	[$\mathrm{km\,s^{-1}}$]

$^{(a)}$ from my analysis

6.2.5 HD 32518

The K1 III giant HD 32518 (= HR 1636 = HIP 24003) hosts most likely a planetary companion with a "minimum mass" of $m \sin i = 3.10 \pm 0.68$ M_{Jup} in a nearly circular orbit. The stellar parameters of HD 32518 are summarized in Tab. 6.9.

The time series of the RV measurements, consisting of 52 spectra, is shown in Fig. 6.15.

The RV curve shows sinusoidal variations with a period of 156.88 days and a semi-amplitude of $K = 106.92\ \mathrm{m\,s^{-1}}$. These parameters were calculated using the orbital fitting programme *GaussFit*. As a first guess for the initial period value I took the most significant frequency appearing in the Lomb-Scargle periodogram (Fig. 6.16) of the RVs after the time analysis. In the case of HD 32518 I used the peak with the strong scargle power of 23.6 at a frequency of $\nu = 0.0064\ \mathrm{c\,d^{-1}}$ corresponding to a period of $P = 156.25$ days. The FAP of this peak is estimated to be $\approx 2.9 \times 10^{-9}$. Thus the final calculated orbital period agrees very well with the first guess derived from the periodogram.

The Keplerian orbit for HD 32518 with a slight eccentricity of $e = 0.057 \pm 0.04$ is a pure sine wave. This host star shows the most circular orbit of the whole *TLS* sample. Apart from the orbital frequency there is a weaker peak with a scargle power of 13 visible in the RV periodogram. This second peak is placed at a frequency of $\nu = 0.0499\ \mathrm{c\,d^{-1}}$ ($P = 20.04$ days) and disappears in the RV residuals. Consequently it has to be an alias frequency and thus cannot possibly be real. Fig. 6.15 (right) shows the RV variations phase-folded to the orbital period. All the orbital elements are listed in Tab. 6.10.

The orbital fit to the data is excellent. There are no points that differ from the solution. This is expressed through a small rms scatter (σ(O–C)) of 18 $\mathrm{m\,s^{-1}}$. In the case of HD 137759 (ι Dra), Frinks et al. (2002) argued that some additional scatter of the order of 10 $\mathrm{m\,s^{-1}}$ is probably instrinsic to the star. In addition the Lomb-Scargle plot (see Fig. 6.16) of the HD 32518 residuals contains no hints for a further signal with a period shorter or longer than the orbital period. In contrast to the saw-toothed RV curve, sinusoidal fits are easier mimicked by rotational modulation. Consequently I had to check very carefully *HIPPARCOS* photometry and Hα variability to confirm

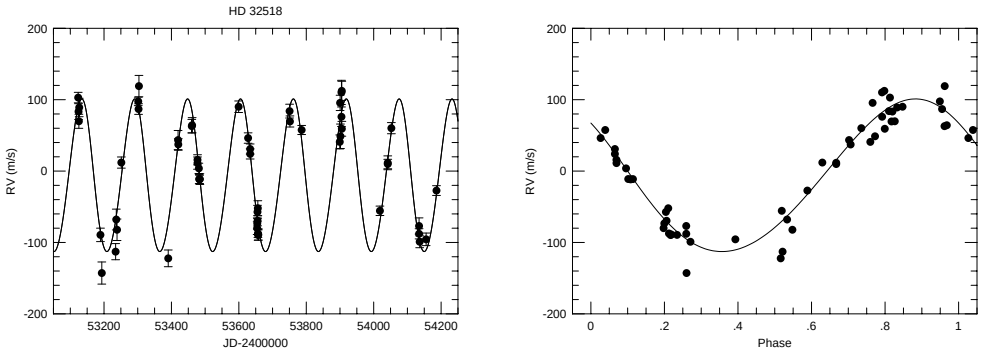

Figure 6.15: Radial velocity measurements for HD 32518 (left). The solid line is the orbital solution. Radial velocity measurements for HD 32518 phased to the orbital period (right). The line represents the orbital solution.

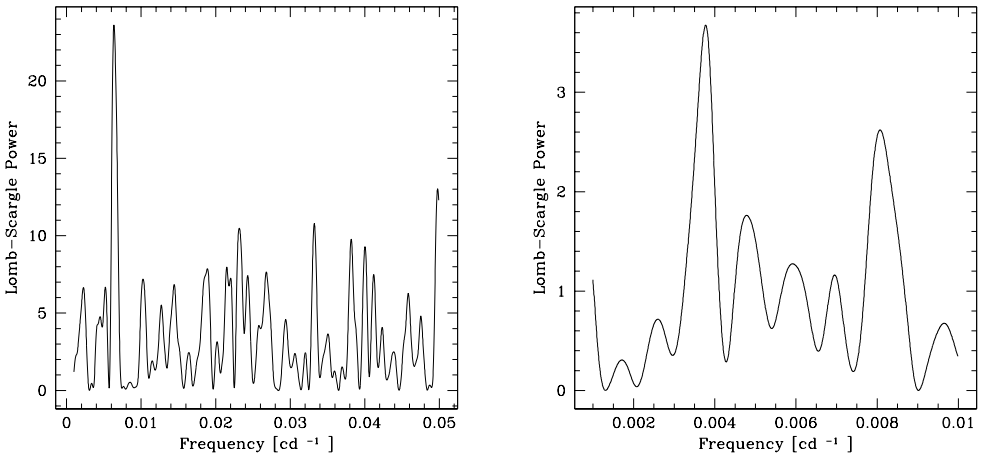

Figure 6.16: Lomb-Scargle periodogram for HD 32518 (left). It exists a very high peak with the scargle power 23.6 at a frequency $\nu = 0.0064\ \mathrm{c\,d^{-1}}$ corresponding to a period of 156.25 days. Lomb-Scargle periodogram of the RV residuals of HD32518 (right). There is no significant peak in the RV residuals.

Table 6.10: Orbital parameters for the companion to HD 32518.

P [days]	156.88 ± 0.48
$T_{periastron}$ [JD]	53623.2767 ± 13.66
K [ms^{-1}]	106.92 ± 4.06
σ(O–C) [ms^{-1}]	18.33
e	0.057 ± 0.04
ω [deg]	46.816 ± 31.99
$f(m)$ [solar masses ($M_\odot$)]	(1.976 ± 0.235) x 10^{-8}
a [AU]	0.59 ± 0.03

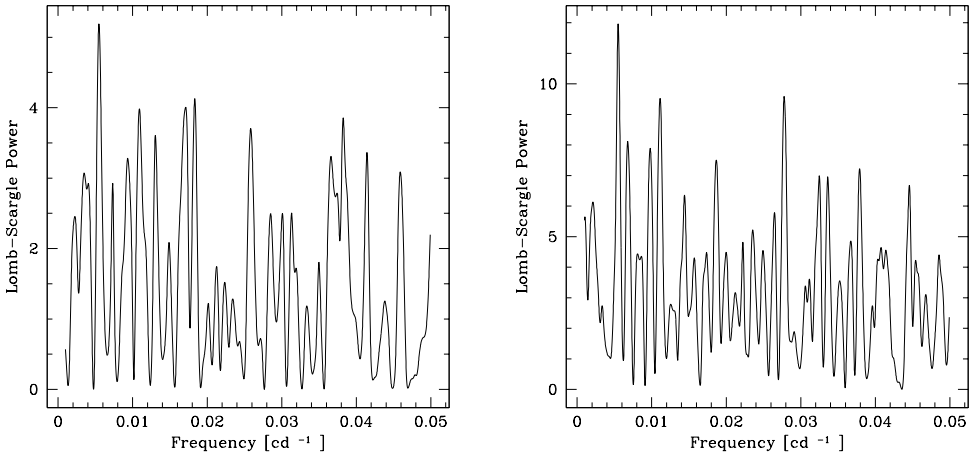

Figure 6.17: Lomb-Scargle periodogram of the *HIPPARCOS* photometry for HD 32518 (left). Lomb-Scargle periodogram of the HD 32518 Hα variations (right).

the planetary companion and to exclude rotational modulation. The *HIPPARCOS* data contain 202 entries. Fig. 6.17 (left) shows the Lomb-Scargle periodogram of the *HIPPARCOS* photometry. Although there is a very weak peak near the orbital frequency this is not significant. The highest (scargle power of 5) of the weaker peaks is at a frequency of 0.0055 c d^{-1} (P = 181.82 days).

The resulting Lomb-Scargle periodogram of the Hα variability is shown in Fig. 6.17 (right). There is no significant peak at the orbital frequency of the substellar companion. But a stronger peak with the scargle power 12 exists at a frequency of ν = 0.0055 c d^{-1} (P = 181.82 days) which is exactly the period of the above mentioned peak in the *HIPPARCOS* photometry. This is quite interesting and it is perhaps a hint for additional rotational modulation at a frequency of ν = 0.0055 c d^{-1} (P = 181.82 days) which causes the RV scatter in the orbital solution fit. The planetary companion is probably confirmed because the peak in the *HIPPARCOS* photometry at the orbital frequency is hardly visible, the significant period in the Hα variability is clearly separated from the period of the substellar companion, the RV scatter is quite small and finally the orbital solution fits very well. HD 32518 shows a slightly sub-solar Fe abundance value.

Table 6.11: Stellar parameters of HD 139357

Spectral type	K4 III	
m_V	5.977 ± 0.005	[mag]
M_V	0.550 ± 0.142	[mag]
B–V	1.198 ± 0.005	[mag]
Parallax	8.24 ± 0.54	[mas]
Distance	39.79 ± 2.61	[pc]
$M_*{}^{(a)}$	1.313 ± 0.235	[$M_\odot$]
$R_*{}^{(a)}$	11.34 ± 0.91	[$R_\odot$]
$t^{(a)}$	3.284 ± 1.614	[Gyr]
$T_{\rm eff}{}^{(a)}$	4700 ± 70	[K]
$[Fe/H]^{(a)}$	-0.128 ± 0.04	[dex]
$\log g^{(a)}$	2.9 ± 0.15	[dex]
micro turbulence$^{(a)}$	1.6 ± 0.8	[km s^{-1}]

$^{(a)}$ from my analysis

Table 6.12: Orbital parameters for the companion to HD 139357.

P [days]	1151.44 ± 24.94
$T_{periastron}$ [JD]	52442.1560 ±
K [ms^{-1}]	159.88 ± 3.45
σ(O–C) [ms^{-1}]	14.26
e	0.128 ± 0.04
ω [deg]	235.373 ± 9.15
$f(m)$ [solar masses ($M_\odot$)]	(4.756 ± 0.565) x 10^{-7}
a [AU]	2.36 ± 0.02

6.2.6 HD 139357

Another exoplanet orbits the slightly metal-poor giant HD 139357 (= HR 5811 = HIP 76311) with the longest period of all Tautenburg host star candidates. The stellar parameters of this star are summarized in Tab. 6.11. The time series (39 spectra) of the RV measurements for HD 139357 is shown in Fig. 6.18 (left).

The radial velocity data reveal a long-term sinusoidal variation in the RV curve with a very long period variation of 1151.44 days. This value is very close to my observing window, which is dangerous due to aliasing (see §6.1.1). Thus further data points are essential to confirm this preliminary result. For the initial stage of orbital fitting an analysis of the Lomb-Scargle periodogram, which delivers the presence of a high scargle power of 18.5 at a frequency of $\nu = 0.0009\mathrm{c\,d^{-1}}$ ($P = 1111.11$ days), was investigated. The FAP of this peak has the value 3.6×10^{-7}. A Keplerian orbit with an eccentricity of $e = 0.13 \pm 0.04$ is the most likely explanation for the RV variability. Fig. 6.18 (right) shows the RV variations phase-folded to the orbital period. The mass function (see Tab. 6.12) delivers a "minimum mass" of $m \sin i = 9.85 \pm 2.17$ M_{Jup} of the substellar companion. The cause of the discrepancy of both derived periods is discussed in §6.2.2. All the orbital elements are listed in Tab. 6.12.

The orbital fit to the data is good resulting in a very low rms scatter of 14 m s^{-1}. Fig. 6.19 exhibits the Lomb-Scargle periodogram of the RV residuals after removal of

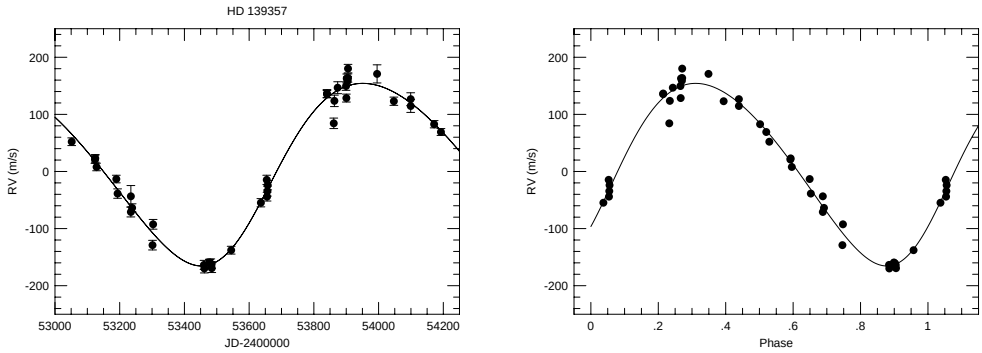

Figure 6.18: Radial velocity measurements for HD 139357 (left). The solid line is the orbital solution. Radial velocity measurements for HD 139357 phased to the orbital period (right).

the orbital contribution due to the exoplanet. No periodic signals are present.

To confirm the planetary companion I searched for significant frequencies in the 106 data points of the *HIPPARCOS* photometry. Fig. 6.20 shows the Lomb-Scargle periodogram of the photometry after calculating the periodogram. There is no peak near the orbital frequency. The highest peak is very weak and it is located at a frequency of 0.0423 c d^{-1} ($P = 23.65$ days).

I also checked the Hα variations (see Fig. 6.20) in the course of time to investigate whether the orbital frequency of the exoplanet is visible in the data. This is not the case. Finally, apart from the confirmed exoplanet, the Hα data show a weak peak at a frequency of 0.0371 c d^{-1} corresponding to a period of $P = 26.98$ days. A similar period with a weak peak is also visible in the *HIPPARCOS* photometry which is possibly an indication that there is rotational modulation or stellar oscillation at this frequency.

It is interesting that a weak peak at more or less the same period of $P = 25$–28 days very often appears in the Lomb-Scargle periodograms of the *HIPPARCOS* data. The cause for this phenomenon is still unexplained. Coincidence is a possibility. However instrumental effects or just plain noise also cannot be excluded.

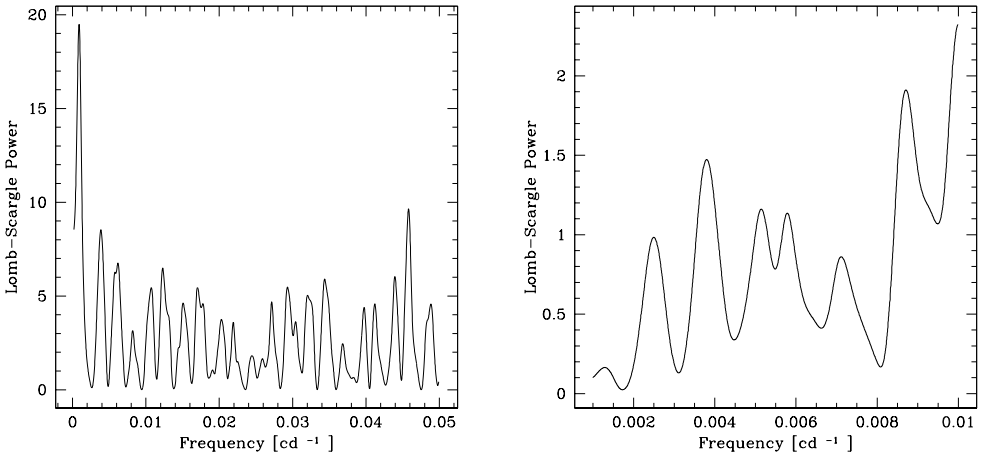

Figure 6.19: Lomb-Scargle periodogram of HD 139357 (left). Lomb-Scargle periodogram of the RV residuals of HD 139357 (right). There in no significant peak in the RV residuals which would be a hint for a second planetary companion.

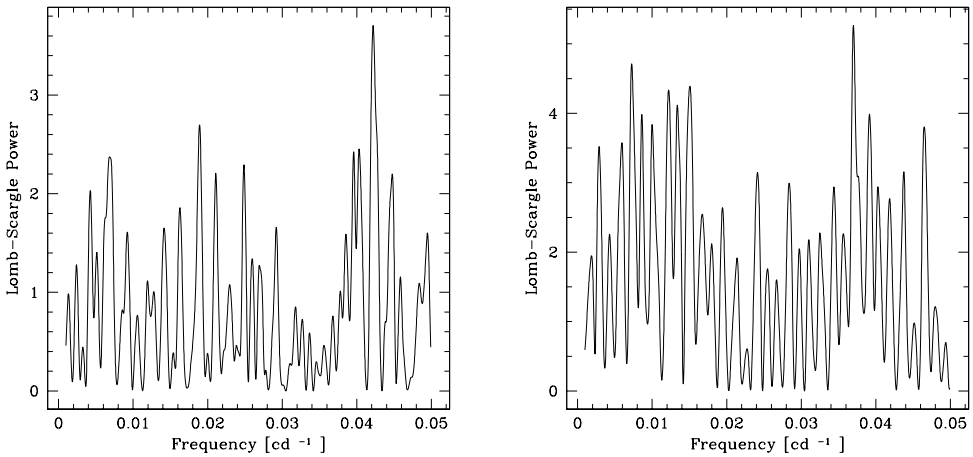

Figure 6.20: Lomb-Scargle periodogram of the *HIPPARCOS* photometry for HD 139357 (left). Lomb-Scargle periodogram of the Hα variations for HD 139357 (right).

Table 6.13: Properties of exoplanets around giants in the literature.

HD	M_* [$M_\odot$]	$m \sin i$ [M_{Jup}]	a [AU]	P [days]	e	$[Fe/H]$ [dex]	t [Gyr]
137759	1.1	8.8	1.3	511	0.71	+0.03	
	1.4 ± 0.2					+0.15	3.2 ± 1.4
104985	1.5	6.3	0.8	198	0.03	-0.35	2.95 ± 0.65
	1.1 ± 0.2					-0.32	5.1 ± 2.5
122430	1.4 ± 0.3	3.7	1.0	345	0.68	-0.05	3.1 ± 1.7
219449		2.9	0.3	182		-0.09	
	1.5 ± 0.3					+0.07	2.5 ± 1.2
59686		5.3	0.9	303	0		
	2.1 ± 0.3					+0.20	1.1 ± 0.4
54719		18.1		305			
163917		21.9		536			
11977	1.9 ± 0.3	6.5	1.9	711	0.4	-0.21	1.3 ± 0.5
47536	0.9 ± 0.1	5.0	1.6	712	0.2	-0.68	9.3 ± 1.9
13189	4.5 ± 2.5	14	1.8	471	0.27	-0.59	
	1.2 ± 0.3					-0.58	4.5 ± 4.0
62509	1.96 ± 0.2	2.3	2.4	590	0.02	-0.07	1.19 ± 0.32
28305	2.7 ± 0.1	7.6	1.9	594	0.15	+0.17	0.63 ± 0.05
17092	2.3 ± 0.3	4.6	1.29	359.9	0.17	+0.18	
167042	1.64 ± 0.13	1.6	1.3	416	0.03	+0.05	2.2 ± 1.0

6.3 Properties of the extrasolar planet systems

General results derived from my precise stellar radial velocity measurements for the *TLS* stars and presented in this chapter were published in the article "Testing planet formation theories with Giant stars" (Pasquini et al. 2008). Parts of the text and figures of this chapter have been taken from this publication. Tab. 6.13 contains the stellar and orbital parameters of giants hosting exoplanets published in the literature. In the case of the two values listed, both values were mentioned in the previous papers and are included in my summary. The parameters of the extrasolar planet systems – parent star and planetary companion – discovered during the Tautenburg survey are listed in Tab. 6.14 to enable a direct comparison.

Bearing in mind the very limited sample of planet-hosting giant stars and con-

Table 6.14: Properties of exoplanets around *TLS* K giants.

HD	M_* [$M_\odot$]	$m \sin i$ [M_{Jup}]	a [AU]	P [days]	e	$[Fe/H]$ [dex]	t [Gyr]
32518	1.13 ± 0.18	3.10	0.59	156.88	0.057	-0.15	5.83 ± 2.58
73108	1.23 ± 0.15	7.20	0.88	271.90	0.424	-0.25	4.60 ± 2.00
77800	1.18 ± 0.20	3.72	1.56	651.91	0.703	-0.25	4.88 ± 2.33
136726	1.80 ± 0.25	11.20	1.54	518.48	0.096	+0.04	1.56 ± 0.54
139357	1.31 ± 0.24	9.85	2.36	1151.44	0.128	-0.13	3.28 ± 1.61
170693	0.98 ± 0.06	3.98	1.19	477.83	0.368	-0.46	9.21 ± 1.93

sidering that not all planetary parameters are known, I work towards the following conclusions especially with respect to the large amount of planets orbiting solar-type stars:

- There is a difference in the metal distribution of MS and evolved planet host stars. Evolved stars are 0.2–0.3 dex more metal-poor than MS parent stars. Interestingly, this difference is similar to that present between planet-hosting and non planet-hosting MS stars.

- The semi-major axes of planets orbiting MS stars range in general from very small (0.05 AU) to 3 AU. However around 1 % of the studied MS stars (Marcy et al. 2004; Jones et al. 2004) have extrasolar gas giant planets with orbital periods of days, placing these so-called "hot Jupiters" within 0.1 AU of their host stars. Apart from "hot Jupiters" 5–10 % of the MS stars harbour exoplanets according to Fischer & Valenti (2005). If it is 5 % then my sample has 2 × the frequency which would support the hypothesis that more massive stars tend to have more massive planets. If it is 10 % then it is the same. In both cases the percentage of "hot Jupiters", which do not exist around giant host stars but would in principle increase the percentage of exoplanets, is not taken into account.

- Contrary to MS stars giants do not possess short-period planets. This is quite expected since these stars have radii typically as large as $R_{\odot}$, therefore short-period planets, particularly "hot Jupiters", would be swallowed up by the stellar envelopes of the stars (see §1). We note that the short-period RV variations in giants may mask the detection of possible short-period planetary companions that may still reside outside the photosphere of the host star. These would have orbital periods of many days, or similar to the periods for stellar oscillations. Such variability if found by RV surveys may be dismissed as due to stellar oscillations rather than a short-period companion (Pasquini et al. 2008). The corresponding large stellar radius results in minimum possible orbital periods of the order of 100 days or slightly less (Galland et al. 2005a). Indeed the shortest period for a planet around a giant is of 198 days for HD104985 (Sato et al. 2003). During my work it turned out that the K giant star HD 32518 hosts a giant planet with an even shorter orbital period of 155 days.

- 6 stars (10 %) of the Tautenburg sample show low-amplitude, long-term radial velocity variations possibly due to planetary companions which is in very good agreement with the southern *FEROS* study from Setiawan et al. (2004a). To determine the frequency of planets around evolved stars I had to take into account that my survey is biased against Saturn mass planets due to the insufficient accuracy of the radial velocity method.

- The companions to ι Dra and 11 UMa have the highest eccentricities ($e = 0.7$) for planets around giant stars. Relatively high eccentricities were also found for the companions to HD 11977 ($e = 0.4$, Setiawan et al. 2005), 4 UMa ($e = 0.42$, Döllinger et al. 2007) and HD 13189 ($e = 0.27$, Hatzes et al. 2006). The values for the eccentricities of this work also show more circular orbits in addition to high eccentricities. It seems that the planetary companions to giant stars can have the wide range of orbital eccentricities (nearly circular and highly eccentric) that are shown by planets orbiting solar-type MS stars (Fig. 6.21). It seems therefore that eccentricity is not affected by the stellar characteristics such as the mass (Pasquini et al. 2008).

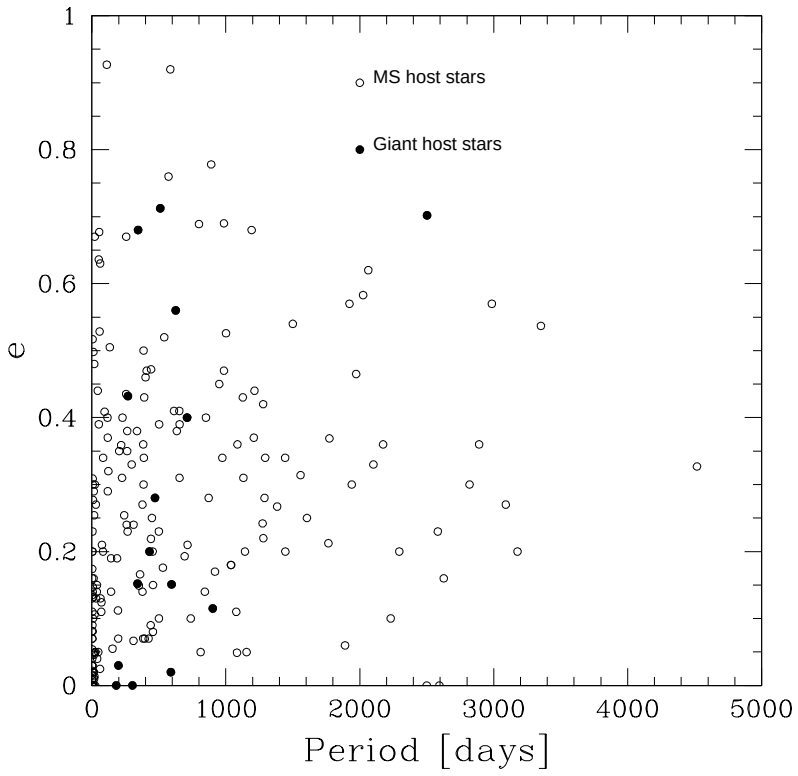

Figure 6.21: Distribution of eccentricities.

- The masses of my sample stars were determined from spectroscopic stellar parameters using the method of Jørgensen & Lindegren (2005). The mass range of my planet host stars is restricted to 1 to 1.8 $M_{\odot}$. The mean of my sample is about 1.2 $M_{\odot}$. The estimated masses for published giant stars hosting planets range from 1 to 3 $M_{\odot}$. Thus giants probe a slightly different mass regime in contrast to MS parent stars (see Fig. 6.22, top and lower right) and Fig. 7.2 (lower right).

  The "minimum masses" of the planetary companions around giant stars occupy the range of 2–14 M_{Jup} (see Fig. 6.22, top right) and orbital periods of several hundred days (Hatzes et al. 2006). Planet "minimum masses" for giants are typically larger than what has been observed around MS stars. This is in accordance with results of Johnson et al. (2007a), based on their search for planets around retired A stars. They discovered that massive stars are more likely to harbour Jupiter-sized planets than lower-mass stars. This result is in agreement with the core accretion theory because it is expected that massive stars have larger planets, possibly due to the larger material content in their disks during the early formation time. Fig. 6.22 (lower right) shows the planet mass distribution for MS stars with masses below 1.1 $M_{\odot}$ while Fig. 6.22 (top right) is the same but for stars (mostly giants) with masses larger than 1.1 $M_{\odot}$. Clearly the distribution of planet "minimum masses" for low-mass MS stars increases towards

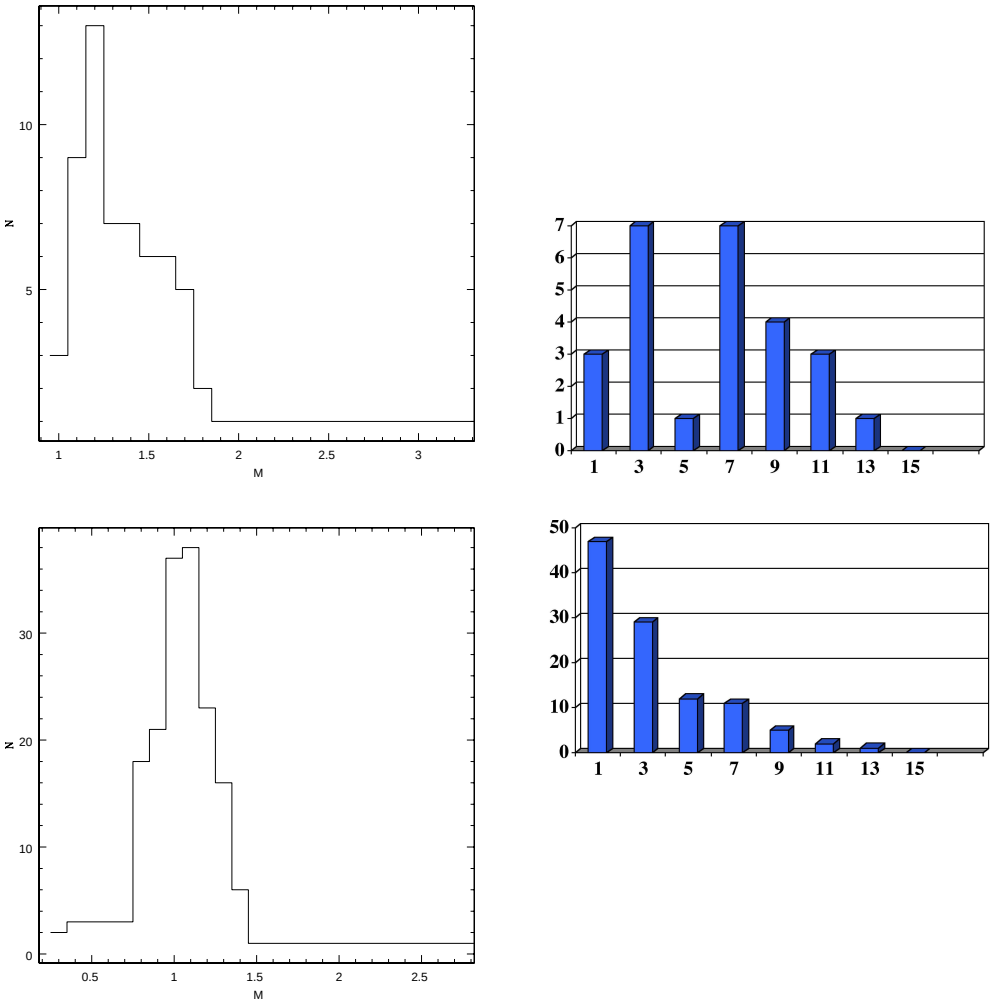

Figure 6.22: Mass distribution of the TLS host stars (top left). Mass distribution of the MS host stars (lower left). In both plots the number of stars N is plotted against the stellar mass M in $M_{\odot}$. Mass distribution of the planets around stars with masses above 1.1 $M_{\odot}$ (dominated by giants) and for stars with smaller masses (top right). The distribution is clearly different, with more massive stars showing a very high frequency of massive planets (Pasquini et al. 2008). Mass distribution of the planets around stars with masses below 1.1 $M_{\odot}$ (lower right) showing the strong increase for small planet mass (Pasquini et al. 2008). In the two plots on the right side the number of planets N is plotted against the planetary mass in M_{Jup}.

lower mass planets, and it is definitely different from the one of more massive stars. Of course we know that there are biases in the giants' sample, in that small "minimum mass" planets are presently out of reach of surveys due to their limited precision and to the intrinsic variability of the stars. Nevertheless, if we assume that the difference between the two distributions is due to observational biases and the distribution was the same as with low-mass stars, the plots of Fig. 6.22 (top and lower right) would imply an extremely high planet occurrence for massive stars (Pasquini et al. 2008).

- According to Fischer & Valenti (2005) the "minimum mass" of detected planets rises with increasing metallicity, suggesting that the total amount of disk material ultimately locked up in the form of planets may be regulated by stellar metallicity. This tendency was derived taking into account only a very small number of gas giant planets around metal-poor stars. In the meantime an enlarged sample of metal-poor host stars was detected. A further tendency, derived from studies on stars with low masses, announced by Ida and Lin (2005) is that more massive stars host more massive planets. My results from the Tautenburg survey confirm the second but not the first trend (Pasquini et al. 2008).

- Fischer & Valenti (2005) found no correlation between metallicity and orbital period or eccentricity. In all cases, the host stars tend to have high metallicity.

- There exist MS host stars, possibly progenitor systems of my host stars, which show similar periods P as my giant parent stars. The b after the HD number indicates the planetary companion. The data are taken from "The extrasolar planets encyclopaedia" arranged by Jean Schneider and available on the webpage http://exoplanet.eu/.

Table 6.15: MS host stars with similar periods P.

HD	P [days]	Spec. Type
208487 b	123	G2 V
231701 b	141.6	F8 V
93083 b	143.58	K3 V
37124 b	154.46	G4 V
202206 b	255.87	G6 V
89744 b	256.61	F7 V
134987 b	260	G5 V
12661 b	263.6	G6 V
40979 b	267.2	F8 V
221287 b	456.1	F7 V
125612 b	502	G3 V
4113 b	526.62	G5 V
114729 b	1131.48	G3 V
111232 b	1143	G8 V
164922 b	1155	K0 V

Chapter 7

Relations between age, mass and metallicity

The scope of this chapter is to investigate whether giant host stars show particular features in contrast to non planet-hosting giant stars and to Main Sequence (MS) stars with and without planets. I will concentrate on the so-called Age-Metallicity Relation (AMR) and Mass-Metallicity Relation (MMR). Both plots show possible correlations of stellar age and mass of a star with metallicity. I intend to examine closely the comparability of an AMR – if such a relation is present for giants – with corresponding results derived from previous dwarf surveys. Furthermore I will investigate whether parent giants and non planet-hosting giant stars show differences in stellar parameters such as age, metallicity and mass. I will compare the results for giants with those published for MS stars. Results discovered during my PhD and presented in this chapter were published in the article "Evolved stars hint to an external origin of enhanced metallicity in planet-hosting stars" (Pasquini et al. 2007). Parts of the text and figures of this chapter have been taken from this publication.

7.1 Age-metallicity relation

The presence of an age-metallicity relation in the solar neighbourhood is still under debate. I shall therefore firstly give a short overview of the different results derived from previous unbiased and volume-limited dwarf surveys. Twarog (1980) was the first to establish an AMR. Edvardsson et al. (1993) also found hints for an AMR which agrees well with Twarog's AMR. Bensby et al. (2004) and Freeman & Bland-Hawthor (2002) investigated the existence of an AMR in the thick and thin disk respectively. The first author found indications for an AMR in the thick disk but for the thin disk Freeman & Bland-Hawthorn (2002) found no evidences for an AMR. As far as old metal-rich stars are concerned, Reddy et al. (2003) also found clear hints for an AMR as well as Gonzalez et al. (1997). Other authors who discussed the possibility of an AMR are Carraro et al. (1998), Feltzing et al. (2001) and Nordström et al. (2004). These three authors published a large dispersion of Fe abundances within all ages which is not the case for the *TLS* and *FEROS* (Fiber-fed Extended Range Optical Spectrograph) survey stars. Moreover Feltzing et al. (2001) and Nordström et al. (2004) found only a few indications of an AMR amongst late-type stars in the neighbourhood of the Sun. The latter study is by far the most complete, using 14,000 dwarfs with accurate

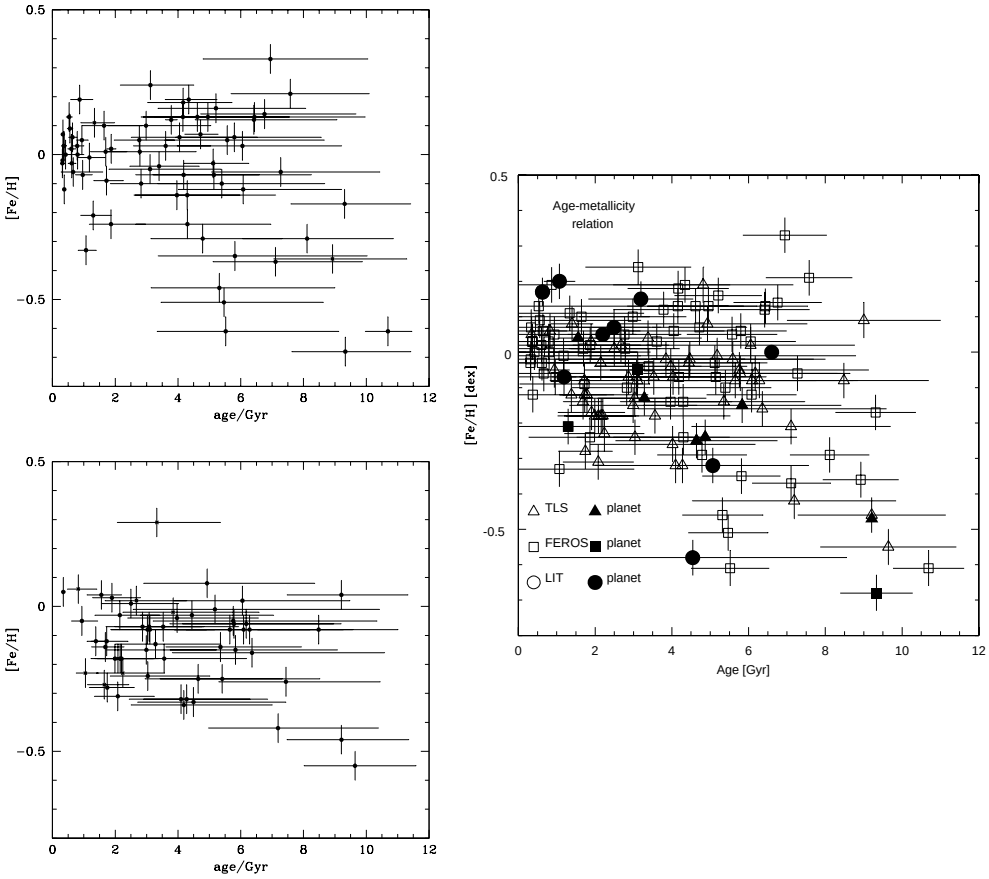

Figure 7.1: The age-metallicity relations for the *FEROS* (top left, da Silva et al. (2006)), *TLS* (lower left) and the combined (right) giant samples. The Fe abundance is in dex.

HIPPARCOS parallaxes. In contrast to these two authors, Rocha-Pinto et al. (2000) found more evidence of a relationship between age and metallicity. Da Silva et al. (2006) derived an AMR from our southern *FEROS* survey using for the first time giants. Adding my selected Tautenburg stars to the *FEROS* sample (Setiawan et al. 2004a) I have now the possiblity to confirm these first indications using an extended sample of around 130 G–K giants in both hemispheres. I found separate evidence of an AMR in the *TLS* as well as in the extended giant sample despite the limited number of sample stars. The age-metallicity relations for the *FEROS* (top left), *TLS* (lower left) and the combined (right) giant samples are shown in Fig. 7.1.

The age-metallicity relation is visible in the plot: young stars are on average more metal-rich than older stars which show lower metallicity values. There is only a small spread in metallicity visible among the youngest stars, which increases with age. A part of the larger scatter at older ages is possibly caused by the age determination method. A further explanation of the larger scatter at higher ages is perhaps migration: old stars were not born in the solar neighbourhood and had the time to migrate from the place where they were born, with possibly different metal abundances, to the solar neigh-

bourhood. Their existence is possibly a hint that a simple ("closed-box") model cannot account for the chemical evolution of open systems like the disk, where gas inflow from external regions seems to have occurred. Thus the interpretation of the AMR result indicates that stars in the solar neighbourhood are formed from interstellar matter of quite homogeneous chemical composition. Observing older stars, stars born in different Galactic locations were sampled and hence a more complex mixture of chemical composition is seen according to da Silva et al. (2006). Therefore the AMR in the solar neighbourhood can be used to derive fundamental informations about the chemical evolution of the disk of the Milky Way with time and to constrain evolutionary models of our Galaxy including its chemical enrichment. Our results are interesting, but not definitive. In fact the sample is limited in size and in selection. For instance it is not volume-limited and some selection biases are present in the Tautenburg sample, which do not include the youngest stars in the top part of the Colour-Magnitude-Diagram (CMD) as well as all stars at the lower of the Red Giant Branch (RGB). As a consequence, young metal-rich and old metal-poor stars are not favoured. Most interesting is that the distribution of planet host giants in the TLS and $FEROS$ survey follow the general giants' distribution, as can be seen in the right panel of Fig. 7.1, which shows the combined age-metallicity distribution provided by the 130 giants analyzed by da Silva et al. 2006 and during my work (Döllinger et al. 2008b). There are no stars with an age > 10 Gyr and super-solar metallicity in the plot.
As mentioned above, the TLS sample contains no stars younger than 1 Gyr. Consequently the AMR plot shows no planet entries in this portion. In the upper right part of the AMR plot there are also non planet-hosting stars located. A possible explanation for the absence of extrasolar planetary companions in both regions is a poor statistic because a reduced number of target stars decreases the probability to detect planets. Thus there seems to be no difference in the AMR between non planet-hosting, i.e. stars for which exoplanets are not yet found but their existence cannot be strictly excluded, and planet host stars. Clearly, with just a few planet candidates this is just a hint. But it would imply that the probability of forming giant planets is independent of age and metallicity.

7.2 Mass-metallicity relation

The topic of this section is to investigate whether giants hosting an exoplanet show different behaviour to non planet-hosting giants in the mass-metallicity relation plot. This figure arises by plotting the mass and the metallicity of the star against each other. An MMR plot was created for both surveys separately as well as for the combined southern and northern giant sample. The corresponding plots are shown in Fig. 7.2. The combined MMR plot (see Fig. 7.2, top right) displays a lack of planetary companions in two regions: stellar mass lower than 1 $M_\odot$ and greater than 2 $M_\odot$. The same feature was also visible in the corresponding values of the AMR plot. The most likely reason for this absence of exoplanets is again probably due to the reduced number of data points in both areas and can possibly confirmed by a short calculation. The MMR is provided by 130 stars. Around 117 stars are contained in the mass range of 1 $M_\odot < M < 2$ $M_\odot$. If 10 % of these stars have planets then I should find at least 12 planets. I found 9 planetary companions which is too less. This number can be increased to 17 by including planets from the literature. However this number is then higher as the calculated one. But this is reasonable because I did not take into account the whole amount of literature sample stars, which is definitely higher as 130

but unfortunately not available for the surveys in which the literature planets were observed. For stars with $M > 2.5$ $M_\odot$ I have only 13 stars. 10 % of 13 is 1. This means I should find at least 1 planet. But I found 0 and so with my small number statistics I cannot make any conclusions. However there is one planet published in the literature for this mass range. I think for the low mass end the same argument can be applied. However the absence of planets could be also really a first indication of a different mass threshold or formation scenario. Recent works have suggested that planetary formation frequency depends on the mass of the host stars with more massive stars being more frequent than low-mass stars (Johnson et al. 2007a). But the last explanation is speculative at this stage. I shall now compare the mass-metallicity plots of both samples. The mass-metallicity plots show the obvious trend that giants with lower metallicity ([Fe/H] $\leq$ -0.4) are only present among stars with the lowest masses. In contrast to the southern sample, my TLS stars are concentrated in the metallicity between [Fe/H] $\geq$ -0.4 and mean solar metallicity with the corresponding mass range 1–2 $M_\odot$, and only a few stars with masses over 2 $M_\odot$ are present, which is caused by the paucity of massive young giants.

A modified version of the MMR plot – including all the published MS host stars – is presented in Fig. 7.2 down to the right. This plot shows with different symbols that there is a slightly shifted mass range covered by the two types of host stars – MS and giants. MS parent stars from the literature are indicated with empty pentagons. The TLS planet-hosting giants are tagged with filled triangles and the $FEROS$ host giant stars are indicates with filled squares. Giants hosting planets taken from the literature are tagged with filled dots. Giants have, on average, a slightly larger mass than the MS stars surveyed for planet search. In detail the masses of giant stars hosting planets range from 0.9 to 3 $M_\odot$ (da Silva et al. 2006; Döllinger et al. 2008b) while in contrast those of MS stars are between $\sim$ 0.75 and $\sim$ 1.5 $M_\odot$. Thus giants really offer the opportunity to study the evolution of planet formation with stellar mass and metallicity beyond what is possible with MS stars.

7.3 Metallicity in MS and giant planet-hosting stars

Before dealing with the metallicity of giant planet-hosting stars I shall give a short summary of the results which have been published so far for MS stars concerning the metallicity. The search for extrasolar planets using the radial velocity method has focused so far on solar-type stars. In the course of these surveys – since the discovery of the first extrasolar planet 51 Peg (Mayor & Queloz 1995) – it turned out that the planet-hosting MS stars tended to be metal-rich compared with stars that do not possess exoplanets. In other words there are hints that giant planets favour metal-rich solar-type stars (Gonzalez 1997, 1998, 2001; Santos et al. 2000, 2001, 2003, 2004; Fischer & Valenti 2005). This behaviour has been confirmed by detailed investigations (Santos et al. 2004; 2005) and has proved not to be caused by spurious selection effects due to the fact that the most important planet search programmes make use of volume-limited samples of stars (Udry et al. 2000; Marcy et al. 2000). Comparing the planet host stars distribution with that of field stars, Santos et al. (2004) verified that planet-hosting MS stars are on average about 0.25 dex more metal-rich than their counterparts (Santos et al. 2004; 2005). According to Fischer & Valenti (2005) as well as Santos et al. (2005) the occurrence of gas giant planets rises from a few per cent at solar metallicity to more than 20 % for stars with twice the metal content of the Sun. From this result, Fischer & Valenti (2005) derived their so-called “Planet-Metallicity

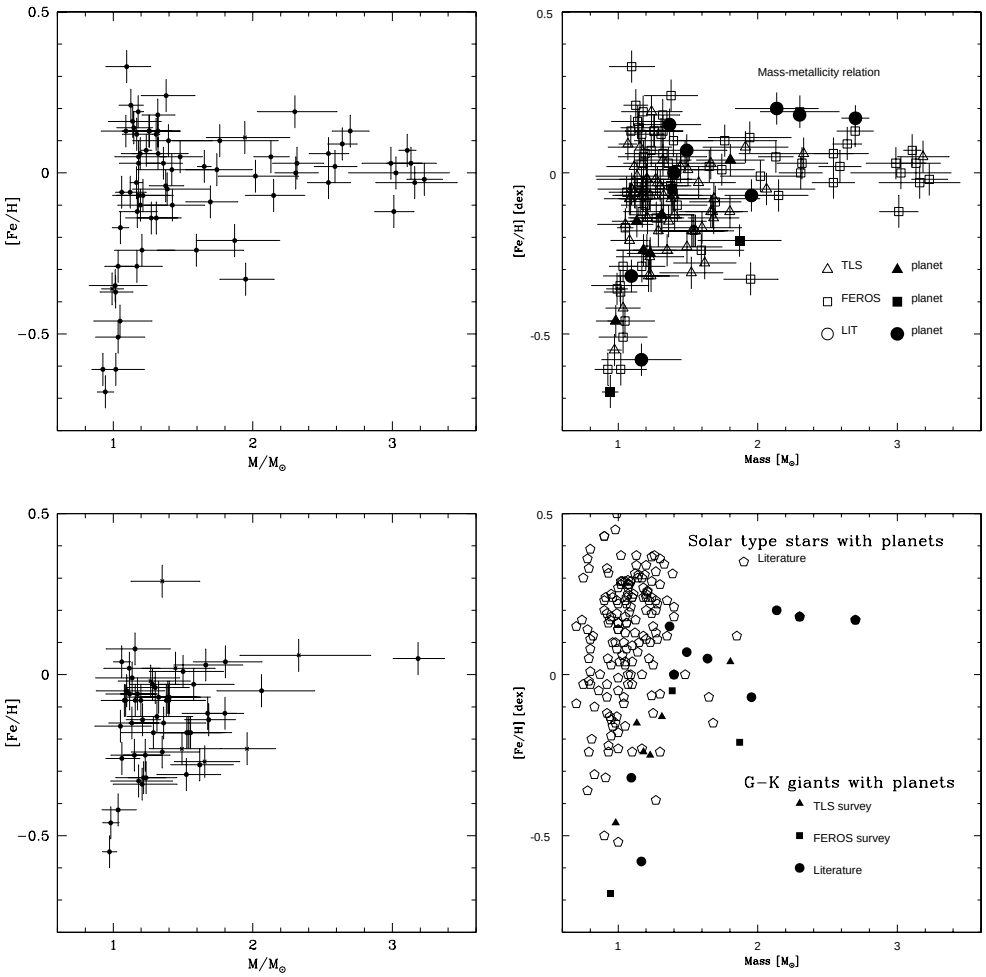

Figure 7.2: The mass-metallicity relations for the *FEROS* (top left, da Silva et al. (2006)) and the *TLS* survey (lower left). The combined MMR of both samples and additional giant host stars from the literature is presented top to the right. The host stars are indicated with filled symbols. The mass-metallicity relation for giant host stars (top right) is also shown in constrast to solar-type parent stars from the literature (lower right). The Fe abundance is in dex.

Correlation" which expresses the probability of formation of a gas giant planet as a function of metallicity.
This was the status a few years ago until several groups – including my own TLS study – started surveys of evolved stars (Setiawan et al. 2003a, 2004a; Sato et al. 2007; Döllinger et al. 2007) because the data published so far for other types of stars – especially giants – were so few and far between and inhibit thus any further analysis and conclusion. After around 3 years of observations and data reduction, the chemical abundance analysis for the Tautenburg planet hosting K giants reveals metal-poor values for the 6 planet-hosting candidates of the TLS sample which corresponds to a 10 % planet occurrence. This is an interesting result because it is in contrast to what is known from the study of planet-hosting MS stars. The number of confirmed exoplanets derived from my TLS survey accounts for more than half of all detected exoplanets around giant stars. However in the literature there are hints from other authors (Schuler et al. 2005; da Silva et al. 2006) who also confirm that planet-hosting giants are metal-poor. To evaluate a comparability between MS and giant host stars I shall investigate the survey conditions of MS and giant stars which are not always exactly the same. The TLS giant survey is not explicitly biased towards metal-rich stars, while the search for planets around MS stars possibly is (Fischer et al. 2005). In addition, giant stars do not possess short-period planets that would have been swallowed up by the expanding stellar envelope. To achieve equal basic conditions for the comparison of MS and giant stars and to exclude selection effects only long-period planets from the MS surveys were taken into account. Despite this restriction, the metal distribution of the dwarfs does not change. To find differences and similarities in the surveys of MS stars and giants Fig. 7.3 shows the metallicity distribution for those monitored as well as the distribution of MS stars hosting planets (small black dots). The dashed red line represents the distribution of the MS planet-hosting stars with periods longer than 180 days. The data for the MS stars hosting planets are taken from "The extrasolar planets encyclopaedia" arranged by Jean Schneider and available on the webpage http://exoplanet.eu/.

The comparison between both types of planet-hosting stars – MS and giants – shows that the shape of the two distributions is similar, but the distribution of the giants is shifted by about 0.3 dex towards lower metallicity. A Kolmogorov-Smirnov test shows that the probability of belonging to the same population is around 10^{-4}. This difference is surprisingly similar to that present between planet-hosting and non planet-hosting MS stars as can be found in the literature (Santos et al. 2004, 2005). Surveys of G–K giants thus reveal that evolved stars hosting planetary companions are indeed not metal-rich. The next step is to explain this trend.
It is important to investigate how this different behaviour of MS and giant stars is correlated with the process of planet formation. The basic question is if this increased metallicity enhances planet formation, or whether the high metallicity is caused instead by the presence of a planetary system. The correlation with the metallicity can thus be either cause or effect. The observed metallicity distribution of both types of host stars of extrasolar planetary systems should be thus very helpful to choose between the two most popular planet formation mechanisms: core accretion and gravitational instability. In the first case, favoured by the core accretion scenario (Pollack et al. 1996), the stars should be overmetallic down to their center. This scenario proposes that a rocky core grows via the accretion of planetesimals up to 10–15 $M_\oplus$ before a protoplanetary nebula loses most of its H and He inventory (Santos et al. 2001; Gonzalez et al. 1998) and until it has sufficient mass to retain H and He and to

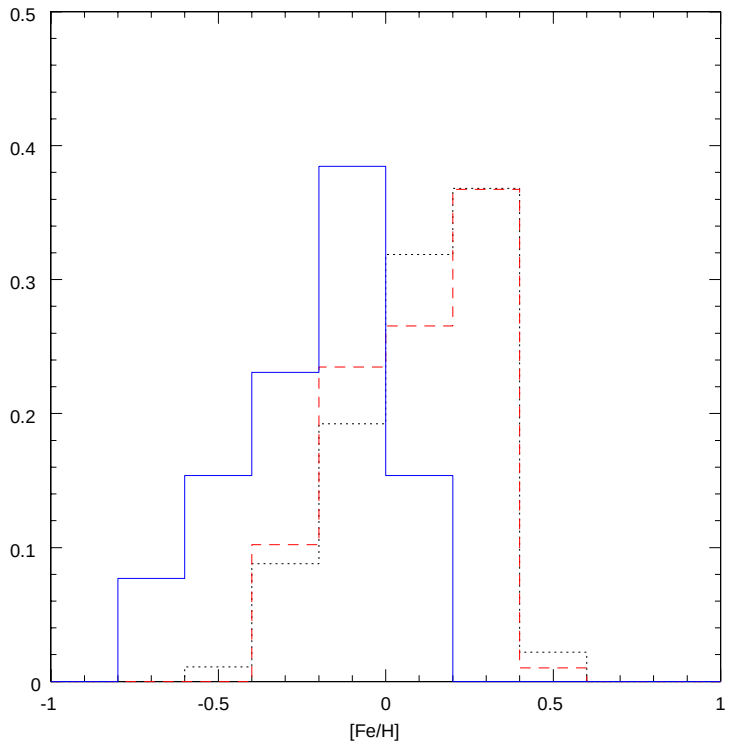

Figure 7.3: Metal distribution for giants hosting exoplanets (full blue line), dwarfs hosting planets with period larger than 180 days (dashed red line) and all dwarfs hosting exoplanets (black dots). The distribution between giants and dwarfs is clearly different, and giants show a distribution shifted to lower metallicity by about 0.2–0.3 dex (Pasquini et al. 2007).

capture gas from the nebula to form an envelope. In this case, the formation of the gas giant planet is very fast and the formation depends strongly on dust content (Ida & Lin 2004). Thus a higher metallicity in proto-planetary nebulae causes a higher frequency of planet formation as a consequence of more dust grains for nucleation (Gilliland et al. 2000). In the second case – not primordial – the higher values for the metallicity are possibly due to the pollution of the convective envelope of the star by the infall of planets and/or planetesimals as well as comets or asteroids (Gonzalez 1998; Laughlin & Adams 1997; Gonzalez 2001; Murray et al. 1998 and Quillen & Holman 2000) onto the star. This pollution can be also caused by the total inward migration of a planet on to the parent star as well as the transfer of material from the disc to the host star as a result of the migration process (Goldreich & Tremaine 1980; Lin et al. 1996) or last but not least to the break-up and infall of one or more planets in multiple systems on to the surface of the star due to gravitational interactions (Rasio & Ford 1996) with other companions. If the star was polluted by the debris of the planetary system, then only the external layers of the atmosphere of the star were affected by this pollution (Laughlin & Adams 1997). Assuming this scenario, the difference in the mass of the convective envelope between MS stars and giants would explain why

the metal excess observed in MS stars is not observed among evolved stars. The reason is that the metal excess produced by this pollution, while visible in the thin atmospheres of solar stars, is completely diluted in the extended, massive atmospheres of the giants. Unfortunately the situation is more complicated because of additional mixing beyond the formal convective boundary, either due to thermohaline convection or "metallic fingers" (Vauclair 2004). The hypothesis of pollution in combination with the convective envelope of evolved stars is a possible explanation to explain the different metallicity between MS and giant stars, but other reasons cannot be excluded. I will explain this working hypothesis in more detail to confirm the plausibility.
While in the Sun the fraction of the solar mass in the convective envelope M_{ce} is $\sim$0.022 $M_\odot$ (log M_{ce} = -1.67), when it reaches its maximum depth along the RGB, this fraction is about 35 times higher, or almost 0.77 $M_\odot$ (log M_{ce} = -0.11). In general, when a 1 $M_\odot$ star becomes a K giant, its convective envelope is of the order of 0.7 $M_\odot$. If the high metallicity observed among MS stars were confined to the superficial layers, with a deepening convective envelope, this would easily be decreased to the artificial abundance for the star. In Fig. 7.4 the fractional mass (in logarithmic units) contained in the convective envelope of stars between 0.8 and 1.5 $M_\odot$ is shown, both on the MS and on the red giant branch, where the convective zone has reached its deepest. This indicates the maximum dilution factor. As an example an excess of 0.25 dex in [Fe/H] (Santos et al. 2005) in a solar star would be diluted to a value less than 1 % in a giant star. Such a quantity is beyond the actual detection capabilities in most observational cases.

If the hypothesis of pollution were validated, an excess of metal-rich stars among MS stars with respect to an equivalent sample of giant stars is expected. In Fig. 7.5 the metal distribution of the giants from da Silva et al. (2006) and Döllinger et al. (2008b) are compared to the distribution of a volume-limited sample of MS stars from Favata et al. (1997) and Santos et al. (2004; 2005). The Favata et al. (1997) sample consists of 91 unbiased G–K dwarfs (see Fig. 7.5) including parent stars (see Fig. 7.3) and non planet-hosting stars.

The distributions of giants and dwarfs are very similar, with the MS stars showing no significant excess in the highest metallicity bins. The comparison between the giants and the Favata et al. (1997) results in particular suggest that the small excess of metal-rich dwarfs is almost perfectly compensated by an excess of solar-metallicity giants, which is exactly the signature which would be expected from pollution. However this excess is mostly due to the coolest MS stars and other aspects, such as age distribution and galactic evaporation should be taken into account to properly compare the data (Favata et al. 1997). Another difference between MS and giant stars is the size of the radius. The *FEROS* and *TLS* giants have radii on average about 10 times larger than solar stars which are determined within the abundance analyses (da Silva et al. 2006; Döllinger et al. 2008b). High metallicity could favour the migration of the planets towards short-period systems; in this case, metal-rich stars would have many more short-period planets than metal-poor stars. These planets would be detected among the MS stars, but not anymore around the giants, because the star, enlarging its radius has swallowed up them. It was noted earlier that in Fig. 7.3 the metallicity distribution is very different for giants than for dwarfs hosting planets with comparable long orbital periods, that is, excluding those with short orbits. This would indicate that the effects of migration, even if present, cannot explain the observed trend. The third main difference between MS stars and giants is, that giants on average have a somewhat higher mass than MS stars surveyed for exoplanets. Taking into account that the mass

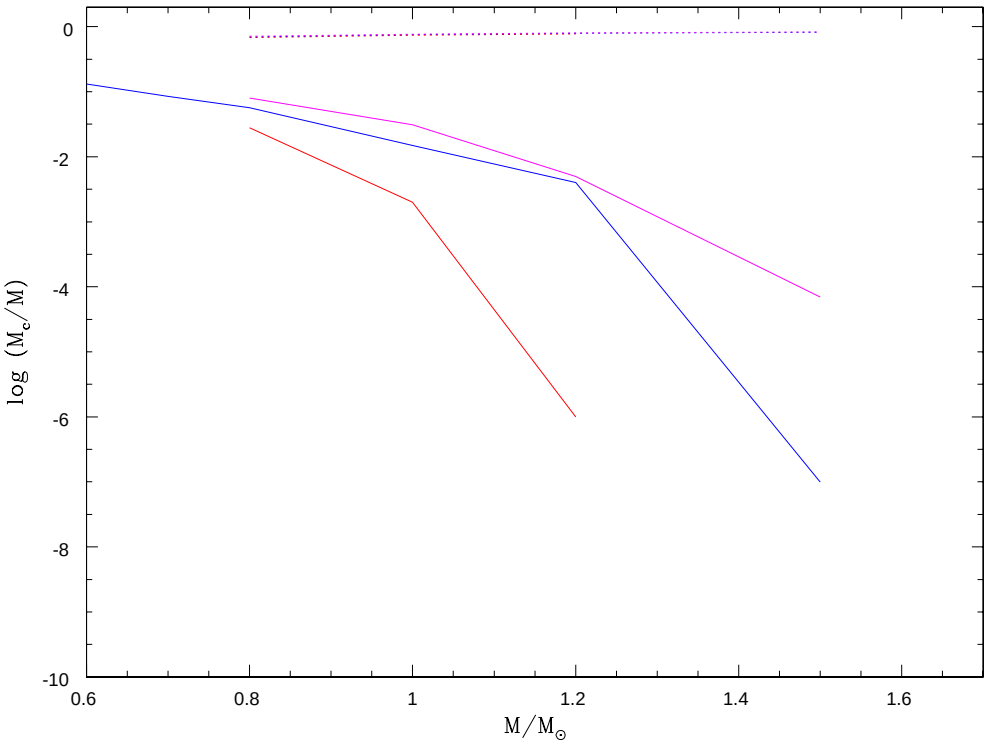

Figure 7.4: Amount of relative mass (logarithmic scale) in the convective envelope for stars of different masses and two phases (main sequence – solid; red giant branch – dotted), and for three different metallicities ($Z = 0.005, 0.017, 0.026$ – red, blue, magenta) The drastic enlargement of the convective mass during the RGB ascent is clearly visible. It is close to a factor ∼50 for a solar-type star (Pasquini et al. 2007).

determination in giant stars suffers large uncertainties, the masses of planet-hosting giants vary between ~ 0.9 and ~ 3 $M_\odot$ (da Silva et al. 2006; Döllinger et al. 2008b), while those of MS stars are between ~ 0.75 and ~ 1.5 $M_\odot$. Since the fraction of planet-hosting giants is largely independent of metallicity, it is feasible that intermediate-mass stars favour a planet formation process, such as gravitational instability, which is independent of metallicity. The metal independent planet formation mechanism could be more efficient in more massive stars, which have more massive disks, and act therefore on giants much more than on MS stars due to their somewhat higher masses. A combination of both previous formation hypotheses working at the same time may be able to produce the observed distribution. Such a dual formation scheme – one metal dependent, a second metal-independent – has indeed been already proposed by Matsuo et al. (2007). The interpretation of the data is not straightforward: a scenario which includes strong differences in planet formation with stellar mass and possibly planet migration is plausible, but the most immediate explanation is that the high metallicity observed among MS stars is caused by pollution of their atmospheres. The metal excess produced by this pollution, while visible in the thin atmospheres of solar-like stars, is completely diluted in the extended, massive envelopes of the giants. This interpretation

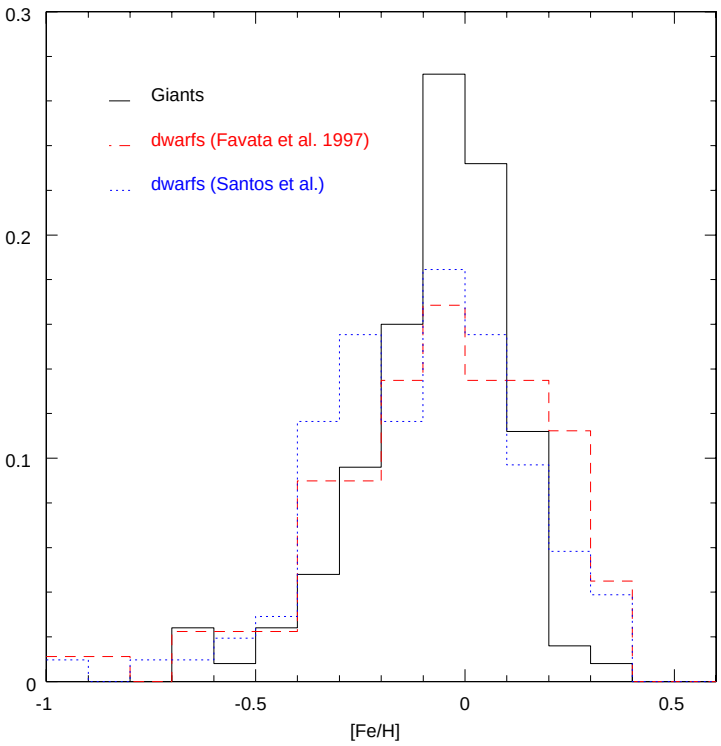

Figure 7.5: Metal distribution for all the giants from the da Silva et al. (2006) and Döllinger et al. (2008b) sample (full black line), for the volume-limited sample of Favata et al. (1997, red-dashed) and Santos et al. (2004, 2005; blue points). An excess of metal-rich stars might be present among the dwarfs. To make such a comparison significant, a number of effects in the sample selection and in the analysis should be considered (Pasquini et al. 2007).

is in apparent contrast with results on MS stars obtained by several groups (Fischer & Valenti 2005; Ecuvillon et al. 2006), which favour the primordial scenario, where stars are born in high metallicity clouds. The possible explanation of this discrepancy is that the effects of pollution on the MS are small and difficult to detect.

Chapter 8

Conclusions

One of the greatest challenge for modern astronomy during the last century was the search for planets around stars beyond our solar system. The idea of their existence goes back to the ancient Greeks more than 2000 years ago. But it was the progress in science and technology over the last twenty years that enabled the discovery of extrasolar planets. The first planets outside our solar system were detected in 1992 around pulsars. Since 1995 with the discovery of 51 Peg we have known of exoplanets around solar-type stars. In the meantime the detected number of extrasolar planets has increased tremendously. At the moment more than 270 have been discovered mostly using the Radial Velocity (RV) method. Despite the advance of this technique, the other detection methods such as transits, microlensing or direct imaging made progress too and a few planets were detected. However the radial velocity method is currently the method of choice for planet-hunting.

In the past solar-type Main Sequence (MS) stars were favoured targets for planet searches, and consequently most of the published planets orbit this type of host star. Very famous in this context are the so-called "hot Jupiters", Jupiter-like planets which are in a very close orbits around their parent stars. Their existence was a big surprise and is still a puzzle. This kind of exoplanet will normally not be present around evolved stars with their enlarged envelope because the planetary companions would be swallowed up.

The knowledge about the existence as well as the frequency of occurrence of planetary companions around other types of stars such as evolved stars was very sparse in contrast to MS stars until a couple of years ago a few groups started some surveys dedicated to G and K giants. One of these surveys – the Tautenburg Observatory Planet Search ($TOPS$) programme – executed with the 2m Alfred Jensch telescope at the Thuringa State Observatory (Thüringer Landessternwarte Tautenburg or TLS) is part of my work and devoted to the search for planets around K giants. At that time giant stars were classified as very difficult targets for planet searches using the RV method. This is because these stars show short-period RV variations in addition to long-period RV variations which can introduce additional scatter in the RV variability.

Despite this possible problem, in February 2004 I started my programme using a sample of 62 giants. The goal of the thesis was to investigate the presence of exoplanets around K giants within the obtainable accuracy of the radial velocity detection method. A previous study in the South (Setiawan et al. 2003a; 2004a) was limited by the achieved RV accuracy of 25–30 $\mathrm{m\,s^{-1}}$ of the Fiber-fed Extended Range Optical Spectrograph ($FEROS$). Using the coudé echelle spectrograph at the TLS which has a resolution of

$R(\frac{\lambda}{\delta\lambda}) \sim 67{,}000$ I was able to achieve during my work a significantly better RV accuracy of 3–5 $\mathrm{m\,s^{-1}}$. It turned out that the higher RV accuracy was essential to differentiate between the different types of RV variability which was an additional aim of my thesis.
Apart from the RV monitoring, a further topic of my work was the determination of Fe abundances as well as the atmospheric stellar parameters such as effective temperature, surface gravity and microturbulence velocity derived from high resolution spectra free of iodine (templates) for the whole sample. This is an important point because it is the first time, to my knowledge, that RV and chemical abundance analysis are connected in the same work and used to determine for instance the age and the mass of the star. Combining the stellar age and mass with the metallicity of the star, the so-called Age-Metallicity Relation (AMR) plot and Mass-Metallicity Relation (MMR) plot was created to investigate correlations.
I determined radial velocities from high resolution spectra taken with the iodine cell. After the time analysis I was able to discriminate between different types of RV variability. The statistics of the Tautenburg survey contain 13 binaries (21 %), 2 stars (3 %) with "constant" radial velocities given a strict limit of $< 10\ \mathrm{m\,s^{-1}}$, 17 stars (27 %) showing short-period RV variations possibly due to stellar oscillations and finally 6 stars (10 %) which show low-amplitude, long-term RV variations possibly due to planetary companions. The RV behaviour of the remaining 24 K giants (39 %) is not clear. Thus with exception of 2 "constant" stars the whole sample shows RV variations which confirms that K giants are RV variable stars.
The detected percentage of exoplanets in my TLS sample is comparable with values derived from a $FEROS$ survey Setiawan et al. (2004b) and confirms that giant planets around giant stars are fairly common. I calculated for my 6 exoplanet candidates and one published binary orbital solutions and I determined all orbital parameters. I used the $HIPPARCOS$ photometry and the Hα activity to confirm the planetary companions and to exclude other causes for the RV variability. The values from the literature for the binary agree very well.
With the templates, I computed Fe abundances and atmospheric stellar parameters. The derived values are in very good agreement with the available literature values. After correlating Fe abundances and RV behaviour it turned out that giant planets around giants do not favour metal-rich stars which is at odds with what it is known from MS stars.
The mass, radius and age of each star were determined by utilising theoretical isochrones and using a modified version of Jørgensen & Lindegren's (2005) method. The metallicity of the star and the age as well as the mass were used to create an AMR and a MMR. I found interesting cases in the plots of metallicity against age and metallicity against mass, namely: the distribution of planet-hosting giants in the TLS and $FEROS$ survey follows the general giants' distribution, the dispersion in the AMR is small when young and increases with age.

Bibiliography

Asida, S.M., and Tuchman, Y. 1997, ApJ, 491, L47
Barden, S.C. 1985, ApJ, 295, 162
Barnes, J. 1993, BAAS, 25, 1435
Barning, F.J.M. 1963, BAN, 17, 22
Beaulieu, J.-P., Bennett, D. P., Fouqué, P., Williams, A., Dominik, M., Jorgensen, U. G., Kubas, D., Cassan, A., Coutures, C., Greenhill, J., and 63 coauthors 2006, Natur, 439, 437
Bensby, T., Feltzing, S., and Lundström, I. 2004, A&A, 421, 969
Biazzo, K. 2007, private communication
Black, D.C., and Scargle, J.D. 1982, ApJ, 263, 854
Bonfils, X., Forveille, T., Delfosse, X., Udry, S., Mayor, M., Perrier, C., Bouchy, F., Pepe, F., Queloz, D., and Bertaux, J.-L. 2005, A&A, 443, 15
Bonfils, X., Mayor, M., Delfosse, X., Forveille, T., Gillon, M., Perrier, C., Udry, S., Bouchy, F., Lovis, C., Pepe, F., and 3 coauthors 2007, A&A, 474, 293
Boss, A.P. 1997, Sci 276, 1836
Butler, R.P., Marcy, G.W., Williams, E., McCarthy, C., Dosanjh, P., and Vogt, S.S. 1996, PASP, 108, 500
Butler, R.P., Vogt, S.S., Marcy, G.W., Fischer, D.A., Wright, J.T., Henry, G.W., Laughlin, G., and Lissauer, J.J. 2004, ApJ, 617, 580
Butler, R.P., Johnson, J.A., Marcy, G.W., Wright, J.T., Vogt, S.S., and Fischer,D.A. 2006, PASP, 118, 1685
Buzasi, D., Catanzarite, J., Laher, R., Conrow, T., Shupe, D., Gautier, T.N., III; Kreidl, T., and Everett, D. 2000, ApJ, 532, 133
Campbell, W.W. 1910, PASP, 22, 99
Campbell, W.W., and Albrecht, S. 1910, LicOB, 5, 174
Carraro, G., Ng, Y.K., and Portinari, L. 1998, MNRAS, 296, 1045
Cayrel de Strobel, G. 1985, IAUS, 111, 137
Cayrel de Strobel, G., Soubiran, C., and Ralite, N. 2001, A&A, 373, 159
Charbonneau, P. 1995, ApJS, 101, 309
Cole, A.A., Tolstoy, E., Gallagher, John S., III, Smecker-Hane, and Tammy A. 2005, AJ, 129, 1465
da Silva, L. 1986, AJ, 92, 451
da Silva, L., Girardi, L., Pasquini, L., Setiawan, J., von der Lühe, O., de Medeiros, J. R., Hatzes, A., Döllinger, M. P., and Weiss, A. 2006, A&A, 458, 603
Delfosse, X., Forveille, T., Mayor, M., Perrier, C., Naef, D., and Queloz, D. 1998, A&A, 338, 67
Delfosse, X., Forveille, T., Beuzit, J.-L., Udry, S., Mayor, M., and Perrier, C. 1999, A&A, 344, 897

Dempsey, R.C., Bopp, B.W., Strassmeier, K.G., Granados, A.F., Henry, G.W., and Hall, D.S. 1992, ApJ, 392, 187
Desidera, S., Gratton, R. G., Endl, M., Barbieri, M., Claudi, R.U., Cosentino, R., Lucatello, S., Marzari, F., Scuderi, S. 2003, A&A, 405, 207
Döllinger, M.P., Pasquini, L., Hatzes, A.P., Setiawan, J., da Silva, L., de Medeiros, J., von der Lüe, O., Girardi, L., di Mauro, M.P., Weiss, A., and Roth, M. 2005, Msngr., 122, 39
Döllinger, M.P., Hatzes, A.P., Pasquini, L., Guenther, E.W., Hartmann, M., Girardi, L., and Esposito, M. 2007, A&A, 472, 649
Döllinger et al. (2008a), in preparation
Döllinger et al. (2008b), in preparation
Dravins, D. 1987, A&A, 172, 200
Duquennoy, A., and Mayor, M. 1991, A&A, 248, 485
Edmonds, P.D., and Gilliland, R.L. 1996, ApJ, 464, L157
Edvardsson, B., Andersen, J., Gustafsson, B., Lambert, D.L., Nissen, P.E., and Tomkin, J. 1993, A&A, 275, 101
Endl, M., Cochran, W.D., Tull, R.G., and MacQueen, P.J. 2003, AJ, 126, 3099
Endl, M., Cochran, W.D., Wittenmeyer, R.A., and Boss, A.P., 2008, ApJ, 673, 1165
Ecuvillon, A., Israelian, G., Santos, N.C., Mayor, M., and Gilli, G. 2006, A&A, 449, 809
Fahlman, G.G., and Glaspey, J.W. 1973 in Astronomical Observations with Television Type Sensors, ed. J.W. Glaspey, and G.A.H. Walker, (Vancouver, B.C.: Inst. of Astronomy and Space Science), 347
Favata, F., Micela, G., and Sciortino, S. 1997, A&A, 323, 809
Fischer, D.A., and Valenti, J.A. 2005, ApJ, 622, 1102
Fischer, D.A., Laughlin, G., Butler, P., Marcy, G., Johnson, J., Henry, G., Valenti, J., Vogt, S., Ammons, M., Robinson, S., and 14 coauthors 2005, ApJ, 620, 481
Fletcher, J.M., Harris, H.C., McClure, R.D., and Scarfe, C.D. 1982, PASP, 94, 1017
Francois, P. 2005, private communication
Frasca, A., and Catalano S. 1994, A&A, 284, 883
Frandsen, S., Carrier, F., Aerts, C., Stello, D., Maas, T., Burnet, M., Bruntt, H., Teixeira, T.C., de Medeiros, J.R., Bouchy, F., and 3 coauthors 2002, A&A, 394, L5
Frandsen, S., Bruntt, H., Grunddahl, F., Kopacki, G., Kjeldsen, H., Arentoft, T., Stello, D., Bedding, T.R., Jacob, A.P., Gilliland, R.L., Edmonds, P.D., Michel, E., and Matthiesen, J. 2007, A&A, 475, 991
Freeman, K.C., and Bland-Hawthorn, J. 2002, ARA&A, 40, 487
Freire Ferrero, R., Frasca, A., Marilli, E., and Catalano, S. 2004, A&A, 413, 657
Frink, S., Mitchell, D.S., Quirrenbach, A., Fischer, D.A., Marcy, G.W., and Butler, R. P. 2002, ApJ, 576, 478
Fuhr, J.R., Martin, G.A., and Wiese, W.L. 1988, Phys. Chem. Ref. Data, 17(S4), 1
Fuhrmann, K., Pfeiffer, M., Frank, C., Reetz, J., and Gehren, T. 1997, A&A, 323, 909
Galland, F., Lagrange, A.-M., Udry, S., Chelli, A., Pepe, F., Queloz, D., Beuzit, J.-L., and Mayor, M. 2005a, A&A, 443, 337
Galland, F., Lagrange, A.-M., Udry, S., Chelli, A., Pepe, F., Beuzit, J.-L., and Mayor, M. 2005b, A&A, 444, 21
Galland, F., Lagrange, A.-M., Udry, S., Beuzit, J.-L., Pepe, F., and Mayor, M. 2006, A&A, 452, 709
Girardi, L., Bressan, A., Bertelli, G., and Chiosi, C. 2000, A&AS, 141, 371
Girardi, L., Bertelli, G., Bressan, A., Chiosi, C., Groenewegen, M.A.T., Marigo, P.,

Salasnich, B., and Weiss, A. 2002, A&A, 391, 195
Gilliland, Ronald L., Brown, T. M., Guhathakurta, P., Sarajedini, A., Milone, E. F., Albrow, M. D., Baliber, N. R., Bruntt, H., Burrows, A., Charbonneau, D., and 14 coauthors 2000, ApJ, 545, L47
Goldreich, P., and Tremaine, S. 1980, ApJ, 241, 425
Gonzalez, G. 1997, MNRAS, 285, 403
Gonzalez, G. 1998, A&A, 334, 221
Gonzalez, G., Laws, C., Tyagi, S., and Reddy, B.E. 2001, AJ, 121, 432
Gratton, L., Gaudenzi, S., Rossi, C., and Gratton, R.G. 1982, MNRAS, 201, 807
Gray, D.F. 1982, ApJ, 255, 200
Griffin, R.F. 1967, ApJ, 148, 465
Griffin, R.F. 1982, Observatory, 102, 82
Griffin, R.F., Harris, H.C., and McClure, R.D. 1983, JRASC, 77 73
Gustafsson, B., Kjaergaard, P., and Anderson, S. 1974, A&AS, 34, 99
Gustafsson, B., Bell, R.A., Eriksson, K., and Nordlund, A. 1975, A&A, 42, 407
Hatzes, A.P., and Cochran, W.D. 1993, ApJ, 413, 339
Hatzes, A.P., and Cochran, W.D. 1994a, ApJ, 422, 366
Hatzes, A.P., and Cochran, W.D. 1994b, ApJ, 432, 763
Hatzes, A.P. 1996, PASP, 108, 839
Hatzes, A.P., and Cochran, W.D. 1998, MNRAS, 293, 469
Hatzes, A.P., Guenther, E.W., Endl, M., Cochran, W.D., Döllinger, M.P., and Bedalov, A. 2005, A&A, 437, 743
Hatzes, A.P., Cochran, W.D., Endl, M., Guenther, E.W., Saar, S.H., Walker, G.A.H., Yang, S., Hartmann, M., Esposito, M., Paulson, D.B., and Döllinger, M.P. 2006, A&A, 457, 335
Hatzes, A.P., and Zechmeister, M. 2007, AAS, 211, 2104
Heintz, W.D. 1971, Doppelsterne. München: Wilhelm Goldmann Verlag. 186
Herbig, G. H. 1985, ApJ, 289, 269
Horne, J.H., and Baliunas, S.L. 1986, ApJ, 302, 757
Hoyle, F., and Schwarzschild, M. 1955, ApJS, 2, 1
Ida, S., and Lin, D.N.C. 2004, ApJ, 616, 567
Ida, S., and Lin, D.N.C. 2005, ApJ, 626, 1045
Jefferys, W., Fitzpatrick, J., and McArthur, B. 1988, Celest. Mech, 41, 39
Johnson, J.A., Butler, R.P,. Marcy, G.W., Fischer, D.A., Vogt, S.S., Wright, J.T., and Peek, K.M.G. 2007a, ApJ, 670, 833
Johnson, J.A., Marcy, G.W., Fischer, D.A., Wright, J.T., Reffert, S., Kregenow, J.M., Williams, P.K.G., and Peek, K.M.G. 2007b, arXiv0711.4367J
Jones, H.R.A., Butler, R.P., and Tinney, C.G. 2004, The distribution of exo-planet properties with semimajor axis. In ASP Conf. Ser. 321 Extrasolar Planets, Today and Tomorrow, ed. Beaulieu, J.P., Lecavelier, A., and Terquem, C., 298
Joshi, B., and Joshi, A. 2005, Sol. Phys., 226, 153
Jørgensen, and B.R., Lindegren, L. 2005, A&A, 436, 127
Keenan, P.C., and Pitts, R.E. 1980, ApJS, 42, 541
Kürster, M., Schmitt, J.H.M., Cutispoto, G., and Dennerl, K. 1997, A&A, 320, 831
Lambert, D.L., and Ries, L.M. 1981, ApJ, 248, 228
Laughlin, G., and Adams, F.C. 1997, ApJ, 491, L51
Lin, D.N.C., Bodenheimer, P., and Richardson, D.C. 1996, Natur, 380, 606
Lomb, N.R. 1976, Ap&SS, 39, 477
Luck, R.E., and Lambert, D.L. 1985, ApJ, 256, 189

Luck, R.E. 1991, ApJS, 75, 579
Luck, R.E., and Challener, S.L. 1995, AJ, 110, 2968
Marcy, G.W., and Butler, R.P. 1992, 104, 270
Marcy, G.W., Butler, R.P., and Vogt, S.S. 2000, ApJ, 536, L43
Marcy, G.W., Butler, R.P., and Fischer, D.A. 2004, A Doppler planet survey of 1330 FGKM stars, ASP Conference Proceedings, 321, 3
Matsuo, T., Shibai, H., Ootsubo, T., and Tamura, M. 2007, ApJ, 662, 1282
Mayor, M., and Queloz, D. 1995, Natur, 378, 355
McArthur, B., Jefferys, W., and McCartney, J. 1994, AAS, 184, 2804
McClure, R.D. 1983, ApJ, 268, 264
McWilliam, A. 1990, ApJS, 74, 1075
Mermilliod, J.-C., Clari, J.J., Andersen, J., Piatti, A.E., and Mayor, M. 2001, A&A, 375, 30
Murray, N., Hansen, B., Holman, M., and Tremaine, S. 1998, Sci, 279, 69
Murray, C.D., and Dermott, S.F. 1999, Solar system dynamics, Cambridge: Cambridge University Press, 592
Mitchell, D.S., Frink, S., Quirrenbach, A., Fischer, D.A., Marcy, G.W., and Butler, R.P. 2003, AAS, 203, 1703
Nicolet, B. 1978, A&ApS, 34, 1
Niedzielski, A., Konacki, M., Wolszczan, A., Nowak, G., Maciejewski, G., Gelino, C.R., Shao, M., Shetrone, M., and Ramsey, L.W. 2007, 669, 1354
Nilsen, P.E., Hoeg, E., and Schuster, W.J. 1997, in Proceedings of the ESA Symposium Hipparcos - Venice "97", ESA SP-402, 225
Nordström, B., Mayor, M., Andersen, J., Holmberg, J., Pont, F., Jørgensen, B.R., Olsen, E.H., Udry, S., and Mowlavi, N. 2004, A&AS, 418, 989
Pasquini, L., and Pallavicini, R. 1991, A&A, 251, 199
Pasquini, L., Randich, S., Zoccali, M., Hill, V., Charbonnel, C., and Nordström, B. 2004, A&A, 424, 951
Pasquini, L., Döllinger, M.P., Weiss, A., Girardi, L., Chavero, C., Hatzes, A.P., da Silva, L., and Setiawan, J. 2007, A&A, 473, 979
Pasquini, L., Döllinger, M.P., Hatzes, A., Setiawan, J., Girardi, L., da Silva, L., and de Medeiros, J.R. 2008, arXiv0802.1532
Perryman, M.A.C., Lindegren, L., Kovalevsky, J., Hoeg, E., Bastian, U., Bernacca, P.L., Crézé, M., Donati, F., Grenon, M., van Leeuwen, F., and 9 coauthors 1997, A&A, 323, L49
Perryman, M.A.C., Brown, A.G.A., Lebreton, Y., Gomez, A., Turon, C., de Strobel, G.C., Mermilliod, J.C., Robichon, N., Kovalevsky, J., and Crifo, F. 1998, A&A, 331, 81
Pollack, J.B., Hubickyj, O., Bodenheimer, P., Lissauer, J.J., Podolak, M., and Greenzweig, Y. 1996, Icarus, 124, 62
Queloz, D., Henry, G.W., Sivan, J.P., Baliunas, S.L., Beuzit, J.L., Donahue, R.A., Mayor, M., Naef, D., Perrier, C., and Udry, S. 2001, A&A, 379, 279
Quillen, A.C., and Holman, M. 2000, AJ, 119, 397
Rasio, F.A., and Ford, E.B. 1996, Sci 274, 954
Reddy, B.E., Tomkin, J., Lambert, D.L., and Allende Prieto, C. 2003, MNRAS, 340, 304
Reffert, S., Quirrenbach, A., Mitchell, D.S., Albrecht, S., Hekker, S., Fischer, D.A., Marcy, G.W., and Butler, R.P. 2006, ApJ, 652, 661
Rivera, E.J., Lissauer, J.J., Butler, R.P., Marcy, G.W., Vogt, S.S., Fischer, D.A.,

Brown, T.M., Laughlin, G., and Henry, G.W. 2005, ApJ, 634, 625
Rocha-Pinto, H.J., Maciel, W.J., Scalo, J., and Flynn, C. 2000, A&A, 358, 850
Ruland, F., Biehl, D., Holweger, H., Griffin, R., and Griffin, R. 1980, A&A, 92, 70
Santos, N.C., Israelian, G., and Mayor, M. 2000, A&A, 363, 228
Santos, N.C., Israelian, G., and Mayor, M. 2001, A&A, 373, 1019
Santos, N.C., Israelian, G., Mayor, M., Rebolo, R., and Udry, S. 2003, A&A, 398, 363
Santos, N.C., Israelian, G., and Mayor, M. 2004, A&A, 415, 1153
Santos, N.C., Israelian, G., and Mayor, M. 2005, A&A, 437, 1127
Sato, B., Ando, H., and Kambe, E. 2003, ApJ 597, L157
Sato, B., Fischer, D.A., Henry, G.W., Laughlin, G., Butler, R.P., Marcy, G.W., Vogt, S.S., Bodenheimer, P., Ida, S., Toyota, E., and 11 coauthors 2005, ApJ, 633, 465
Sato, B., Izumiura, H., Toyota, E., Kambe, E., Takeda, Y., Masuda, S., Omiya, M., Murata, D., Itoh, Y., Ando, H., and 4 coauthors 2007, ApJ, 661, 527
Scargle, J.D. 1982, ApJ, 263, 835
Schlegel, D.J., Finkbeiner, D.P., and Davis, M. 1998, ApJ, 500, 525
Schuler, S.C., Kim, J.H., Tinker, M.C., Jr., King, J.R., Hatzes, A.P., and Guenther, E.W. 2005, ApJ, 632, L131
Setiawan, J., Hatzes, A.P., von der Lühe, O., Pasquini, L., Naef, D., da Silva, L., Udry, S., Queloz, D., and Girardi, L. 2003a, A&A, 397, 1151
Setiawan, J., Pasquini, L., da Silva, L., von der Lühe, O., and Hatzes, A. 2003b, A&A, 398, L19
Setiawan, J., Pasquini, L., da Silva, L., Hatzes, A.P., von der Lühe, O., Girardi, L., de Medeiros, J.R., and Guenther, E. 2004, A&A, 421, 241
Setiawan, J., da Silva, L., Pasquini, L., Hatzes, A.P., von der Lühe, O., Girardi, L., and Guenther, E. 2004b, ASPC, 318, 283
Setiawan, J., Rodmann, J., da Silva, L., Hatzes, A.P., Pasquini, L., von der Lühe, O., de Medeiros, J.R., Döllinger, M.P., and Girardi, L. 2005, A&A, 437, L31
Smith, P.H., McMillan, R.S., and Merline, W.J. 1987, ApJ, 317, L79
Steenbock, W. 1985, in Cool Stars with Excesses of Heavy Elements, ed. M. Jascheck, and P.C. Keenan (Dordrecht: Reidel), 231
Stothers, R.B., and Chin, C.-W., 1995 ApJ, 400, 297
Takeda, G., Ford, E.B., Sills, A., Rasio, F.A., Fischer, D.A. and Valenti, J.A. 2007, ApJS, 168, 297
Tomkin, J., and Lambert, D.L. 1983, Ap. J., 273, 722
Toner, C.G., and Gray, D.F. 1988, ApJ 334, 1008
Twarog, B.A. 1980, ApJ, 242, 242
Udry, S., Bonfils, X., Delfosse, X., Forveille, T., Mayor, M., Perrier, C., Bouchy, F., Lovis, C., Pepe, F., Queloz, D., and Bertaux, J.-L. 2007, A&A, 469, 43
Valenti, J.A., and Basri, G.B. 1992, BAAS, 24, 1288
Valenti, J.A., Butler, R.P., and Marcy, G.W. 1995, PASP, 107, 966
Valenti, J.A., Harper, G.M., Bennett, P.D., and Linsky, J. L. 1996, ASPC, 109, 577
Valenti, J.A., and Fischer, D.A. 2005, ApJS, 159, 141
Vauclair, S. 2004, ApJ, 605, 874
van Leeuwen, F., Evans, D.W., Grenon, M., Grossmann, V., Mignard, F., and Perryman, M.A.C. 1997, A&A, 323, L61
Walker et al. 1989 Wallenhorst, S.G. 1980, ApJ, 241, 229
Ward, W. 1997, ApJ, 482, L211
Wood, P.R. 2006, Convection in Astrophysics, Proceedings IAU Symposium No. 239, F. Kupka, I.W. Roxburgh, and K.L. Chan, eds.